UNIVERSIDADE ESTADUAL PAULISTA
"JÚLIO DE MESQUITA FILHO"
INSTITUTO DE QUIMICA DE ARARAQUARA

ERIKA VIVIANA GODOY ALARCON

Synthesis, Electronics and Electrochemistry of Electro-Active Peptide Structures and Heterocyclic Compounds

Thesis in cotutelle with the University of Minho-Portugal presented to the Institute of Chemistry, São Paulo State University-Brazil, in fulfillment of the requirements for the degree of Doctor of Philosophy in chemistry

Supervisor: Prof. Dr. Paulo Roberto BUENO
Prof. Dra. Maria Manuela MARQUES RAPOSO
Co-Supervisor: Prof. Dr. Eduardo MAFFUD CILLI

Araraquara
2025

Alarcon, Erika Viviana Godoy
A321s Synthesis, electronics and electrochemistry of electro-active peptide structures and heterocyclic compounds / Erika Viviana Godoy Alarcon – Araraquara: [s.n.], 2025
215 p.: il.

Thesis (doctor) – Universidade Estadual Paulista, Instituto de Química
Advisor: Paulo Roberto Bueno
Advisor: Maria Manuela Marques Raposo
Co-advisor: Eduardo Maffud Cilli

1.Quantum electrodynamics. 2. Charge transfer. 3. Impedance spectroscopy. 4. Peptides – Synthesis. 5. Heterocyclic compounds. I. Title.

Sistema de geração automática de fichas catalográficas da Unesp. Biblioteca do Instituto de Química, Araraquara. Dados fornecidos pelo autor(a).

Essa ficha não pode ser modificada

UNIVERSIDADE ESTADUAL PAULISTA
"JÚLIO DE MESQUITA FILHO"
INSTITUTO DE QUIMICA DE ARARAQUARA

ERIKA VIVIANA GODOY ALARCON

Síntese, Eletrônica e Eletroquímica de Estruturas Peptídicas Eletroativas e Compostos Heterociclicos

Tese em cotutela com a Universidade do Minho-Portugal apresentada ao Instituto de Química, Universidade Estadual Paulista-Brazil como parte dos requisitos para obtenção do título de doutora em Química.

Orientadores: Prof. Dr. Paulo Roberto BUENO
Prof. Dra. Maria Manuela MARQUES RAPOSO
Coorientador: Prof. Dr. Eduardo MAFFUD CILLI

Araraquara
2025

UNIVERSIDADE ESTADUAL PAULISTA

Câmpus de Araraquara

CERTIFICADO DE APROVAÇÃO

TÍTULO DA TESE: "Synthesis, Electronics and Electrochemical Properties of Electro-Active Peptide Structures and Heterocyclic Compounds"

AUTORA: ERIKA VIVIANA GODOY ALARCÓN
ORIENTADOR: PAULO ROBERTO BUENO
COORIENTADORA: MARIA MANUELA MARQUES RAPOSO

Aprovada como parte das exigências para obtenção do Título de Doutora em Química, pela Comissão Examinadora:

Assinado por : **MARIA MANUELA MARQUES RAPOSO**
Num. de Identificação: BI062977814
Data: 2025.04.11 18:38:08 +0100

CARTÃO DE CIDADÃO

Prof.ª Dr.ª MARIA MANUELA MARQUES RAPOSO (Participaçao Virtual)
Departamento de Química / Universidade do Minho - Minho - Portugal

Prof. Dr. PAULO ROBERTO BUENO (Participaçao Virtual)
Departamento de Fisica e Matematica / Instituto de Quimica - UNESP - Araraquara

gov.br
Documento assinado digitalmente
PAULO ROBERTO BUENO
Data: 11/04/2025 14:10:45-0300
Verifique em https://validar.iti.gov.br

Prof. Dr. CHRISTOPHER MICHAEL ASHTON BRETT (Participaçao Virtual)
Departamento de Química / Universidade de Coimbra - Portugal

Prof.ª Dr.ª SUSANA PAULA GRAÇA COSTA (Participaçao Virtual)
Departamento de Química / Universidade do Minho - Portugal

Prof. Dr. BRUNO CAMPOS JANEGITZ (Participaçao Virtual)
Ciências da natureza, Matemática e Educação / Universidade Federal de São Carlos - UFSCAr - Araras

Araraquara, 11 de abril de 2025

Impacto potencial

A investigação desenvolvida nesta tese de doutoramento traz avanço na eletroquímica quântica ao estabelecer a capacitância quântica como um importante parâmetro experimental para a determinação da constante de velocidade de transferência eletrônica em reações eletroquímicos com ausência de difusão, como monocamadas automontadas de peptídeos redox. A nova abordagem permite dar um significado isoscópico para a energia de reorganização de Marcus, possibilitando um controle mais preciso e um entendimento mais acurado das propriedades de transferência eletrônicas em escala molecular. Além do impacto teórico, a pesquisa permitiu contribuir para o desenvolvimento de um biossensor em que as propriedades quânticas associadas a resistência e capacitância de uma interface de grafeno modificada com moléculas heterociclicas *push-pull* para detecção de marcadores genéticos, demonstrando a aplicabilidade das propriedades de comunicação eletrônica fundamentada na teoria da *quantum rate* em dispositivos de grafeno molecularmente funcionalizados (resultando no pedido do depósito da patente BR1020250030357). Os resultados da investigação desta tese não apenas fortalecem a base científica da teoria da *quantum rate*, mas também impulsionam o desenvolvimento futuro de novas tecnologias de sensoriamento baseadas em interfaces moleculares altamente estruturadas.

Potential impact

The research conducted in this doctoral thesis advances quantum electrochemistry by establishing quantum capacitance as a key experimental parameter for determining the electron transfer rate constant in electrochemical reactions without diffusion, such as redox peptide self-assembled monolayers. This novel approach provides an isoscopic interpretation of Marcus's reorganization energy, enabling more precise control and a deeper understanding of electron transfer properties at the molecular scale. Beyond its theoretical impact, the research has contributed to the development of a biosensor in which quantum properties related to resistance and capacitance were explored in a graphene interface modified with *push-pull* heterocyclic molecules for genetic marker detection. This demonstrated the applicability of electronic communication properties grounded in quantum rate theory in molecularly functionalized graphene devices, leading to the filing of patent application BR1020250030357. The findings of this thesis not only strengthen the scientific foundation of quantum rate theory but also drive the future development of new sensing technologies based on highly structured molecular interfaces.

Curriculum Vitae

Name: Erika Viviana GODOY ALARCON
Citation Name: EVG Alarcón
Birth date: 19/02/1993 – Bucaramanga (Santander) – Colombia
Professional address: UNESP-Instituto de Química, Departamento de Físico-Química
Rua Prof. Francisco Degni, 55, Bairro Quitandinha
CEP: 14800-060, Araraquara, São Paulo, Brazil

Education

Araraquara, Brazil **Braga, Portugal** **02/2020 – 01/2025**	**Ph.D in Chemistry** São Paulo State University - UNESP Scholarship: São Paulo Research Foundation- FAPESP, process n^o 2019/27510-5 **Ph.D in Applied Chemistry** University of Minho - UMINHO Thesis: *Synthesis, Eletronics and Electrochemical Properties of Electro-Active Peptides Structures and Heterocyclic Compounds* Supervisors: Prof. Dr. Paulo Roberto Bueno Prof. Dra. Maria Manuela Marques Raposo Co-supervisor: Prof. Dr. Eduardo Maffud Cilli
Bucaramanga, Colombia **02/2012 – 12/2017**	**B.Sc. in Chemistry** Industrial University of Santander - UIS Final degree project: *Evaluation of Electrical Impedance Spectroscopy as a Technique for the Detection of Gram-Positive and Gram-Negative Bacteria* Supervisor: Prof. Dr. David Miranda Mercado Co-supervisors: Prof. Dr. Ángel Manuel Melendez Reyes Prof. Dra. Stelia Carolina Mendez Sanchez

Professional Positions 💼

Braga, Portugal **08/02/2023 – 10/02/2024**	**International internship under a cotutelle agreement** University of Minho Scholarship: São Paulo Research Foundation-FAPESP, process n^{o} 2022/08575-1 ‣Synthesis of *push-pull* heterocyclic molecules functionalyzed with anchoring-capable groups onto electrodes for electrochemical studies
Bucaramanga, Colombia **07/2018 – 07/2019**	**Co-supervisor of a Bachelor's student** Industrial University of Santander - UIS ‣Study of the Potential Effect on the Electrochemical Deposition of Mercury-Cadmium Selenide onto Titanium and its Implications for Use in Solar Cells
Bucaramanga, Colombia **03/2019– 05/2019**	**Researcher Support Professsional** Industrial University of Santander - Santander League Against Cancer ‣Project: Validation of Electrical Impedance Spectroscopy in Liquid Phase as a Screening Technique for Cervical Cancer
Bucaramanga, Colombia **09/2018 – 11/2018**	**Professional Support of Education Project** Industrial University of Santander ‣Structuring educational projects for physics doctoral program
Bucaramanga, Colombia **05/2017 – 07/2017** **09/2017 – 12/2017**	**Administrative Assistant** Office of Academic Affairs of Industrial Universty of Santander ‣Research group classification process for COLCIENCIAS, conducting purchases, and supporting CIMBIOS and CMN research groups

Honors 🏆

- ✔ *Merit award:* Best Poster Award, in 74th Annual Meeting of the International Society of Electrochemistry, Lyon-France (2023)

Publications & Preprints

Published

- MERCADO, D. A.; ALARCÓN, E. V. G.; V-NIÑO, E. D. Time evolution of electrical impedance spectra of *Staphylococcus aureus* and *Escherichia coli* bacteria. *Bioelectrochemistry*. 155, 108557, doi:10.1016/j.bioelechem.2023.1085576 (2024)

- PINZÓN, E. F.; ALARCÓN, E. V. G.; SÁNCHEZ, Y. P.; BUENO, P. R. Quantum rate dynamics and charge screening at the nanoscale level. *Physical Chemistry Chemical Physics*. 24(26):16200–16206, doi:10.1039/D2CP00199C (2022).

- ALARCÓN, E. V. G.; SANTOS, A.; BUENO, P. R. Perspective on quantum electrochemistry. A simple method for measuring the electron transfer rate constant. *Electrochimica Acta*. 398:139219, doi:10.1016/j.electacta.2021.139219 (2021).

- GONZÁLES-CAMACHO, F. A.; DURAN-URIBE, E. S.; GODOY-ALARCÓN, E. V.; MIRANDA, D. A.; MELÉNDEZ, A. M. Composition control by bath temperature and use of supporting electrolyte in electrodeposited mercury cadmium selenide thin films. *Journal of Physics: Conference Series*. 119(1)012001, doi:10.1088/1742-6596/1119/1/012001 (2018).

Patent

- BUENO, P.R., RAPOSO, M.M.M.; ALPUIM, J.P, BORME, J.G.O.; PINZON, E.F.; GODOY, E.V.; SANTOS, J.P.; DOMINGUES, T.C.; Attomolar Sensors and Applications of Photoelectric Devices with Quantum Resistive-Capacitive (RC) Transducer Signal from Single-Layer Graphene (SLG) Modified with Organic Semiconductor Quantum Dots. 2025, Brasil. Invention Patent. Patent number: BR1020250030357. Registration institution: INPI – National Institute of Industrial Property. 14/02/2025

Congress

- Poster: *ALARCON, E.V.G., SANTOS, A., BUENO, P.R*. Quantum rate theory principles and experimental measurements of the electron transfer rate constant. Presented at 74^{th} Annual meeting of the International Society of Electrochemistry, France, 2023.

- Poster: *ALARCON, E.V.G., SANTOS, A., BUENO, P.R., CILLI, E.M., BUENO, P.R*. "Electrochemical behavior of a redox peptide self-assembled monolayer modified interface". Presented at 1^{st} National congress of physics, chemistry and engineer of materials (online), 2021.

- Poster: *ALARCON, E.V.G., MIRANDA, D. A., MELÉNDEZ, A. M.*. What are the causes of low reproducibility in electrical impedance measurements in a tetrapolar cell. Presented at XVII Colombia congress of chemistry, Colombia, 2017.

Scientific Events

- II Colombian congress of electrochemistry and 2^{nd} Symposoium on Nanoscience and Nanotechnology, Bucaramga, Colombia, 2016.

To my parents, Alfonso and Josefina-
for their love, and unwavering belief in me

Acknowledgements

I gratefully acknowledge the São Paulo Research Foundation (FAPESP) for the scholarship granted, process n^{o} 2019/27510-5. I thank Professor Paulo Bueno for his guidance, insightful discussions, and the freedom to explore my ideas in the lab. I am deeply grateful to Professor Manuela Raposo for her unwavering support, both in research and personally, as well as her dedication throughout my process. I sincerely thank Professor Eduardo Maffud Cilli for his hands-on mentorship, constant availability, and for treating me as a colleague, which greatly boosted my confidence as a researcher. I sincerely thank my colleagues from the Nanobionics research group for the enriching discussions that shaped both my thesis and professional growth. A special thanks to my dear friend Yuliana for her unwavering support and invaluable friendship—sharing this journey with you made even the hardest days more bearable. I am also grateful to Lais and Leandro for their invaluable advice on balancing life as a PhD student, which helped me appreciate the entire journey. To Gabi and Thamires, your calm and peaceful nature brought me tranquility and a fresh perspective during challenging times. To Nicolas, whose insightful questions deepened my understanding, and to Isabella, who encouraged me to stand by my ideas. I also appreciate Edgar and Adriano for their timely academic insights. I am deeply grateful to Sarah for her invaluable support in peptide synthesis, and for your warm friendship, which made my lab days much more enjoyable. To Professor Manuela's research group, thank you for welcoming me so kindly in Portugal—I found a true treasure in your friendship. Special thanks to Nunita, Sónia, and Raquel for their patience, guidance, and excellent advice in the organic lab. I also cherish the great moments shared with Francisca, Cátia, Mariana, Ângela, Mathilde, and Inês. Lastly, my heartfelt appreciation to the Duarte Pereira family for giving me a home in Portugal. I appreciate the lab technicians, Elisa Matos (RMN lab), the office staff—especially Rose Portasio, Wennia Limonti, and Cidália Moreira—for their support, and UNESP and UMINHO for the facilities.

I am deeply grateful to my dear friend Monica for her unwavering support and encouragement and belief in me have meant more than words can express. To Silvia and Nenu, your unwavering support and warmth have shown me that true friendship knows no distance. My deepest gratitude goes to my parents Alfonso and Josefina, my sister Laura, and my love, Luisk—for you, I am here today. Thank you for always believing in me, even in the moments when I doubted myself. Your unconditional love has been my greatest source of strength, my safe haven, and my motivation to keep going. I cannot thank you enough for being my home, my foundation, and my greatest supporters.

"No se puede vivir con miedo, menos hacias las cosas que te hacen mas feliz."

Juliana Velasquez, Mar Adentro

Abstract

Electron transfer and transport in molecular structures are crucial for understanding biological processes, that inspire technological innovations. Traditionally, chemists have focused on electron transfer (ET) rate, while physicists have focused on molecular conductance analysis. Recent efforts have aimed at connecting the principles behind these phenomena. A key advance was based on the perception that both phenomena are correlated with the meaning of the quantum capacitance C_q that depends on the density-of-states and which, considering statistical mechanics, has the occupancy of the states governed by Fermi-Dirac statistics, providing the basement for quantum rate theory (QRT). This thesis applies the principles of QRT to investigate two types of junctions within electrolytic environments: formed by electro-active peptides and π-conjugated heterocyclic compounds. For a redox-active peptide self-assembled monolayer (SAM) anchored to a metallic electrode, the quantum nature of the ET rate constant (k) was proposed based on measurement C_q, in which two degeneracy rules were introduced: one tied to electron spin characteristics and the other associated with superposition of electrostatic and quantum mechanical energies.

The influence of the electrolyte environment on electron coupling κ was examined and the quantification of environmental effects on the ET dynamics was investigated. Building on these insights, further investigations were conducted to explore how the components of the SAM structure, specifically the linker groups and peptide bridges, affect quantum ET dynamics. Although linker groups were found to modulate the characteristics of SAM without disrupting conductance, the bridge component of the SAM structure affects the energy barrier and consequently the κ. These findings underscored the importance of molecular architecture in the control of ET processes, establishing a direct connection between structural design and ET dynamics. Another goal of this thesis was to study the observed adiabatic electron communication in *push-pull* heterocyclic molecular junctions, which were engineered by anchoring *push-pull* molecules on metallic gold interfaces. Further, the same approach was made with graphene for biological sensing purposes. In both situations, the QRT principles were applied conveniently to explain the results.

In summary, this thesis integrates molecular design, synthesis, and QRT principles to investigate electrodynamics in electrolytic media. It provides quantum insights into non-adiabatic ET in peptide SAMs and adiabatic electron communication in *push-pull* heterocyclic molecular junctions. By unifying electrochemistry and electronics, the findings enhance our understanding of electrodynamics in molecular systems, offering a foundation for future technological applications.

Resumo

A transferência e o transporte eletrônico em estruturas moleculares são cruciais para a compreensão de processos biológicos que inspiram inovações tecnológicas. Tradicionalmente, os químicos têm-se concentrado na taxa de transferência eletrônica (ET), enquanto os físicos têm-se focado na análise de condutância molecular. Esforços recentes têm procurado conectar os princípios adjacentes a esses dois fenômenos. Um avanço significativo foi a percepção de que ambos os fenômenos estão correlacionados com o conceito de capacitância quântica (C_q), que depende da densidade de estados e, considerando a mecânica estatística, possui a ocupação dos estados governada pela estatística de Fermi-Dirac, fornecendo a base para a teoria de taxas quânticas (QRT). Esta tese aplica os princípios da QRT para investigar dois tipos de junções moleculares em ambientes eletrolíticos: formadas por peptídeos eletroativos e compostos heterociclicos π-conjugados. Para uma monocamada auto-organizada (SAM) de peptídeo redoxativo ancorada a um eletrodo metálico, a natureza quântica da constante de taxa de ET (k) foi proposta com base na medição de C_q, na qual duas regras de degenerescência foram introduzidas: uma relacionada com as características do spin eletrônico e outra associada à superposição das energias eletrostática e mecânica quântica. A influência do ambiente eletrolítico no acoplamento eletrônico (κ) foi examinada, e a quantificação dos efeitos ambientais na dinâmica de ET foi investigada. Com base nesses *insights*, investigações adicionais foram conduzidas para explorar como os componentes da estrutura da SAM, especificamente os grupos de ligação e as pontes peptídicas, afetam a eletrodinâmica quântica do ET. Embora os grupos de ligação modulassem as características da SAM sem interromper a condutância, o componente da ponte na estrutura da SAM afeta a barreira de energia e, consequentemente, o κ. Esses resultados ressaltaram a importância da arquitetura molecular no controle dos processos de ET, estabelecendo uma conexão direta entre o design estrutural e a eletrodinâmica de ET. Outro objetivo desta tese foi estudar a comunicação eletrônica adiabática observada em junções moleculares heterociclicas *push-pull*, que foram projetadas ao ancorar moléculas *push-pull* em interfaces de ouro metálico. Além disso, a mesma abordagem foi usada utilizando grafeno tendo como objetivo a sua aplicação em bio(sensores). Em ambas as situações, os princípios da QRT foram convenientemente aplicados para explicar os resultados. Em resumo, esta tese integra o design molecular, a síntese e os princípios da QRT para investigar a eletrodinâmica em meios eletrolíticos. Ela fornece *insights* quânticos sobre ET não adiabático em SAMs de peptídeos e comunicação eletrônica adiabática em junções moleculares heterociclicas *push-pull*. Ao unificar a eletroquímica e a eletrônica, os resultados ampliam a compreensão da eletrodinâmica em sistemas moleculares, oferecendo uma base para futuras aplicações tecnológicas.

Resumo extendido

A QRT surgiu da necessidade de unificar a compreensão da ET e do ET_p em arranjos moleculares, dois fenômenos eletrodinâmicos tradicionalmente estudados separadamente por químicos e físicos. Enquanto os químicos investigam a dinâmica da ET em meios eletrolíticos, focando no entendido da constante de velocidade k para descrever a velocidade de troca eletrônica entre espécies D e A, os físicos analisam o ET_p em sistemas de estado sólido, utilizando a condutância G como parâmetro fundamental, baseado no formalismo de Landauer. Essa separação disciplinar levou ao desenvolvimento de abordagens metodológicas distintas, dificultando uma visão integrada dos processos eletrônicos e eletroquímicos. No entanto, a necessidade de compreender fenômenos eletrodinâmicos em sistemas moleculares complexos, como a cadeia de transporte de elétrons na membrana mitocondrial — essencial para a sustentação da vida na terra — ou a condução eletrônica em biofilmes de *Geobacter*, com potencial para aplicações tecnológicas avançadas, tornou essencial um entendimento de como se dá a convergência entre esses conceitos.

Nesse contexto, Abraham Nitzan foi pioneiro ao propor uma correlação teórica entre k e G em junções moleculares. Embora essa correlação tenha sido estudada em alguns sistemas, discrepâncias foram evidentes e associadas as diferenças conceituais e experimentais entre as medições eletroquímicas em meio líquido (para k) e medições de G em ambiente seco. A abordagem da QRT avança a compreensão da correção entre k e G ao introduzir o conceito de C_μ como elo, por meio da relação simples $k = G/C_\mu$. Isso permite modelar esses processos por meio de circuitos equivalentes com elementos quânticos resistivos e capacitivos. Neste caso, a combinação em séries destes elementos possibilita estabelecer um tempo característico RC, definido como $\tau = R_q C_\mu$. Dessa forma, a QRT fornece uma base teórica e experimental capaz de descrever a comunicação entre estados eletrônicos, seja em processos de transferência eletrônica envolvendo reações redox, seja em processos de transporte eletrônico sem participação de eventos redox. Além disso, a teoria pode ser aplicada a arranjos moleculares sobre eletrodos independentemente do tipo de acoplamento eletrodo-molécula, sejam eles adiabáticos ou não adiabáticos. Isso ocorre devido à incorporação do coeficiente de transmissão κ na definição de G, a qual pode ser escrita como $G = NG_0\kappa$, onde quando $\kappa = 1$ tem-se processos adiabáticos e quando $\kappa \gg 1$ tem-se processos não adiabáticos.

A QRT tem sido continuamente aperfeiçoada, refletindo a sua natureza dinâmica e evolutiva como uma base teórica para descrever a eletrodinâmica em sistemas moleculares e nanoscópicos em meio eletrolítico, incluindo grafeno, semicondutores inorgânicos e pontos quânticos. Além disso, a QRT desempenha um papel central no desenvolvimento de biossensores baseados em SAMs de peptídeos contendo grupos

redox, nos quais a transdução de sinal ocorre via C_q. Esses avanços conceituais e as suas aplicações motivou a presente investigação, cujo objetivo central foi aprofundar a compreensão das propriedades quânticas associadas à eletrodinâmica em dois tipos específicos de moléculas orgânicas: peptídeos funcionalizados com grupos redox, já anteriormente explorados no contexto da QRT no que se refere a aplicação em sensores, e compostos heterociclos π-conjugados, introduzidos nesta tese como uma nova abordagem para a compreensão dos mecanismos de ET_p em meio eletrolítico.

As SAMs de peptídeos marcados com grupos redox foram escolhidas como alvo nesta tese por sua relevância como sistemas modelo para o estudo da ET em distâncias moleculares longas, um fenômeno fundamental em processos biológicos como a respiração celular e a catálise enzimática. Inspirados nas cadeias biológicas de ET, que envolvem proteínas e cofatores orgânicos e inorgânicos, esses peptídeos organizados em SAMs sobre eletrodos permitem investigar a ET não-adiabática por tunelamento quântico de forma controlada. Além disso, diferentemente de proteínas naturais, que podem apresentar limitações experimentais devido à sua instabilidade estrutural em diferentes condições, os peptídeos sintéticos podem ser manipulados com precisão por meio da SPPS o que leva a uma flexibilidade estrutural que possibilita a adaptação das moléculas de acordo com os requisitos específicos, seja para investigações fundamentais em eletrodinâmica, seja para aplicações tecnológicas como o desenvolvimento de biossensores.

Além dos peptídeos redox, esta tese também aborda o estudo de moléculas heterociclicas *push-pull*, cujo interesse decorre de as suas propriedades eletrônicas singulares e do potencial para aplicações tecnológicas avançadas. Caracterizadas pela presença de grupos D e A de elétrons conectados por uma ponte π-conjugada, estas moléculas exibem uma deslocalização eletrônica intrínseca que facilita a transferência de carga intramolecular. Este comportamento, amplamente explorado na literatura, tem impulsionado sua aplicação em dispositivos optoeletrônicos, como OFETs, OLEDs e materiais óticos não-lineares (NLO) e quimiosensores óticos. No contexto desta tese, um aspecto particularmente relevante das moléculas *push-pull* é a sua interação com eletrodos, que levanta questões fundamentais sobre a ET_p que, diferentemente da ET redox que ocorre sem reações redox, envolve a comunicação direta (sem presença de efeitos de tunelamento) entre estados eletrônicos da molécula e do eletrodo. Este fenômeno abre novas perspectivas para o desenvolvimento de tecnologias eletrônicas e biossensores baseados em propriedades quânticas, tema que foi estudado no último capítulo da tese.

Esta tese resulta de cinco anos de pesquisa, nos quais a síntese orgânica, a eletroquímica e a QRT constituíram os pilares fundamentais da investigação. O trabalho está estruturado em cinco capítulos, sendo que o primeiro descreve o estado do arte enquanto que os outros quatro capítulos abordam as principais questões científicas

relacionadas a estes sistemas. Para os sistemas baseados em peptídeos, as seguintes perguntas de investigação foram formuladas: i) como pode ser demonstrada experimentalmente a natureza quântica da ET em SAMs de peptídeos marcados com grupos redox?; ii) de que forma o ambiente eletrolítico modula a natureza quântica da ET e qual sua relação com a teoria de Marcus?; iii) como as características estruturais da SAM, incluindo os grupos de ancoragem e a composição da ponte peptídica, afetam o acoplamento eletrônico, a distribuição de estados quânticos e a eficiência do transporte de carga?. Já para os sistemas baseados em moléculas heterociclicas *push-pull*, a questão central a investigar foi: i) as propriedades quânticas associadas à eletrodinâmica dessas estruturas podem ser exploradas em função do desenho/concepção das estruturas para seu melhor acoplamento em eletrodos?; além disso, ii) tais propriedades podem ser usadas como sinais de transdução para o desenvolvimento de dispositivos biossensores?

A fim de responder à primeira questão de investigação, o Capítulo 2 apresenta a análise de k, derivada dos primeiros princípios da mecânica quântica no âmbito da QRT, aplicada à ET em SAM de peptídeos marcados com ferroceno, considerado como um sistema heterogêneo eletroquímico sem difusão, revelando a natureza intrinsecamente quântica do evento de ET. A QRT estabelece que k, pode ser obtida experimentalmente a partir da C_q, uma propriedade mensurável em curvas de CV em baixas velocidades de varredura s, por meio da normalização da i por s e da análise de espectros capacitivos obtidos a partir da resposta de impedância no V_F. A metodologia desenvolvida demonstrou que a relação entre G e C_q permite acessar a cinética do processo de ET ao considerar a dinâmica de carga nos estados eletrônicos, assumindo regras específicas de degenerescência relacionadas ao spin do elétron e à compensação de carga promovida pelo meio eletrolítico, composto pelo solvente e pelo eletrólito suporte. Além disso, a comparação entre os valores de k obtidos pelo método do QR e pelo método de Laviron revelou que, embora ambos resultem em k equivalentes, diferem fundamentalmente em seus princípios. O método de Laviron, ancorado na teoria cinética clássica, opera em um regime afastado do equilíbrio, enquanto a abordagem quântica se fundamenta no regime de equilíbrio.

Essa análise evidenciou que, em sistemas confinados, como as SAMs redox, os efeitos quânticos são amplificados e desempenham um papel central na determinação de k, justificando a necessidade de um tratamento quântico para uma descrição precisa desses processos. Dessa forma, a QRT não apenas corroborou a natureza quântica da ET nesses sistemas, mas também forneceu um caminho experimental para determinar k a partir da C_q, um parâmetro diretamente acessível em medições eletroquímicas convencionais como CV e EIS. Assim, o estudo propõe um novo paradigma para a análise da cinética de ET, onde a influência do ambiente

eletroquímico e a natureza discreta dos estados eletrônicos são incorporadas, superando as limitações das descrições clássicas e estabelecendo um novo horizonte para a compreensão da reatividade eletrônica em escala molecular.

A segunda questão de investigação, relacionada com a influência do ambiente eletrolítico nas propriedades da eletrodinâmica quântica do processo de ET sob a perspectiva da QRT e sua relação com a teoria de Marcus, foi abordada no Capítulo 3. A abordagem tradicional, baseada no modelo contínuo da teoria de Marcus, considera os efeitos dielétricos do solvente, caraterizado pela ε, sob a estabilização da configuração nuclear das espécies redox. No entanto, os resultados experimentais obtidos neste estudo, conduzido em misturas de água e acetonitrila com uma composição iônica fixa, revelaram que a influência do solvente e os íons do eletrólito desempenham um papel essencial, modulando as propriedades dielétricas locais e promovendo o acoplamento entre estados clássicos e quânticos da ET. Essa análise evidenciou que a reorganização energética, definida como λ e central na teoria de Marcus, pode ser reinterpretada em termos capacitivos, adquirindo um significado quântico.

Diferentemente dos modelos clássicos, que tratam os efeitos do solvente independentemente da estrutura eletrônica dos reagentes, a QRT incorpora tanto a energia de solvatação externa quanto a energia eletrônica interna, estabelecendo uma relação fundamental entre ambas. Essa interdependência, imposta pelas condições de eletroneutralidade do meio, permite distinguir dois regimes de solvatação: (i) solvatação implícita, na qual a permissividade dielétrica ε influencia k conforme previsto pela teoria de Marcus, e (ii) solvatação explícita, em que a solvatação preferencial altera a relação entre ε e k por meio de mudanças no acoplamento eletrônico, refletidas no parâmetro κ. Assim, este estudo reforça as limitações dos modelos clássicos na descrição da interação entre solvente, estrutura eletrônica e cinética reacional, destacando a QRT como uma base mais abrangente para a compreensão da ET em sistemas eletroquímicos.

No quarto capítulo, foi investigada a influência das características estruturais da SAM, incluindo a composição da ponte peptídica e os grupos de ancoragem, sobre a dinâmica da ET e seus parâmetros eletrônicos associados. Dentre esses parâmetros, κ foi de particular interesse, pois a sua sensibilidade a efeitos externos, como a influência do solvente, estudada no capítulo 3, sugere um possível papel relevante na resposta a modificações estruturais. Para explorar essa relação, foram realizadas variações na ponte peptídica, incluindo o aumento do número de aminoácidos, o que levaria a uma modificação na distância entre o eletrodo e a sonda redox, e a introdução de resíduos específicos, como a Gln, cujo grupo amida na cadeia lateral poderia afetar as interações intermoleculares. Além disso, foram modificados os grupos de ancoragem, incorporando unidades mono e bidentadas contendo um ou dois

átomos de enxofre, respectivamente. Os resultados demonstraram que a N, no V_F, desempenha um papel central na determinação de k. Mesmo em sistemas onde κ apresentava valores elevados, uma redução significativa em N levou a uma queda expressiva em k, evidenciando que a densidade de estados acessíveis tem um impacto mais relevante do que o acoplamento eletrônico na regulação da cinética de ET. Além disso, a análise da ancoragem revelou que ligantes bidentados favorecem um maior acoplamento eletrônico, resultando em k mais elevados. Assim, este estudo expande as investigações anteriores sobre o efeito do meio eletrolítico, ao demonstrar que o grupo de ancoragem da SAM também modula de forma significativa as propriedades eletrônicas do sistema. Os resultados reforçam a aplicabilidade da QRT na análise estrutural da ET em sistemas heterogêneos sem difusão e fornecem diretrizes fundamentais para otimização estruturada de interfaces eletrônicas baseadas em peptídeos.

Finalmente, o último capítulo desta tese (capítulo 5) consiste no design, síntese e aplicação de moléculas heterociclicas do tipo *push-pull* com grupos de ancoragem projetados para promover sua imobilização em eletrodos de ouro e grafeno, possibilitando a investigação de suas propriedades eletrodinâmicas quânticas por meio da QRT, bem como para potencial aplicação como biosensores. No caso das moléculas destinadas à imobilização em ouro, foi estabelecida uma via de síntese promissora. No entanto, várias dificuldades, como a baixa solubilidade de alguns precursores, bem como a instabilidade dos grupos protetores tiol, limitaram a obtenção direta dos compostos pretendidos. Por outro lado, foram sintetizados com sucesso cinco compostos com design apropriado para imobilização em grafeno as quais apresentavam grupos que promoviam interações π-π *stacking* com a superfície do eletrodo, além de grupos carboxila que poderão ser usados para aplicação em plataformas biossensoras. Após a obtenção destas moléculas, a sua imobilização em eletrodos de grafeno permitiu a análise das propriedades eletrodinâmicas do ET_p, caracterizado pela comunicação eletrônica entre os estados eletrônicos da molécula e do eletrodo. Esta investigação, realizada sob a perspectiva da QRT e em um ambiente eletroquímico, revelou aspectos fundamentais da estrutura eletrônica das moléculas, permitindo a sua utilização como sinal transdutor no desenvolvimento de um biossensor genômico. Os resultados obtidos no âmbito das moléculas heterociclicas do tipo *push-pull*, provam o design apropriado e a metodologia de sintese eficaz, ampliando o potencial de sensores moleculares baseados em propriedades quânticas para aplicações em diagnóstico molecular.

List of Abbreviations

A	**A**cceptor state (or specie or group)
ACN	Acetonitrile
AcOH	Acetic acid
Ala	Alanine
ATP	Adenosine triphosphate
CV	**C**yclic **V**oltammetry
Cys	Cysteine
D	**D**onor state (or specie or group)
DCM	Dichloromethane
DIC	*N,N'*-Diisopropylcarbodiimide
DIPEA	*N,N*-Diisopropiletilamina
DMAc	*N,N*-Dimethylacetamide
DMAP	4-Dimethylaminopyridine
DME	Dimethoxyethane
DMF	Dimethylformamide
DNA	Deoxyribonucleic acid
DOS	**D**ensity-**o**f-**S**tate
ECS	**E**lectrochemical Impedance-derived **C**apacitive **S**pectroscopy
EDODT	2,2'-(Ethylenedioxy)diethanethiol
EIS	**E**lectrochemical **I**mpedance **S**pectroscopy
Eq	Equation
ESI	Electrospray ionization
ET	**E**lectron **T**ransfer
EtOAc	Ethyl acetate
EtOH	Ethyl alcohol
Et_2O	Ethyl ether
ET_p	**E**lectron **T**trans**p**ort
Fc	Ferrocene
Fc^+	Oxidized form of ferrocene
Fmoc	9-fluorenylmethyloxycarbonyl
FRA	**F**requency **R**esponse **A**nalysis
FWHM	**F**ull **W**idth at **H**alf **M**aximum

Gln	Glutamine
Glu	Glutamic acid
HBTU	*N,N,N′,N′*-Tetramethyl-O-(1H-benzotriazol-1-yl) uroniumhexafluorophosphate
Hex	Hexane
HOBt	Hydroxybenzotriazole
HOMO	**H**ighest **O**ccupied **M**olecular **O**rbital
HPLC	**H**igh **P**erformance **L**iquid **C**hromatography
L_a	**L**ipoic acid
LUMO	**L**owest **U**noccupied **M**olecular **O**rbital
Lys	Lysine
MO	**M**olecular **O**rbital
MS	**M**ass **S**pectrometry
Mtt	Methyltrityl
N.D	**N**ot **D**one
NH_4OAc	Ammonium Acetate
NMR	**N**uclear **M**agnetic **R**esonance
N.P	**N**ot **P**urified
OCP	**O**pen **C**ircuit **P**otential
P.E	Petroleum ether
PyBOP	Benzotriazole-1-yl-oxy-tris-pyrrolidino-phosphonium hexafluorophosphate
QRS	**Q**uantum-**R**ate **S**pectroscopy
QRT	**Q**uantum-**R**ate **T**heory
r^2	Coefficient of regression
RC	**R**esistive **C**apacitive circuit
SAM	**S**elf-**A**ssembled **M**onolayer
SD	**S**tandard **D**eviation
SLG	**S**ingle **L**ayer **G**raphene
SPPS	**S**olid-**P**hase **P**eptide **S**ynthesis
$TBAClO_4$	Tetrabutylammonium perchlorate
TFA	Trifluoroacetic acid
TIS	Triisopropylsilane
TLC	**T**hin **L**ayer **C**hromatography
TMS	Tetramethylsilane
Trt	Trithyl
TST	**T**ransition **S**tate **T**heory
UV	**U**ltra**V**iolet

List of Symbols and Units

A_e	electroactive area	cm^{-2}
$\mathbf{c}_*$	Fermi velocity	$\mathrm{m\,s}^{-1}$
C	capacitance	$\mathrm{F\,cm}^{-2}$
$C^*(\omega)$	complex capacitive function	
C'	imaginary capacitive component	$\mathrm{F\,cm}^{-2}$
C''	real capacitive component	$\mathrm{F\,cm}^{-2}$
C_{dl}	double layer capacitance	$\mathrm{F\,cm}^{-2}$
C_e	electrostatic capacitance	$\mathrm{F\,cm}^{-2}$
C_m	monolayer capacitance	$\mathrm{F\,cm}^{-2}$
C_q	quantum capacitance	$\mathrm{F\,cm}^{-2}$
$C_{q,a}$	anodic capacitive value	$\mathrm{F\,cm}^{-2}$
$C_{q,c}$	cathodic capacitive value	$\mathrm{F\,cm}^{-2}$
C_t	non-Faradaic capacitance	$\mathrm{F\,cm}^{-2}$
C_μ	electrochemical capacitance	$\mathrm{F\,cm}^{-2}$
e	elementary charge	C
$E^\ddagger$	Activation energy	eV
E^0	Gibbs energy	$\mathrm{J\,mol}^{-1}$
E_F	Fermi level	eV
V_F	formal potential	V
E_e	electrostatic energy	eV
E_q	quantum energy	eV
f	Fermi–Dirac distribution function	
f_r	relaxation (or resonance) frequency	Hz (s^{-1})
G	quantum conductance	mS

G_0	conductance quantum	mS
g_e	redox degeneracy	
g_s	electron spin degeneracy	
h	Planck constant	$\mathrm{eV\,Hz^{-1}}$
$\hbar$	reduced Planck constant	eV s
i	electric current	A
i_{pa}	anodic peak current	A
i_{pc}	cathodic peak current	A
i_a/i_c	redox current peak ratio	
$\mathbf{j}$	complex number	
k	electron transfer rate constant	$\mathrm{s^{-1}}$
$\mathbf{k}$	wave-vector	$\mathrm{m^{-1}}$
k_B	Boltzmann constant	$\mathrm{eV\,K^{-1}}$
L	separation length	nm
n	individual quantum channel	
N	total number of quantum channels	
p	momentum	
q	charge	C
R	resistance	Ω
R_K	Klitzing constant	Ω
R_q	quantum resistance	Ω
R_{qt}	internal monolayer resistance	Ω
R_s	series resistance	Ω
R_t	non-Faradaic relaxation resistance	Ω
s	scan rate	$\mathrm{V\,s^{-1}}$
T	temperature	K or °C
V	electric potential	V
V_F	formal potential	V
V_{out}	potential outside electrochemical window	V

V_p	potential peak	V
V_{pa}	anodic potential peak	V
V_{pc}	cathodic potential peak	V
$\bar{x}$	mean value	
Z^*	complex impedance	
Z'	imaginary impedance component	Ω
Z''	real impedance component	Ω
α	transfer coefficient	
α_c	deviation parameter Cole	
β	tunneling decay parameter	Å^{-1}
ΔV_p	peak-to-peak separation	V
ν	frequency	Hz (s^{-1})
ν_{ET}	electron transfer frequency	s^{-1}
ν_{EC}	electron communication frequency	s^{-1}
κ	transmission coefficient	
λ	reorganization energy	eV
μ	chemical potential	eV
$\sigma_{\bar{x}}$	standard error of the mean	
τ	time constant	s
ϕ	phase angle	$^\circ$
ω	angular frequency	rad s^{-1}
ω_r	relaxation angular frequency	rad s^{-1}
ω_c	characteristic angular frequency	rad s^{-1}

Contents

Context

This thesis investigates the electrodynamics of two types of interfaces formed by redox-peptides and *push-pull* heterocyclic molecules, which revealed weak and strong electronic coupling with the electrode, respectively. These molecular structures can be attached to metallic electrodes allowing to investigate the electrodynamics using the premises of the QRT, which is a quantum electrodynamics theory that correlates with experiments through a quantum resistive-capacitive dynamics. The approach not only provides insight into quantum electrodynamics phenomenon but also allows the examination of the electronic and electrochemistry of these junctions through time-dependent methods such as Electrochemical Impedance Spectroscopy (EIS). By applying a time-dependent potential perturbation to a molecular interface in dynamics charge equilibrium, in the presence of an electrolyte environment, the system's characteristic time constant ($\tau = RC$) can be determined. This τ is directly related to quantum electrodynamics owing to be associated with a characteristic frequency, $\nu = 1/\tau = E/h$, where $E = e^2/C$ represents the energy. In the case of redox-tagged SAMs based on peptide structures, which exhibit non-adiabatic ET, the $\nu_{ET} \propto E/h\kappa$ corresponds to the ET rate constant. Conversely, for junctions formed by monolayers of π-conjugated *push-pull* heterocyclic molecules, the electrodynamics are adiabatic, and the $\nu_{EC} \propto E/h$ reflects the rate of electronic communication between the quantum molecular states and the electrode. As key parameters, ν_{ET} or ν_{EC}, through the measurement of C_q and R_q, capture the nature of the electrodynamics in these systems, providing a detailed understanding of their behavior at the molecular scale.

The motivation for a comparative study of redox-tagged SAMs and *push-pull* heterocyclic molecular junctions is outlined in Chapter 1. Electro-active peptides provide valuable insights to understand ET that can be correlated with biological processes, undergoing in proteins, whereas *push-pull* heterocyclic molecules, with a donor-π spacer-acceptor structure, provide useful applications in opto-electronics. Together, these systems offer the opportunity to understand the differences and similarities between electronics (ET_p event) and electrochemistry (ET event). The goal of this thesis is to explore how QRT enhances our understanding of two interconnected phenomena: ET_p and ET, within electrolyte environments. QRT allows the investigation of ET and ET_p processes with the main differences involving adiabatic (in the case of

ET_p) or non-adiabatic (in the case of ET) events which, as is the case of the present study, involves ET (presence of redox reaction) or electron communication (absence of redox reaction). The ability of the QRT to describe both phenomenon is related to the fact that both phenomenon are ruled by quantum electrodynamics. Accordingly, to better introduce the context of this thesis, it is structured into two parts: the first focuses on non-adiabatic ET in redox-peptide SAMs, while the second examines adiabatic electronic communication in *push-pull*-type heterocyclic molecular interfaces.

The first part of the thesis focuses on the synthesis and electrochemical behavior of redox-tagged SAMs, where the ET process is mediated by peptide bridge structures. These bridges enable non-adiabatic ET to occur under diffusionless electrodynamic control, with $\nu_{ET} = \kappa e^2/hC_q$, where κ is the transmission coefficient. Experimentally, ν_{ET} depends on the measurement of C_q, as introduced in Chapter 2. Chapter 3 further explores the influence of electrolyte properties on κ, demonstrating that ET dynamics depends on electronic coupling. Building on the findings from Chapter 2 and Chapter 3, Chapter 4 examines how variations in redox-tagged structures, such as linker groups and peptide bridges, affect ET dynamics, with interpretations guided by QRT. The final part of the thesis, Chapter 5, based on the fact that quantum states in *push-pull* molecular junction can be accessed and communicate with the electrode despite of the the absence of ET, was focused on the design and synthesis of *push-pull* heterocyclic molecules containing anchoring groups to be anchored on graphene electrodes, with the aim to access their electrodynamic properties through QRS with application in biological sensing.

The highlights of each chapter are introduced below:

- The quantum nature of ET dynamics in redox-tagged SAMs was demonstrated and a straightforward methodology was proposed for calculating the ET rate constant through the measurement of C_q using CV or EIS methods.

- The role of the electrolyte environment in the ET dynamics was studied in redox-tagged SAMs in which it was demonstrated how the external potential of the solvent addressed by the meaning of electrostatic capacitance affects the redox quantum states and how this correlates with the Marcus's ET theory.

- The kinetics of redox-tagged peptide-based SAMs were critically influenced by the linker group, the peptide's amino acid composition, and the electrode-probe distance. These structural factors were shown to alter κ, influencing G and C_q terms that quantifies the ET dynamics.

- A synthetic route for *push-pull* heterocyclic molecules designed for anchoring to gold electrodes was developed. Additionally, a series of *push-pull* heterocyclic molecules, featuring anchoring groups to promote $\pi - \pi$ stacking with

graphene electrodes, were synthesized for electrodynamics studies and quantification using QRT were performed with a demonstrated potential application in biological sensing assays.

0.1 Objective

The main goal of this thesis was to demonstrate that by carefully designing and synthesizing molecular assemblies capable of being anchored onto electrodes, it is possible to address their electronics and electrochemistry through a theory based on the first principles of quantum mechanics referred to as QRT. This theoretical approach was used to interpret the electrodynamics occurring in two molecular systems: (a) one constituted of redox-tagged peptides undergoing ET via non-adiabatic process and another (b) *push-pull* semiconducting molecules in which ET is absent but where exist an electronic communication that follows an adiabatic dynamics. Both electrodynamics were investigated in electrolytic environments in which QRT provided a quantum mechanical description that unify electronics and electrochemistry.

Chapter 1

State-of-the-art

Molecules are sophisticated and structurally complex nanostructures. Not only do they possess intriguing electronic properties, but they also offer remarkable flexibility. Through the art of chemical synthesis, their chemical structure can be tailor to meet specific requirements. This ability to manipulate matter at the molecular level became an important assumption after Richard P. Feynman's landmark talk, "Plenty of Room at the Bottom", delivered to the American Physical Society in 1959 (FEYNMAN, 1959). Feynman's vision urged scientists to delve deeper into the microscopic world. He advocated for the development of tools to explore this new frontier and construct systems capable of probing its mysteries. Feynman's lecture emphasized the need for a paradigm shift. He challenged scientists to move beyond the familiar laws of classical physics, which govern the macroscopic world, and embrace the realm of quantum mechanics. By doing so, he anticipated the discovery of entirely new phenomena and possibilities. Following this pivotal address, the concept of molecular engineering, previously explored by Arthur R. Von Hippel a few years earlier (VON HIPPEL, 1956), gained significant traction. The prospect of building materials from the ground up, one molecule at a time, started to appear achievable.

Building on this challenging perspective, organic molecules, characterized by their carbon-based backbones, present promising molecular structures for exploration. Traditionally, organic molecules with fully saturated bonds have been considered electrical insulators (BOULAS *et al.*, 1996). However, those modified with donor *D* and acceptor *A* structures or containing unsaturated bonds have demonstrated remarkable electronic properties, expanding their range of applications (INOKUCHI, 2006; SPANGGAARD; KREBS, 2004; QI; TIAN; YU, 2018; GATTO *et al.*, 2013). Beyond their electronic behavior, many organic molecules also exhibit optical, electromechanical, and magnetic properties, further enhancing their versatility (SONG *et al.*, 2020; M. FERNANDES *et al.*, 2018; BATISTA *et al.*, 2008). Understanding how charges move in organic molecular structures is critical. This knowledge not only unveils the secrets behind fundamental biological processes like cellular respiration but also holds the

key to revolutionary technological advancements in fields such as molecular and organic electronics (FAHLMAN *et al.*, 2019; OWENS; MALLIARAS, 2010; MARQUÉS-GONZÁLEZ; LOW, 2016). To explore the fundamental phenomena underlying these properties and their electronic applications, researchers have proposed constructing molecular assemblies directly on electrode surfaces for electrochemistry studies. This approach allows the tailoring of molecular structures for specific functions and gaining deeper insights into charge movement within these structures (LI, Y. *et al.*, 2014; WANG, J. *et al.*, 2024; ECKERMANN *et al.*, 2010).

The adoption of organic molecular assemblies on surfaces emerged from experimental and theoretical evidence showing that devices based on molecules exhibit superior performance compared to those relying on bulk materials (WHITESIDES; KRIEBEL; MAYERS, 2005; BUENO, 2018b; LI, Y. *et al.*, 2014; REDONDO-GÓMEZ *et al.*, 2024). This superiority arises from the ability to tailor the intrinsic properties of organic molecules by modifying their chemical structures through conventional synthesis. By meticulously designing of organic molecular systems and their assemblies on electrodes, researchers developed highly efficient solar cells (REGINATO *et al.*, 2018), advanced organic electronics (WANG, J. *et al.*, 2024), and novel sensors (VANOVA *et al.*, 2021). Another exciting avenue for molecular assemblies on electrodes, is their potential to mimic the remarkable efficiency of biological charge transport (OWENS; MALLIARAS, 2010). Certain biological structures excel at conducting charges over long distances (GRAY; WINKLER, 2003), and understanding these mechanisms may allow researchers to replicate this efficiency in synthetic man-made systems. This could pave the way for designing biological mimetic materials with superior conductivity, potentially revolutionizing fields like energy storage and bioelectronics (ZHANG; LU; WAIGH, 2021; JUHANIEWICZ; PAWLOWSKI; SEK, 2015). Additionally, molecular interfaces offer unique properties at the molecular scale, driven by quantum effects prevalent at the nanoscale (PINZÓN *et al.*, 2024; SÁNCHEZ; SANTOS; BUENO, 2022; ALARCÓN; SANTOS; BUENO, 2021; NIETO *et al.*, 2024). Despite significant progress, gaps remain in the understanding of quantum phenomena, and translating theoretical insights into practical experimental applications continues to be a challenging that requires scientific attention.

It is important to emphasize that the electrochemical and electronic properties of organic molecular interfaces are driven by their intrinsic electrodynamics, which can vary depending on whether the systems involve electrochemical reactions or not and whether the processes are adiabatic or non-adiabatic. This thesis focuses on two intriguing subgroups of organic molecules that exemplify these diverse electrodynamics: redox-tagged peptides and *push-pull* heterocyclic molecules. The key difference between these two subgroups lies in the nature of their electrodynamics associated with their molecular structure and the presence or absence of redox states. Peptides

modified with redox moieties undergo electron transfer (ET) through redox reactions that alter the oxidation states. This serves as a simplified model for ET reactions, mimicking those present in proteins, which are essential for processes such as cellular respiration. In contrast, *push-pull* heterocyclic molecules, a specialized class of organic semi-conductive molecules, exhibit significant electrodynamics without undergoing redox reactions. Their delocalized π-electron systems create charge distribution asymmetry, enabling electronic communication through their structure without changes in oxidation state, when communicating with the electrode. This differs from traditional "ET" and emphasizes the wave characteristics of the electrons in the adiabatic transport (NIETO *et al.*, 2024). The purpose of this thesis lies in the design and synthesis of these two types of organic structures, peptides and *push-pull* heterocyclic molecules, to form molecular assemblies on electrode surfaces, with the goal of investigating ET and transport phenomena. Molecular modifications are used to construct these assemblies and to examine how changes affect the electrodynamics and the electron communication with the electrode. The QRT approach, a powerful tool for both theoretical and experimental analyses, is employed to interpret the electrodynamics from a quantum mechanical perspective.

This state-of-the-art framework elucidates the significance of analyzing the electrodynamics of redox-tagged peptides and *push-pull* heterocyclic molecular interfaces, and how QRT enhances our understanding of the phenomenon involved in their electrodynamics and electron communication with electrodes in each case. Sections 1.1 and 1.2 explore the motivation behind constructing electro-active peptide SAMs, which are important, as a model, for understanding ET that occurs in proteins and that helps to have insights into essential cellular mechanisms. Section 1.3 focus on *push-pull* molecular assemblies on surfaces, emphasizing their potential in technological device applications associated with their unique optoelectronic properties. The intrinsic electrodynamics operating in these two types of organic structures will be studied using the QRT approach, as detailed in Section 1.4 of this chapter. The versatility of the QRT in studying various electrodynamics phenomena across different systems constitutes a strength. The coupling modes can be non-adiabatic, as observed in redox-tagged peptide SAMs undergoing ET, or adiabatic, as in *push-pull* molecular assembly in which the communication with the electrode occurs in the absence of ET reactions.

1.1 Long-distance electron transport in biological structures

Biological structures have intrigued researchers because of their extraordinary ability to transport charges efficiently across large molecular distances (10-30 Å) at rapid speeds (LANE, 2005; GRAY; WINKLER, 2003). To shed light on this phenomenon, scientists from fields such as physics, chemistry, biology, and engineering have developed a variety of theories, experiments, and models (MARCUS; SUTIN, 1985; WINKLER; GRAY, 2014; ECKERMANN *et al.*, 2010; SHAH *et al.*, 2015; BUREŠ, 2014). One of the major challenges is to comprehend how electrons can traverse such long distances within protein complexes. Much of the focus is on understanding the role of "molecular bridges" and the factors that affect ET rates in the complex biological environment. Discovering how these phenomena work not only enhances our knowledge of fundamental biological processes but also opens promising opportunities for advances in bioelectronics, renewable energy, and other technological areas.

ET reactions, involving the transfer of electrons between molecules by altering their oxidation states, are known as redox reactions. Accordingly, ET is one of the most important fundamental chemical concepts in chemistry and biochemistry, driving redox reactions, which are ubiquitous in biological systems, and underpinning essential life processes. For example, within our cells, mitochondria act as powerhouses for cellular respiration, generating the energy necessary for cellular growth and reproduction. This energy production is facilitated by the electron transport (ET_p) chain formed by complexes of proteins embedded in the inner mitochondrial membrane. The ET_p chain establishes a proton gradient, which ultimately drives the synthesis of adenosine triphosphate (ATP), the cell's primary energy currency (Figure 1.1). Similarly, in photosynthetic eukaryotic cells, the electrons are transported within protein complexes and fueling the synthesis of carbohydrates by harnessing proton gradients (LANE, 2005).

One of the earliest mechanism for understand the biological ET, proposed by Albert Szent-Györgyi in 1941 (SZENT-GYÖRGYI, 1941), drew an analogy to semiconductors. He hypothesized that electrons could travel between enzymes within relocated electronic states similar to those found in solids. This proposal relied on the close proximity of numerous atoms within proteins, leading to the formation of overlapping valence orbitals and the effective collapse of the energy gap between them. Consequently, electrons could potentially absorb energy and move freely across the protein structure. However, this idea failed to explain ET in systems that did not involve the absorption of UV radiation, a requirement for overcoming the proposed energy gap in Szent-Györgyi's model. The energy gap in his model far exceeded

both thermal energy (K_BT) and the energy of photons typically absorbed by biological structures in the UV range (EVANS; GERGELY, 1949).

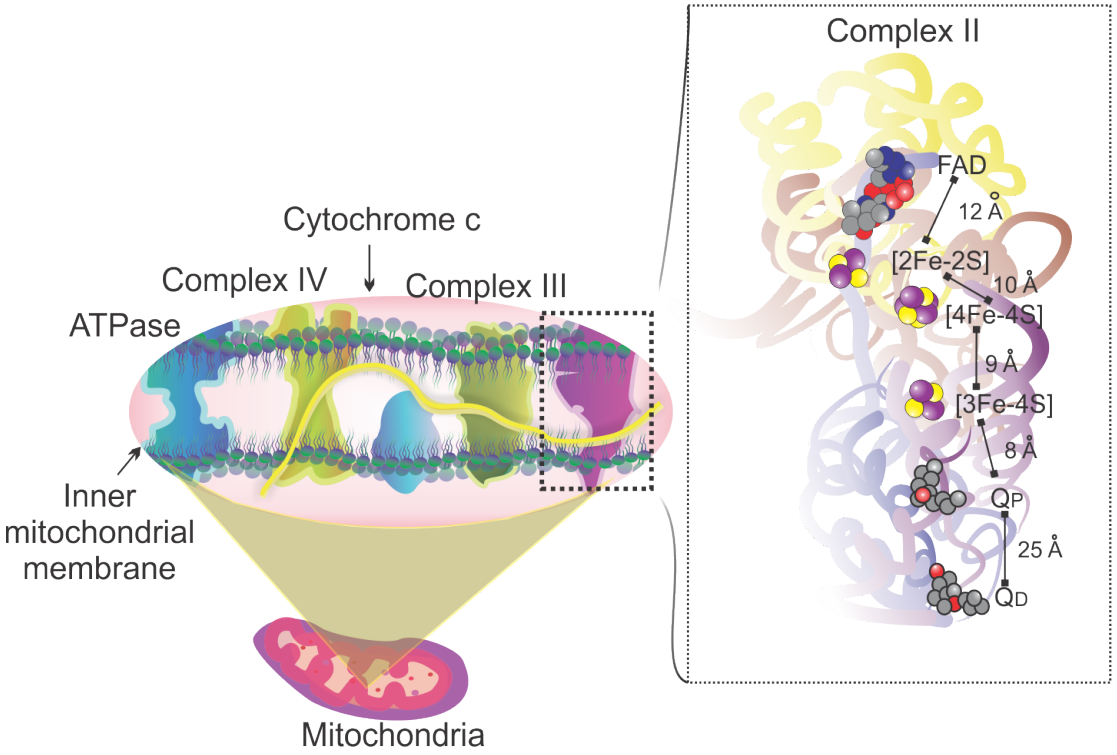

Figure 1.1: a) Schematic diagram of the inner mitochondrial membrane, where the ET_p chain is located. Complexes II, III, and IV, as well as ATP synthase, are shown. Complex I and the carrier ubiquinone (Coenzyme Q) are not depicted. The coenzyme Q is responsible for transferring electrons from either Complex I or II to Complex III. The electron flow through the complexes is illustrated by the yellow curvy line. Cytochrome *c* shuttles electrons between Complexes III and IV (LANE, 2005). b) Ribbon diagram of Complex II (menaquinol oxidoreductase, QFR). A simplified representation of the fumarate reductase (Frd) flavoprotein (FrdA) subunit is shown in yellow, while the iron-sulfur protein subunits FrdB, FrdC, and FrdD are presented in brown, blue, and purple, respectively. The redox cofactors, separated by estimated distances, are inserted in the protein matrix (CECCHINI, 2003).

Source: Author (2024)

Another proposed mechanism, promoted by Professor Chance, centered on thermally induced conformational changes. This model suggested that fluctuations in protein structure could bring redox cofactors into close proximity, facilitating ET along a chain. However, experimental evidence contradicted this hypothesis, leaving it incomplete. The study published in 1966 (DE VAULT; CHANCE, 1966) investigated the temperature dependence of light-induced cytochrome oxidation in chromatium bacteria. Notably, the researchers observed cytochrome oxidation continued even at cryogenic temperatures. Furthermore, the oxidation rate became independent of temperature beyond a certain point. This temperature-independent slow the oxidation process, suggesting the presence of an energy barrier for ET. However, the

low thermal energy at these temperatures would not allow the electron to overcome this barrier classically.

The phenomenon of ET occurring despite the electron lacking sufficient thermal energy to surpass the energetic barrier prompted chemists to explore an alternative explanation for this event. During this period, the concept of the tunneling mechanism, which had been accepted by physicists years earlier to elucidate charge conduction in solid-state systems (MERZBACHER, 2002), caught the interest of chemists (MARCUS, 1964; MARCUS; SUTIN, 1985). In the 1960s, Rudolph Marcus (MARCUS, 1956), along with Levich and Dogondze (DOGONADZE; LEVICH, 1959) independently, turned to the tunneling mechanism to clarify ET chemical reactions in homogeneous and heterogeneous settings (see Figure 1.2*a, b*). Marcus's ET theory, built upon the Franck-Condon principle and potential energy surface models (see Figure 1.2*c*), provides a quantitative framework to predict ET rates. A central element of the theory is the reorganization energy, λ, which includes contributions from both the inner coordination shell (changes in bond lengths and angles) and the outer coordination shell (solvent polarization) (MARCUS, 1956; MARCUS, 1964). This ET theory, later extended to biological systems (MARCUS; SUTIN, 1985), aimed to elucidate the rate at which electrons could be transferred between two spatially separated chemical species: D and A. A key parameter in this context is the ET rate constant, k, expressed by the Marcus equation (MARCUS, 1964) as

$$k = \kappa \frac{k_B T}{h} \exp\left(-\frac{E^{\ddagger}}{k_B T}\right), \tag{1.1}$$

where k_B, T, and h correspond to the Boltzmann constant, temperature, and Planck constant, respectively. The activation energy ($E^{\ddagger}$) is a function of the electron driving force (E^0) and of the reorganization energy of the solvent environment λ: $E^{\ddagger} = (E^0 + \lambda)^2/4\lambda$, which encapsulates the energy changes in the molecular environment due to ET, calculated using dielectric continuum models or more detailed molecular descriptions (MARCUS, 1964).

Marcus's theory also accounts for the adiabatic character of ET processes via the transmission coefficient κ, which depends exponentially on the *D-A* spatial separation L, e.g. $\kappa \propto \exp(-\beta L)$, where β is determined by the intervening medium, which can be vacuum, solution environment or a protein matrix environment (WINKLER; GRAY, 2014). The overlap of electron wave functions between D and A is crucial for κ, reflecting the medium's properties, such as dielectric constants and structural rigidity (MARCUS, 1964). These refinements enabled Marcus's framework to consistently align with experimental observations across diverse domains, including chemical, electrochemical, and biological. Thus, the Marcus equation provides a robust framework for understanding the dynamics of ET in various chemical and biological

settings.

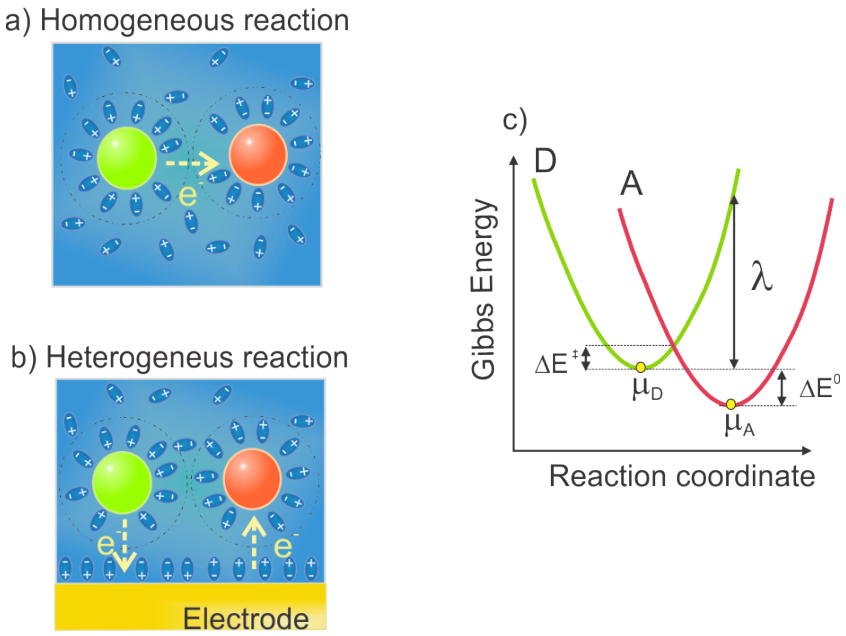

Figure 1.2: a) Schematic representation of ET reactions within Marcus model where D and A species are depicted as spheres surrounded by the solvent. These solvent molecules are specifically oriented to form the activated complex, and the energy required for ET is associated with the λ of the solvent. The ET process occurs in a solvent environment and a homogeneous reaction setting. b) Illustration of an ET process considered a heterogeneous situation occurring at the interface between an electrode and electroactive chemical species embedded in a solution environment. c) Gibbs energy curves of the D and A as a function of the reaction coordinate for a homogeneous ET reaction. The chemical potential μ of the D and A are presented in the minimum point of the energy surfaces curves as μ_D and μ_A, respectively.

Source: Author (2024).

The understanding of electron tunneling through an energetic barrier at a specific rate between two spatially separated chemical species gained momentum in biology as it became a cornerstone for explaining ET between cofactors in protein matrices (MARCUS; SUTIN, 1985). This concept aligned well with the semiclassical ET theory of Marcus (Eq. 1.1), which predicts k based on $E^{\ddagger}$ and tunneling parameters. In 2003, Gray and Winkler provided compelling experimental support for tunneling mechanism operating in redox proteins (GRAY; WINKLER, 2003). They developed an innovative experimental system (Figure 1.3) in which a Ru complex was covalently linked to cytochrome c at controlled distances. This setup allowed precise measurement of k as a function of L upon laser excitation, the Ru(II) complex transferred an electron to a reducing probe in solution, becoming Ru(III), which then accepted an electron from the protein's iron center.

Crucially, the experiments revealed that k varied significantly, even when L was held constant. This observation underscored the pivotal role of the intervening molecular bridge in modulating ET efficiency. Specifically, the bridge can influence ET by

lowering the effective energy barrier or by enhancing the electronic coupling between D and A states. Gray and Winkler quantified this effect using the attenuation factor β, which characterizes how quickly electronic coupling decays with increasing D-A separation. Their findings demonstrated that the bridge's chemical nature, whether it promotes stronger coupling or provides a more favorable energy pathway, plays a decisive role in ET dynamics. For peptides and proteins, typical β values range from 0.6 to 1.4 $Å^{-1}$ reflecting the variable efficiency of ET through different biological structures.

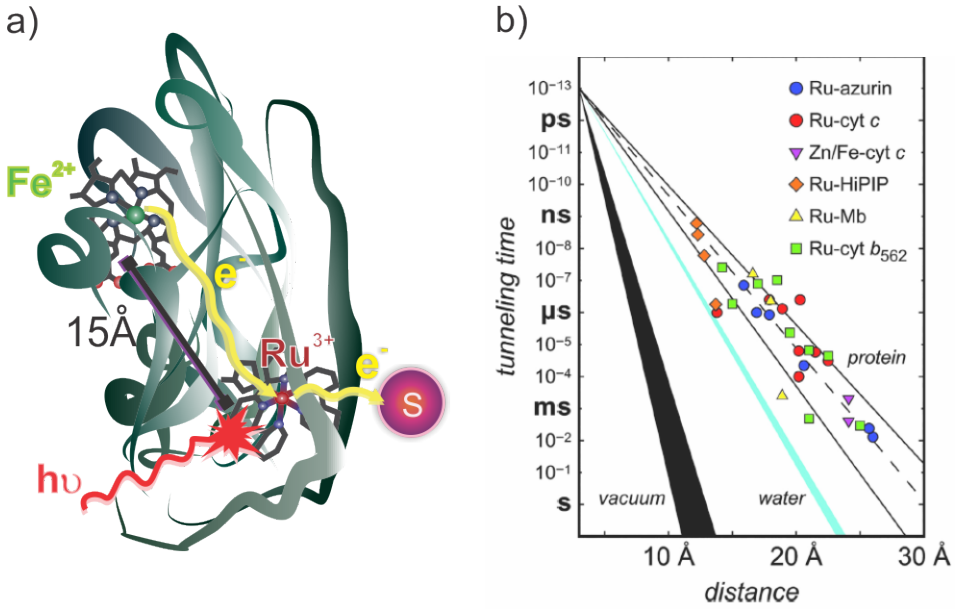

Figure 1.3: a) Ribbon representation of a heme-containing protein modified with a ruthenium complex, illustrating the intermolecular flash-quench model for measuring electron transfer rates. Briefly, a quencher in solution (S) oxidizes the photosensitizer (Ru^{2+}), which has been excited by a short laser pulse. Subsequently, the heme center in the protein (Fe^{2+}) transfers an electron to the oxidized sensitizer (Ru^{3+}), which is positioned at a known distance. b) Tunneling timetable for ET process in Ru-modified proteins: azurin (blue circles), cyt c (red circles), myoglobin (yellow triangles), cyt b562 (green squares), HiPIP (orange diamonds), and for interprotein ET Fe:Zn-cyt c crystals (fuchsia triangles). The black and cyan wedges represent tunneling through vacuum and water, respectively. The solid lines depict the predicted tunneling pathways for coupling along β-strands (1 A^{-1}) and α-helices (1.3 A^{-1}) (GRAY; WINKLER, 2005).

Source: (a) Author (2024). (b) Reprinted with permission from Copyright ©2005, The National Academy of Sciences

These findings indicated that the molecular bridge does more than passively mediate ET; it actively participates in the process. This observation led to the proposal of the superexchange mechanism as a more suitable explanation for ET in biological structures (GRAY; WINKLER, 2003; GIESE; GRABER; CORDES, 2008). Unlike tunneling, where the bridge plays a passive role, superexchange involves active mediation by the bridge, facilitating ET through virtual states. These virtual states do not host the electron but create a coherent pathway, enhancing coupling between D

and A and maintaining efficiency over greater distances. However, while the superexchange mechanism explains ET over moderate distances in biological systems, its effectiveness diminishes at greater ranges. This mechanism is typically suited for distances up to 20 Å (GRAY; WINKLER, 2009). Beyond this range, especially when ET occurs at higher-than-expected rates, other mechanisms are likely to come into play.

For long-range ET_p, such as those observed in systems like *Geobacter sulfurreducens*, mechanisms like sequential hopping and metallic-like conductance (also referred to as ballistic transport), have been proposed (ESHEL; PESKIN; AMDURSKY, 2020; MALVANKAR; VARGAS; NEVIN, K., *et al.*, 2015). Sequential hopping involves stepwise ET through intermediate redox-active sites, a process particularly important in protein complexes or cofactor chains (GRAY; WINKLER, 2005; WINKLER; GRAY, 2014). In this process, the redox-active sites act as energetically aligned intermediates that bridge the gap between D and A, facilitating efficient ET, reflected in the value of k. In contrast, metallic-like conductance resembles metallic conductivity, where electrons move with minimal scattering and high efficiency over long distances. In this mechanism, conductance G is the relevant parameter, as the structure provides a continuous pathway for electron movement. In *Geobacter sulfurreducens* structures like microbial nanowires and pili have been shown to serve as conduits, enabling the ET_p efficiently over micrometer scales (MALVANKAR; VARGAS; NEVIN, K. P., *et al.*, 2011; MALVANKAR; VARGAS; NEVIN, K., *et al.*, 2015).

The diverse mechanisms proposed for long-range ET_p, and described above, are not mutually exclusive or incorrect. Each mechanism offers reasonable insights and is supported by valid ideas and experimental results. This diversity reflects the complexity and sophistication of ET_p processes in biological systems, where different mechanisms may operate under varying conditions or coexist within the same system. Consequently, it is challenging to select a single mechanism to comprehensively explain all aspects of long-range ET_p, underscoring the need for integrative frameworks that unify these perspectives into a cohesive model (BUENO, 2024). Quantum Rate Theory (QRT) offers a unifying framework that bridges classical ET theories and quantum principles. By correlating the k from superexchange with the G from metallic-like transport through quantum capacitance (C_q), QRT provides a cohesive model, as demonstrated in the case of *Geobacter sulfurreducens* (BUENO; SCHROTT, *et al.*, 2015; BUENO, 2024). This framework accounts for coherent electron flow along cytochrome-based nanowires, maintaining high efficiency across micrometer distances. This comprehensive approach, exemplified in *Geobacter sulfurreducens* biofilms, underscores QRT's critical role in resolving debates on long-range ET_p in bioenergetic processes.

The efforts on understanding of mechanisms governing biological ET_p are motivated by the potential to manipulate molecular electronics and electrochemistry for applications ranging from molecular electronics and energy conversion up to sensing (VILAN; ASWAL; CAHEN, 2017; BUENO, 2018b; BUENO, 2024). However, the inherent complexity of protein conformations, combined with the experimental challenges of maintaining their structural integrity and stability, makes these investigations particularly difficult. To overcome these challenges, the use of peptides, the building blocks of proteins, immobilized on electrodes, has allowed the investigation of ET_p within an electrochemistry framework (ECKERMANN *et al.*, 2010; JUHANIEWICZ; PAWLOWSKI; SEK, 2015; SHAH *et al.*, 2015; REDONDO-GÓMEZ *et al.*, 2024) which somehow facilitates the analysis and the study of ET reactions under complex environmental conditions.

1.2 Redox-tagged peptides self-assembly monolayers

Peptides are linear oligomers constructed from α-amino acids. Each amino acid features a central α-carbon atom covalently bonded to an -NH_2 group, a -COOH group, a H atom, and a side chain. The side chain dictates the unique properties and functionality of each amino acid. Peptides are formed through amide bond formation, a condensation reaction between the α-NH_2 of one amino acid and the α-COOH group of another, releasing a H_2O molecule. The key advantage of peptides lies in their amenability to functionalization. Established synthetic methods, such as solid phase peptide synthesis (SPPS) (MERRIFIELD, 1963), allow for the design and fabrication of peptides with specific functionalities tailored to experimental needs. This tunability, compared to the more complex and challenging modifications of proteins, has made peptides valuable tools for the experimental investigation of ET processes using electrochemical techniques (ECKERMANN *et al.*, 2010; SHAH *et al.*, 2015).

The interest in immobilized peptides on electrodes, forming molecular assemblies to assess ET mechanism through electrochemical techniques, stems from the aspiration to replicate the intricate biological conditions where ET processes occur (JUHANIEWICZ; PAWLOWSKI; SEK, 2015; ECKERMANN *et al.*, 2010). The rationale behind immobilizing peptide structures on surfaces is rooted in the understanding that ET processes within biological systems typically involve redox cofactors, which vary from organic to inorganic compounds separated by a polypeptide matrix (LANE, 2005; GRAY; WINKLER, 2005). Therefore, the concept revolves around assembling peptides on a controllable source of electrons, namely electrode, to create an organized molecular monolayer that emulates a polypeptide matrix structures in proteins. This approach also involves incorporating a redox moiety, such as a

ferrocene complex, at the top end of the molecular assembly, thus presenting an intriguing strategy to simulate the biological conditions of ET. It is evident that two primary strands of interest exist in the investigation of redox peptide immobilized on electrodes: one is focused on fundamental studies aimed at comprehending ET in biological systems, while the other is oriented toward technological advancements, for instance, the development of biological sensors (VANOVA *et al.*, 2021; BRANDÃO *et al.*, 2023; GARROTE; SANTOS; BUENO, 2020).

Molecular SAMs on electrodes, constructed from peptides, are a type of two-dimensional nanoscale structure. These SAMs comprise three essential components: a linker (or anchor) group, a molecular bridge, and a tail functional group. First, the linker group facilitates the chemical and electronic coupling between two parts of the SAM's structure with differing chemical natures (REDONDO-GÓMEZ *et al.*, 2024). Meanwhile, the molecular bridge is distinguished by discrete and defined electron energy levels, contrasting with the electrode's sea of electrons that forms a continuum of electronic states. Gold electrodes are popular for building peptide-tagged SAMs due to their relatively inert nature and strong attraction to sulfur-containing molecules, which creates a strong Au-S bond (HÄKKINEN, 2012). For this reason, linker groups often contain organosulfur moieties like: i) alkanethiols (e.g., cysteamine), ii) disulfide bonds (e.g., lipoic acid), and iii) Cys residues with thiol side chains (REDONDO-GÓMEZ *et al.*, 2024). The second component of SAMs, the molecular bridge acts as a spacer, between the electrode and the tail functional group, and can be designed for specific intend. For instance, in ET studies, the bridge might be composed of amino acids that promote the formation of helical peptides. It is because helical structures have been shown to be particularly efficient for ET (AMDURSKY, 2015).

The design of the peptide sequence influences not only the functionality of the SAM but also its mechanism of formation. While the linker group rapidly chemisorbed to the electrode surface, the organization and stability of the entire SAM are determined by the slower interactions within the molecular bridge (ULMAN, 1996). Finally, the tail functional group plays a crucial role in defining the purpose of the peptide SAMs. It serves as the chemical moiety amenable to modification, enabling the accommodation of various functionalities such as a redox probe for electrochemical reaction studies or the linkage of macromolecules of biological interest like antibodies or DNA sequences, forming the basis of biological sensor applications (VANOVA *et al.*, 2021; GARROTE; SANTOS; BUENO, 2020).

Considering the versatility of chemically modifying peptide structures through synthesis methods such as SPPS, various factors influencing the ET process in macromolecular biological machines has been studied. Factors affecting the ET such as chain length (ARIKUMA *et al.*, 2010), backbone conformation (TAKEDA; MORITA;

KIMURA, 2008; MATSUSHITA; UJI; KIMURA, 2018; GALKA; KRAATZ, 2002), dipole orientation (WATANABE; MORITA; KIMURA, 2005), the presence of counterions (ORLOWSKI; CHOWDHURY; KRAATZ, 2007), amino acid composition (BRANDÃO *et al.*, 2023), among others (SHAH *et al.*, 2015), have been evaluated utilizing the electro-active peptides SAMs setting and electrochemical techniques. Some important findings to highlight include the work of Shunsaku Kimura and colleagues, who reported the longest ET through peptides with lengths around 10 nm (ARIKUMA *et al.*, 2010). They suggest that the intrinsic peptide backbone acts as electron stepping stones, allowing efficient ET over long distances. Additionally, the importance of strong intermolecular interactions within the peptide monolayer has been recognized (KRAATZ *et al.*, 2004; TAKEDA; MORITA; KIMURA, 2008). These interactions, influenced by factors such as lateral hydrogen bonding and different packing densities, significantly affect the kinetics of the ET process.

It is important to highlight that in the previously mentioned works (ARIKUMA *et al.*, 2010; TAKEDA; MORITA; KIMURA, 2008; MATSUSHITA; UJI; KIMURA, 2018; GALKA; KRAATZ, 2002; WATANABE; MORITA; KIMURA, 2005; SHAH *et al.*, 2015), k was used as the central parameter for gauging the impact of these factors on ET rates in such nanoscale junction structures. This kinetic parameter has been measured from CV, using the Butler-Volmer formalism (LAVIRON, 1979), chronoamperometry (CA) by analyzing current decay (WATANABE; MORITA; KIMURA, 2005), and EIS by adjusting circuits based on the Randles circuit (CREAGER; WOOSTER, 1998). These experimental approaches rely on theoretical frameworks to interpret ET behavior, with the semi-classical Marcus theory of homogeneous ET (MARCUS, 1956) serving as a cornerstone. However, ET processes in nanoscale junctions, such as redox-peptide SAMs on gold electrodes, are dominated by quantum phenomena, including distributed molecular energy levels and quantum tunneling, in which classical theories are not adequate to describe the phenomenon. Therefore, a quantum-based theory is essential for accurately modeling ET dynamics, considering the role of electronic structure for ET phenomenon, permitting to optimize SAM structures for diverse applications.

1.3 *Push-pull*-based heterocyclic structures and junctions

Organic molecules featuring a delocalized π-system of electrons have garnered significant attention for their use in advanced functional materials. A notable subclass of these molecules, characterized by a unique structural design comprising donor/D (*push*) and acceptor/A (*pull*) groups connected by a π-conjugated molecular bridge, are widely known as *push-pull* systems ($D - \pi - A$). This distinctive conformation

creates an asymmetry in charge distribution in the molecule by forming a new low-energy molecular orbital (MO), imparting specific electronic properties that have placed these molecules at the forefront of advanced materials chemistry area (BUREŠ, 2014). One of the most significant properties extensively studied in the literature is intermolecular charge transfer (ICT), which through excitation induced by visible light perturbation, making *push-pull* heterocyclic molecules generally colored and known as charge-transfer chromophores. Specifically, an electron in the highest occupied molecular orbital (HOMO) located on the *D* moiety is photoexcited and transferred to the lowest unoccupied molecular orbital (LUMO) primarily located on the *A* group. Therefore, the efficiency of ICT depends on the electronic strengths of the *D* and *A* groups, facilitated by the electronic nature of π-conjugated bridge (ZHU, H. *et al.*, 2016).

Intrigued by the versatile interplay of charge dynamics within *push-pull* heterocyclic systems, materials chemists, optoelectronic engineers, and organic electronics researchers have extensively investigated them, stemmed from the unique ability of these molecules to both conduct electricity and interact with light. Harnessing these properties, scientists have explored their use in developing innovative organic devices such as organic field-effect transistor (OFETs) (ALLARD *et al.*, 2008; CHANG; HSIEH, 2013; FERNANDES; CASTRO, *et al.*, 2021), for nonlinear optical (NLO) (M. FERNANDES *et al.*, 2018), and in solar cell technologies like dye-sensitized and organic photovoltaic cells (REGINATO *et al.*, 2018; HAINS *et al.*, 2010). Organic light-emitting diodes (OLEDs) (SONG *et al.*, 2020) and chemosensors (FERREIRA; RAPOSO; COSTA, 2018; OKDA *et al.*, 2019; LI, C. *et al.*, 2016) are other promising applications. This widespread research on conjugated systems aims to unlock their full potential by deepening our understanding and control of their optoelectronic properties. A primary strategy involves a fine-tuning of the molecular structure by strategically altering electron-withdrawing, electron-releasing, and π-bridge elements. This approach is driven by the well-established link between a molecule's chemical structure and ICT (BUREŠ, 2014).

Many studies have focused on the variations of particular *D*, π-bridge, and *A* scaffolds of the *push–pull* system, evaluating their effects on the optoelectronic properties (BUREŠ, 2014). Five-membered heterocycles, like pyrrole and thiophene, are well-defined and widely used as *D* component of these structures (FERNANDES; CASTRO, *et al.*, 2021), which contain six delocalized electrons spread across the ring,

thanks to a lone pair on their heteroatom Nitrogen or Sulfur. In contrast, electron-withdrawing groups such as nitro and cyano are some of the most widely used electron *A* moieties, comprising complex conjugated heterocyclic cores, such as imidazo-phenanthroline and pyridine, that have also been studied as promising auxiliary electron *A* heterocycles (BATISTA *et al.*, 2008; WANG, T. *et al.*, 2020). Additionally, the importance of the π-conjugated bridge that connects the *D* and *A* moieties/groups has been noticed with the bridge composed of multiple bonds like olefinic and acetylenic moieties, or with a more complex structure incorporating aromatic and heteroaromatic spacers, such as bithiophene or benzothiadiazole heterocycles, that creates a π-conjugated pathway that enhances communication between the *D* and *A* groups (BUREŠ, 2014; M. FERNANDES *et al.*, 2018; FERNANDES; PEREIRA, *et al.*, 2018).

The assembly of *push-pull* heterocyclic molecules on substrates has attracted considerable attention due to the strong influence of morphology on their optoelectronic properties, which are more effectively controlled on electrode than when free in solution environment (LI, Y. *et al.*, 2014). These organized junctions hold significant potential for optimizing electronic properties, particularly at the nanometric scale, where quantum mechanical effects begin to dominate the electrodynamics (BUENO, 2018b; NIETO *et al.*, 2024), forming structured molecular films based on *push-pull* heterocyclic molecules on substrates that facilitates in-depth studies of the electrodynamics at the interfaces. A crucial strategy in fabricating the junctions involves the incorporation of specific functional groups that form stable interactions with the electrode. For example, thiol groups allows the fabrication of SAMs on gold substrates, enabling the formation of both charged and neutral *push-pull* heterocyclic SAMs (MALYTSKYI *et al.*, 2015; ASHWELL; TYRRELL; WHITTAM, 2003). This strategy significantly enhances the electronic properties of *push-pull* heterocyclic molecules, such as molecular rectification (ASHWELL; URASINSKA; TYRRELL, 2006), by ensuring ordered orientation, optimal packing density, and improved electronic coupling within the SAM. Additionally, *push-pull* heterocyclic molecular SAMs, using thiol group as linker are promise for photoactive applications, including light detectors (KENFACK *et al.*, 2011), and have recently been highlighted for their value in fundamental studies of electrodynamics (NIETO *et al.*, 2024), in which the resonant quantum conductance dynamics of a molecular junction, formed by a *push-pull* heterocyclic molecule anchored on gold electrodes (see Figure 1.4*a*), has been demonstrated to operate according to QRT principles.

QRT, as discussed in the following section 1.4, serves as a crucial theoretical tool that enables access to the electronic structure, permitting to investigate ET_p in various types of junctions by using electrochemical measurements. For instance, in reference (NIETO *et al.*, 2024) the π–conjugated *push-pull* molecular assembly was constructed through the chemical bonding of the -COOH group of a π-conjugated

molecule to the -NH_2 group of cysteamine molecules previously anchored on a gold electrode surface (see Figure 1.4*a*) and the C_q was measured (from the Nyquist plot, see Figure 1.4*b*), permitting to obtain the DOS of the system. The DOS of organic molecular assembly contains information on the electrodynamics of communication between the resonant states of the molecule and electrode states. The resulting DOS or C_q-voltage shape has a Gaussian-shaped response (see Figure 1.4*c*). These findings are significant as they open the door for designing specific *push-pull* heterocyclic structures for molecular electronics and sensing application based on the use of the DOS of the junction as a transduction signal.

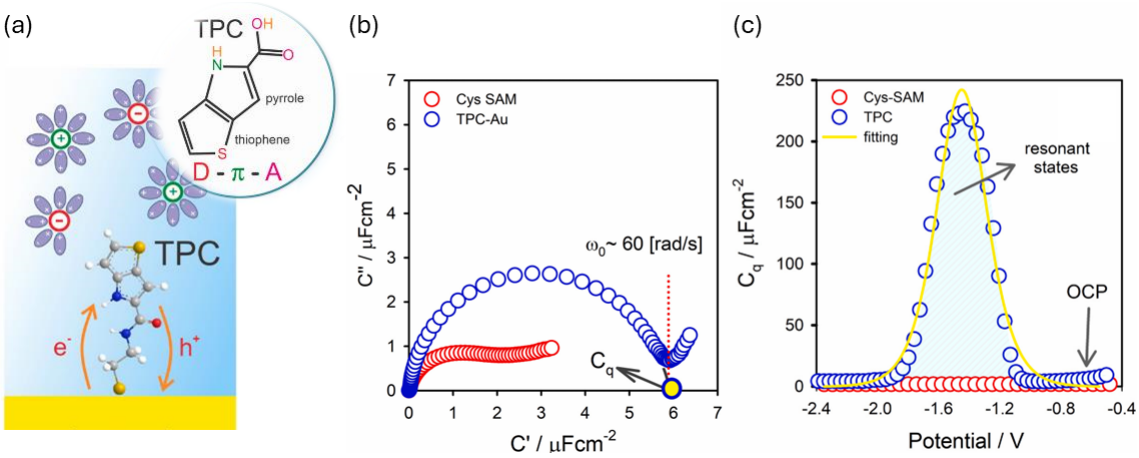

Figure 1.4: (a) Schematic illustration of an electrochemical, diffusionless setup featuring 4*H*-thieno[3,2-*b*]pyrrole-5-carboxylic acid (TPC) molecule confined by cysteamine linker group on an electrode surface, forming a single-contact molecular junction structure, surrounded by an electrolyte. (b) Nyquist capacitive plot recorded at the OCP permitted to determine the characteristic frequency ν of the molecular junction. (c) Distribution of C_q states obtained by scanning the potential at the characteristic frequency identified in (b).

Source: Adapted from (NIETO et al.*, 2024). Copyright 2024 Elsevier*

Another interesting anchoring group for constructing *push-pull* heterocyclic molecular junctions is pyrene. Due to the tendency for π-π stacking with similar structures, attributed to its four fused benzene rings, pyrene interacts strongly with graphene surfaces, providing a robust and stable attachment through non-covalent interactions (GARRIDO *et al.*, 2021; LIU; TANG; GOODING, 2012). Graphene, a monolayer of aromatic carbon atoms arranged in a honeycomb lattice, has garnered significant attention in electronics and material science because of its remarkable electronic, optical, mechanical, and thermal properties. Graphene's distinctive electronic structure gives rise to its exceptional properties, which can be adjusted by modifying it with π-conjugated organic molecules, such as pyrene and derivatives. These modifications allow researchers to alter the surface characteristics of graphene while preserving its core structure. This approach enables the creation of advanced junctions and devices that utilize graphene's inherent strengths, while adding new functionalities through

π-π stacking interactions, which holds great potential for molecular electronics, biological sensors, and energy storage devices, where combining organic molecules with graphene may lead to improved performance and innovative capabilities of the junctions (ALPUIM *et al.*, 2023) .

1.4 Quantum electrodynamics within redox-tagged and *push-pull* SAMs

In previous sections, two types of organic molecular assemblies on electrodes were introduced, i.e. junctions based on redox-tagged peptides (Section 1.2) and *push-pull* heterocyclic molecules (Section 1.3) with the two systems exhibiting distinct electronic coupling but with both following quantum electrodynamics principles with QRT premises. Redox-tagged peptide junctions exhibit redox activity and ET reactions is present with ET mechanism operating in transferring electrons between the redox states within the peptide SAM and the electrode, a process consistent with non-adiabatic ET reactions. In contrast, *push-pull* heterocyclic molecular interfaces involve electron communication between D and A states/groups with those of the electrode, a process which was identified as adiabatic and that does not involve redox reactions. Despite these differences, both systems follows quantum electrodynamics and QRT premises that provides a comprehensive understanding of ET and ET_p from a fully quantum-mechanical perspective.

The emergence of QRT arose from the need to unify the understanding of ET and ET_p, constituting two different phenomena that traditionally have been studied separately by chemists and physicists (BUENO, 2024, 2023; BUENO, 2018b; NITZAN, 2001). Chemists primarily focused on the ET dynamics in wet conditions, with k as the central observable, that permits to analyze the rate of the electron exchange between D and A species (MARCUS, 1993). Physicists, on the other hand, examined ET_p in solid-state systems, emphasizing the conductive properties of molecules and using molecular G as the primary parameter within the Landauer formalism (LANDAUER, 1957; IMRY; LANDAUER, 1999). Hence, this disciplinary setting and division of two associated but distinct phenomena that conducts to different environments and methodologies for studying ET and ET_p. The convergence of the concepts behind these phenomena became essential to address the differences between short and long-range electrodynamics as critical for our understanding of processes involving oxidative phosphorylation in the mitochondrial ET_p chain (LANE, 2005; GRAY; WINKLER, 2003), or ET_p across *Geobacter* biofilms (BUENO, 2024).

Abraham Nitzan is regarded as a pioneer in proposing a theoretical correlation

between k and G (NITZAN, 2001) concepts. Nitzan suggested a linear correlation between these two parameters based on their similarities regarding the dependence with respect to L ($\propto \exp(-\beta L)$) and by assuming that the electronic structure of the molecule in solution environment is not significantly different from its structure when connected to metal leads. The Nitzan's expression, Eq. 1.2, includes the electronic coupling parameter Γ between left (l) and right (r) electrodes with the nearest segment of the molecular bridge (D, A) such as that

$$G \approx \frac{8e^2}{\pi^2 \Gamma_D^l \Gamma_A^r} k_{D \to A} \tag{1.2}$$

was theoretically proposed, but that is not able to explain the correlation between k and G concepts universally. For instance, the relationship of Eq. 1.2 cannot explain the correlation for some molecular bridges, such as alkanes and peptide nucleic acid oligomers (WIERZBINSKI *et al.*, 2013). The k of a ferrocene-labeled molecular structure of varying lengths, containing a Cys bonded to a gold electrode via an S-Au bond, was determined using electrochemical techniques, and G for these structures, without the redox probe and with Cys at each end of the molecule, was measured by bonding one side to a gold electrode while the other side interacted with a gold tip, corresponding to measuring G using a scanning tunneling microscope-based break-junction setup. The k and G values were plotted against the molecular length, and β was thus determined, from which it was observed that despite the exponential decrease of both parameters with increasing length, β obtained from G (β_G) and k (β_k) differed for the same structures (WIERZBINSKI *et al.*, 2013). The linear correlation between k and G proposed by Nitzan was observed only when β_G and β_k were equivalent, where it was established that $G = ak^b$, in which $b = \beta_G/\beta_k$. The differences in the β values were attributed to different experimental configurations used to obtain k and G, as well as the differing conditions of the measurements (dry for G and wet for k). In light of this, although the correlation between the rate of ET through a molecular bridge and the conductance properties of this bridge had been established with certain successful, the Nitzan's approach is not complete or universal.

QRT approach help us to better understand the correlation between k and G through the meaning of electrochemical capacitance C_μ, which can be experimentally validated (BUENO, 2023; BUENO, 2018a) through low-frequency time-dependent electrochemical measurements. The key parameter linking k and G concepts is the C_μ, which, is not entirely new, but has been referred in the electrochemical field as pseudo-capacitance (BÜTTIKER; THOMAS; PRÊTRE, 1993). According to QRT, electrodynamics involving molecular assemblies with accessible electronic states through electrode (faradaic or non-faradaic) response, can be modeled using a quantum RC

circuit (see Figure 2.2*a*), with a characteristic time constant, $\tau = R_q C_\mu$, or its corresponding frequency $\nu = 1/\tau$, that represents the rate of communication between two quantum states. Whether the electrodynamics involves an ET process, such as in a redox reaction, ν (or ν_{ET}) corresponds to k. In the absence of an ET process, where the electrodynamics can be adiabatic (as in monolayers of π-conjugated *push-pull* heterocyclic molecules (NIETO *et al.*, 2024)), ν (or ν_{EC}) reflects the frequency at which the electronic states of the molecule and the electrode resonate. Accordingly, QRT approach introduces a general expression for the ν_{ET} or the frequency of communication ν_{EC}, as shown in Eq. 1.3, connecting it to G through the meaning of C_μ such as

$$\nu = \frac{G}{C_\mu} = 1/\tau. \tag{1.3}$$

In Eq. 1.3, G is defined as the Landauer conductance, which corresponds to the quantum conductance described by the Landauer formalism (LANDAUER, 1957; SÁNCHEZ; SANTOS; BUENO, 2022) for ET_p, in which electrons behave as waves through an ideal conductive quantum channel undergoing minimal or coherent scattering transport. At the molecular scale, G, can be quantized in discrete units of conductance quantum $G_0 = g_s e^2/h$, where g_s states for the electron spin degeneracy, h for the Planck constant, and $1/R_K = e^2/h$ accounts for the reciprocal of the von Klitzing constant $R_K = h/e^2 \sim 25.8\ \mathrm{k\Omega}$ (VON KLITZING, 2019). The Landauer description of G is crucial as it captures the scattering properties of the conductor, which determine the probability of electron transport through individual quantum channels n at a given chemical potential μ. These scattering properties are mathematically described by the scattering matrix, $\sum_{n=1}^{N} T_n(\mu)$, which is directly related to the probability of scattering events. In the case of quantum channels formed between D and A states in a ET process, the dynamics depends on the electron coupling, which governs the transmittance probability based on the scattering characteristics of the quantum channels.

Accordingly, depending on the nature of the electronic coupling, the transfer (or communication) process can be either adiabatic or non-adiabatic (ZHU, G. Y. *et al.*, 2021). In an adiabatic process, ET occurs with high transmittance probability due to significant wave-function overlap, between D and A states or resonance processes, allowing the electronic system to evolve slowly while remaining in its ground state, which is typically associated with a coherent quantum transport, where electrons move through the system without inelastic scattering, maintaining phase coherence. Conversely, in a non-adiabatic process, ET is probable but with less transmittance probability which often is governed by quantum tunneling, where ET occurs through an electric potential barrier, in which the transmission matrix element simplifies to κ,

which depends on the L between D and A states such as that $\kappa \propto \exp(-\beta L)$. Consequently, the Landauer's quantum conductance can be expressed as $G = NG_0\kappa$, where N represents the total number of quantum channels through which the electron is transmitted, and the general quantum rate expression defined by the QRT (Eq. 1.3) takes the form

$$\nu = \frac{G_0}{C_\mu} \sum_{n=1}^{N} T_n(\mu) = g_s \frac{Ne^2}{hC_\mu} \kappa, \tag{1.4}$$

from which it is notable that by incorporating the transmission matrix to describe ν, it allows for a comprehensive electrodynamics with varying electronic coupling characteristics that includes tunneling as a specific setting of the transmission matrix, hence leading to κ. For instance, when $\kappa \ll 1$, it is indicative of processes governed by non-adiabatic dynamics (see Figure 1.5 *b*) such as in the case of redox-tagged peptide SAMs studied in this thesis, in which weaker electronic coupling leads to ET primarily governed by quantum tunneling. Conversely, adiabatic systems, are characterized by $\kappa \approx 1$, such as the *push-pull* heterocyclic molecular junctions also discussed in this work, which follows stronger electronic coupling characteristics. This strong coupling allows electrons to "communicate between states" with minimal energy loss (see Figure 1.5 *a*). Hence, the transmission matrix and its meaning within a κ description plays a pivotal role that enables the detailed analysis of electrodynamics across adiabatic and non-adiabatic junction processes, highlighting the versatility of QRT approach in addressing different experimental settings (BUENO, 2023).

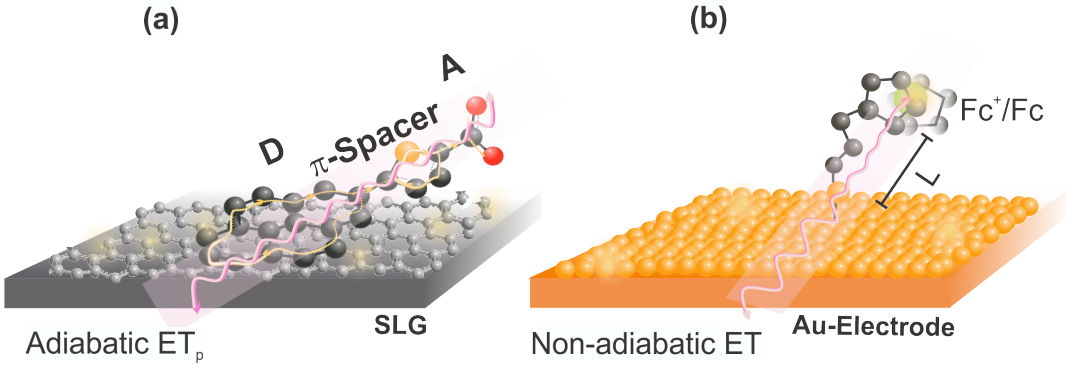

Figure 1.5: Schematic representation of two types of electrodynamics occurring at molecular interfaces assembled on electrodes. (a) Adiabatic ET$_p$: electrode modified with a push-pull heterocyclic molecule, anchored via π-stacking interactions through its pyrene D group. Electronic communication between the electrode and molecule states represented as a continuous wave, which maintain its amplitude and frequency without scattering. (b) Non-adiabatic electron transfer in which there a gold electrode modified with a redox-active molecule of length L comprising a ferrocene moiety. ET occurs through tunneling process represented as a wave with an initially high amplitude at the electrode interface that gradually diminishes at the redox center. This decay is representative of the attenuation of the ET wave transmission.

Source: Author (2024)

The equivalent C_μ of the junction result in a series combination of C_e and C_q, each having a different physical meaning (BUENO, 2019; BUENO, 2023; BUENO; DAVIS, 2014). For instance, the C_e accounts for the energy $E_e = e^2/C_e$ associated with the spatial separation of charges, attributed to the electrolytic solution environment (composed of the supporting electrolyte and the solvent in which it is dissolved), whereas C_q accounts for the energy $E_q = e^2/C_q$ associated with the electronic states occupancy. According, the charging of electronic states occurs concomitantly to the external action of the electrolyte structure, solvation and counter-ions effects, which helps to shield the occupying states of the electronic structure, leading to an additional degeneracy ($g_e = 2$) associated to the overlap of E_e and E_q energy states. Consequently, the total electrochemical equivalent energy $E_\mu = E_e + E_q = g_e E_q$ of the interface can be expressed in terms of C_q as $E_\mu = g_e(e^2/C_q)$ and Eq. 1.4 can be restated as (BUENO, 2023; BUENO, 2018a)

$$\nu = g_s \frac{Ne^2}{h} \kappa \left(\frac{1}{C_e} + \frac{1}{C_q} \right) = g_s g_e \frac{Ne^2}{hC_q} \kappa. \tag{1.5}$$

The rate ν in Eq. 1.5 is related to the amount of charge $dq = -edn$ transferred due to a change in chemical potential $d\mu$, where dn represents the differential number of available electronic states in the system, and e is the elementary charge. A change in electric potential dV corresponds to a change in potential energy, expressed as $-edV = E_F - \mu = d\mu$, where E_F is the Fermi level and μ is the chemical potential. The quantity $C_q = e^2(dn/d\mu)$ is proportional to the DOS, with $dn/d\mu$ representing the change in the number of available states per unit of chemical potential. At finite temperature, C_q is governed by the Fermi-Dirac distribution, which describes the probability of state occupancy as $f = 1/(1 + \exp(eV/k_BT))$, where f is the occupation probability (BUENO; CRUZEIRO, *et al.*, 2021; BUENO, 2018a) such as

$$C_q = \frac{e^2 N}{k_B T} f(1 - f), \tag{1.6}$$

permitting us to rewritten Eq. 1.4 as

$$\nu = g_s g_e \kappa \frac{k_B T}{h} f(1 - f)^{-1} = g_s g_e \kappa \frac{k_B T}{h} f^{-2} \exp(eV/k_B T). \tag{1.7}$$

By applying a Boltzmann approximation to the Fermi-Dirac distribution of Eq. 1.7, where $f \approx \exp(-eV/k_BT) \gg 1$, and neglecting degeneracy effects, Eq. 1.7 reduces to Eq. 1.1, i.e., to the semiclassical Marcus ET theory, hence demonstrating that Marcus ET theory is a particular setting of the QRT. In this framework, the energy term $eV = \mu - E_F$ is related to the $E^\ddagger$ as stated in the TST premises. The applied voltage shifts the μ, which corresponds to an effective change in $E^\ddagger$, and determines the

driving force for the ET. Marcus ET theory incorporates λ and E^0, while QRT extends this by accounting for the solvent's role as an effective energy E_e that shields charges within quantum state energy E_q. Accordingly, QRT provides a direct correlation between the electrostatic environment contribution and the underlying electronic structure contribution to the ET dynamics, with the states of energy being accessible through the measurement of C_q (LOPES; PINZÓN, *et al.*, 2024; NIETO *et al.*, 2024; PINZON; SANTOS; BUENO, 2021; PINZÓN *et al.*, 2024). QRT approach to study ET dynamics enables a more detailed understanding of the role of the electronic structure in governing electrodynamics processes allowing to study both ET (electrochemistry) and ET_p (electronics) aspects of the electrodynamics with an electrolyte environment. The contribution of electronic structure is often neglected in the semiclassical Marcus theory (BUENO, 2019; BUENO, 2023).

Note also that Eq. 1.5 within the QRT correlates with Planck-Einstein relationship $E = h\nu$ by noting that $E_\mu = g_e(e^2/C_q)$ is the total electrochemical energy and thus $\nu \propto E/h$ states for describing the electrodynamics with the meaning of ν in a QRT approach, extending the analysis as a general quantum electrodynamics phenomenon in which the wave vector $\mathbf{k}$ is directly proportional to the energy, as predicted by $E = \mathbf{p} \cdot \mathbf{c}_* = \hbar\mathbf{k} \cdot \mathbf{c}_*$, where p is the momentum, $\mathbf{c}_*$ is the Fermi velocity and $\hbar$ is the $h/2\pi$, a formulation that underscores the wave-particle duality of electrodynamics phenomena, consistent with de Broglie's relation $\mathbf{p} = \hbar\mathbf{k}$ and Dirac's relativistic wave mechanics. Accordingly, QRT provides a comprehensive framework to analyze the quantum electrodynamics meaning of ET and ET_p in a unified way.

QRT premises has been used over the years for studying the electronic structure and quantum properties of various systems under conventional electrochemical setting (LOPES; SANTOS; BUENO, 2021; LOPES; PINZÓN, *et al.*, 2024; PINZÓN *et al.*, 2024; PINZON; SANTOS; BUENO, 2021; ALARCÓN; SANTOS; BUENO, 2021; SÁNCHEZ; SANTOS; BUENO, 2022; NIETO *et al.*, 2024), where the low-energy perturbation that addresses the meaning of ν, permits to establish a communication between electrode and different low-dimensional structures consisting of redox-tagged (in the presence of redox reactions) or not (absence) permitting researchers to study the electrodynamics within graphene (LOPES; SANTOS; BUENO, 2021; LOPES; PINZÓN, *et al.*, 2024), quantum dots (PINZÓN *et al.*, 2024), and metal-oxide semiconductive junctions (PINZON; SANTOS; BUENO, 2021) besides of permitting to address the electrodynamics of redox-tagged peptide SAM junction (ALARCÓN; SANTOS; BUENO, 2021; SÁNCHEZ; SANTOS; BUENO, 2022) and *push-pull* heterocyclic molecular assemblies (NIETO *et al.*, 2024). The study of the electrodynamics of these junctions is the focus of the present thesis to address.

References

ALARCÓN, E. V. G.; SANTOS, A.; BUENO, P. R. Perspective on quantum electrochemistry. A simple method for measuring the electron transfer rate constant. **Electrochimica Acta**, Elsevier, v. 398, p. 139219, 2021.

ALLARD, S. *et al.* Organic semiconductors for solution-processable field-effect transistors (OFETs). **Angewandte Chemie International Edition**, Wiley Online Library, v. 47, n. 22, p. 4070–4098, 2008.

ALPUIM, P. *et al.* Molecular Characterization and DNA-sensing using Graphene Electrochemical Devices under Illumination. *In:* IEEE. 2023 IEEE Nanotechnology Materials and Devices Conference (NMDC). 2023. p. 571–572.

AMDURSKY, N. Electron transfer across helical peptides. **ChemPlusChem**, Wiley Online Library, v. 80, n. 7, p. 1075–1095, 2015.

ARIKUMA, Y. *et al.* Electron hopping over 100 Åalong an α helix. **Angewandte Chemie International Edition**, Wiley Online Library, v. 49, n. 10, p. 1800–1804, 2010.

ASHWELL, G. J.; TYRRELL, W. D.; WHITTAM, A. J. Molecular rectification: self-assembled monolayers of a donor–(π-bridge)–acceptor chromophore connected via a truncated Au–S–(CH 2) 3 bridge. **Journal of Materials Chemistry**, Royal Society of Chemistry, v. 13, n. 12, p. 2855–2857, 2003.

ASHWELL, G. J.; URASINSKA, B.; TYRRELL, W. D. Molecules that mimic Schottky diodes. **Physical Chemistry Chemical Physics**, Royal Society of Chemistry, v. 8, n. 28, p. 3314–3319, 2006.

BATISTA, R. M. *et al.* Synthesis and characterization of novel (oligo) thienyl-imidazophenanthrolines as versatile π-conjugated systems for several optical applications. **Tetrahedron**, Elsevier, v. 64, n. 39, p. 9230–9238, 2008.

BOULAS, C. *et al.* Suppression of charge carrier tunneling through organic self-assembled monolayers. **Physical Review Letters**, APS, v. 76, n. 25, p. 4797, 1996.

BRANDÃO, S. T. *et al.* Designing Quantum Capacitive Peptide Interfaces for Electroanalytical Applications. **Analytical Chemistry**, ACS Publications, v. 95, n. 36, p. 13470–13477, 2023.

BUENO, P. R. **The Nanoscale Electrochemistry of Molecular Contacts**. Springer, 2018a. (SpringerBriefs in Applied Sciences and Technology). ISBN 978-3-319-90486-3.

BUENO, P. R.; DAVIS, J. J. Measuring Quantum Capacitance in Energetically Addressable Molecular Layers. **Analytical Chemistry**, v. 86, n. 3, p. 1337–1341, 2014. ISSN 0003-2700.

BUENO, P. R. Common principles of molecular electronics and nanoscale electrochemistry. ACS Publications, 2018b.

BUENO, P. R. Nanoscale origins of super-capacitance phenomena. **Journal of Power Sources**, Elsevier, v. 414, p. 420–434, 2019.

BUENO, P. R.; SCHROTT, G. D., *et al.* Biochemical capacitance of Geobacter sulfurreducens biofilms. **ChemSusChem**, Wiley Online Library, v. 8, n. 15, p. 2492–2495, 2015.

BUENO, P. R. On the fundamentals of quantum rate theory and the long-range electron transport in respiratory chains. **Chemical Society Reviews**, Royal Society of Chemistry, 2024.

BUENO, P. R. Quantum rate theory and electron-transfer dynamics: A theoretical and experimental approach for quantum electrochemistry. **Electrochimica Acta**, Elsevier, v. 466, p. 142950, 2023.

BUENO, P. R.; CRUZEIRO, V. W. D., *et al.* The density-of-States and equilibrium charge dynamics of redox-active switches. **Electrochimica Acta**, Elsevier, v. 387, p. 138410, 2021.

BUREŠ, F. Fundamental aspects of property tuning in push–pull molecules. **RSC Advances**, Royal society of chemistry, v. 4, n. 102, p. 58826–58851, 2014.

BÜTTIKER, M.; THOMAS, H.; PRÊTRE, A. Mesoscopic capacitors. **Physics Letters A**, Elsevier, v. 180, n. 4-5, p. 364–369, 1993.

CECCHINI, G. Function and structure of complex II of the respiratory chain. **Annual Review of Biochemistry**, Annual Reviews 4139 El Camino Way, PO Box 10139, Palo Alto, CA 94303-0139, USA, v. 72, n. 1, p. 77–109, 2003.

CHANG, G.-P.; HSIEH, K.-H. High-performance semiconductors based on oligocarbazole–thiophene derivatives for solution-fabricated organic field-effect transistors. **Thin Solid Films**, Elsevier, v. 527, p. 291–298, 2013.

CREAGER, S. E.; WOOSTER, T. T. A new way of using ac voltammetry to study redox kinetics in electroactive monolayers. **Analytical Chemistry**, ACS Publications, v. 70, n. 20, p. 4257–4263, 1998.

DE VAULT, D.; CHANCE, B. Studies of photosynthesis using a pulsed laser: I. Temperature dependence of cytochrome oxidation rate in chromatium. Evidence for tunneling. **Biophysical journal**, Elsevier, v. 6, n. 6, p. 825–847, 1966.

DOGONADZE, R. R.; LEVICH, V. Theory of radiationless electronic transitions between ions in solutions. *In:* 1. DOKL. Akad. Nauk SSSR. 1959. v. 124, p. 123–126.

ECKERMANN, A. L. *et al.* Electrochemistry of redox-active self-assembled monolayers. **Coordination Chemistry Reviews**, Elsevier, v. 254, n. 15-16, p. 1769–1802, 2010.

ESHEL, Y.; PESKIN, U.; AMDURSKY, N. Coherence-assisted electron diffusion across the multi-heme protein-based bacterial nanowire. **Nanotechnology**, IOP Publishing, v. 31, n. 31, p. 314002, 2020.

EVANS, M.; GERGELY, J. A discussion of the possibility of bands of energy levels in proteins electronic interaction in non bonded systems. **Biochimica et Biophysica Acta**, Elsevier, v. 3, p. 188–197, 1949.

FAHLMAN, M. *et al.* Interfaces in organic electronics. **Nature Reviews Materials**, Nature Publishing Group UK London, v. 4, n. 10, p. 627–650, 2019.

FERNANDES, S. S.; CASTRO, M. C. R., *et al.* Push-pull heterocyclic dyes based on pyrrole and thiophene: synthesis and evaluation of their optical, redox and photovoltaic properties. **Coatings**, MDPI, v. 12, n. 1, p. 34, 2021.

FERNANDES, S. S.; PEREIRA, A., *et al.* Benzothiadiazole derivatives functionalized with two different (hetero) aromatic donor groups: Synthesis and evaluation as TiO_2 sensitizers for DSSCs. **Dyes and Pigments**, Elsevier, v. 151, p. 89–94, 2018.

FERREIRA, R. C. M.; RAPOSO, M. M. M.; COSTA, S. P. Heterocyclic amino acids as fluorescent reporters for transition metals: Synthesis and evaluation of novel furyl-benzoxazol-5-yl-l-alanines. **New Journal of Chemistry**, Royal Society of Chemistry, v. 42, n. 5, p. 3483–3492, 2018.

FEYNMAN, R. P. Plenty of Room at the Bottom. *In:* LITTLE BROWN BOSTON, MA, USA. APS annual meeting. 1959. p. 1–7.

GALKA, M. M.; KRAATZ, H.-B. Electron Transfer Studies on Self-Assembled Monolayers of Helical Ferrocenoyl-Oligoproline-Cystamine Bound to Gold. **ChemPhysChem**, Wiley Online Library, v. 3, n. 4, p. 356–359, 2002.

GARRIDO, M. *et al.* Supramolecular assembly of pyrene-tetrathiafulvalene hybrids on graphene: structure–property relationships and biosensing activity. **Journal of Materials Chemistry C**, Royal Society of Chemistry, v. 9, n. 33, p. 10944–10951, 2021.

GARROTE, B. L.; SANTOS, A.; BUENO, P. R. Label-free capacitive assaying of biomarkers for molecular diagnostics. **Nature Protocols**, Nature Publishing Group UK London, v. 15, n. 12, p. 3879–3893, 2020.

GATTO, E. *et al.* Mimicking nature: a novel peptide-based bio-inspired approach for solar energy conversion. **Chemphyschem: a European Journal of Chemical Physics and Physical Chemistry**, v. 15, n. 1, p. 64–68, 2013.

GIESE, B.; GRABER, M.; CORDES, M. Electron transfer in peptides and proteins. **Current Opinion in Chemical Biology**, Elsevier, v. 12, n. 6, p. 755–759, 2008.

GRAY, H. B.; WINKLER, J. R. Electron flow through proteins. **Chemical physics letters**, Elsevier, v. 483, n. 1-3, p. 1–9, 2009.

GRAY, H. B.; WINKLER, J. R. Electron tunneling through proteins. **Quarterly reviews of biophysics**, Cambridge University Press, v. 36, n. 3, p. 341–372, 2003.

GRAY, H. B.; WINKLER, J. R. Long-range electron transfer. **Proceedings of the National Academy of Sciences**, National Acad Sciences, v. 102, n. 10, p. 3534–3539, 2005.

HAINS, A. W. *et al.* Molecular semiconductors in organic photovoltaic cells. **Chemical Reviews**, ACS Publications, v. 110, n. 11, p. 6689–6735, 2010.

HÄKKINEN, H. The gold–sulfur interface at the nanoscale. **Nature Chemistry**, Nature Publishing Group UK London, v. 4, n. 6, p. 443–455, 2012.

IMRY, Y.; LANDAUER, R. Conductance viewed as transmission. **Reviews of Modern Physics**, APS, v. 71, n. 2, s306, 1999.

INOKUCHI, H. The discovery of organic semiconductors. Its light and shadow. **Organic electronics**, Elsevier, v. 7, n. 2, p. 62–76, 2006.

JUHANIEWICZ, J.; PAWLOWSKI, J.; SEK, S. Electron transport mediated by peptides immobilized on surfaces. **Israel Journal of Chemistry**, Wiley Online Library, v. 55, n. 6-7, p. 645–660, 2015.

KENFACK, G. T. *et al.* Triazolobithiophene light absorbing self-assembled monolayers: synthesis and mass spectrometry applications. **Molecules**, MDPI, v. 16, n. 10, p. 8758–8774, 2011.

KRAATZ, H.-B. *et al.* Electron transfer through H-bonded peptide assemblies. **The Journal of Physical Chemistry B**, ACS Publications, v. 108, n. 52, p. 20164–20172, 2004.

LANDAUER, R. Spatial variation of currents and fields due to localized scatterers in metallic conduction. **IBM Journal of Research and Development**, IBM, v. 1, n. 3, p. 223–231, 1957.

LANE, N. **Power, sex, suicide: mitochondria and the meaning of life**. Oxford University Press, 2005.

LAVIRON, E. General expression of the linear potential sweep voltammogram in the case of diffusionless electrochemical systems. **Journal of Electroanalytical Chemistry and Interfacial Electrochemistry**, Elsevier, v. 101, n. 1, p. 19–28, 1979.

LI, C. *et al.* Design and characterization of red fluorogenic push–pull chromophores holding great potential for bioimaging and biosensing. **Organic & Biomolecular Chemistry**, Royal Society of Chemistry, v. 14, n. 39, p. 9253–9261, 2016.

LI, Y. *et al.* Self-assembly of intramolecular charge-transfer compounds into functional molecular systems. **Accounts of Chemical Research**, ACS Publications, v. 47, n. 4, p. 1186–1198, 2014.

LIU, J.; TANG, J.; GOODING, J. J. Strategies for chemical modification of graphene and applications of chemically modified graphene. **Journal of Materials Chemistry**, Royal Society of Chemistry, v. 22, n. 25, p. 12435–12452, 2012.

LOPES, L. C.; SANTOS, A.; BUENO, P. R. Measuring quantum conductance and capacitance of graphene using impedance-derived capacitance spectroscopy. **Carbon**, Elsevier, v. 184, p. 821–827, 2021.

LOPES, L. C.; PINZÓN, E. F., *et al.* Electrochemical measurement of the electronic structure of graphene via quantum mechanical rate spectroscopy. **Electrochimica Acta**, Elsevier, v. 480, p. 143837, 2024.

M. FERNANDES, S. S. *et al.* Push–pull N,N-diphenylhydrazones bearing bithiophene or thienothiophene spacers as nonlinear optical second harmonic generators and as photosensitizers for nanocrystalline TiO_2 dye-sensitized solar cells. **ACS Omega**, ACS Publications, v. 3, n. 10, p. 12893–12904, 2018.

MALVANKAR, N. S.; VARGAS, M.; NEVIN, K., *et al.* Structural basis for metallic-like conductivity in microbial nanowires. **MBio**, Am Soc Microbiol, v. 6, n. 2, p. 10–1128, 2015.

MALVANKAR, N. S.; VARGAS, M.; NEVIN, K. P., *et al.* Tunable metallic-like conductivity in microbial nanowire networks. **Nature Nanotechnology**, Nature Publishing Group UK London, v. 6, n. 9, p. 573–579, 2011.

MALYTSKYI, V. *et al.* Synthesis, self-assembly and characterization of a novel push–pull thiophene-based chromophore on a gold surface. **RSC Advances**, Royal Society of Chemistry, v. 5, n. 33, p. 26308–26315, 2015.

MARCUS, R. A. On the theory of oxidation-reduction reactions involving electron transfer. I. **Journal of Chemical Physics**, American Institute of Physics, v. 24, n. 5, p. 966–978, 1956.

MARCUS, R. A.; SUTIN, N. Electron transfers in chemistry and biology. **Biochimica et Biophysica Acta-Bionergetics**, Elsevier, v. 811, n. 3, p. 265–322, 1985.

MARCUS, R. A. Chemical and electrochemical electron-transfer theory. **Annual Review of Physical Chemistry**, v. 15, n. 1, p. 155–196, 1964.

MARCUS, R. A. Electron transfer reactions in chemistry: theory and experiment (Nobel lecture). **Angewandte Chemie International Edition in English**, Wiley Online Library, v. 32, n. 8, p. 1111–1121, 1993.

MARQUÉS-GONZÁLEZ, S.; LOW, P. J. Molecular electronics: history and fundamentals. **Australian Journal of Chemistry**, CSIRO Publishing, v. 69, n. 3, p. 244–253, 2016.

MATSUSHITA, D.; UJI, H.; KIMURA, S. Effect of oscillation dynamics on long-range electron transfer in a helical peptide monolayer. **Physical Chemistry Chemical Physics**, Royal Society of Chemistry, v. 20, n. 22, p. 15216–15222, 2018.

MERRIFIELD, R. B. Solid phase peptide synthesis. I. The synthesis of a tetrapeptide. **Journal of the American Chemical Society**, ACS Publications, v. 85, n. 14, p. 2149–2154, 1963.

MERZBACHER, E. The early history of quantum tunneling. **Physics Today**, American Institute of Physics, v. 55, n. 8, p. 44–50, 2002.

NIETO, E. F. P. *et al.* Quantum rate electrodynamics and resonant junction electronics of heterocyclic molecules. **Electrochimica Acta**, Elsevier, v. 501, p. 144749, 2024.

NITZAN, A. A relationship between electron-transfer rates and molecular conduction. **The Journal of Physical Chemistry A**, ACS Publications, v. 105, n. 12, p. 2677–2679, 2001.

OKDA, H. E. *et al. N*, *N*-Diphenylanilino-heterocyclic aldehyde-based chemosensors for UV-vis/NIR and fluorescence Cu (II) detection. **New Journal of Chemistry**, Royal Society of Chemistry, v. 43, n. 19, p. 7393–7402, 2019.

ORLOWSKI, G. A.; CHOWDHURY, S.; KRAATZ, H.-B. Reorganization energies of ferrocene-peptide monolayers. **Langmuir**, ACS Publications, v. 23, n. 25, p. 12765–12770, 2007.

OWENS, R. M.; MALLIARAS, G. G. Organic electronics at the interface with biology. **MRS bulletin**, Cambridge University Press, v. 35, n. 6, p. 449–456, 2010.

PINZON, E. F.; SANTOS, A.; BUENO, P. R. Density of States of a Nanoscale Semiconductor Interface as a Transduction Signal for Sensing Molecules. **ACS Applied Electronic Materials**, ACS Publications, v. 3, n. 8, p. 3411–3417, 2021.

PINZÓN, E. F. *et al.* Quantum rate as a spectroscopic methodology for measuring the electronic structure of quantum dots. **Journal of Materials Chemistry C**, Royal Society of Chemistry, v. 12, n. 13, p. 4606–4617, 2024.

QI, L.; TIAN, H.; YU, H.-Z. Binary thiolate DNA/ferrocenyl self-assembled monolayers on gold: a versatile platform for probing biosensing interfaces. **Analytical Chemistry**, ACS Publications, v. 90, n. 15, p. 9174–9181, 2018.

REDONDO-GÓMEZ, C. *et al.* Peptide-based self-assembled monolayers (SAMs): what peptides can do for SAMs and vice versa. **Chemical Society Reviews**, Royal Society of Chemistry, 2024.

REGINATO, G. *et al.* Design and synthesis of organic sensitizers with enhanced anchoring stability in dye-sensitized solar cells. **Pure and Applied Chemistry**, De Gruyter, v. 90, n. 2, p. 363–376, 2018.

SÁNCHEZ, Y. P.; SANTOS, A.; BUENO, P. R. Quantum Mechanical Meaning of the Charge Transfer Resistance. **Journal of Physical Chemistry C**, v. 126, p. 3151–3162, 6 2022.

SHAH, A. *et al.* Electron transfer in peptides. **Chemical Society Reviews**, Royal Society of Chemistry, v. 44, n. 4, p. 1015–1027, 2015.

SONG, J. *et al.* Organic light-emitting diodes: pushing toward the limits and beyond. **Advanced Materials**, Wiley Online Library, v. 32, n. 35, p. 1907539, 2020.

SPANGGAARD, H.; KREBS, F. C. A brief history of the development of organic and polymeric photovoltaics. **Solar Energy Materials and Solar Cells**, Elsevier, v. 83, n. 2-3, p. 125–146, 2004.

SZENT-GYÖRGYI, A. Towards a new biochemistry? **Science**, American Association for the Advancement of Science, v. 93, n. 2426, p. 609–611, 1941.

TAKEDA, K.; MORITA, T.; KIMURA, S. Effects of monolayer structures on long-range electron transfer in helical peptide monolayer. **The Journal of Physical Chemistry B**, ACS Publications, v. 112, n. 40, p. 12840–12850, 2008.

ULMAN, A. Formation and structure of self-assembled monolayers. **Chemical Reviews**, ACS Publications, v. 96, n. 4, p. 1533–1554, 1996.

VANOVA, V. *et al.* Peptide-based electrochemical biosensors utilized for protein detection. **Biosensors and Bioelectronics**, Elsevier, v. 180, p. 113087, 2021.

VILAN, A.; ASWAL, D.; CAHEN, D. Large-area, ensemble molecular electronics: motivation and challenges. **Chemical Reviews**, ACS Publications, v. 117, n. 5, p. 4248–4286, 2017.

VON HIPPEL, A. Molecular engineering. **Science**, American Association for the Advancement of Science, v. 123, n. 3191, p. 315–317, 1956.

VON KLITZING, K. Essay: Quantum Hall Effect and the New International System of Units. **Physical Review Letters**, v. 122, n. 20, 2019. ISSN 0031-9007.

WANG, J. *et al.* Self-Assembled Monolayers of Push–Pull Chromophores as Active Layers and Their Applications. **Molecules**, MDPI, v. 29, n. 3, p. 559, 2024.

WANG, T. *et al.* Fluorescent chemosensors based on conjugated polymers with *N*-heterocyclic moieties: two decades of progress. **Polymer Chemistry**, Royal Society of Chemistry, v. 11, n. 18, p. 3095–3114, 2020.

WATANABE, J.; MORITA, T.; KIMURA, S. Effects of dipole moment, linkers, and chromophores at side chains on long-range electron transfer through helical peptides. **The Journal of Physical Chemistry B**, ACS Publications, v. 109, n. 30, p. 14416–14425, 2005.

WHITESIDES, G. M.; KRIEBEL, J. K.; MAYERS, B. T. Self-assembly and nanostructured materials. **Nanoscale Assembly: Chemical Techniques**, Springer, p. 217–239, 2005.

WIERZBINSKI, E. *et al.* The single-molecule conductance and electrochemical electron-transfer rate are related by a power law. **ACS Nano**, ACS Publications, v. 7, n. 6, p. 5391–5401, 2013.

WINKLER, J. R.; GRAY, H. B. Long-range electron tunneling. **Journal of the American Chemical Society**, ACS Publications, v. 136, n. 8, p. 2930–2939, 2014.

ZHANG, L.; LU, J.; WAIGH, T. Electronics of peptide-and protein-based biomaterials. **Advances in Colloid and Interface Science**, Elsevier, v. 287, p. 102319, 2021.

ZHU, G. Y. *et al.* Crossover between the adiabatic and nonadiabatic electron transfer limits in the Landau-Zener model. **Nature Communications**, Nature Publishing Group UK London, v. 12, n. 1, p. 456, 2021.

ZHU, H. *et al.* Intramolecular charge transfer and solvation of photoactive molecules with conjugated push–pull structures. **ChemPhysChem**, Wiley Online Library, v. 17, n. 20, p. 3245–3251, 2016.

Chapter 2

Quantum rate theory and electron transfer dynamics in redox-tagged peptides on electrode

The QRT permits to correlate the ET that describes the dynamics of redox reactions, where k is the primary parameter of interest, with ET_p commonly studied in molecular junctions in solid-state physics, where G is the key parameter. The theory connects these two phenomena, traditionally studied separately, by introducing a quantum state related to electronic states, known as C_q (BUENO, 2020). The relationship between k and G through C_q has enabled the study of ET processes in electro-active molecules at SAMs interfaces (BUENO, 2023). The study of redox reactions in diffusionless systems from a quantum perspective falls within the realm of quantum electrochemistry (BOCKRIS; KHAN, 2012). This field combines the principles of quantum mechanics with electrochemistry to understand the behavior of electrochemical systems at the quantum level. Although quantum electrochemistry has been recognized as a field of electrochemistry since the 1960s, its development has been slow. In our opinion, this is because the initial introduction of these quantum concepts, into the electrochemical systems, did not allow for easy testing within traditional experimental setups. Consequently, the knowledge developed in quantum electrochemistry has remained primarily at a theoretical level. As will be presented in this chapter, the QRT not only provides a quantum interpretation of the existing quantum rates in ET reactions, but also allows experimental access to quantum properties like C_q and G, with the aim to elucidate the quantum mechanical meaning of k within electrochemical reactions. In summary, the kinetics of the ET process is studied in this chapter using redox-tagged peptide SAM interfaces and following the QRT with two main purposes:

- ☑ To demonstrate the quantum mechanical nature of ET kinetics in a diffusionless heterogeneous electrochemical reaction occurring within an redox peptide SAM and;

- ☑ To establish a straightforward methodology for calculating k of ET in redox-tagged peptide SAMs by experimentally determining C_q through CV and/or EIS.

The results discussed herein have been published in (ALARCÓN; SANTOS; BUENO, 2021).

2.1 Introduction

In electrochemistry, k of ET, is a fundamental parameter that characterizes the rate at which electrons are transferred between a redox-active species and an electrode. Determining this kinetic constant is essential for studying various factors that can influence ET behavior in systems including electro-active molecular SAMs (SHAH *et al.*, 2015). Understanding these factors not only helps elucidate important biological processes, such as oxidative phosphorylation in cellular respiration (as was mentioned in the introduction section 1.1), but also enables the control of reaction kinetics to optimize the performance of electrochemical systems. This is particularly crucial in the development of technologies like biological sensors, where the precise control of ET properties is necessary for enhancing sensitivity and accuracy.

The study of the ET process in redox molecular SAMs, based on the measurement of the parameter k, has significantly enriched our understanding of ET through biological macro-structures. These studies have also led to the optimization of ET processes for technological development. Fundamental insights from electrochemical studies have revealed factors influencing the tunneling and hopping mechanisms that govern ET in macromolecular structures. One important factor is the distance of the molecular bridge, which determines the efficiency of electrodynamics (ARIKUMA *et al.*, 2010; MANDAL; KRAATZ, 2012; SHAH *et al.*, 2015). Additionally, changes in molecular structure, induced by ligand binding or environmental variations, have been identified as modulators of ET (MATSUSHITA; UJI; KIMURA, 2018; TAKEDA; MORITA; KIMURA, 2008; WATANABE; MORITA; KIMURA, 2005; FINKLEA; RAVENSCROFT; SNIDER, 1993). These insights have been applied to the development of technological devices like biological sensors. By immobilizing molecules on electrodes, researchers have created sensitive and specific sensors for detecting various analytes, including glucose, DNA sequences, and proteins (VANOVA *et al.*, 2021; GARROTE; SÁNCHEZ, *et al.*, 2024; QI; TIAN; YU, H.-Z., 2018; BRANDÃO *et al.*, 2023). Furthermore, the knowledge gained from electrochemical studies of ET kinetics has been important in identifying conditions and designing molecular structures that optimize molecular electronic devices and integrate molecules into electronic circuits (GATTO *et al.*, 2013; YU, J.; HORSLEY; ABELL, 2016).

Given the importance of experimentally determining k in the fundamental study of ET reactions in electrochemistry, particularly for redox-tagged molecular SAMs, various electrochemical experimental strategies have been proposed over the years (ECKERMANN *et al.*, 2010). Electrochemical techniques based on potential sweep methods, such as CV (BOITEL-AULLEN *et al.*, 2021; MALECKA *et al.*, 2020; HORSLEY *et al.*, 2014), and potential step methods, such as chronoamperometry (CA) (CHIDSEY, 1991; WATANABE; MORITA; KIMURA, 2005), where the electrode is driven far from equilibrium, have been employed. For instance, one of the most well-known methods for determining the kinetic parameters of diffusionless systems is Laviron's method (LAVIRON, 1979). In 1979, Etienne Laviron presented an elegant mathematical expression for obtaining k by analyzing the difference between the redox potential peaks (ΔV_p) obtained from potential sweep techniques as a function of the scan rate (s), under conditions where diffusion control is absent. A detailed experimental procedure for the Laviron's method is presented in the experimental subsection of this chapter (Section 2.2.4). Additionally, the determination of k has also been achieved under equilibrium conditions by applying a small alternating signal at steady state, using techniques such as AC voltammetry (CREAGER; WOOSTER, 1998) and EIS methods (ARIKUMA *et al.*, 2010; MATSUSHITA; UJI; KIMURA, 2018). These methods involve perturbing the system with a small-magnitude alternating signal to determine the kinetic parameters.

While electrochemical techniques are powerful tools for experimentally determining the kinetic constant of ET reactions in these interesting molecular systems, it is important to emphasize that the most critical aspect of a kinetic study is the fundamental analysis of k (FLETCHER, 2010). This analysis relies on the appropriate kinetic theories used to interpret the experimental results. In this context, as discussed in the Chapter 1, the most significant theory is the semi-classical Marcus theory. Originally developed for homogeneous reactions between species in solution (MARCUS, 1956), this theory was later extended to heterogeneous reactions between electrodes and species in solution (GERISCHER, 1990), as well as adsorbed electro-active molecules (CHIDSEY, 1991). However, applying the Eq. 1.1 derived from Marcus theory for homogeneous ET reactions in the context of heterogeneous electrochemical systems, where a redox species is immobilized on the electrode, known as diffusionless reactions, has still been controversial.

In this chapter, we demonstrate the quantum nature of ET rates in systems comprising a redox-tagged peptide SAM using the QRT approach. The key experimental variable of interest is C_q, which correlates with the charge of reduction and oxidation electronic states. This capacitance is obtained not only as the real capacitance at low frequencies, where the semicircle of the capacitive Nyquist plot closes, but also

by examining the faradaic current at the formal potential (V_F) in a simple current-potential curve at low s and defining certain degeneracy rules of the redox reaction at equilibrium charge dynamic state (BUENO; CRUZEIRO, *et al.*, 2021). The k obtained through the QRT approach are compared with those determined using Laviron's method, which is based on the classical Butler-Volmer theory. Additionally, we provide background information on Laviron's approach and discuss its equivalence with the quantum interpretation of ET rates.

2.2 Materials and methods

The experimental methodology detailed in this section was also used in other chapters in this thesis. Therefore, this section 2.2 will be referenced in other chapters, particularly chapters 3 and 4.

2.2.1 Chemical reagents

Table 2.1 lists the reagents and materials used, which includes: i) the synthesis of ferrocene-labeled peptides by SPPS, ii) the purification and characterization of the crude peptide by HPLC, iii) the mechanical and electrochemical cleaning of gold electrodes, and iv) the electrochemical measurements. The table also specifies the suppliers of used materials. Aqueous solutions were prepared using Milli-Q water (Simplicity® water purification system, Millipore, 18.2 MΩ cm at 25°C).

2.2.2 Peptide synthesis and characterization

The ferrocene-labeled peptide Fc-Glu-Ala-Ala-Cys-Cys was synthesized using SPPS with Fmoc chemistry, as described in (ALARCÓN; SANTOS; BUENO, 2021) and presented in the Figure 2.1. The SPPS was performed on Rink amide resin (0.52 mmol g^{-1}). The coupling cycle to obtain Glu-Ala-Ala-Cys-Cys was conducted as follows: i) The Fmoc protecting group on the NH_2 groups of the first amino acid was removed with 20% (v/v) 4-methyl-piperidine/DMF, initially for 1 min followed by 20 min. ii) The COOH group of the subsequent amino acid was activated using a two-fold molar excess of HOBt/DIC in DMF. The coupling reactions were carried out at room-temperature on a shaker for 2 h, and the coupling cycle was repeated. The ninhydrin test was employed to confirm the removal of the Fmoc group (indicated by a blue color) and the incorporation of each amino acid (indicated by a yellow color). Then, the ferrocene moiety (3-ferrocenylpropionic anhydride) was coupled to the N-terminal Glu in the presence of DMAP (0.1-fold excess) first for 2h and then

Table 2.1: List of chemical reagents used in Chapter 2.

Reagent	Company	Purpose
N-α-Fmoc-S-trityl-L-cysteine (Fmoc-Cys(Trt)-OH)[a]	AAPPTEC	Amino acids for peptide synthesis
N-Fmoc-L-alanine (Fmoc-Ala-OH)[a]	AAPPTEC	
N-α-Fmoc-L-glutamic acid β-*tert*-butyl ester (Fmoc-Glu(OtBu)-OH)[a]	AAPPTEC	
Rink amide resin (0.52 mmol g^{-1})	AAPPTEC	
N,N′-Diisopropylcarbodiimide (DIC)	Sigma-Aldrich	Coupling reagents for the peptide synthesis
Hydroxybenzotriazole (HOBt)	Sigma-Aldrich	
4-Methylpiperidine	Sigma-Aldrich	Reagent for Fmoc removal
Dimethylformamide (DMF)	Sigma-Aldrich	Solvent of peptide synthesis
3-Ferrocenylpropionic anhydride	Sigma-Aldrich	Coupling of the ferrocene (Fc) redox probe in the synthesized peptide
4-Dimethylaminopyridine (DMAP)	Fluka Chemika	
Benzotriazole-1-yl-oxy-tris-pyrrolidino-phosphonium hexafluorophosphate (PyBOP)	Fluka Chemika	
Triisopropylsilane (TIS)	Fluka Chemika	Cleavage coktail and resin precipitation
Trifluoroacetic acid (TFA)	Sigma-Aldrich	
2,2′-(ethylenedioxy)diethanethil (EDDT)	Sigma-Aldrich	
Ethyl ether anhydrous	Sigma-Aldrich	
HPLC-grade acetonitrile (ACN)	Sigma-Aldrich	Solvent for peptide synthesis, SAM fabrication, and electrochemical characterization
Tetrabutylammonium perchlorate ($TBAClO_4$)	Sigma-Aldrich	Electrolyte for electrochemical characterization
Alumina suspensions (1 μm, 0.3 μm, and 0.05 μm)	Buehler	Mechanical polishing of gold electrodes
Polishing cloths (MASTERTEX®)	Buehler	
Sodium hydroxide (NaOH)	Sigma-Aldrich	Electrochemical cleaning of gold electrodes
Ethyl alcohol (EtOH)	Sigma-Aldrich	
Sulfuric acid (H_2SO_4)	Qhemis	

[a]Fmoc (9-fluo-renylmethyloxycarbonyl)

PyBOP/DIPEA in DMF twofold excess was added to activate the carboxyl group of Fc, over 24 h.

The cleavage of the peptide from the resin was performed with a TFA/TIS/EDDT/H_2O (94:1:2.5:2.5 $^{v}/_{v}$) mixture for 1.5 h. The peptide was then precipitated using ice-cold diethyl ether, and extracted in a mixture of TFA/H_2O (0.045% $^{v}/_{v}$, solvent A) and TFA/ACN (0.036% $^{v}/_{v}$, solvent B). The precipitation and extraction stages were carried out in cycles, each consisting of vortexing, sonication, and centrifugation for 5 min each. Finally, the peptide-containing supernatant was freeze-dried. The purification of the crude peptide was conducted using HPLC with a semi-preparative reverse phase Phenomenex C18 column (250 $\times$ 10 mm, 5 μm particle size) and employed the linear gradient from 25% to 55% of solvent B for almost 90 min. The purity of peptide was qualitatively analyzed by HPLC using an analytical Shimadzu system with a reverse phase column (ZORBAX 300SB-C18, 4.6 $\times$ 150 mm, 5 μm particle size, detection at 220 nm), and using the linear gradient of 5 % to 95% of solvent B for 30 min with flow rate of 1 mL min^{-1}. Finally, the identity of the peptide was confirmed by ion-trap mass spectrometry (MS) using a Brucker system in positive ion mode (see Appendix A). The pure peptide was stored in the solid phase at 4 C°, until it was required in the incubation process with the gold electrode.

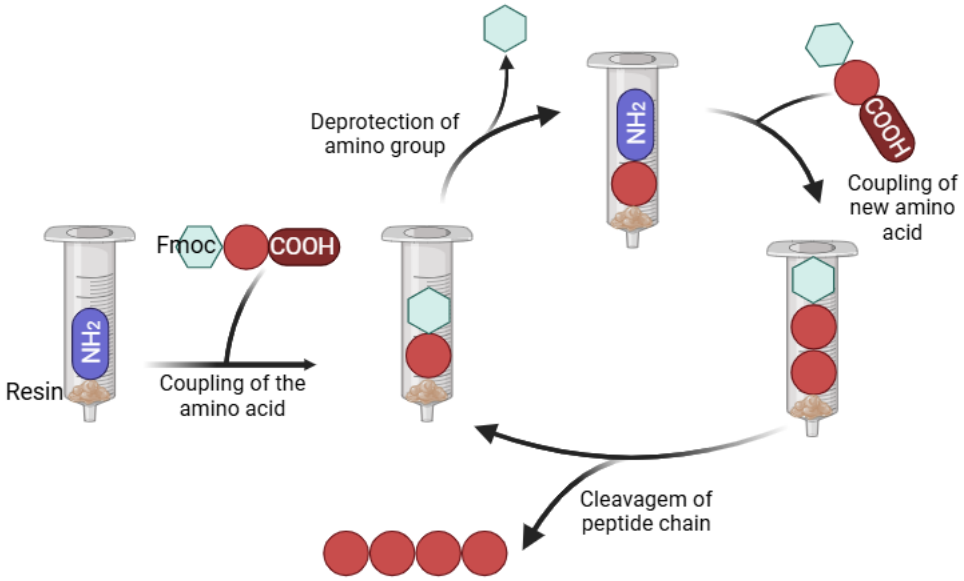

Figure 2.1: Scheme illustrating the synthesis of a peptide via SPPS using Fmoc chemistry. The process involves repeated cycles of Fmoc deprotection and amino acid coupling to assemble the desired peptide sequence. After synthesis, the peptide was cleaved from the resin. The resulting crude peptide was then purified using HPLC.

Source: Author (2024) created with BioRender.com

2.2.3 Equipment and electrodes

Electrochemical measurements were conducted using a conventional three-electrode cell setup. The counter and reference electrodes consisted of a platinum mesh and Ag | AgCl (3M KCl), respectively. The working electrode was a gold electrode from METROHM (diameter of 2 mm, geometric area of 0.03142 cm^2), modified with the ferrocene-labeled peptide. The supporting electrolyte used was 20 mM $TBAClO_4$ in ACN/H_2O (1:4 v/v). EIS and CV measurements were carried out in a Metrohm Autolab potentiostat controlled by NOVA 1.8 software and possessed a Frequency Response Analysis (FRA) module.

Mechanical and electrochemical cleaning of the working electrode: The gold electrodes[1] were polished sequentially using aluminum suspensions with decreasing particle sizes (1, 0.3, and 0.05 μm) on MASTERTEX® polishing cloth. After each polishing step with alumina suspension, the electrode was rinsed with H_2O and cleaned ultrasonically in H_2O for 5 min to remove any residual alumina particles on the surface. Next, the electrode surface underwent electrochemical cleaning via CV in 0.5 M NaOH (100 cycles from -1.7 to -0.5 V at 100 mV s^{-1}). This was followed by rinsing with H_2O and stirring in EtOH for 20 min. Subsequently, the gold surface was further treated electrochemically with 25 successive CV scans in 0.5 M H_2SO_4 (from -0.2 to 1.5 V at 100 mV s^{-1}). Finally, the electrode was rinsed with H_2O and immersed in the corresponding incubation solution. The electroactive surface area (A_e = 0.044 $\pm$ 0.001 cm^2)[2] was determined by integrating the cathodic peak of the last cycle of the sulphuric acid cleaning step, using the value of 410 μC cm^{-2} as a reference of charge of a polycrystalline gold inter-face (TRASATTI; PETRII, 1992). To ensure consistent electrochemical responses in the formation of well-organized SAMs, we monitored the quality of the gold surfaces by assessing the surface roughness. This was calculated by dividing the A_e by the electrode geometry area, ensuring this ratio remained below than 1.8.

The lyophilized ferrocene-labeled peptide, obtained after the purification process, was dissolved in a solution of ACN/H_2O (1:1,v/v) to a concentration of 2 mM. The cleaned electrode was then immersed in this solution for 16 h in a dark place at room-temperature (25°C) to induce the formation of SAM. Subsequently, the modified gold surface was rinsed sequentially with 1:1 ACN/H_2O and H_2O, following the procedure outlined in reference (GARROTE; SANTOS; BUENO, 2020).

[1] Gold electrode of 2 mm diameter from METROHM, geometric area of 0.03142 cm^2

[2] A_e value corresponds to the average of three different modified electrodes

2.2.4 Electrochemical measurements

CV was performed at 0.1 V s^{-1} to evaluate the quality of the monolayer and the electrochemical behavior of the ferrocene-labeled peptide monolayer. The V_F of the SAMs was resolved as $V_F = (V_{pa} + V_{pc})/2$, where V_{pa} and V_{pc} are the oxidation and reduction potential peaks, respectively, as shown in Figure 2.4. Additionally, CV was used to determine the k using Laviron's method and to measure the C_q of the molecular interface. The CV scans were conducted in two ranges from 0.0 to 0.7 V (with s of 0.1-1 V s^{-1}) and from -0.1 to 0.9 V (with s of 7-20 V s^{-1}), comprising four cycles at each s.

Laviron's method is widely used in the literature to determine the kinetic parameters of ET occurring in diffusionless systems, such as redox molecular SAMs (LAVIRON, 1979). This method involves performing CV measurements at different s. For a one electron process, a key requirement of this method is that the difference between V_{pa} and V_{pc}, i.e ΔV_p, addressed at the highest anodic (i_{pa}) and cathodic (i_{pc}) current peaks, must be greater than 200 mV. From the CV plots, the V_{pa} and V_{pc} are extracted from the voltammogram and plotted against the logarithm of the s. Therefore, two branches are obtained, referred to as the anodic and cathodic regimes. From the slopes of the anodic and cathodic branches (involving one-electron redox reaction), $RT/(1-\alpha)F$ and $RT/(\alpha)F$, respectively, the parameter α is obtained, which is known as the ET coefficient[3]. Here, R represents the ideal gas constant, T is the temperature, and F is the Faraday constant. The s obtained by extrapolating the anodic (s_a) and cathodic (s_c) branches to the abscissa-intercepts at the V_F (low s), is directly related to the anodic (k_a) and cathodic (k_c) kinetic constants as follows

$$k_a = \frac{(1-\alpha)F}{RT} s_a \tag{2.1}$$

and

$$k_c = -\frac{\alpha F}{RT} s_c \tag{2.2}$$

2.2.5 EIS measurements and capacitive spectra

EIS measurements were conducted at two potentials: one outside the redox window V_{out} and the other at the V_F. The measurements were performed over a frequency range of 100 kHz to 0.1 Hz, using a sinusoidal perturbation with a peak-to-peak amplitude of 10 mV. The EIS data were verified for compliance with the constraints of linear systems using Kramers-Kronig analysis, facilitated by the FRA AUTOLAB

[3]The ET coefficient typically ranges between 0 and 1 and reflects the degree of symmetry of the activation energy barrier for the oxidation or reduction reaction. For Laviron's method, α should be close to 0.5, indicating a symmetrical energy barrier. However, if α is not too different from 0.5, it will not pose a major obstacle to determining the k.

software. Capacitive data were preferred over impedance data for analyzing diffusionless electrochemical reactions in redox-tagged peptide SAMs because the system is dominated by charge storage and relaxation rather than mass transport limitations.

Capacitive spectra were obtained by computing the complex capacitance $C^*(\omega)$ function from the complex impedance $Z^*(\omega)$ by the relationship: $C^*(\omega) = 1/j\omega Z^*(\omega)$, where $j = \sqrt{-1}$ is the complex number, $\omega = 2\pi\nu$ is the angular frequency, and ν is the linear frequency. The real (C') and the imaginary (C'') components of $C^*(\omega) = C' + jC''$, are determinated using the mathematical equations $C' = \phi Z''$ and $C'' = \phi Z'$, where Z' and Z'' denote the real and imaginary components of impedance, respectively. ϕ is defined as $\phi = 1/(\omega|Z|^2)$, with $|Z|$ representing the modulus of the impedance (BUENO; MIZZON; DAVIS, 2012; BUENO, 2018; BUENO; BENITES; DAVIS, 2016).

Table 2.2: Description of the elements obtaining by equivalent circuit fitting depicted in Figure 2.2.

	Element	Description	Graphical determination	Associated time-scale τ
non-Faradaic	C_m monolayer capacitance	The monolayer capacitance is the sum of the double layer C_{dl} and the capacitance of the monolayer's bulk properties C_b, which represents the capacitance of the layer without ion ingress.	Real capacitive value achieved at high frequency in the capacitive Nyquist plot.	
	C_t capacitance	The ionic capacitance captures the response of the monolayer to ionic relaxation, providing a characteristic "fingerprint" of how ions interact with and relax within the monolayer.	Semi-circle diameter of the capacitive Nyquist plot defined at low frequencies.	
	R_t resistance	Resistance associated to the ion relaxation process inside the bulk of the film.	Not possible	$\tau_t = R_t C_t$
Faradaic	C_q quantum capacitance	Charge storage due to the occupancy of electronic states during the redox reaction.	Semi-circle diameter of the capacitive Nyquist plot defined at low frequencies.	
	R_{qt} quantum resistance	Resistance of each quantum channel that comprises the monolayer.	Not possible.	$\tau = R_{qt} C_q$

Source: (SÁNCHEZ; SANTOS; BUENO, 2022).

The function $C^*(\omega)$ characterizes both non-faradaic and faradaic processes, since these processes involve relaxation dynamics, the capacitive response can be modeled using the Cole-Cole equation (SÁNCHEZ; SANTOS; BUENO, 2022; GOES *et al.*, 2012; LEHR *et al.*, 2017):

$$C^*(\omega) = C_{\omega\to\infty} + \frac{C_{\omega\to 0}}{1 + (j\omega\tau^*)^{(1-\alpha)}} \tag{2.3}$$

where $C_{\omega\to\infty}$ and $C_{\omega\to 0}$, correspond to the capacitances at high and low frequencies, respectively. The parameter τ^* represents the characteristic relaxation time, while α ($0 \leq \alpha \leq 1$) accounts for deviations from ideal relaxation. For the non-faradaic process, the complex capacitance $C^*_{nf_a}(\omega)$ was evaluated at V_{out}. In this context, $C_{\omega\to\infty}$, denoted as C_m, represents the capacitance of the monolayer in the absence of ion ingress, whereas $C_{\omega\to 0}$, denoted as C_t, accounts for ionic interactions and relaxation within the monolayer and has an associated ionic relaxation time, τ_t, that follows the relation $\tau = R_t C_t$, where R_t is the corresponding resistance. Deviations from ideal Debye relaxation are described by the parameter α_t ($0 \leq \alpha_t \leq 1$), yielding the following expression for non-faradaic relaxation:

$$C^*_{nf_a}(\omega) = C_m + \frac{C_t}{1 + (j\omega\tau_t)^{(1-\alpha_t)}} \tag{2.4}$$

The faradaic process, associated with electronic relaxation, was analyzed at V_F and is described by:

$$C^*_{f_a}(\omega) = C_t + \frac{C_q}{1 + (j\omega\tau)^{(1-\alpha_q)}} \tag{2.5}$$

where the relaxation time τ is given by $\tau = R_q C_q$, and as discussed in section 1.4 of the Chapter 1, it is inversely related to k. The C_q and R_q represent the quantized capacitive and resistive elements associated with the occupation of electronic states and electron transmission through quantum channels. This relationship underscores how the capacitive response provides direct insight into the kinetics of ET, linking interfacial electrochemistry with quantum transport phenomena.

The capacitive and resistive components of both the non-faradaic and faradaic processes were estimated graphically from the capacitive Nyquist semicircle plots, as ilustrated in the Figure 2.2*b* and *c* and detailed in Table 2.2, and also by fitting these data using an equivalent circuit model representing the interfacial processes (SÁNCHEZ; SANTOS; BUENO, 2022). This circuit model comprises two branches: one describing non-faradaic processes and the other representing faradaic processes, as illustrated in Figure 2.2*a*.

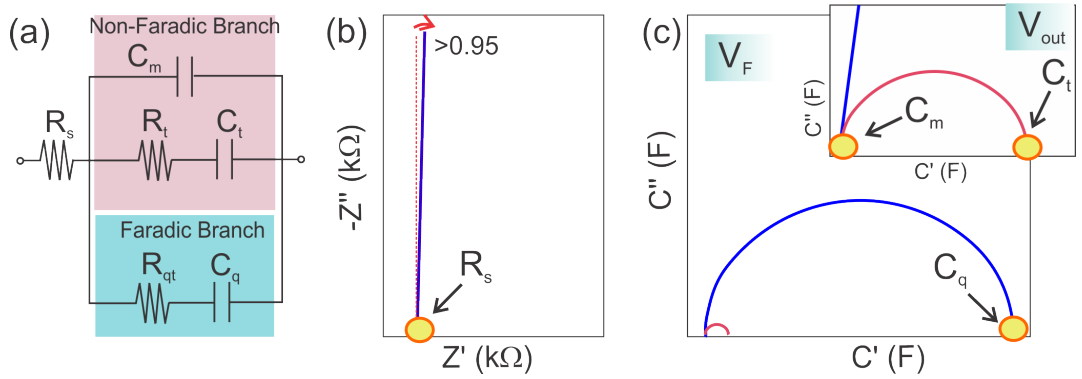

Figure 2.2: (a) Equivalent circuit for a diffusionless interfacial electrochemical process, consisting of two branches: one corresponding to the non-faradaic phenomenon (pink box) and the other to the faradaic phenomenon (blue box). The meanings of the circuit elements are detailed in the Table 2.2, appendix B. R_s represents the series resistance, accounting for contributions from both solution and contact resistances (SÁNCHEZ; SANTOS; BUENO, 2022). Several elements of the circuit can be identified in the complex impedance and capacitive diagrams, as shown in (b) and (c) and are used to the circuital fitting. (b) Representation of an impedimetric Nyquist plot for a diffusionless electrochemical system, where R_s is identified at high frequencies, and the α constant phase element (CPE) exponent close to 1 (> 0.95) means the surface is smooth and uniform at the molecular level (BRETT, 2022). (c) Illustration of complex capacitive diagram of (b) indicating C_q value at low frequencies at V_F (Formal potential). At V_{out} (potential out of faradaic window of the CV), the capacitive Nyquist is shows in the inset where the C_m and C_t, at high and low frequencies, respectively, are identified.
Source: Author (2024)

2.3 Results and discussion

The quantum nature of the ET rate of an electro-active molecular SAM is now experimentally demonstrated following the QRT approach and electrochemical techniques (ALARCÓN; SANTOS; BUENO, 2021). The type of molecular surface evaluated in this study, ferrocene-labeled peptide SAM, represents a specific model of a diffusionless heterogeneous ET process that is also electrochemically reversible. In a diffusionless heterogeneous process, the ET occurs between the electrode and redox species that are confined to surfaces at a fixed distance (see Figure 2.3). In this scenario, the rate-limiting step is the ET itself, not the diffusion of the redox species. The faradaic current[4] resulting from ET during the electrochemical reaction can be expressed as the time derivative of the faradaic charge (q). Given that $q = C_q V$, the faradaic current can be defined as $i = C_q(dV/dt)$, where C_q is associated with the charge of redox states according with the QRT and dV/dt represents the s. Therefore, the linear relation of i with s allows to obtain the C_q from a simple current-potential curve, using $C_q = i/s$. This measurable observable enables the determination of k in accordance with the QRT. The theory, establishes a correlation between k and G_0 through the

[4]The faraday current is the current contribution that is effectively related to the redox reaction, as indicated in the red region of Figure 2.4.

concept of C_q, as discussed in section 1.4. The k of the redox reaction is determined under equilibrium charge dynamics between the oxidation and reduction reactions, reflecting the intrinsic kinetics of the ET process. This equilibrium state is achieved at E_F (BUENO, 2018; BUENO; CRUZEIRO, *et al.*, 2021), where E_F/e is the V_F, and at low s in an electrochemically reversible system. Therefore, the experimental property C_q should also be determined in this equilibrium state.

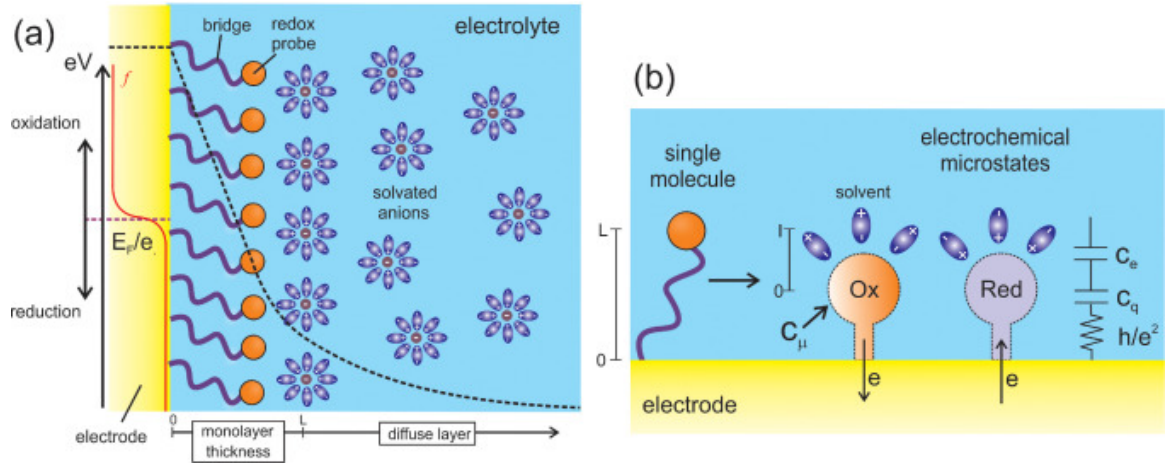

Figure 2.3: (a) Schematic illustration of a typical ferrocene-labeled peptide monolayer anchored on a metallic interface, where E_F/e accounts for the V_F. Inside the monolayer the potential decay associated with non-faradaic process is expected to be linear. The redox probe (ferrocene Fc) is represented as a orange dot connected to the electrode through a 'bridge' (the backbone of the peptide structure). Depending on the applied energy in the electrode, ferrocene can be reduced (Fc) or oxidized (Fc^+). (b) The quantum RC circuit consists of a quantum resistor (h/e^2) and a capacitor (C_q), representing a single redox molecule anchored to an electrode. At the equilibrium state defined by V_F the reduced and oxidized electrochemical microstates are achieved. In this state, the C_q reaches its maximum value and is compensated by the capacitance of the surrounding solvent (C_e).

Source:(ALARCÓN; SANTOS; BUENO, 2021)

Reversible electrochemical behavior is observed for redox molecules anchored to an electrode surface that obey a Langmuir isotherm, provided that the redox molecule is strongly anchored to a homogeneous surface, with diffusion and resorption phenomena being neglecting, and no interaction between the anchored species (HONEYCHURCH; RECHNITZ, 1998). Thus, an ideal reversible system should exhibit a CV profile with symmetric and equivalent anodic (i_{pa}) and cathodic (i_{pc}) peaks ($i_{pa}/i_{pc} = 1$), zero separation between V_{pa} and V_{pc}, i.e, $\Delta V_p = V_{pa} - V_{pc} = 0$, a full width at half maximum of the peak (FWHM) characteristic for a one-electron process of 90.6 mV, i_{pa} and i_{pc} varying proportionally with the s. Using these criteria, the reversibility of the redox process of the ferrocene-labeled peptide SAM attached to the gold electrode was evaluated through CV (see Figure 2.4).

The effective formation of the SAM was initially confirmed by the linear correlation between the i and s at scan rates below 1 V s^{-1} (Figure 2.5). Table 2.3 summarizes the criteria for electrochemical reversibility based on CV profiles of the redox-tagged peptide SAM obtained at various scan rates. The CV profiles showed symmetric Gaussian-shaped peaks for the the oxidation ($Fc \rightarrow Fc^{+} + e^{-}$) and reduction ($Fc^{+} + e^{-} \rightarrow Fc$) processes with i_{pa}/i_{pc} close to 1, indicating good electrochemical reversibility (Figure 2.4). Notably, the FWHM of the peaks was less than the theoretical value of 90.6 mV for an ideal reversible behavior. However, this deviation from the theoretical value can be attributed to attractive interactions between the electroactive species on the surface. Additionally, the ΔV_p was minimal but non-zero, and it increased with higher s. These deviations are expected in practical experimental conditions due to inherent imperfections in the system (LAVIRON, 1974).

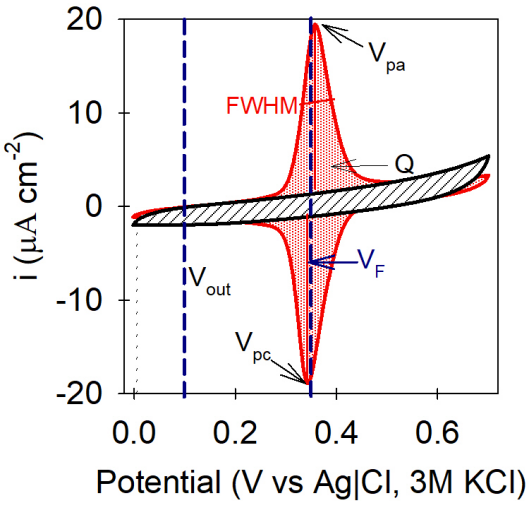

Figure 2.4: Cyclic voltammogram of ferrocene-labeled peptide monolayer anchored to a gold electrode. key parameters for analyzing the current-voltage electrochemical curve are presented. The anodic and cathodic potential peaks are shown as V_{pa} and V_{pc}, respectively. The red shaded region represents the amount of faradaic charge (Q) attributed to the redox process, which is dominant. The V_F and the V_{out}, where the non-faradaic capacitive contribution is determined, are presented. area shaded with vertical lines corresponds to the non-faradaic charge contribution

Source: Adapated from (ALARCÓN; SANTOS; BUENO, 2021)

Considering the linear relationship between i and s in a diffusionless electrochemical transfer process C_q can be directly determined from a CV curve obtained at a low s, since $C_q = i/s$. At these low s, the reaction kinetics are relatively slow, allowing the system to maintain a quasi-equilibrium state. Consequently, the i is primarily controlled by the rate at which the potential is scanned, resulting in $i \propto s$. Thus, Figure 2.5 demonstrates that normalizing i by s from different CVs generates capacitive-potential curves that collapse into a single master curve. As presented in this work, at the equilibrium charge dynamic condition, i.e., at V_F, the experimental observable

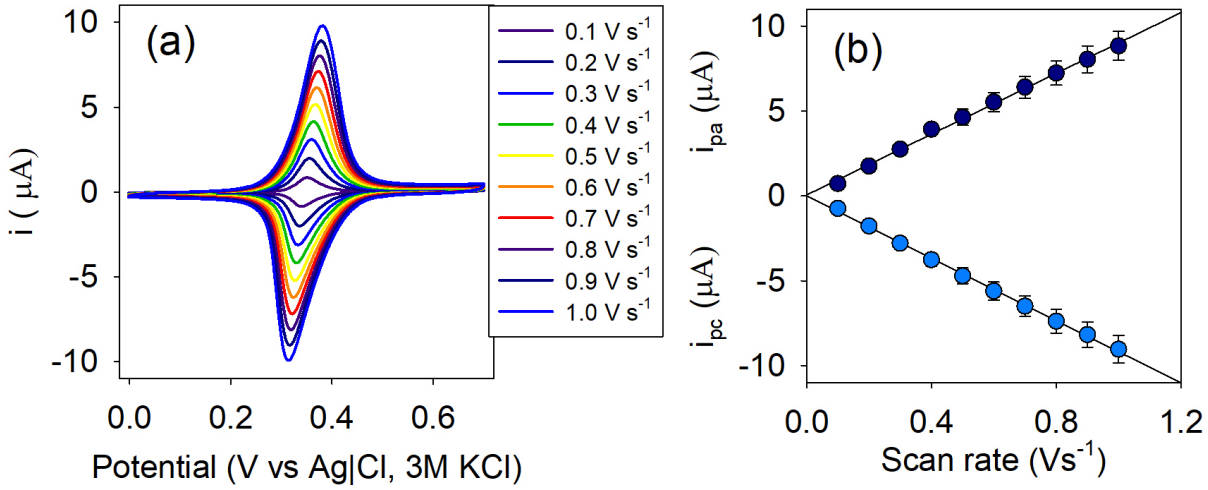

Figure 2.5: (a) Cyclic voltammograms at different s lower than 1 V s^{-1}. (b) Linear regression of i versus s obtained from the cyclic voltammograms showed in (a). The faradaic currents i_{pa} and i_{pc}, were acquired at the highest anodic and cathodic current peaks, respectively.
Source: Adapted from (ALARCÓN; SANTOS; BUENO, 2021)

Table 2.3: Criteria parameters of reversibility obtained by cyclic voltammetry profiles of ferrocene-labeled peptide SAM

s		ΔV_p	V_F	FWHM
V s^{-1}	i_{pa}/i_{pc}	mV		
0.1	0.97 ± 0.02	11 ± 1	346 ± 2	63 ± 1
0.3	0.99 ± 0.01	27 ± 2	343 ± 2	70 ± 6
0.5	0.98 ± 0.01	39 ± 2	344 ± 2	77 ± 6
0.7	0.98 ± 0.01	50 ± 2	345 ± 3	82 ± 5
1.0	0.98 ± 0.01	69 ± 6	343 ± 5	89 ± 5

C_q can be determined for both the anodic and cathodic processes. Furthermore, as will be demonstrated, this approach allows for the determination of k based on the QRT analysis.

Given the general equation of ν in the QRT (Eq. 1.5, introduced in section 1.4, Chapter 1), it can be applied to determine k for a non-adiabatic electrodynamic process, such as that occurring in the redox-peptide SAM system, under certain assumptions. First, the tunneling transmission coefficient κN, modulated by the quantum channels and defined in $G = G_0 \kappa N$, is assumed to adjust for optimal electron transmission efficiency at the interface (SÁNCHEZ; SANTOS; BUENO, 2022), i.e., $\kappa N \sim 1$. Second, the charge storage resulting from the redox reaction involving one electron is assumed to be compensated by the charge screening of the electrolyte. It follows that C_e equals C_q at V_F. This phenomenon is treated as an electrostatic degeneracy

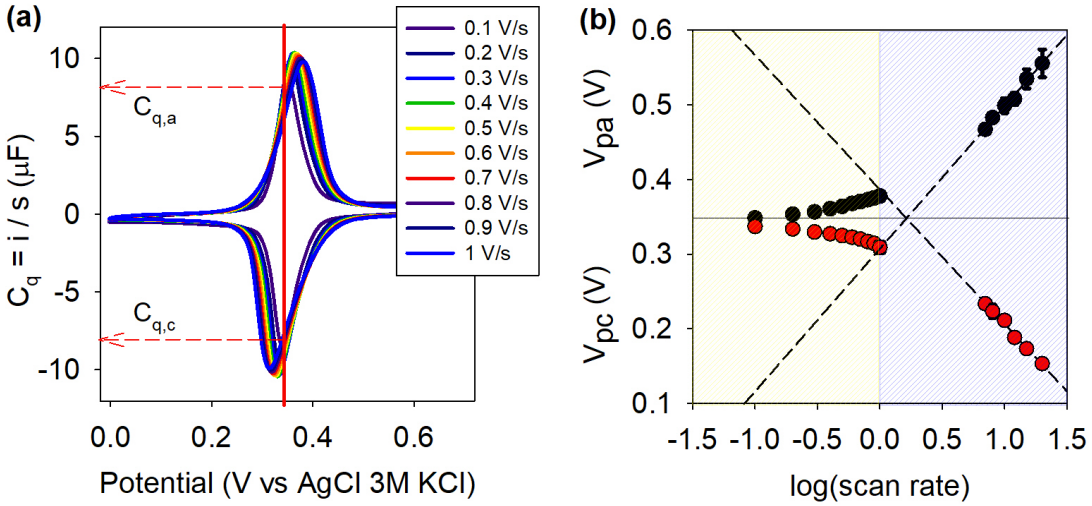

Figure 2.6: (a) The capacitance-potential curve is obtained by normalizing the current-potential curves by the s, at scan rates lower than 1 V s^{-1}, following the relation $C = i/s$. These normalized curves collapse into a single master curve. The capacitance values C_{qa} and C_{qc} determined at the formal potential V_F, are indicated in the figure. These values are then used to calculate k as predicted by the QRT. (b) The V_{pa} and V_{pc}, obtained from the cyclic voltammograms carried out at different scan rates, were plotted as a function of the logarithm of the s. At the conditions where $\Delta V_p \geq 200$ mV is met, a linear regression was obtained. The linear regression equations of the anodic and cathodic processes were V_{pa}= 0.19 $log(s)$ - 0.31 and V_{pc}= -0.18 $log(s)$ - 0.39, respectively. For the Ferrocene-labeled peptide SAM evaluated in this study, this condition corresponds to scan rates higher than 7 V s^{-1}.

Source: Adapted from (ALARCÓN; SANTOS; BUENO, 2021)

state (g_e). Therefore, the simplified equation for k depends solely on the experimental variable C_q, and includes G_0 being equal to $g_s e^2/h$, along with the degeneracy rules for both the spin ($g_s = 2$) and $g_e = 2$, it leads to

$$k = 4\frac{e^2}{hC_q} \tag{2.6}$$

where quantum rate (QR) method proposed here for calculating k, relies on: i) determining the experimental observable C_q from a current-potential curve, ii) correctly identifying the "degeneracy" of a diffusionless electrochemical reaction when the electrode potential is set at the Fermi level, and iii) interpreting it within its quantum mechanical context associated with Eq. 2.6. Table 2.4 presents the kinetic parameters obtained from the quantum rate method in the equilibrium charge dynamic states achieved at the V_F. Since the cyclic voltammograms, i/s versus V, collapse into a single master curve (see Figure 2.6), we selected the s of 0.3 V s^{-1} as the representative curve to determine k. The k obtained from the QR method was compared with the k obtained from the Laviron's method.

Laviron's equation builds upon the classical kinetic theory of Butler-Volmer, providing a practical approach to extract kinetic parameters from CV data acquired far

from the equilibrium charge dynamics regime (LAVIRON, 1979). This is applicable under conditions of varying degrees of reversibility, where experimental conditions result in ΔV_p greater than 200 mV. Under these conditions, α and k can be easily determined using the Eq. 2.1 and Eq. 2.2. By plotting V_{pa} and V_{pc} *versus* the logarithm of s within the compliant experimental range achieved at scan rates higher than 7 V s^{-1}, two straight lines were obtained. The slope of $-2.3RT/\alpha nF$ and $2.3RT/(1-\alpha)nF$ for the cathodic and anodic peaks respectively, allows for the determination of α. The s_a and s_c of Laviron's equations, which are associated with the intrinsic kinetic constants of the anodic and cathodic processes, were determined by extrapolating the straight lines at the V_F. Table 2.4 presents the kinetic parameters obtained from Laviron's method (α and k) and the QR method (C_q and k). By analyzing the confidence intervals of k calculated by both methods, we can observe that they overlap. This indicates that both methods yield comparable results for determining k for the diffusionless heterogeneous ET process of the redox-tagged peptide anchored on the electrode.

Table 2.4: kinetics parameters obtained using the QR method at a V_F of approximately 0.34 V with a s of 0.3 V s^{-1} and compared with those obtained from Laviron's method. The standard deviation corresponds to measurements performed in three independent experiments on three different ferrocene-labeled peptide modified electrodes.

	QR method	Laviron's method
Anodic	$C_{qa} = 8.8 \pm 0.5\ \mu$F	$(1-\alpha_a) = 0.31 \pm 0.02$
	$k_a = 17.6 \pm 0.8\ s^{-1}$	$s_a = 1.5 \pm 0.2$
		$k_a = 19 \pm 2\ s^{-1}$
Cathodic	$C_{qc} = 9.1 \pm 0.5\ \mu$F	$\alpha_c = 0.33 \pm 0.2$
	$k_c = 17.1 \pm 0.9\ s^{-1}$	$s_c = 1.7 \pm 0.2$
		$k_c = 22 \pm 3\ s^{-1}$

2.3.1 Theoretical equivalence between Laviron's and the QR Methods

In this section, it will be discussed the theoretical equivalence between Laviron's traditional method of calculating k and the QR method associated with the Eq. 2.6. First, it will be assumed a symmetric situation for the ET in such a way that α is 1/2, which is appropriate for the equilibrium charge dynamics regime (BUENO; CRUZEIRO, *et al.*, 2021). This assumption implies that the forward and reverse rate constants are equal, i.e, $k_\alpha = k_a = k_c$, at the equilibrium charge dynamics state. Additionally, under these symmetric conditions, also $s_a = s_c = s$. Second, it is important to note the

equivalence $F/RT = e/k_BT$. This equivalence highlights the link between macroscopic thermodynamic properties and microscopic statistical properties, effectively scaling energy with temperature and bridging large-scale averages with individual particle behavior. In this context, F and R are related to e and k_B, respectively, through Avogadro's number N_A, as $F = eN_A$ and $R = k_BN_A$. This connection allows us to relate macroscopic quantities to microscopic properties. Consequently, we can rewrite Laviron's Eq. 2.1 and Eq. 2.2 into a single Eq, due to $k_\alpha = k_a = k_c$, and in terms of k_B and e, and $\alpha = 1/2$, leading to

$$k_\alpha = \frac{e}{2k_BT}s. \tag{2.7}$$

As discussed in chapter 1 (section 1.4), in QRT the electrodynamics is modelled as a quantum RC circuit with a characteristic τ. In the ET dynamics framework, τ is associated to k through the relation $k = 1/\tau$. Here, τ is defined as $\tau = R_qC_\mu$, and $R_q = 1/G_0$ for ET of one electron within a single quantum channel. Now, taking into account the thermal broadening effects (BUENO, 2020), the C_μ is given by $C_\mu = (2e^2/k_BT)f(1-f)$. Since $f = 1/2$ at the V_F, and considering $C_q = C_e$ involves a $g_e = 2$, C_μ is redefined as $C_q = e^2/4k_BT$. Additionally, considering that this capacitance is associated with a term of energy, as $E = e^2/C_q = 4k_BT$, and potential $V = e/C_q = 4k_BT/e$. By substituting $4k_BT/e = e/C_q$ in Eq. 2.7, we can establish $k_\alpha = C_q/e$. Finally, allowing for $s = V/\tau$ and $R_q = h/g_se^2$, where $g_s = 2$ we arrived to $k_\alpha = k$, demonstrating that 2.7 is equivalent to

$$k_\alpha = \frac{C_q}{e}\left(\frac{V}{R_qC_q}\right) = 4\frac{e^2}{hC_q}. \tag{2.8}$$

In summary, Laviron's equation for calculating k can be effectively substituted with Eq. 2.8, which, while incorporating quantum mechanical considerations that offer valuable insights into the ET behaviour, maintains the same conceptual integrity. As will be demonstrated above, Eq. 2.8 simplifies the calculation of k by providing a straightforward approach using a single electrochemical current-potential scan.

2.3.2 Confirmation of the method to determinate k using impedance-derived capacitance spectroscopy

For electrochemical heterogeneous diffusionless processes, impedance-derived electrochemical spectroscopy (ECS) is a powerful tool to study the electrodynamics of redox processes. Figure 2.7 shows the capacitive Nyquist plots of the non-faradaic and faradaic responses. The capacitance associated with the non-faradaic process, known as C_t, corresponds to the diameter of the semicircle (BUENO; DAVIS, 2020) of black dots, with an estimated value of $C_t \sim 6$ μF cm^{-2}. This value is just 3% of the

capacitive response of the faradaic process, $C_q \sim 230\ \mu F\ cm^{-2}$, which is estimated from the diameter of the semicircle of square blue dots obtained at V_F. These results indicate the dominance of the faradaic relaxation over the non-faradaic relaxation at V_F. This was further demonstrated by the spectral subtraction of the capacitive Nyquist plots for the faradaic and non-faradaic responses, resulting in a semicircle of square green dots. It is important to highlight that $C_q \sim 230\ \mu F\ cm^{-2}$ is equivalent to 10.4 μF for an electroactive area of 0.044 cm^{-2}. When the QR method is applied, as discussed previously, k accounts for $2G_0/C_q$ and using the C_q determined by the ECS, k is 15 s^{-1}. In Table 2.5 presents the kinetic parameters obtained from this technique, namely C_q and k. Considering the standard deviation of three ferrocene-labeled peptide modified electrodes, the value of k is consistent with those obtained from the current-potential curve. Therefore, the comparative analysis of CV and ECS methods with that of Laviron demonstrates that the quantum rate interpretation of k is consistent.

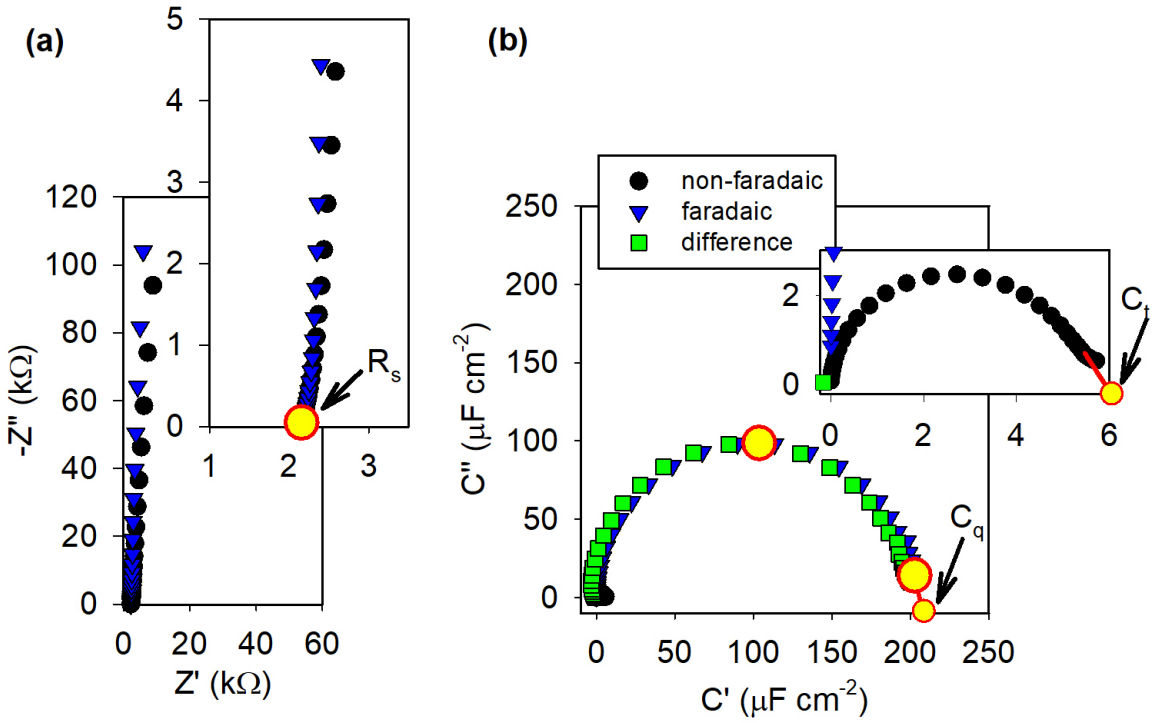

Figure 2.7: (a) Complex impedance diagram of the ferrocene-labeled peptide SAM acquired at V_{out} and V_F, representing the non-faradaic and faradaic responses, respectively. R_s accounts for the series combination of solution and contact resistance. (b) Complex capacitance diagram corresponding to (a), where the green dotted curve represents the spectral subtraction of the non-faradaic response from the faradaic response, showing that the faradaic response predominates over the non-faradaic.

Source: Adapted from (ALARCÓN; SANTOS; BUENO, 2021)

Determining k from experimental techniques such as CV and ECS provides a

Table 2.5: Kinetic parameters obtained using the QR method and ECS approach at V_F, compared with those obtained from CV conducted at a s of 0.3 V s^{-1}.

By ECS	By CV
C_q = 10.2 ± 0.7 μF	C_{qa} = 8.8 ± 0.5 μF C_{qc} = 9.1 ± 0.5 μF
k = 15 ± 1 $^{-1}$	k_a = 17.6 ± 0.8 $^{-1}$ k_c = 17.1 ± 0.9 s^{-1}

powerful analytical approach. However, the key insight here lies in the reinterpretation of k through QRT, which frames ET as a quantized process occurring through discrete electronic states in a redox-tagged peptide SAM. A fundamental assumption in deriving Eq. 2.6 was that κN adjusts to maximize electron transfer efficiency, reflected in the G, reaching the quantized value of $G_0 = 77.5$ μS (or equivalently $R_q = 1/G_0 = 12.9$ KΩ). This was experimentally validated by determining the R_q, which was found to be ∼12.6 kΩ, through circuit fitting of capacitive Nyquist spectra using an RC equivalent model, as described in section 2.2.5. The R_q is an intrinsic component of ET kinetics, representing a global resistance composed of the series resistance (R_s which includes contact and solution resistance) and R_{qt}, such as $R_q = 2\pi(R_s + R_{qt})$. The values of R_{qt}, R_s, R_q, and G are summarized in Table 2.6.

Table 2.6: Elements related to G involved in the ET process extracted form the circuit analysis.

R_{qt}	R_s	R_q	G
	Ω		μS
50 ± 9	2013 ± 92	12600 ± 70	77.3 ± 0.4

The existence of $\kappa = exp(-\beta L)$, in $G = G_0 \kappa N$, confirms the non-adiabatic nature of the ET process, occurring through a tunneling regime as predicted by Marcus theory (MARCUS, 1964), where charge transport is modulated by quantum channels of length L. The parameter β was estimated from the quantum rate model as ~ 1.6 Å^{-1}, aligning well with the literature values (FINKLEA; HANSHEW, 1992). This estimation was made using $L = 1.8$ nm a value reported for a similar peptide structure lacking a terminal Cys moiety (determined by ellipsometry) (PICCOLI *et al.*, 2018), and N from the C_q acquired at V_F where half of the quantum states are occupied and half remain unoccupied ($f = 1/2$, in Eq. 1.6), yielding $N = 4k_BTC_q/e^2 \sim 6.4$ x10^{12} states. These results further validates the quantum mechanical interpretation of ET kinetics in a non-adiabatic process, reinforcing the role of the quantized G in

describing ET within molecular-scale electrochemical systems (SÁNCHEZ; SANTOS; BUENO, 2022).

2.4 Conclusion

The quantum nature of the ET rate in diffusionless electrochemical heterogeneous systems, characterized by electroactive species confined on an electrode surface, was demonstrated by analyzing the kinetic constant using the QRT approach derived from the first principles of quantum mechanics. The quantum rate kinetic equation relates the G to the thermally broadened C_q, which, due to its quantum nature, considers equilibrium charge dynamics. At this equilibrium state, the experimentally observable C_q can be obtained from an ordinary CV curve conducted at low scan rates where electrochemical reversibility is evident. By extracting this quantum property, related to the charge of electronic states during a redox reaction, and assuming specific degeneracy rules (one associated with the electron's spin and the other with charge compensation resulting from charging electronic states), we can calculate k from the QRT interpretation. This is achieved by experimentally obtaining the C_q from the CV curve by normalizing the current response by the s, taking into account $C_q = i/s$ for the condition $i \propto s$. Applying this experimental method based on the QRT approach, the k was calculated and compared with the value obtained from the Laviron's method. The comparison demonstrated the equivalence between these two methods in determining this kinetic constant.

Dissimilarity between the quantum rate and the traditional Laviron's methods for obtaining k lies in the fact that the former is applying to the equilibrium regime while the latter is applying to the far-from-equilibrium regime. Additionally, the QRT is grounded in quantum mechanics, whereas Laviron's method is based on classical kinetics theory. Nevertheless, it is crucial to recognize the need to consider ET in confined systems, such as redox-tagged molecular SAM, as a quantum event, where the electron behaves as a wave-particle in accordance with quantum mechanics. The confined environment enhances quantum effects, which should be included in the ET kinetic equation. Therefore, the QRT allows us not only to observe the ET process in these types of systems as a quantum event but also to experimentally calculate it through the observable property C_q obtained from an ordinary CV curve.

References

ALARCÓN, E. V. G.; SANTOS, A.; BUENO, P. R. Perspective on quantum electrochemistry. A simple method for measuring the electron transfer rate constant. **Electrochimica Acta**, Elsevier, v. 398, p. 139219, 2021.

ARIKUMA, Y. *et al.* Electron hopping over 100 Åalong an α helix. **Angewandte Chemie International Edition**, Wiley Online Library, v. 49, n. 10, p. 1800–1804, 2010.

BOCKRIS, J. O.; KHAN, S. U. **Quantum electrochemistry**. Springer Science & Business Media, 2012.

BOITEL-AULLEN, G. *et al.* Electron transfer inside a decaferrocenylated rotaxane analyzed by fast scan cyclic voltammetry and impedance spectroscopy. **ChemElectroChem**, Wiley Online Library, v. 8, n. 18, p. 3506–3511, 2021.

BRANDÃO, S. T. *et al.* Designing Quantum Capacitive Peptide Interfaces for Electroanalytical Applications. **Analytical Chemistry**, ACS Publications, v. 95, n. 36, p. 13470–13477, 2023.

BRETT, C. M. Electrochemical impedance spectroscopy in the characterisation and application of modified electrodes for electrochemical sensors and biosensors. **Molecules**, MDPI, v. 27, n. 5, p. 1497, 2022.

BUENO, P. R. **The Nanoscale Electrochemistry of Molecular Contacts**. Springer, 2018. (SpringerBriefs in Applied Sciences and Technology). ISBN 978-3-319-90486-3.

BUENO, P. R.; BENITES, T. A.; DAVIS, J. J. The mesoscopic electrochemistry of molecular junctions. **Scientific Reports**, Nature Publishing Group UK London, v. 6, n. 1, p. 18400, 2016.

BUENO, P. R.; DAVIS, J. J. Charge transport and energy storage at the molecular scale: from nanoelectronics to electrochemical sensing. **Chemical Society Reviews**, Royal Society of Chemistry, v. 49, n. 21, p. 7505–7515, 2020.

BUENO, P. R.; MIZZON, G.; DAVIS, J. J. Capacitance spectroscopy: a versatile approach to resolving the redox density of states and kinetics in redox-active self-assembled monolayers. **The Journal of Physical Chemistry B**, ACS Publications, v. 116, n. 30, p. 8822–8829, 2012.

BUENO, P. R. Electron transfer and conductance quantum. **Physical Chemistry Chemical Physics**, Royal Society of Chemistry, v. 22, n. 45, p. 26109–26112, 2020.

BUENO, P. R. Quantum rate theory and electron-transfer dynamics: A theoretical and experimental approach for quantum electrochemistry. **Electrochimica Acta**, Elsevier, v. 466, p. 142950, 2023.

BUENO, P. R.; CRUZEIRO, V. W. D., *et al.* The density-of-States and equilibrium charge dynamics of redox-active switches. **Electrochimica Acta**, Elsevier, v. 387, p. 138410, 2021.

CHIDSEY, C. E. D. Free-energy and temperature-dependence of electron-transfer at the metal-electrolyte interface. **Science**, v. 251, n. 4996, p. 919–922, 1991. ISSN 0036-8075.

CREAGER, S. E.; WOOSTER, T. T. A new way of using ac voltammetry to study redox kinetics in electroactive monolayers. **Analytical Chemistry**, ACS Publications, v. 70, n. 20, p. 4257–4263, 1998.

ECKERMANN, A. L. *et al.* Electrochemistry of redox-active self-assembled monolayers. **Coordination Chemistry Reviews**, Elsevier, v. 254, n. 15-16, p. 1769–1802, 2010.

FINKLEA, H. O.; HANSHEW, D. D. Electron-transfer kinetics in organized thiol monolayers with attached pentaammine (pyridine) ruthenium redox centers. **Journal of the American Chemical Society**, ACS Publications, v. 114, n. 9, p. 3173–3181, 1992.

FINKLEA, H. O.; RAVENSCROFT, M. S.; SNIDER, D. A. Electrolyte and temperature effects on long range electron transfer across self-assembled monolayers. **Langmuir**, ACS Publications, v. 9, n. 1, p. 223–227, 1993.

FLETCHER, S. The theory of electron transfer. **Journal of Solid State Electrochemistry**, Springer, v. 14, n. 5, p. 705–739, 2010.

GARROTE, B. L.; SANTOS, A.; BUENO, P. R. Label-free capacitive assaying of biomarkers for molecular diagnostics. **Nature Protocols**, Nature Publishing Group UK London, v. 15, n. 12, p. 3879–3893, 2020.

GARROTE, B. L.; SÁNCHEZ, Y. P., *et al.* Electron transmittance by means of quantum capacitive states as a signal amplification mechanism for biosensing applications. **Sensors and Actuators B: Chemical**, Elsevier, v. 399, p. 134786, 2024.

GATTO, E. *et al.* Mimicking nature: a novel peptide-based bio-inspired approach for solar energy conversion. **Chemphyschem: a European Journal of Chemical Physics and Physical Chemistry**, v. 15, n. 1, p. 64–68, 2013.

GERISCHER, H. The impact of semiconductors on the concepts of electrochemistry. **Electrochimica Acta**, v. 35, n. 11-12, p. 1677–1699, 1990. ISSN 0013-4686.

GOES, M. S. *et al.* A dielectric model of self-assembled monolayer interfaces by capacitive spectroscopy. **Langmuir**, ACS Publications, v. 28, n. 25, p. 9689–9699, 2012.

HONEYCHURCH, M. J.; RECHNITZ, G. A. Voltammetry of adsorbed molecules. Part 1: Reversible redox systems. **Electroanalysis: An International Journal Devoted to Fundamental and Practical Aspects of Electroanalysis**, Wiley Online Library, v. 10, n. 5, p. 285–293, 1998.

HORSLEY, J. R. *et al.* Unraveling the interplay of backbone rigidity and electron rich side-chains on electron transfer in peptides: the realization of tunable molecular wires. **Journal of the American Chemical Society**, ACS Publications, v. 136, n. 35, p. 12479–12488, 2014.

LAVIRON, E. Surface linear potential sweep voltammetry: Equation of the peaks for a reversible reaction when interactions between the adsorbed molecules are taken into account. **Journal of Electroanalytical Chemistry and Interfacial Electrochemistry**, Elsevier, v. 52, n. 3, p. 395–402, 1974.

LAVIRON, E. General expression of the linear potential sweep voltammogram in the case of diffusionless electrochemical systems. **Journal of Electroanalytical Chemistry and Interfacial Electrochemistry**, Elsevier, v. 101, n. 1, p. 19–28, 1979.

LEHR, J. *et al.* Mapping the ionic fingerprints of molecular monolayers. **Physical Chemistry Chemical Physics**, Royal Society of Chemistry, v. 19, n. 23, p. 15098–15109, 2017.

MALECKA, K. *et al.* Redox-active monolayers self-assembled on gold electrodes—effect of their structures on electrochemical parameters and DNA sensing ability. **Molecules**, MDPI, v. 25, n. 3, p. 607, 2020.

MANDAL, H. S.; KRAATZ, H.-B. Electron transfer mechanism in helical peptides. **The Journal of Physical Chemistry letters**, ACS Publications, v. 3, n. 6, p. 709–713, 2012.

MARCUS, R. A. On the theory of oxidation-reduction reactions involving electron transfer. I. **Journal of Chemical Physics**, American Institute of Physics, v. 24, n. 5, p. 966–978, 1956.

MARCUS, R. A. Chemical and electrochemical electron-transfer theory. **Annual Review of Physical Chemistry**, v. 15, n. 1, p. 155–196, 1964.

MATSUSHITA, D.; UJI, H.; KIMURA, S. Effect of oscillation dynamics on long-range electron transfer in a helical peptide monolayer. **Physical Chemistry Chemical Physics**, Royal Society of Chemistry, v. 20, n. 22, p. 15216–15222, 2018.

PICCOLI, J. *et al.* Redox Capacitive Assaying of C-Reactive Protein at a Peptide Supported Aptamer Interface. **Analytical Chemistry**, v. 90, n. 5, p. 3005–3008, 2018. ISSN 0003-2700.

QI, L.; TIAN, H.; YU, H.-Z. Binary thiolate DNA/ferrocenyl self-assembled monolayers on gold: a versatile platform for probing biosensing interfaces. **Analytical Chemistry**, ACS Publications, v. 90, n. 15, p. 9174–9181, 2018.

SÁNCHEZ, Y. P.; SANTOS, A.; BUENO, P. R. Quantum Mechanical Meaning of the Charge Transfer Resistance. **Journal of Physical Chemistry C**, v. 126, p. 3151–3162, 6 2022.

SHAH, A. *et al.* Electron transfer in peptides. **Chemical Society Reviews**, Royal Society of Chemistry, v. 44, n. 4, p. 1015–1027, 2015.

TAKEDA, K.; MORITA, T.; KIMURA, S. Effects of monolayer structures on long-range electron transfer in helical peptide monolayer. **The Journal of Physical Chemistry B**, ACS Publications, v. 112, n. 40, p. 12840–12850, 2008.

TRASATTI, S.; PETRII, O. Real surface area measurements in electrochemistry. **Journal of Electroanalytical Chemistry**, Elsevier, v. 327, n. 1-2, p. 353–376, 1992.

VANOVA, V. *et al.* Peptide-based electrochemical biosensors utilized for protein detection. **Biosensors and Bioelectronics**, Elsevier, v. 180, p. 113087, 2021.

WATANABE, J.; MORITA, T.; KIMURA, S. Effects of dipole moment, linkers, and chromophores at side chains on long-range electron transfer through helical peptides. **The Journal of Physical Chemistry B**, ACS Publications, v. 109, n. 30, p. 14416–14425, 2005.

YU, J.; HORSLEY, J. R.; ABELL, A. D. Turning electron transfer 'on-off'in peptides through side-bridge gating. **Electrochimica Acta**, Elsevier, v. 209, p. 65–74, 2016.

Chapter 3

Beyond the dielectric continuum model: electrolyte influence on ET process from a quantum electrodynamics perspective

Traditionally, the role of solvents in ET reactions has been understood through Marcus theory's continuum model, which emphasizes the dielectric properties of the medium and the stabilizing effect of solvent dipoles on D and A species. However, in electrochemical systems, electrolyte ions contribute far beyond these conventional solvent effects, by modulating local dielectric properties and screening quantum-state charges, they introduce complexities that cannot be fully captured by continuum models alone. As demonstrated in this chapter, and as we have previously discussed in our work on quantum-rate electrodynamics in nanoscale systems (PINZÓN *et al.*, 2022), the ionic characteristics of the electrolyte play a pivotal role in bridging classical and quantum energy states, a fundamental aspect within the framework of QRT. The concept of reorganization energy, introduced by Marcus ET theory, a special case of QRT, is reinterpreted in capacitive terms with quantum mechanical significance. Through experimental investigation of ET behavior across varying water/acetonitrile ratios while maintaining a fixed ionic pair, we elucidate the intricate interplay between solvent polarity, ionic screening, and quantum-state coupling, revealing the explicit role of the electrochemical environment. This analysis advances our understanding of electrolyte-modulated diffusionless heterogeneous ET processes beyond the traditional dielectric continuum analysis. Thus, the specific objective of this chapter is as follows:

- ☑ To demonstrate the fundamental role of electrolyte, consisting of ions and solvent, in modulating the electrodynamics of the ET of redox-tagged peptide SAMs by bridging classical and quantum energy states within the framework of QRT.

The results presented in this chapter are part of a manuscript currently in preparation for submission entitled "*Beyond Dielectric Continuum Model: The Role of Electrolyte on the Rate of Electron Transfer Reactions from a Quantum Electrodynamics Perspective*".

3.1 Introduction

The solvent plays a critical role in ET processes between a D and A species, as highlighted by the groundbreaking contributions of Rudolph Marcus, for which he received the Nobel Prize in 1992. Marcus' theory of ET (MARCUS, 1956) revolutionized the understanding of reaction kinetics by incorporating the active participation of the solvent into the framework of the energetic of the process, which resolves the low-rate dynamics of ET reactions. Building on the Arrhenius equation ($k = Aexp^{-E^{\ddagger}/k_BT}$) and TST, Marcus identified that the $E^{\ddagger}$, in the k equation (Eq.1.1) (HUSH, 1961), is not only determined by E^o, being equal to potential energy (-eV) differences between D and A states, but also by λ associated with solvent dynamics (see Figure 3.1). In this context, the solvent acts as both a stabilizing and dynamic medium, modulating the rate at which ET occurs by facilitating or hindering the reorganization process.

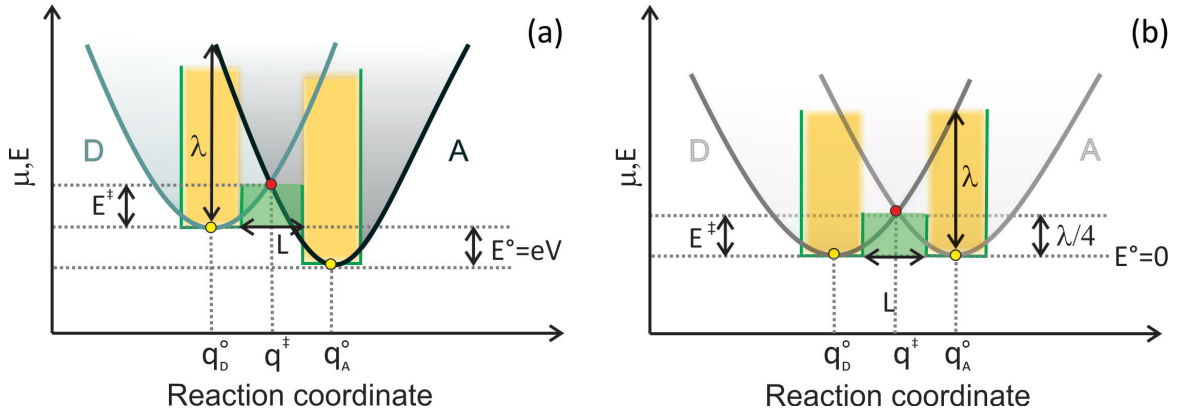

Figure 3.1: One-dimensional parabolic energy potential well for ET following a TST. These curves correspond to the plot of potential energy E or a chemical potential μ against the reaction coordinate q. (a) A non-adiabatic condition for oxidant (D) and reduced (A) states with different chemical potentials quantified by E or μ of the minimum of the curves as E^0 = -eV. This minimum corresponds to a reaction coordinate of D (q^0_D) and A states (q^0_A) for which, in a hypothetical situation in which $E^0 = 0$, E and μ are equivalent, indicating a transition from D to A that is referred to occur at the equilibrium condition, as shown in (b) whereas (a) corresponds to the non-equilibrium condition. In other words, the equilibrium condition of (b) corresponds to the situation in which both parabolas have a common minimum state of energy, for which, $E^{\ddagger} = \lambda/4$, according to Marcus ET theory.

Source: Author (2024)

In ET processes involving metallocene self-exchange reactions, where a metal center is sandwiched between organic ligands, such as those occurring in the ET of redox-tagged molecular SAMs, λ_{in} is typically considered negligible compared to the

λ_{out} contribution (WEAVER; MCMANIS III, 1990; FAWCETT; OPALLO, 1994). This energy, which arises from solvent reorganization, is a critical factor in Marcus ET theory and is described by the equation $\lambda_{out} = (e)^2(1/4\pi\varepsilon_0)(1/2r_D + 1/2r_A - 1/L)(1/\varepsilon_\infty + 1/\varepsilon)$ (MARCUS, 1956; FLETCHER, 2010), where ε_0 represent the vacuum permittivity, ε_∞ and ε, the optical and static dielectric constants of the solvent, respectively. The geometric factor in this equation can be referred to as δ (including ε_0), the radii r_D and r_A of the D and A species, and the distance between them, L. Since the ε_∞ governs fast electronic response of the medium, which responds too quickly to significantly affect solvent reorganization energy, λ, a purely classical concept within Marcus ET theory, can be simplified and stated as being inversely proportional to ε of the environment, i.e., $\lambda \sim (e^2/\varepsilon\delta)$.

Marcus' adoption of the continuum model for the solvent underscores the importance of solvent dipoles in stabilizing D and A through its dielectric properties, captured by ε. However, this implicit treatment of the solvent, which assumes a continuum dielectric response, limits the analysis of its explicit role in ET kinetics. In electrochemical systems, for instance, the presence of electrolyte supporting salts can significantly influence ET kinetics in diffusionless heterogeneous systems such ferrocene-labeled molecular SAM (NORMAN; BADIA, 2011). The ions in the electrolyte can screen charges and modify the local environment, altering the effective dielectric properties and impacting the ET rate (WONG *et al.*, 2020; ORLOWSKI; CHOWDHURY; KRAATZ, 2007). Thus, while Marcus theory emphasizes the importance of the solvent in ET by introducing λ as a key energetic parameter, which depends primarily on ε, it overlooks the impact of ion-pairing, as well as specific solvent-solute interactions, which can be presented in more complex systems such as those found in liquid mixtures (ZHUANG; WANG, 2016).

In this context, water-acetonitrile mixture has been successful not only in obtaining ferrocene-labeled peptide SAM, since it is using as the incubation medium, but also in advancing the electrochemical evaluation of ET processes from the perspective of QRT (SÁNCHEZ; SANTOS; BUENO, 2022; ALARCÓN; SANTOS; BUENO, 2021; BRANDÃO *et al.*, 2023). Specifically, the 1:4 (v/v) ratio of water-acetonitrile has enabled to evaluate the quantum characteristics associated with the ET process and assess the potential of these systems as biosensor platforms (GARROTE; SANTOS; BUENO, 2020; GARROTE; SÁNCHEZ, *et al.*, 2024; BRANDÃO *et al.*, 2023). However, the role of mixed solvents in influencing the kinetics of ET in redox-active peptides in this binary mixed solvent system has not yet been fully explored. Therefore, in this chapter, we aim to investigate the effect of varying water-acetonitrile mixture on k by altering the v/v proportion. The significance of this study lies in its application of QRT, within which Marcus ET theory emerges as a particular case in the semi-classical limit (more details in section 1.4 of Chatper 1). By adopting a quantum

perspective, QRT provides deeper insight into how the electrolyte – comprising both the mixed solvent and electrolyte salt – affects the ET process from a quantum perspective. This is particularly relevant for cases where an "explicit" analysis of solvent effects on ET rate dynamics is required. By examining key electrodynamic quantum properties such as C_q, G, and k, this study offers a more comprehensive understanding of solvent contributions to ET processes.

3.2 Materials and methods

As the experimental methodology used in this study follows the key steps outlined in Section 2.2, including the synthesis and formation of the redox-peptide SAM and subsequent electrochemical measurements, only the additional details specific to this chapter will be presented.

3.2.1 Chemical reagents

The same chemical reagents listed in Table 2.1 were used in this chapter. Milli-Q water (Simplicity® water purification system, Millipore, 18.2 MΩ cm at 25°C) was used to prepare all aqueous solutions. For the study presented in this chapter, three electrolytes were prepared, each containing 20 mM $TBAClO_4$ as the supporting electrolyte, dissolved in binary mixed solvents. The solvents were prepared by varying the volume-to-volume (v/v) ratios of water and ACN as follows: 20% ACN, 50% ACN, and 80% ACN.

3.2.2 Equipment and electrodes

In this study, the same as in Chapter 2, a conventional three-electrode cell was used, consisting of a platinum mesh as the counter electrode, a reference electrode Ag | AgCl (3M KCl) and a gold working electrode modified with a ferrocene-tagged peptide SAM. The electrochemical measurements were conducted using a Metrohm Autolab potentiostat equipped with a FRA module, and controlled by NOVA 1.8 software. The preparation of the gold electrode surface, followed the same procedures detailed in subsection 2.2.3.

3.2.3 Electrochemical measurements

Electrochemical measurements were carried out on three different electrolytes composed of the water-acetonitrile binary mixture with different proportion v/v (20%, 50%, and 80% of ACN) all containing the same supporting salt concentration of 20

mM $TBAClO_4$. CV was performed over a potential window of 0.0 to 0.7 V (versus Ag | AgCl, 3 M KCl) at different scan rates to evaluate the successful formation of the SAM and the electrochemical behavior of ET. Measurements of EIS were taken at the V_F (obtained from the CV at 0.2 Vs^{-1}) and at V_{out}, a potential out of the faradaic window. A peak-to-peak amplitude of 10 mV was applied across a frequency range from 100 kHz to 0.1 Hz. The lowest frequency where the capacitive semicircle closed for each system was first identified and then applied to conducted EIS measurements at potentials range within the Faradaic window to obtain the DOS profile. The data from these measurements were treated to obtain the capacitive response as detailed in subsection 2.2.4 of Chapter 2. The measurements conducted in each of the three electrolyte media were performed in triplicate, it means three independently modified working electrode were used.

3.3 Results and discussion

The impact of the electrolyte environment, composed of a binary mixed solvent with variable proportions and a fixed supporting electrolytic salt, on the quantum electrodynamics of ET in redox-tagged peptide SAMs (Fc-pep-SAM) was investigated by analyzing key quantum properties such as C_q, G, and k, along with their associated parameters, κ and N. Additionally, building on the established equivalence between Marcus ET theory and QRT under conditions where they align, particularly in homogeneous settings with $E^0 \sim \lambda$, the theoretical significance of λ was further explored within the quantum mechanical framework of QRT. Notably, the case of mixed solvents at the Fc-pep-SAM interface provides an example of the explicit effect of the solvent where the solvation occurs preferentially through ACN moieties and the effect on the rate extend beyond simple changes in the energy term $E_\mu = g_e e^2/C_q$, which is related to λ. In this context, the solvent environment was shown to influence κ a key parameter associated with electronic coupling, which plays a crucial role in modulating both the quantum rate and the energetic framework of quantum electrodynamics, which follows the Planck-Einstein relationship, $E = h\nu$, where ν corresponds to k in the redox reaction.

These findings were contrasted with previous studies on Fc-C_{11}-SAM (BUENO; DAVIS, 2014b,c; MIRANDA; BUENO, 2016, 2019), which illustrate the implicit (dielectric continuum) effect of the solvent over ET rate dynamics, where the influence of different electrolytes, variations in solvent and supporting electrolyte salt, was examined. In that system, the QRT approach was correlated with Marcus ET theory, illustrating how solvent effects were implicitly accounted for through the dielectric continuum model, as reflected in the effect of ε on k. The implicit (continuum) and

explicit solvation situations, studied in the present work, is illustratively depicted in Figure 3.2.

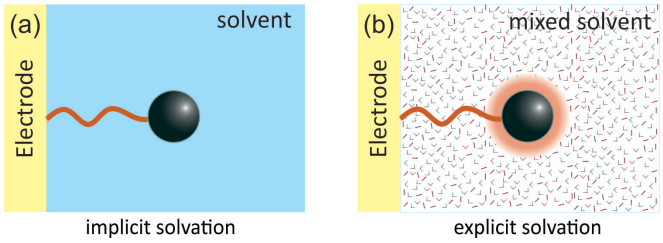

Figure 3.2: (a) Depiction of the implicit (continuum) effect of a solvent over a redox state attached to the electrode. In this situation ε of the solvent is uniform in the entire space and there is no differences between local and bulk dielectrics. (b) Depicts the explicit situation in which the dielectric environment around of the redox state is different from that of the bulk, reflecting the explicit local effect and characteristics of the solvation around the redox centers. Particularly, in the present study, the explicit situation is modulated by a mixed solvent composition of ACN and H_2O molecules, where the solvation over the redox centers are preferentially conducted by ACN moieties of the solvent.

3.3.1 Theoretical meaning of reorganization energy within QRT

In the classical Marcus theory of ET, λ arises from the solvent's influence on nuclear coordinates and is treated as a purely classical parameter. It is directly related to the dielectric properties of the medium, which is modeled as a dielectric continuum characterized by its ε, through the relationship $\lambda \sim e^2/\varepsilon\delta$. Since $\varepsilon\delta$ has units of capacitance (Farads, F), it can be interpreted as a capacitive electrostatic contribution from the solvent environment, consequently, λ can be expressed as $\lambda \propto e^2/C_{e,\lambda}$. Now, if is considered the scenario in which, the energy term, $E^{\ddagger} = (E^0 + \lambda)^2/4\lambda$, in the Marcus expression of k, Eq. 1.7 (see Section 1.1 of Chapter 1), given $E^0 \sim \lambda$, under this condition, $E^{\ddagger}$ equates to λ, which *per se* is equivalent to $E^{\ddagger} \propto e^2/C_{e,\lambda}$.

An equivalent analysis of the energy term, $E_\mu = E_e + E_q$, in the expression for k within the QRT, where $eV = E_\mu$ (Eq. 1.7, Section 1.4 of Chapter 1), can be established. The electrostatic energy component, $E_e = e^2/C_e$, which arises from the electrolyte environment, equates to the quantum component, $E_q = e^2/C_q$, which accounts for the occupancy of electronic states, as $e^2/C_q \sim e^2/C_e$. This equivalence of capacitance suggests an intrinsic relationship between the external (solvent) and internal (electronic structure) energy contributions. Moreover, this condition of electroneutrality ensures that the charge associated with electronic states due to redox reactions is effectively shielded by the electrolyte (electric-field screening) by the action cation/anion pairs of charges within the electrolyte, thereby allowing the relationship $E \propto h\nu = G/C_\mu$ to hold and consequently, the ET dynamics must conform to quantum electrodynamics within the QRT framework. As a result, E_μ can be rewritten

in terms of the solvent environment as $E_\mu \sim g_e(e^2/C_e)$, where $g_e = 2$ is the degeneracy factor redox (ALARCÓN; SANTOS; BUENO, 2021) or electrostatic (BUENO, 2023). Given that $C_{e,\lambda} \propto \epsilon\delta$ and that C_e represents the dielectric contribution of the electrolyte to the redox states, there is no fundamental distinction between $C_{e,\lambda}$ and C_e in either Marcus ET or QRT. In both frameworks, these capacitances capture the influence of the solvent's external potential on D and A states in ET reactions. Notably, E_μ, which can be experimentally determined by measurement C_q as $E_\mu = g_e e^2/C_q \sim g_e e^2/C_e$, inherently incorporates the effects of the electrochemical environment and establishes a direct correlation with the λ, offering a physical interpretation of its significance within the QRT framework.

Building on the previous discussion, we can conclude that because $E_q \sim E_e$, aligns with Marcus' definition of λ under the condition $E^0 \sim \lambda$, ensuring electroneutrality throughout the ET process. This condition, which is not accounted for in the dielectric continuum approach of Marcus ET theory, prevents E_q never exceeds Ee, and necessitates the presence of ionic species in the solvent to shield electronic charges, which within the QRT framework is understood as a consequence of quantum electrodynamics principles, where the interaction between the electrolyte environment and the frontier molecular orbitals influences the ET dynamics. Therefore, QRT provides a broader framework for interpreting ET rate dynamics by incorporating both implicit (solvent dielectric) and explicit (ionic environment) contribution. In both cases, these effects can be analyzed by measurement G and $C_q \sim C_e$, allowing a direct assessment of how the dielectric properties of the solvent influence ET kinetics. The following subsections will illustrate how QRT enables the interpretation of electrolyte-dependent quantum ET dynamics in diffusionless redox reactions under different electrolyte conditions.

3.3.2 External effect of solvent on redox moieties and DOS

According to QRT, the screening effect provided by the electrolyte, represented by C_e compensates for C_q such that $C_e \sim C_q$, leads to the electrochemical energy expression $E_\mu = g_e e^2/C_q$ which can be determined by the experimental observable C_q obtained by time-dependent electrochemical methods (ALARCÓN; SANTOS; BUENO, 2021; SÁNCHEZ; SANTOS; BUENO, 2022; BUENO, 2023) such as presented in Chapter.2. Both, C_q and E_μ, can be evaluated under equilibrium conditions at V_F which is reached by adjusting the electrode potential V according to $eV = \mu - E_F$, where μ is the chemical potential of electrons in electrode and E_F the fermi level ($V_F = E_F/e$).

In this study, we expected that changes in the electrolyte medium would influence C_e and, consequently, reflected in the C_q, as reported in previous studies of Fc-C_{11}-SAM (BUENO; DAVIS, 2014b; BUENO; MIZZON; DAVIS, 2012; MIRANDA;

BUENO, 2016, 2019). However, as shown in Table.3.1, when V was set to the equilibrium state (i.e., at the V_F, where electronic states of the redox moiety and electrode align), the C_q values, obtained by fitting the capacitive Nyquist (Figure 3.3*a*) using the equivalent circuit shown in Figure 2.2, as well as N, obtained from C_q where $f = 1/2$ in Eq. 1.6, given $N = 4k_BTC_q/e^2$, did not vary across the three different electrolyte media as presented in the Table 3.1.

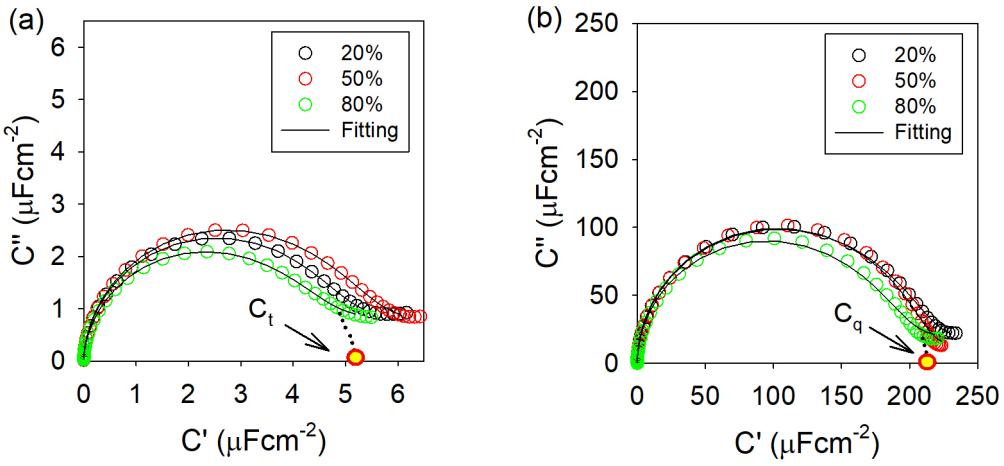

Figure 3.3: Nyquist plot showing the capacitive response at $Vout$ (a) and V_F (b) for three different electrolytes, each containing 20 mM TBAClO4 dissolved in a binary aqueous solvent mixture with 20% (green), 50% (red), and 80% (black) ACN. C_t and C_q are highlighted in (a) and (b) respectively.

Source: Author (2024)

Table 3.1: Main values of equivalent circuit elements and the obtained parameters related to the electronic and electrochemical properties governing the electron transfer process according to the quantum rate theory.

Parameter	20%	50%	80%
C_q (μF)	10.1 ± 0.7	9.8 ± 0.3	10.4 ± 0.3
R_q (kΩ)	13.1 ± 0.4	10.6 ± 0.3	8.0 ± 0.2
G (μS)	77 ± 2	94 ± 3	125 ± 2
N (x10^{12} states)	6.5 ± 0.4	6.3 ± 0.2	6.7 ± 0.2
κ (x10^{-13})	1.53 ± 0.07	1.94 ± 0.04	2.41 ± 0.05
k (s^{-1})	15.3 ± 0.7	19.3 ± 0.4	24.0 ± 0.5

Since the energy of the assembly is derived from C_q, i.e., $E_\mu = g_e Ne^2/C_q$, and C_q remains unchanged at equilibrium (defined at V_F), E_μ is also invariant across different solvent conditions as reflected in the determined value of 0.21 eV (see Table 3.2) and confirmed by the minimum energy plotted in Figure 3.4*a*, obtained from the data of DOS profile (see Figure 3.5). The invariance of this minimum E_μ, which is related

to λ as discussed in subsection 3.3.1, was compared to the solvent effect observed in Fc-C_{11}-SAM, a system previously studied (BUENO; DAVIS, 2014b), as illustrated in Figure 3.4*b*. In the case of Fc-pep-SAM, the explicit solvation effect, where ACN preferentially interacts with Fc moieties (ROWE; CREAGER, 1994), maintains E_μ unchanged, while in contrast, for Fc-C_{11}-SAM, the solvent exerts an implicit effect, leading to a shift in E_μ, consistent with Marcus ET theory, where the dielectric properties of the solvent influence λ. A clearer representation of the agreement between the effect of the solvent on the Fc-C_{11}-SAM and the Marcus continuum model is evident in the observed increase in λ with the solvent ε as shown in Figure B.2*b* (Appendix B), which contrasts with Fc-pep-SAM, where λ remains invariant with ε (see Figure B.2*a*, Appendix B), further reinforcing the distinct solvation mechanisms at play in these systems and how through the QRT analysis these differences are revealed.

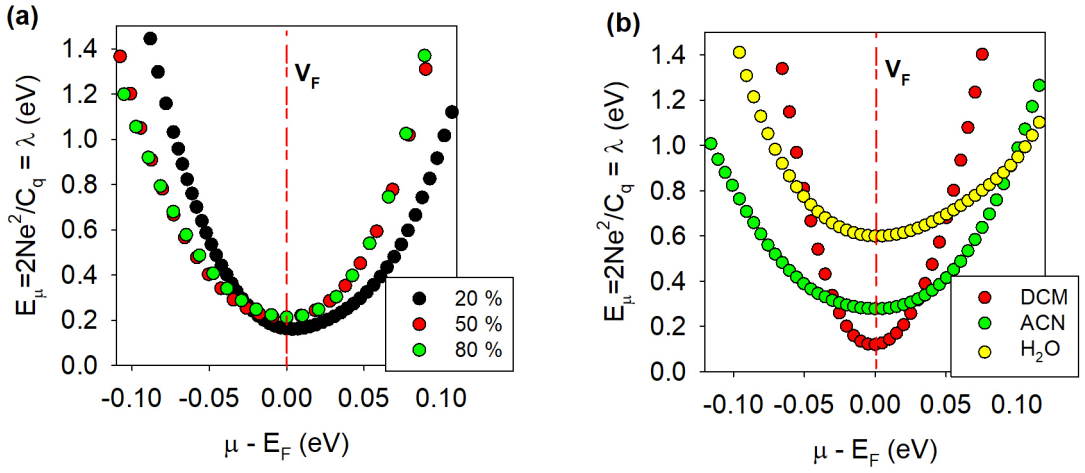

Figure 3.4: The λ energy distribution estimated from the electrochemical energy of the assembly, given by $E_\mu = g_e N(e^2/Cq) \sim \lambda$, according to $E_e \sim E_q$ defined by the QR theory, as a function of potential energy for (a) Fc-pep-SAM and (b) Fc-C_{11}-SAM.The value of N was obtained from the area under the DOS curve (see Figure 3.5), calculated via integration.

Source: Author (2025)

Because the energy is related to the quantum rate ν (or k in redox reactions) in electrodynamic processes such as ET in diffusion-less electrochemical systems (redox SAM), according with the Planck-Einstein relationship $E_\mu = hk$ and QRT premises, the experimental results show that k remains unaffected by variations in solvent composition for Fc-pep-SAM, with values of 7.7 ± 0.9 s^{-1}, 7.9 ± 0.4 s^{-1}, and 7.4 ± 0.4 s^{-1} for 20%, 50%, and 80% of ACN, respectively. This indicate that the dielectric properties of the medium when considered as continuum, captured in ε, has no significant impact on k suggesting that electron transfer in Fc-pep-SAM does not follow the implicit solvation effects predicted by Marcus ET theory. Instead, the results support a scenario where solvation occurs explicitly via preferential ACN-Fc interactions. ACN is known to interact strongly with ferrocene moieties at the Fc-pep-SAM

interface, as well as with the hydrophobic perchlorate anion (ClO_4^-) present in the electrolyte (ROWE; CREAGER, 1994). This preferential solvation effect stabilizes the Fc moieties and counterions, effectively suppressing any influence of increasing water content in the solvent mixture. Consequently, the absence of solvent-dependent changes in k reinforces that solvation occurs explicitly through ACN-Fc interactions rather than implicitly via the dielectric environment, as would be expected from Marcus ET theory (MARCUS, 1993).

The DOS of the Fc-pep-SAM and Fc-C_{11}-SAM interface, shown in Figure 3.5, was determined following the procedure outlined in (PINZÓN *et al.*, 2022; BUENO, 2023; BUENO; DAVIS, 2014b) and as presented in the experimental subsection 3.2.3. Notably, for Fc-C_{11}-SAM, although both the C_q (at V_F, where the DOS reaches its maximum, corresponding to an occupancy probability of $f = 1/2$) and the DOS shape vary with solvent composition, the total N_{total} obtained from the integral of the DOS curve, remains constant at $N_{total} \sim 1.37 \pm 0.3 \times 10^{-14}$ states cm^{-2} (BUENO; DAVIS, 2014b; BUENO; DAVIS, 2014a)). The solvent polarity affects the DOS shape, which can be attributed to conformational and electronic rearrangements within the monolayer as response to environmental changes, influencing the localization of electrons in the system. Despite these variations, the stability of N_{total} across different solvent conditions implies that, from a classical perspective related to molecular coverage of the electrode surface (BUENO; DAVIS, 2014b), the monolayer remains structurally intact. In contrast, for Fc-pep-SAM, where ACN plays an explicit role, both the DOS shape and N_{total} remain unchanged across different solvent mixtures, indicating a distinct solvent interaction mechanism compared to Fc-C_{11}-SAM.

3.3.3 Solvent impact on the electronic coupling and on energy states

Unlike C_q, the G varied with the water/ACN ratio, as shown in Table 3.1. As the ACN content in the mixture increased (or ε decreased), G rose, deviating further from its quantum limit, $G_0 \sim 77.5$ μS. Given the expression $G = \kappa G_0 N$ and the fact that both G_0 and N remain invariant across different solvents for Fc-pep-SAM, as discussed previously, κ emerges as the key factor governing the quantum electrodynamics and responding to the solvent environment. In an ET reaction governed by tunneling, κ follows the relation $\kappa \propto \exp(-\beta L)$, where L represents the effective tunneling distance and β is the decay parameter (MARCUS, 1964). In the complex binary solvent mixture, explicit solvation effects, such as the preferential solvation of Ferrocene by ACN or water interacting with the peptide (NIKITINA *et al.*, 2018; MATSUSHITA; UJI; KIMURA, 2018), could lead to changes in both L (due to conformational rearrangements of the redox center) and β (possibly due to variations in bridge hydration). These factors together influence κ and consequently the overall conductance

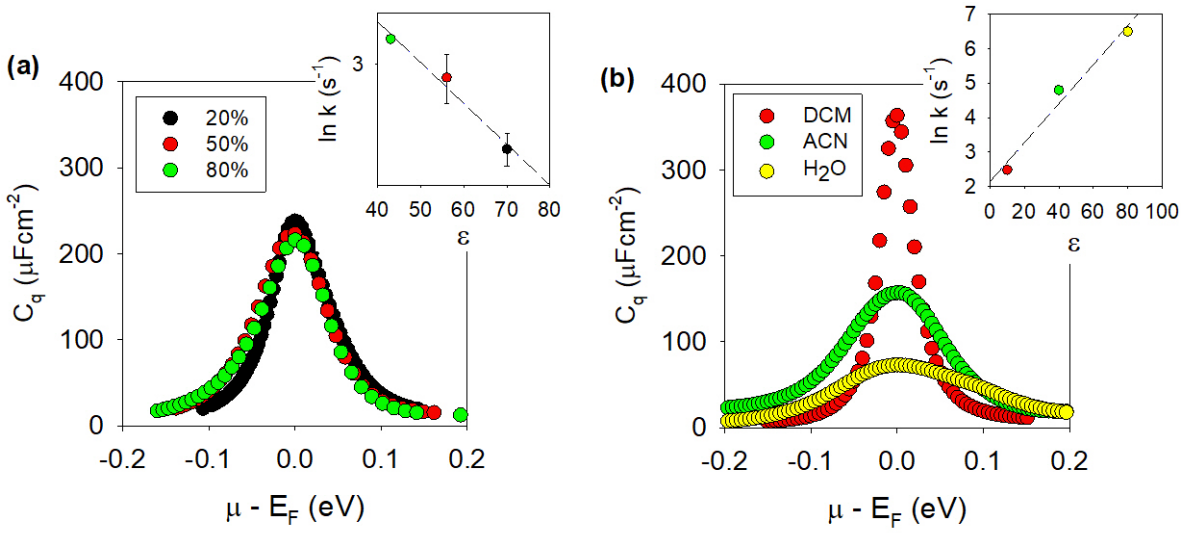

Figure 3.5: Solvent effect on the DOS dispersion of electroactive monolayers. Insets exhibits the linear relationship of logarithmic k and ε. (a) DOS shapes for Fc-pep-SAM measured in different solvent mixture of water/ACN, (b) DOS shapes for Fc-C_{11}-SAM measured in different solvents, such as DCM, ACN and water. Dielectric constant values of mixed solvent taken from ref (GAGLIARDI *et al.*, 2007). Data figure in (b) are adapted from ref (BUENO; DAVIS, 2014b).

Source: Author (2025)

behavior observed in the different solvent environments.

The increase in κ leads to a corresponding rise in G (Table 3.1), which, given its relationship with the kinetic constant, also results in a higher k, as expressed by $k = g_e G/C_q = g_e g_s(e^2/hC_q)\kappa$. As shown in Figure 3.6, κ decreases with increasing ε (or decreasing ACN content in the mixture), consequently, k, (or $\ln k$), also decreases as ε increases as presented at inset in Figure 3.5*a*. These results were unexpected, as they contradict Marcus theory predictions, since at V_F where $E^0 = 0$ and $E^{\ddagger} \sim \lambda/4$, k is inversely related to λ, and given that $\lambda \propto 1/\varepsilon$, thus $\ln k$ would be expected to increase linearly with ε, as confirmed in the solvent conditions used for the Fc-C11-SAM system (BUENO; DAVIS, 2014b), shown at inset of Figure 3.5*b*. However, for the Fc-pep-SAM system, the dielectric properties (i.e., ε) did not affect λ or $E\mu$, as discussed in the previous subsection, instead the effect of ε was reflected in variations of κ, which is directly proportional to k. This explains the observed inverse relationship between $\ln k$ and ε in a binary mixed solvent system, an example of an explicit solvent effect, a behavior that cannot be predicted by the continuum model of Marcus theory but that was revealed by the QRT.

In the previous subsection, the electrochemical energy, E_μ, of the quantum electrodynamic of ET reaction of the Fc-pep-SAM in different conditions of water/ACN ratio, was analyzed solely as a function of C_q, without considering the influence of G, i.e., $E_\mu = g_e e^2/C_q$. Now, after examining the effects of the solvent environment on G and κ and their impact on k, the energy being $E_\mu = Nhk \propto Nh(g_e G/C_q)$, was further

analyzed. Given that $G = NG_0\kappa$ and $G_0 = g_s e^2/h$, it is obtain $E_\mu = g_e g_s N^2(e^2/C_q)\kappa$, since G_0 is a constant and N remains unchanged across different solvent environments, E_μ is influenced by variations in κ. This effect is evident in the minimum value observed in Figure 3.6 and is further supported by the values of E_μ determined from circuit elements obtained by fitting circuit (Figure 2.2) to the Nyquist capacitive plots measured at V_{out} and V_F.

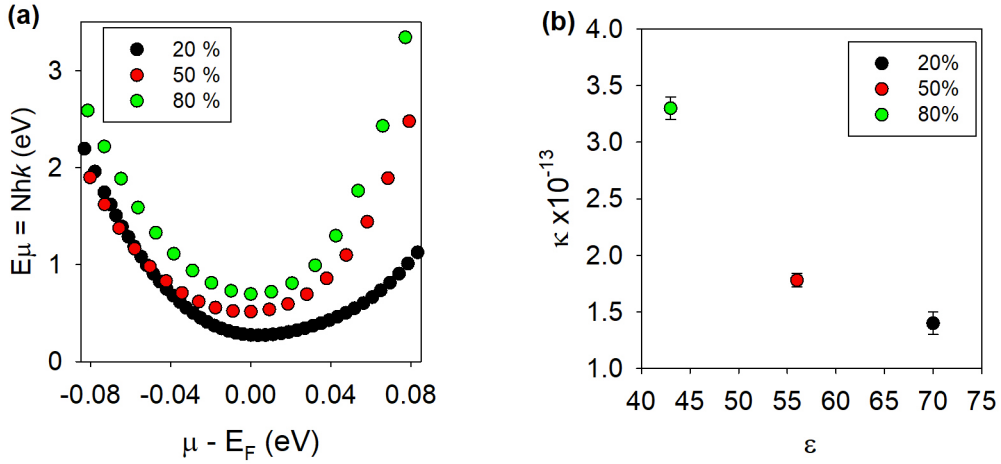

Figure 3.6: Plots of (a) E_μ distribution in function of potential energy and (b) transmission coefficient κ in function of ε of electroactive SAM in 20% (black), 50% (red) and 80% (green) ACN proportion. E_μ was calculated using the DOS distribution data. ε values of mixed solvent taken from ref (GAGLIARDI *et al.*, 2007).

Source: Author (2025)

Table 3.2: The determination of E_μ was carried out using analytical calculations and graphical methods (minimum point in the E_μ distribution in Figure 3.4 and Figure 3.6). Analytically, E_μ was calculated using the relationships $E_\mu = g_e N e^2/C_q$ and $E_\mu = Nhk$, where $k = g_e G/C_q$. The values of C_q and G were obtained through circuital analysis presented in Table 3.1. The parameter N was determined in two ways: (i) by using this value of C_q and the Eq. 1.6 (at $f = 1/2$, *i.e* at V_F, N_{V_F}), and (ii) by integrating the DOS curve in Figure 3.5, N_{total}.

		20%	50%	80%
N	N_{V_F}	$6.5 \pm 0.4 \times 10^{12}$	$6.3 \pm 0.2 \times 10^{12}$	$6.7 \pm 0.2 \times 10^{12}$
	N_{total}	$5.2 \pm 0.7 \times 10^{12}$	$6.9 \pm 0.5 \times 10^{12}$	$6.7 \pm 0.4 \times 10^{12}$
E	$E = 2e^2N/C_q^{\S}$ (eV)	0.21 ± 0.00	0.21 ± 0.00	0.21 ± 0.00
	$E = Nhv^{\dagger}$ (eV)	0.41 ± 0.01	0.50 ± 0.01	0.67 ± 0.01
	$E = Nhv^{\P}$ (eV)	0.33 ± 0.07	0.55 ± 0.04	0.66 ± 0.02
E_{min} from Figure 3.4 (eV)		0.16 ± 0.0	0.21 ± 0.00	0.21 ± 0.01
E_{min} from Figure 3.6 (eV)		0.26 ± 0.06	0.56 ± 0.06	0.67 ± 0.05

$^{\S}\kappa = 1$, N_{V_F}; $^{\dagger}\kappa \leq 1$, N_{V_F}, $^{\P}\kappa \leq 1$, N_{total}

3.4 Conclusion

This study demonstrated how QRT provides a physicochemical interpretation of λ within the Marcus ET theory, aligned with the principles of quantum electrodynamics. Unlike classical ET models, which treat solvent effects independently of the electronic structure of reactants, QRT incorporates both external solvation energy ($\lambda \sim E_e = e^2/C_e$) and internal electronic energy ($E_q = e^2/C_q$), being a direct relationship between E_e and E_q, leading to $\lambda \sim e^2/C_e \sim e^2/C_q$ to compliance with quantum electrodynamics. This interdependence arises from electroneutrality conditions imposed by ions in the solvent, a fundamental aspect of QRT absent in classical ET theory. By embedding Marcus ET within a broader QRT framework, this work establishes λ as an isoscopic physicochemical phenomenon, where molecular dynamics and quantum states are inherently coupled. This perspective explains diffusion-less electrochemical reaction rates and allows for a refined distinction between solvation environments: (i) implicit solvation, where solvent dielectric properties influence the k in accordance with Marcus ET predictions, and (ii) explicit solvation, where preferential solvation (e.g., ACN in a binary mixture) reveals a distinct relationship between ε and k, mediated through changes in the electronic coupling (reflected in κ).

Overall, these findings emphasize the limitations of classical ET models in capturing the intricate interplay between solvent environment, electronic structure, and reaction kinetics. By integrating both quantum and classical perspectives, QRT provides a more comprehensive framework for understanding ET dynamics, revealing solvation effects beyond the scope of traditional approaches.

References

ALARCÓN, E. V. G.; SANTOS, A.; BUENO, P. R. Perspective on quantum electrochemistry. A simple method for measuring the electron transfer rate constant. **Electrochimica Acta**, Elsevier, v. 398, p. 139219, 2021.

BRANDÃO, S. T. *et al.* Designing Quantum Capacitive Peptide Interfaces for Electroanalytical Applications. **Analytical Chemistry**, ACS Publications, v. 95, n. 36, p. 13470–13477, 2023.

BUENO, P. R.; DAVIS, J. J. Measuring Quantum Capacitance in Energetically Addressable Molecular Layers. **Analytical Chemistry**, v. 86, n. 3, p. 1337–1341, 2014a. ISSN 0003-2700.

BUENO, P. R.; DAVIS, J. J. Elucidating redox-level dispersion and local dielectric effects within electroactive molecular films. **Analytical Chemistry**, ACS Publications, v. 86, n. 4, p. 1997–2004, 2014b.

BUENO, P. R.; DAVIS, J. J. Measuring quantum capacitance in energetically addressable molecular layers. **Analytical Chemistry**, ACS Publications, v. 86, n. 3, p. 1337–1341, 2014c.

BUENO, P. R.; MIZZON, G.; DAVIS, J. J. Capacitance spectroscopy: a versatile approach to resolving the redox density of states and kinetics in redox-active self-assembled monolayers. **The Journal of Physical Chemistry B**, ACS Publications, v. 116, n. 30, p. 8822–8829, 2012.

BUENO, P. R. Quantum rate theory and electron-transfer dynamics: A theoretical and experimental approach for quantum electrochemistry. **Electrochimica Acta**, Elsevier, v. 466, p. 142950, 2023.

FAWCETT, W. R.; OPALLO, M. The kinetics of heterogeneous electron transfer reaction in polar solvents. **Angewandte Chemie International Edition in English**, Wiley Online Library, v. 33, n. 21, p. 2131–2143, 1994.

FLETCHER, S. The theory of electron transfer. **Journal of Solid State Electrochemistry**, Springer, v. 14, n. 5, p. 705–739, 2010.

GAGLIARDI, L. G. *et al.* Static Dielectric Constants of Acetonitrile/Water Mixtures at Different Temperatures and Debye- Hückel A and a 0 B Parameters for Activity Coefficients. **Journal of Chemical & Engineering Data**, ACS Publications, v. 52, n. 3, p. 1103–1107, 2007.

GARROTE, B. L.; SANTOS, A.; BUENO, P. R. Label-free capacitive assaying of biomarkers for molecular diagnostics. **Nature Protocols**, Nature Publishing Group UK London, v. 15, n. 12, p. 3879–3893, 2020.

GARROTE, B. L.; SÁNCHEZ, Y. P., *et al.* Electron transmittance by means of quantum capacitive states as a signal amplification mechanism for biosensing applications. **Sensors and Actuators B: Chemical**, Elsevier, v. 399, p. 134786, 2024.

HUSH, N. S. Adiabatic theory of outer sphere electron-transfer reactions in solution. **Transactions of the Faraday Society**, Royal Society of Chemistry, v. 57, p. 557–580, 1961.

MARCUS, R. A. On the theory of oxidation-reduction reactions involving electron transfer. I. **Journal of Chemical Physics**, American Institute of Physics, v. 24, n. 5, p. 966–978, 1956.

MARCUS, R. A. Chemical and electrochemical electron-transfer theory. **Annual Review of Physical Chemistry**, v. 15, n. 1, p. 155–196, 1964.

MARCUS, R. A. Electron transfer reactions in chemistry: theory and experiment (Nobel lecture). **Angewandte Chemie International Edition in English**, Wiley Online Library, v. 32, n. 8, p. 1111–1121, 1993.

MATSUSHITA, D.; UJI, H.; KIMURA, S. Effect of oscillation dynamics on long-range electron transfer in a helical peptide monolayer. **Physical Chemistry Chemical Physics**, Royal Society of Chemistry, v. 20, n. 22, p. 15216–15222, 2018.

MIRANDA, D. A.; BUENO, P. R. Chemical Hardness of Mesoscopic Electrochemical Systems Directly Analyzed from Experimental Data. **Journal of Physical Chemistry C**, v. 123, n. 34, p. 21213–21223, 2019. ISSN 1932-7447.

MIRANDA, D. A.; BUENO, P. R. Density functional theory and an experimentally-designed energy functional of electron density. **Physical Chemistry Chemical Physics**, v. 18, n. 37, p. 25984–25992, 2016. ISSN 1463-9076.

NIKITINA, V. A. *et al.* Solvent effect on electron transfer through alkanethiols. **Journal of Electroanalytical Chemistry**, Elsevier, v. 819, p. 58–64, 2018.

NORMAN, L. L.; BADIA, A. Microcantilevers modified with ferrocene-terminated self-assembled monolayers: effect of molecular structure and electrolyte anion on the redox-induced surface stress. **The Journal of Physical Chemistry C**, ACS Publications, v. 115, n. 5, p. 1985–1995, 2011.

ORLOWSKI, G. A.; CHOWDHURY, S.; KRAATZ, H.-B. Reorganization energies of ferrocene-peptide monolayers. **Langmuir**, ACS Publications, v. 23, n. 25, p. 12765–12770, 2007.

PINZÓN, E. F. *et al.* Quantum Rate Dynamics and Charge Screening at the Nanoscale Level. **Chemical Communications**, v. x, p. 000, y 2022.

ROWE, G. K.; CREAGER, S. E. Interfacial solvation and double-layer effects on redox reactions in organized assemblies. **The Journal of Physical Chemistry**, ACS Publications, v. 98, n. 21, p. 5500–5507, 1994.

SÁNCHEZ, Y. P.; SANTOS, A.; BUENO, P. R. Quantum Mechanical Meaning of the Charge Transfer Resistance. **Journal of Physical Chemistry C**, v. 126, p. 3151–3162, 6 2022.

WEAVER, M. J.; MCMANIS III, G. E. Dynamical solvent effects on electron-transfer processes: recent progress and perspectives. **Accounts of Chemical Research**, ACS Publications, v. 23, n. 9, p. 294–300, 1990.

WONG, R. A. *et al.* Probing consequences of anion-dictated electrochemistry on the electrode/monolayer/electrolyte interfacial properties. **Nature Communications**, Nature Publishing Group UK London, v. 11, n. 1, p. 4194, 2020.

ZHUANG, B.; WANG, Z.-G. Molecular-Based Theory for Electron-Transfer Reorganization Energy in Solvent Mixtures. **The Journal of Physical Chemistry B**, ACS Publications, v. 120, n. 26, p. 6373–6382, 2016.

Chapter 4

The effect of linker and bridge groups on the electron transfer rate dynamics

This chapter delves into the role of linker and bridge components in redox-tagged peptide SAMs and their impact on ET dynamics when anchored to the electrode through the linker group. The ET dynamics are analyzed using QRT and its associated methodologies. The linker group anchors the peptide structure to the electrode, while the bridge serves primarily as the electronic coupling element, facilitating ET between the discrete states of the peptide and the electrode. By employing QRT, we gain a quantum mechanical perspective to:

- ☑ Evaluate the effect of the bridge structure in the ET dynamics as well as
- ☑ Investigate the effect of the linker group in the electron coupling component of ET dynamics within QR theoretical analysis. The use of the QRT permits to understand the effect of linker and bridge group from a quantum mechanical perspective.

4.1 Introduction

Redox-tagged peptide SAMs serve as molecular models to study ET and ET_p in biochemistry, particularly the long-range transport of electrons between states of biological macromolecules (GRAY; WINKLER, 2009; SHAH *et al.*, 2015). Synthetic modifications of peptides provide valuable insights into how such alterations affect ET dynamics, as revealed through the k parameter within the framework of QRT, as discussed in Chapter 1. As highlighted in section 1.2 of Chapter 1, the coupling between the electrode and the redox-tagged SAM is mediated by the linker group. This group chemically and electronically bridges the metallic DOS of the electrode and the redox DOS of the SAM (FELICIANO; BUENO, 2020). Commonly used linkers include the amino acid Cys and lipoic acid molecule, which anchor peptides to electrodes via thiol groups that form covalent bonds with gold atoms (REDONDO-GÓMEZ *et al.*,

2024). These linkers can establish bidentate or monodentate bonds, depending on their chemical structure.

For example, Kraatz *et al.* employed Cys to study the effects of dipole moments (WAIN *et al.*, 2008) and molecular dynamic (MD) on ET through α helical peptides (MANDAL; KRAATZ, 2006), while using cystamine to evaluate hydrogen bonding (KRAATZ *et al.*, 2004). Kimura and colleagues utilized lipoic acid to investigate ET through helical peptides with varying chain lengths (ARIKUMA *et al.*, 2011) and compared two linkers, a disulfide with a methylene chain and a thiophenyl group, to assess their effects on ET (WATANABE; MORITA; KIMURA, 2005). Similarly, Abell and coworkers (BROOKSBY *et al.*, 2011) used a long-chain alkanethiol linker to study ET through a peptide SAM containing a ferrocene moiety. Furthermore, Wrochem *et al.* (VON WROCHEM *et al.*, 2010) demonstrated that bidentate bonding provides superior electronic coupling at the gold surface compared to monodentate configurations. This improvement was attributed to the HOMO structure of the bidentate configuration, which is thought to reduce the charge injection barrier at the metal-molecule interface.

The strength of the electronic communication is not only influenced by the nature of the linker group but also by the distance between the redox probe and electrode (SHAH *et al.*, 2015; HAN *et al.*, 2020), which has been investigated by adjusting the number of amino acids comprising the peptide bridge (SHAH *et al.*, 2015; ECKERMANN *et al.*, 2010). Two types of mechanisms have been invoked to elucidate ET and ET_p efficiency involving redox-tagged SAM, referred to tunneling and hopping mechanism. Primarily hopping mechanism is considered to govern for distances larger than 2 nm (ARIKUMA *et al.*, 2010; CORDES; GIESE, 2009) depending on the parameter β. For instance, for β higher than 0.6 $Å^{-1}$ tunneling mechanism is considered to govern the transport of electrons whereas lower than these values hoping mechanism is dominant (JUHANIEWICZ; PAWLOWSKI; SEK, 2015).

It is essential to underscore the intricate relationship between the distance of a peptide and its structural conformation, especially when it is integrated to a SAM. This complexity arises due to changes in amino acid structures. For instance, adding extra amino acid groups not only influences the overall length of the peptide but also alters the structural conformation of the monolayer (JUHANIEWICZ; PAWLOWSKI; SEK, 2015; SEPUNARU *et al.*, 2015). These additional amino acids modify the intricate network of interactions among neighboring peptides within the monolayer, collectively influencing its structure (KRAATZ *et al.*, 2004; MANDAL; KRAATZ, 2006). Consequently, the ET process is not solely dictated by the linear increase in distance resulting from the addition of amino acids, but are co-influenced by a combination of factors, including peptide length, structural conformation, and interactions with neighboring peptides within the monolayer (TAKEDA; MORITA; KIMURA, 2008).

A comprehensive understanding of the actual effect of the peptide-bridge composition on the ET dynamics requires a comprehensive consideration of these multifaceted factors, where the length of the peptide is just one part of the complex mix of elements influencing the overall process.

In this context, QRT provides a robust framework for analyzing the complex interplay of these factors and their effects on ET dynamics. By applying QRT, this chapter aims to advance our understanding of how modifications to peptide linkers and bridges influence ET processes at the molecular level. Specifically, the chapter investigates the role of peptide length, conformation, and inter-peptide interactions in shaping the efficiency of ET in redox-tagged SAMs. This understanding is particularly relevant for the design and optimization of redox-active biosensing interfaces, where C_q serves as a key transducer signal (BRANDÃO *et al.*, 2023), contributing to the development of more effective biological sensors with enhanced sensitivity and performance.

4.2 Materials and methods

The experimental methodology carried out in this chapter is similar to that outlined in section 2.2 and is further supplemented by the details provided in this section 4.2.

4.2.1 Chemical reagents

In Chapter 2,Table 2.1 lists the primary reagents used throughout the development of this thesis. However, due to specific modifications in the synthesis process needed to obtain the electroactive peptides discussed in this chapter, additional reagents are listed in Table 4.1. Additionally, the information about the sources and purposes of these extra reagents is also presented. All aqueous solutions were prepared using Milli-Q water (Simplicity® water purification system, Millipore, 18.2 MΩ cm at 25°C).

4.2.2 Synthesis and characterization of redox-tagged peptides

To investigate the effect of the linker group on ET, three peptides were designed and synthesized: Fc-EAAC (denoted as Fc-pep-C), Fc-EAACC (denoted as Fc-pep-CC), and Fc-EAAK(L_a) (denoted as Fc-pep-K(L_a), where L_a is the lipoic acid). Their skeletal structures are shown in Figure 4.1. Additionally, to study the effect of the bridge on ET, four redox-tagged peptides with varying numbers and types of amino

Table 4.1: List of chemical reagents used in chapter 4.

Reagent	Company	Purpose
Rink amide resin (0.678 mmol g^{-1})	AAPPTEC	Solid phase peptide synthesis
N-Fmoc[a]-N-trityl-L-glutamine (Fmoc-Gln(Trt)-OH)	AAPPTEC	Amino acids for peptide synthesis
N-Fmoc[a]-N-4-methyltrityl-L-Lysine (Fmoc-Lys(Mtt)-OH)	AAPPTEC	
N,N,N′,N′-Tetramethyl-O-(1H-benzotriazol-1-yl) uroniumhexafluorophosphate (HBTU)	Sigma-Aldrich	Coupling of the ferrocene (Fc) in the synthesized peptide
Dichloromethane (DCM)	Sigma-Aldrich	Peptide-protecting group cleavage
Ethanol (EtOH)	Sigma-Aldrich	Solvent for peptide incubation
(±)-α-Lipoic acid (L_a)	Sigma-Aldrich	Linker group

acids were designed and synthesized: Fc-ECC, Fc-EAACC, Fc-EAAQAACC, and Fc-EAAQAAQAACC, hereafter referred to as Fc-3aa, Fc-8aa, Fc-5aa, and Fc-11aa respectively (See Figure 4.4).

The peptides were synthesized using SPPS following the protocol detailed in the experimental subsection 2.2.2 of chapter 2, applicable to all peptides listed in Table 4.2, except Fc-pep-K(L_a). For this peptide, the coupling of the first amino acid, Fmoc-Lys(Mtt)-OH, was repeated due to a positive result in the Kaiser test after the initial coupling, indicating that the NH_2 group on the resin remained reactive. Additionally, an extra preparatory step was performed for Fc-pep-K(L_a) prior to the coupling of the Fc moiety.

Specifically, after synthesizing Fmoc-EAAK-resin, the protecting group of the NH_2 of the Lys side chain, methyltrityl (Mtt), was cleaved under mild conditions using a 1% TFA solution in DCM. The cleavage reaction was allowed to proceed for approximately 2 min with shaking. After this initial period, the resin was washed three times with DCM, and the cleavage mixture was added again to repeat the process. This procedure was repeated multiple times until the reaction solution changed from yellow to colorless. Subsequently, a positive Kaiser test confirmed the successful deprotection of the NH_2 group on the Lys side chain, which was then coupled to the carboxylic group of L_a by adding it in a two-fold excess along with HATU/DIPEA coupling reagents in DMF. The coupling reaction was performed with shaking for 2 h. The success of the L_a coupling was verified by a negative Kaiser test, indicated by the persistence of a yellow solution.

The Fc moiety (3-ferrocenylpropionic anhydride) was coupled to the N-terminal

of the Glu residue in the peptides (Fc-pep-C and Fc-pep-CC, Fc-3aa) by adding a 0.1-fold excess of DMAP in DMF, shaking for 2 h, and then adding a two-fold excess of PyBOP/DIPEA in DMF overnight. For the other peptides (Fc-pep-K(L_a), Fc-8aa, and Fc-11aa), HBTU/DIPEA was used instead of PyBOP/DIPEA after DMAP addition. After Fc coupling, the cleavage of the resin and protecting groups, as well as the precipitation and extraction of the peptides, was carried out using the procedure detailed in the experimental subsection 2.2.2, chapter 2.

The peptide-containing supernatants were lyophilized, and the crude peptides were purified by HPLC using the methods described in the Table 4.2. Purification was achieved through preparative HPLC with a linear elution gradient on a C-18 column. In this gradient, the concentration of organic solvent B (TFA/ACN 0.036% v/v) gradually increased over time. These methods were chosen based on chromatogram profiles obtained from an initial analysis of crude peptides, which were run through a gradient program of 5% to 95% solvent B over 30 min at a flow rate of 1 mL min^{-1}. From this initial analysis, the retention times of the major peaks were used to fine-tune the elution solvent % B for each peptide, taking into account the differences between analytical and preparative HPLC column types.

Analytical HPLC revealed retention times (and purity in parentheses) as follows: 13.9 min for Fc-pep-C (95%), 14.5 min (93%) for Fc-pep-CC, 14.7 min for Fc-3aa (96.6%), 15.7 min (91%) for Fc-8aa, 15.3 min (78%) for Fc-11aa, and 17.7 min (90%) for Fc-pep-K(L_a). The identity of each peptide was confirmed using ion-trap MS on a Bruker system in positive ion mode. HPLC chromatograms and mass spectra of the purified peptides are provided in Appendices A, D, E, J, K, L. The lower purity observed for Fc-11aa, the peptide with the highest number of amino acids, was attributed to the presence of a minor secondary peak near the main peak in the chromatogram (see Appendix L). Nevertheless, the mass spectrum showed the highest-intensity signal corresponding to the expected m/z of the peptide.

The synthesis yields of the peptides were estimated by comparing the final mass obtained after purification with the theoretical mass calculated from the initial molar scale of synthesis. The yields for Fc-pep-C, Fc-pep-K(L_a), Fc-3aa, Fc-5aa, Fc-8aa, and Fc-11aa were 14%, 2%, 2.6%, 6%, 2.2%, and 1.7%, respectively. These low yields are attributed to several factors, including challenges in anchoring the Fc moiety, its instability under cleavage conditions, and the formation of intramolecular disulfide bonds, which resulted in the generation of dimeric peptides. Despite the low yields, the synthesis remains suitable for electrochemical analysis due to the small quantities required for the formation of SAMs. Finally, the purified redox-tagged peptides were dissolved in an H_2O/ACN mixture to prepare 2 mM solutions. These solutions were aliquoted into 300 μL portions in 1.5 mL Eppendorf tubes, lyophilized, and stored at 4,°C in the solid phase until needed for incubation with the gold electrode.

Table 4.2: Summary of synthesized peptides and HPLC purification characteristics using semipreparative column and linear elution gradient. The purification method employed a linear elution gradient with a flow rate of 5 mL min^{-1}, using solvent A (0.045% TFA/H_2O) and solvent B. Amino acids are represented by their one-letter codes: Alanine (A), Cysteine (C), Glutamate (E), Glutamine (Q), and Lysine (K). Lipoic acid, used as a linker group, is denoted as L_a.

Peptide	Code	Chromatography Column	Purification Method
Fc-ECC	Fc-3aa	C18, Polaris (250 mm x 10 mm, particle size 5 μ m)	20 to 50% of solution B for 90 min
Fc-EAAC	Fc-pep-C	C18, Polaris (250 mm x 10 mm, particle size 5 μ m)	15 to 45% of solution B for 60 min
Fc-EAACC	Fc-5aa or Fc-pep-CC	C18, Aaapptec (250 mm x 10 mm, particle size 5 μ m)	25 to 55% of solution B for 90 min
Fc-EAAK(L_a)	Fc-pep-K(L_a)	C18, Sepax (250 mm x 10 mm, particle size 10 μ m)	25 to 65% of solution B for 30 min
Fc-EAAQAACC	Fc-8aa	C18, Sepax (250 mm x 10 mm, particle size 10 μ m)	315 to 30% of solution B for 130 min
Fc-EAAQAAQAACC	Fc-11aa	C18, Sepax (250 mm x 10 mm, particle size 10 μ m)	25 to 55% of solution B for 90 min

Estimation of the length of redox-tagged SAMs by MD

A classical MD simulation was carried out on ferrocene-labeled SAMs over gold (Fc-SAM/Au) in aqueous solution environment. The simulation used the AMBER99SB (HORNAK *et al.*, 2006) force field within the GROMACS software package (BERENDSEN; SPOEL; DRUNEN, 1995). For Fc-pep-C parametrization, the classical bonded terms were derived from the OPLS-AA (JORGENSEN; TIRADO-RIVES, 1988) force field, with atomic charges and equilibrium geometries obtained from quantum mechanical calculations (BAYLY *et al.*, 1993). A gold slab was modeled with four layers of Au atoms, interacting via van der Waals forces, and a constraint was applied to maintain the Au-S bond throughout the simulation. The system was equilibrated at 300 K using the Nosé-Hoover thermostat (NOSÉ, 1984) in the NVT ensemble, followed by a 200 ps run under the NPT ensemble to equilibrate solvent density and pressure. The final production run was performed for 2 ns in the NPT ensemble.

4.2.3 Equipment and electrodes

Electrochemical measurements were performed using an AUTOLAB potentiostat in a three-electrode electrochemical cell, as described in subsection 2.2.3 of chapter 2. The system comprised a gold working electrode, an Ag | AgCl (3 M KCl) reference electrode, and a platinum mesh counter electrode. Prior to peptide incubation, the gold working electrode underwent a standardized pretreatment process to ensure a clean and reproducible surface. This process involved sequential mechanical polishing with alumina suspensions of varying particle sizes, followed by electrochemical cleaning in both basic and acidic media, as detailed in subsection 2.2.3.

Fabrication of redox-tagged SAMs

The purified peptides, contained in eppendorf tubes in solid phase, were dissolved in 300 μL of ACN/H_2O (1:1,$^v/_v$). Aliquots of 75 μL of the solution were then transfered into four eppendorf tubes. The pre-treated gold electrode, after being dried with N_2, was carefully deposited into the peptide solution, ensuring no bubble formation on the electrode surface during immersion. The tops of the eppendorf tubes containing the electrodes were sealed with parafilm and stored in the dark at 24 °C for 16 h.

4.2.4 Electrochemical measurements

Electrochemical techniques, including CV and EIS, were employed to evaluate the quality and electrochemical behavior of the redox-tagged SAMs. A supporting electrolyte solution of 20 mM $TBAClO_4$ in ACN/H_2O (1:4, 1:4, $^v/_v$) was used in all electrochemical measurements. Key parameters, such as C_q, R_q, and k, were analyzed to investigate the impact of the linker and bridge groups on the ET dynamics.

CV measurements

The quality and successful formation of the SAMs were initially evaluated through CV at low scan rates, using a potential window of 0.0 to 0.7 V (four cycles) *versus* Ag | AgCl (3 M KCl). To investigate the SAMs, formed by the peptides synthesized for the linker effect study, CVs were recorded at a s of 0.1 V s^{-1}. In contrast, a higher s of 0.4 V s^{-1} was applied to analyze SAMs designed to assess the impact of the molecular bridge. This choice was necessary due to the absence of well-defined redox peaks at lower scan rates, which hindered reliable electrochemical characterization.

Stripping of redox-tagged peptide SAM from gold electrode

CV was performed in a potential range from -0.45 V to -1.45 V at a s of 10 mV s^{-1} for 3 cycles. The measurements were conducted in a 0.1 M NaOH solution, which was purged with N_2 for 15 min prior to the experiment. The working electrode was a polycrystalline gold electrode modified with SAMs of redox peptides as previously described in section 4.2.3. The desorption of thiol groups was realized for the SAMs formed with the peptides: Fc-pep-C, Fc-pep-CC, and Fc-pep-k(L_a).

EIS measurements

V_F were determined from the CV as the average between V_{pa} and V_{pc} at the s used in the initial quality evaluation of SAMs, over which a peak-to-peak amplitude of 10 mV was applied with a range from 100 kHz to 0.05 Hz. Additionally, a potential far from the faradaic window of the voltammogram, referred to as V_{out}, was also applied under the same conditions as V_F for measuring EIS spectra from which C' and imaginary C'' were obtained as described in subsection 2.2.4 of chapter 2.

Equivalent circuit analysis

The values of the circuital elements were obtained by fitting capacitive spectra, using the equivalent circuit as detailed in the section. 2.2.5 of the Chapter 2.

4.3 Results and discussion

The results and discussion in this section are organized around two key factors: the linker group and the peptide-bridge.

4.3.1 The effect of the linker group in the ET dynamics

The effects of the linker group were investigated using three peptide structure: Fc-pep-C, Fc-pep-CC, and Fc-pep-K(L_a) (see Figure 4.1). The peptide design were inspired by Fc-pep-C, a well-established component in capacitive biosensor devices (PICCOLI *et al.*, 2018; BRANDÃO *et al.*, 2023; GARROTE; SANTOS; BUENO, 2020; GARROTE; SÁNCHEZ, *et al.*, 2024; GARROTE; LOPES, *et al.*, 2024). Fc-pep-C is a tetrapeptide designed to facilitate specific chemical modifications. The first amino acid, Glu, was selected because of its side chain, which contains a carboxyl group that can be chemically modified to attach macromolecules of biological interest, such as antibodies or DNA (GARROTE; SANTOS; BUENO, 2020). The next two amino acids, Ala, were chosen because it is one of the major amino acids that promote α-helix formation, leading to the creation of a more compact monolayer (WATANABE; MORITA;

KIMURA, 2005; TAKEDA; MORITA; KIMURA, 2008; ARIKUMA *et al.*, 2011). This compactness is attributed to the nonpolar methyl groups in the Ala side chain, which do not interfere with the hydrogen bonding network of the helix. The final amino acid, Cys, was included because of its thiol group, which is an excellent linker for bonding the peptide bridge to the gold electrode (WAIN *et al.*, 2008; VERICAT *et al.*, 2006; REDONDO-GÓMEZ *et al.*, 2024). The Fc moiety is finally bonded to the α amine group of the Glu.

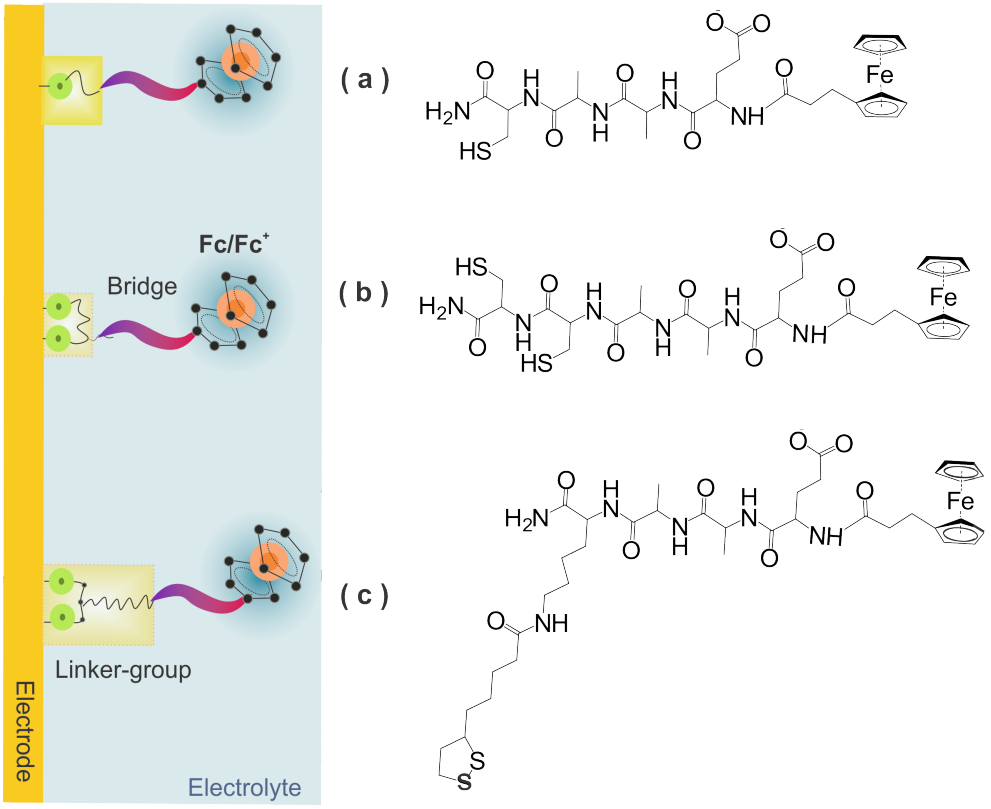

Figure 4.1: Schematic representation of the gold electrode functionalized with three different redox-active peptides, each featuring a distinct linker group capable of forming either monodentate or bidentate coordination with the electrode surface: (a) Fc-pep-C with a single cys (monodentate), or (b) Fc-pep-CC with two cys, and (c) Fc-pep-K(L_a) with L_a (bidentate). Although the illustration depicts all three peptides anchored to the same electrode, in practice, separate SAMs were formed for each peptide. On the right, the skeletal structures of the three peptides emphasize the differences in their linker groups, which influence their interaction with the gold surface and ET dynamics.

Source: Author (2024)

Given that the linker group of Fc-pep-C is chemically bonded to the gold electrode via monodentate ligation, as demonstrated by stripping analysis (see appendix G), where only a single atom, specifically the sulfur from the thiol group of Cys, bonds to the metal surface, it is aimed to compare the effects of bidentate ligation on the ET dynamics using two approaches: the first involved adding an additional Cys residue to the peptide, providing an extra thiol group for binding, and the second involved replacing the Cys linker with a L_a, in which L_a is attached to the -NH_2 group of the

Lys side chain. This enables bidentate bonding (see appendix G) and also increases the distance between the electrode and the bridge (see Figure 4.1).

The formation of the SAMs were confirmed by the linear correlation between the i_{pc} and i_{pa} peaks with s, as determined from CV curves (see Appendix of Figure F). This linear relationship is a confirmation of the diffusionless ET dynamics as discussed previously in chapter. 2. CV profiles acquired at a s of 0.1 V s^{-1} (see Figure 4.2*a*) exhibited symmetric, Gaussian-like peaks centered around V_{pa} and V_{pc}, corresponding to the oxidation and reduction processes of the Fc moiety, $Fc \rightarrow Fc^{+} + e^{-}$ and $Fc^{+} + e^{-} \rightarrow Fc$, respectively. The observed differences in V_F, highlighted in Table. 4.3, reflect the varying energy levels at which the oxidized and reduced forms of the electroactive peptides are in equilibrium with the electrode's Fermi level. Specifically, the Fc-pep-K(L_a) SAM exhibited the lowest V_F, whereas the Fc-pep-C SAM showed the highest V_F, indicating that Fc-pep-C, which features a monodentate linker, requires greater energy to achieve alignment between the electrode and the SAM compared to Fc-pep-K(L_a), which forms a bidentate ligation. These findings underscore the critical role of linker coordination in modulating ET efficiency. The small $\Delta V_p \approx 0$ and the near-unity ratio of peak currents ($i_{pa}/i_{pc} \approx 1$), as presented in Table 4.3, confirmed the quasi-reversible ET dynamics. The FWHM is less than the characteristic value of 90.6 mV for both Fc-pep-C and Fc-pep-CC SAMs, but is higher for Fc-pep-K(L_a) SAM. The FWHM values suggest, from a classical perspective, dominant attractive interactions between R and O species for Fc-pep-C and Fc-pep-CC SAMs and repulsive for Fc-pep-K(L_a) (LAVIRON, 1974).

Table 4.3: Criteria parameters of reversibility obtained by CV profiles of ferrocene-labeled peptide SAM with different linker group.

Peptide	i_{pa}/i_{pc}	V_F	ΔV_p mV	FWHM
Fc-pep-C	0.922 ± 0.006	363 ± 5	19 ± 6	70 ± 6
Fc-pep-CC	0.987 ± 0.005	344 ± 9	14 ± 1	63 ± 7
Fc-pep-K(L_a)	0.928 ± 0.003	330 ± 4	19 ± 8	105 ± 1

The effect of the linker on the k was evaluated within the framework of QRT, permitted because the kinetics follow a diffusionless dynamic regime, the equivalence between the semi-classical and quantum rate approaches, both relying on the meaning C_q, allows k to be determined using the QR method, with validation provided by Laviron's method, as previously discussed in Chapter 2. In the QR method, k

was obtained by assessing C_q at V_F, either through the analysis of the ratio i/s extracted from current-potential curves (see Figure 4.2 *b*) or via time-dependent methods such as impedance, which examines capacitive spectra, as noted in Figure 4.3 *b*. In Chapter 2, it was demonstrated that Laviron's method enables the determination of k under experimental conditions where $\Delta V_p \geq 200$ mV, which provides a linear correlation between V_{pa} (and/or V_{pc}) with the $log(s)$, a condition that depends on the specific structure of the studied SAM. For instance, s greater than 5 V s^{-1} were required to meet this condition for Fc-pep-C, while higher s of over 6 V s^{-1} and 7 V s^{-1} were necessary for Fc-pep-K(L_a) and Fc-pep-CC, respectively. The CV and corresponding V_p *versus* $log(s)$ plots for all three SAMs studied in this subsection are shown in Appendix H and the values of k determined by this method were compared with those obtained from the QR method in Table 4.4.

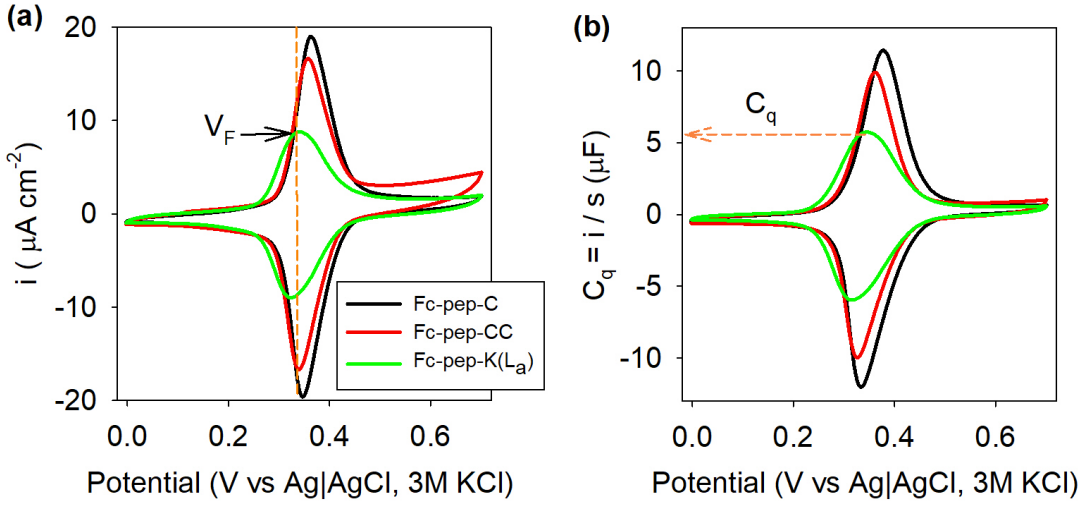

Figure 4.2: (a) Comparison of CVs for the three SAMs with different linker groups, recorded at 0.1 V s^{-1} in a solution of 20 mM $TBAClO_4$ in ACN/H_2O (1:4, v/v). (b) Capacitive-potential curves obtained by normalized CV curves (0.4 V s^{-1}). The current and capacitance-potential curves in (a) and (b) represent a typical measurement taken from three different modified working electrodes for each peptide SAM evaluated. The V_F and C_q of the Fc-pep-K(L_a) SAM are highlighted in (a) and (b), respectively.

Source: Author

The characteristic master curve of i/s *versus* V was successfully obtained here for the Fc-pep-C and Fc-pep-CC SAMs. However, for Fc-pep-K(L_a) SAM, the master curve was only observable at scan rates greater than 0.4 V s^{-1}, as shown in Figure I.1, (Appendix I), which was attributed to the differences SAM structure that exhibited broader faradaic peaks in the CV as compared to the other peptides, as can be noticed in Figure 4.2 *a*. The linker group of this peptide, L_a bonded to the side chain of Lys, was initially chosen because longer hydrocarbon chains typically result in stronger van der Waals interactions between neighboring molecules in the SAM, promoting a more tightly packed and well-ordered SAM (MIURA *et al.*, 1998) and expected to lead

to a more defined CV profile. However, it is possible that the tighter packing due to the longer carbon chains, combined with the negative charge on the carboxyl group of Glu at the electrolyte solution's pH (6.7), leaded to increased repulsion between neighboring molecules in the SAM, thereby causing variations in the electrochemical environment of the ferrocenyl moiety. It is important to note that while the QR method is effective for determining k, from the CV data, caution is warranted, particularly when the SAM structure causes deviations from the expected master curve, as seen in the Fc-pep-K(L_a) case. Structural factors, can lead to capacitance-potential curves that deviate from the ideal, especially at lower s.

Table 4.4: Kinetic parameters determined for three ferrocene-tagged SAMs each with a different linker groups using both QR and Laviron's method. The experimental variable C_q for calculating k using the QR method was obtained from CV at 0.4 V s^{-1} and ECS at V_F at the low-frequency region of the Nyquist spectra. The parameters obtained from CV corresponded solely to the anodic process. The standard error for each parameter was calculated from three independent measurements of three distinct modified working electrodes for each type of peptide structure.

Peptide	QR method		Laviron's method
	CV	ECS	
Fc-pep-C	$C_{qa} = 8.9 \pm 0.5$ μF $k_a = 18 \pm 2$ s^{-1}	$C_q = 12.7 \pm 0.3$ μF $k = 12.3 \pm 0.8$ s^{-1}	$(1 - \alpha_a) = 0.30 \pm 0.01$ $s_a = 1.4 \pm 0.1$ $k_a = 16 \pm 2$ s^{-1}
Fc-pep-CC	$C_{qa} = 8.0 \pm 0.7$ μF $k_a = 20 \pm 3$ s^{-1}	$C_q = 9.9 \pm 0.2$ μF $k = 15.6 \pm 0.3$ s^{-1}	$(1 - \alpha_a) = 0.31 \pm 0.02$ $s_a = 1.5 \pm 0.2$ $k_a = 18 \pm 2$ s^{-1}
Fc-pep-K(L_a)	$C_{qa} = 4.9 \pm 0.6$ μF $k_a = 32 \pm 4$ s^{-1}	$C_q = 6.5 \pm 0.0$ μF $k = 24.2 \pm 0.9$ s^{-1}	$(1 - \alpha_a) = 0.29 \pm 0.01$ $s_a = 2.2 \pm 0.4$ $k_a = 25 \pm 5$ s^{-1}

Table 4.5 confirms that, within experimental error, the values of G for the three redox-tagged SAMs were close to the quantum limit of $G_0 \sim 77.5$ μS, and no significant differences were observed among the peptides with different linker groups. A similar trend is observed for κ, which were estimated from the values of G obtained from circuit analysis, using $\kappa = G/G_0N$, where N was determined from C_q, that at the V_F, it simplifies to $C_q = e^2N/4k_BT$. A stronger electron coupling, reflected in higher κ, were expected in SAMs chemisorbed via two points of ligation (VON WROCHEM *et al.*, 2010). Both Fc-pep-CC and Fc-pep-K(L_a) SAMs, with their bidentate ligation, exhibited higher κ than Fc-pep-C featuring a monodentate ligation (Table 4.5). Notably, Fc-pep-K(L_a) SAM, which combines a bidentate ligation with a longer alkyl chain, displayed a significantly higher κ. This result was unexpected, as a longer

alkyl chain typically increases the separation between the electrode and the redox probe, thereby reducing κ (MARCUS, 1964). Thus, the observed κ for Fc-pep-K(L_a) suggests that bidentate ligation enhances electronic coupling, while the alkyl chain may influence the SAM structure in a way that optimizes the energy barrier for electron tunneling. This interplay likely compensates for the increased separation[1], leading to an overall enhancement of κ. These findings highlight the complex interplay between linker structure, alkyl chain length, and electronic coupling, where multiple factors contribute to the overall tunneling behavior and κ.

Note that N (Table. 4.5) varied significantly among the SAMs, with the highest value observed for the monodentate bonding peptide Fc-pep-C and the lowest for the bidentate bonding Fc-pep-K(L_a). Despite the differences in N, no significant differences in $G \propto N$ were observed among the SAMs, indicating that there is a quantum limit of transport for each quantum channel state. The classical counterpart of N is the molecular coverage which refers to the amount of molecules anchored to the electrode. It is expected that fewer molecules are anchored on the electrode when the linker group promotes bidentate bonding. Considering Avogadro's number and the electroactive surface area of the electrodes, the molecular coverage for Fc-pep-C, Fc-pep-CC, and Fc-pep-K(L_a) were calculated as 2.7 $\pm$ 0.1 x 10^{-10}, 2.4 $\pm$ 0.1 x 10^{-10}, and 1.4 $\pm$ 0.1 x 10^{-10} mol cm^{-2}, respectively. The consideration of N as the DOS rather than classical molecular coverage is more appropriated with the QRT. Unlike classical descriptions that treat electrons as Boltzmann (non-degenerate) particles without electronic structure or quantum state occupancy, the DOS perspective acknowledges the intrinsic quantum nature of charge transport. Molecular coverage, while informative from a structural standpoint, merely provides a numerical estimation of molecular population over the electrode's surface and does not capture the quantum characteristics of electronic states or the properties of quantum transport channels associated with non-adiabatic R_q or G.

The parameter N is closely related to the meaning of C_q, which is perhaps the most important property of the junction and the ET rate, as it is associated with the energy $e^2/C_q = h\nu$ of the ET dynamics, as outlined in section 1.4, of the Chapter 1. The C_q values were obtained from an analysis of capacitive Nyquist plots, as noticed in Figure 4.3 *b*, at the lower frequency limit. The circuit elements associated with the relaxation process permits to obtain $\tau = R_q C_q$ and thus $\nu = k \propto e^2/C_q$ for each SAM, as summarized in Table 4.5, where it can be observed that C_q differed among the SAMs

[1]The length L of the barrier for Fc-pep-C and Fc-pep-CC SAMs, estimated from MD simulation, yielding 1.4 nm and 1.5 nm, respectively, whereas for Fc-pep-K(L_a) the value, assuming a fully stretched peptide structure, resulted in an estimated length of 2.4 nm, predicted using PyMOl. Despite the larger estimated L value for the Fc-pep-K(La) SAM, which would typically suggest weaker electronic coupling leading to lower κ, the favorable nature of the linker structure was highest among the three peptide SAMs evaluated.

with distinct linker groups. The highest C_q was observed for the SAM containing a single Cys, while a lower C_q was recorded for SAMs with bidentate ligation. Notably, the lowest was obtained for the Fc-pep-K(L_a) SAM, demonstrating that charge occupancy depends on the linker group. However, the observed variations cannot be only attributed to the monodentate or bidentate nature of the contacts, but also the way each linker affects the molecular conformation and the exposition of the Fc centers to the electrolyte.

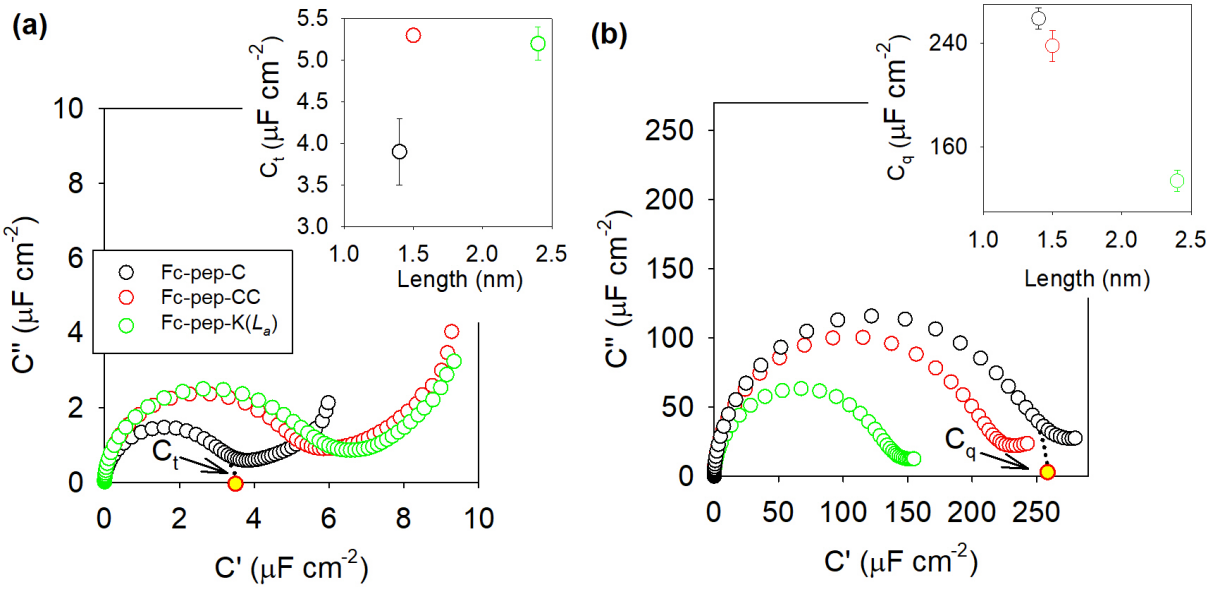

Figure 4.3: Capacitive Nyquist diagrams for Fc-pep-C, Fc-pep-CC, and Fc-pep-(KL_a) SAMs, acquired (a) at V_{out}, where C_t of the non-faradaic response is determined at where the semicircle closure, and (b) at 0.36 V, 0.34 V, and 0.33 V, respectively, corresponding to the V_F of each SAM, where the faradaic C_q response is addressed. The inset in (a) and (b) show C_t and C_q as function of the estimated length, respectively. The plots are representative (average) C^* diagrams of modified electrodes for each peptide SAM performed on three different modified electrodes for each SAM. The C_t values are presented in appendix I.

Source: Author

Within the framework of QRT, k can be evaluated independently of other parameters providing deeper insight into the role of the linker group in modulating the ET process. By comparing the k values obtained from the QR method, using both CV and ECS for addressing C_q, with those derived from Laviron's method, it was found that the fastest ET process occurred in the peptide Fc-pep-K(L_a), whereas the slowest was in Fc-pep-C (see Table 4.4). However, considering the standard error, when k was derived from CV measurements, either using the QR method or Laviron's approach, there was no significant difference in k between Fc-pep-C and Fc-pep-CC with the QR method, nor between Fc-pep-C, Fc-pep-CC, and Fc-pep-K(L_a) using Laviron's method. As discussed in Chapter 2, the QR method's kinetic equation, grounded in quantum mechanics, treats ET as a quantum event influenced by

the confined environment and electrode structure. While CV-based determination of C_q has limitations, ECS provides greater precision, leading to more accurate k.

The k values determined from the equivalent circuit analysis of ECS data using the QR method reveal differences among the three peptide SAM structures, as shown in Table 4.5, where k was lower for the monodentate Fc-pep-C SAM compared to the bidentate Fc-pep-CC and Fc-pep-K(L_a) SAMs. Notably, the highest k value was unexpected found for Fc-pep-K(L_a), despite its longer alkyl chain, which increases tunneling distance. However, the finding aligns with the fact that k is also inversely dependent of $C_q \propto N$ and so k also depends on the DOS and not only on the coupling κ parameter that controls the tunneling distances. In summary, while the electronic coupling is important for modulating the ET dynamics, the results and the QRT demonstrates the ability of the method to evaluate the influence of the different parameters separately, suggesting the importance of the DOS contribution besides the coupling κ.

Table 4.5: Parameters related with the ET, within the QRT approach. k values were calculated using Eq. 1.5. Equivalent circuit elements, such as C_q, as well as R_s and R_{qt} (see Table I.1, of appendix. I) used to determinate R_q according to $R_q = 2\pi(R_s + R_{qt})$, were obtained by fitting the raw impedance data using the equivalent circuit shown in Figure 2.2 for the three SAMs

Parameter	Fc-pep-C	Fc-pep-CC	Fc-pep-K(L_a)
C_q (μF)	12.7 ± 0.6	9.9 ± 0.8	6.5 ± 0.0
$R_q(k\Omega)$	13.40 ± 0.23	12.6 ± 0.1	12.6 ± 0.6
G (μS)	78 ± 6	77 ± 4	79 ± 4
k (s^{-1})	12.3 ± 1.4	15.6 ± 0.6	24.2 ± 1.2
N (x10^{12} states)	8.2 ± 0.4	6.4 ± 0.5	4.0 ± 0.4
κ (x10^{-13})	1.2 ± 0.1	1.6 ± 0.1	2.5 ± 0.1

4.3.2 The effect of the bridge structure in the ET dynamics

Four ferrocene-tagged peptide structures with varying numbers and types of amino acids were designed and synthesized with the aim of assessing how these chemical structural variations in the bridge of the SAMs affects the redox activity and the overall kinetics of the ET reaction. These changes were expected to influence the peptides' interactions with the electrode surface and surrounding medium with consequences in electron tunneling coupling between the redox center and the electrode.

By comparing peptides with different structures, we aimed to clarify how these modifications impact the ET process and to better understand the role of peptide-bridge in electron transfer kinetics.

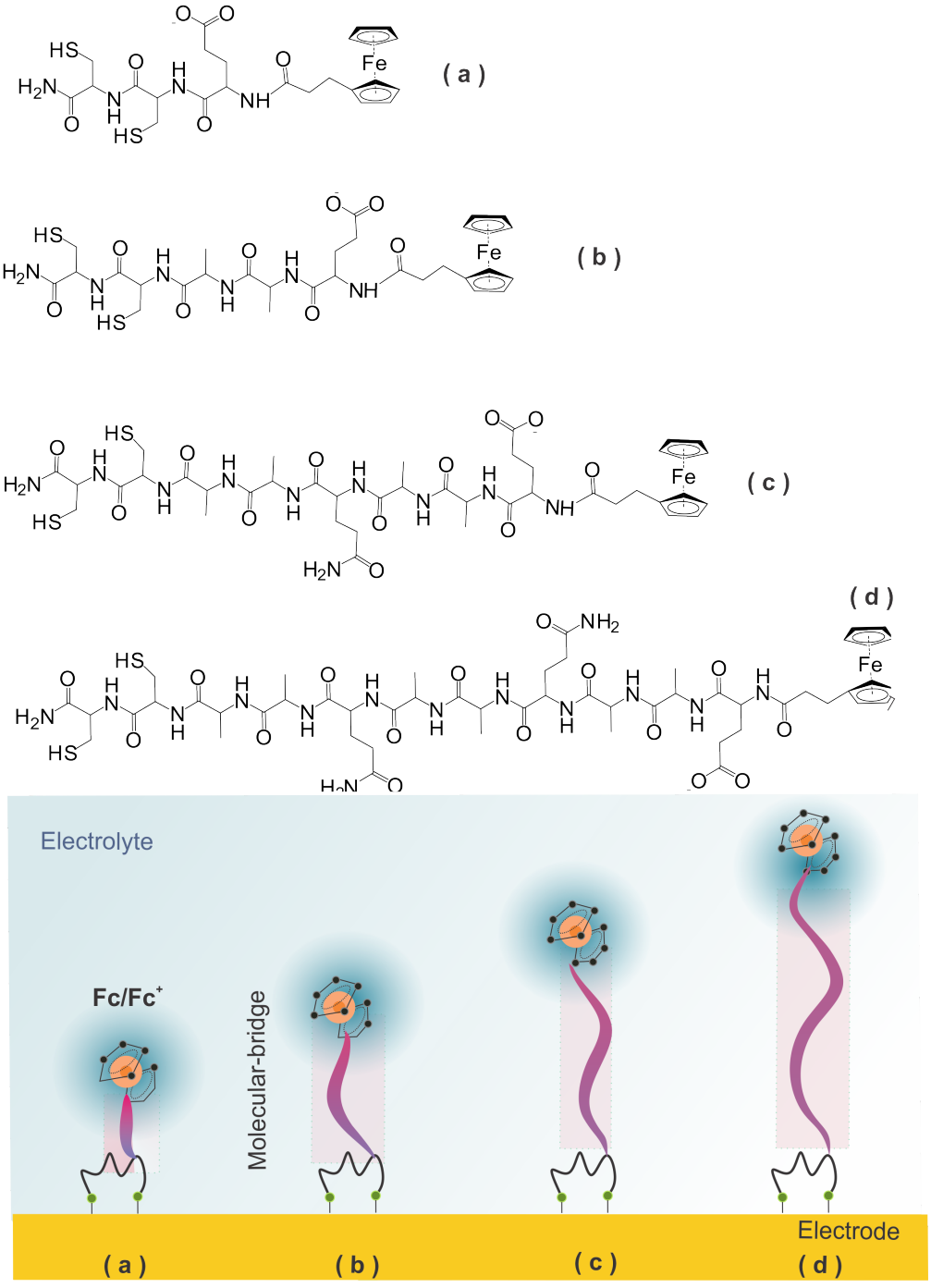

Figure 4.4: On the top, the skeletal structures of the four peptide featuring a bridge structure composed with different type and number of amino acids: (a) Fc-3aa, (b) Fc-5aa, (c) Fc-8aa, and (d) Fc-8aa, which are forming SAMs on gold electrode, illustrated on the bottom. Although the illustration depicts all four peptides anchored to the same electrode, in practice, separate SAMs were formed for each peptide.

Source: Author (2024)

The peptide Fc-EAACC, referred here to as Fc-5aa, was selected as the reference

structure for designing the three other peptides used in this study. This peptide structure contains two Cys residues capable of forming two bonds with the electrode. A shorter peptide Fc-ECC, denoted as Fc-3aa, was designed with only three amino acids: two Cys residues acting as the linker group and a Glu with a free carboxyl group on its side chain, while its N-terminus was functionalized with a Fc moiety. The third peptide, Fc-EAAQAACC, referred to as Fc-8aa, consists of eight amino acids. It was built using the initial sequence of the model peptide Fc-EAA, with the addition of a glutamine (Gln, Q) residue, and ends with the sequence AACC, where two Cys residues served as the electrode-bridge linker. The longest peptide, Fc-EAAQAAQAACC (denoted Fc-11aa), contains eleven amino acids that include two Gln residues, which was specifically chosen due to its ability to form hydrogen bonds via its side chain, which features an amide group spaced by two methylene groups (-CH_2-).

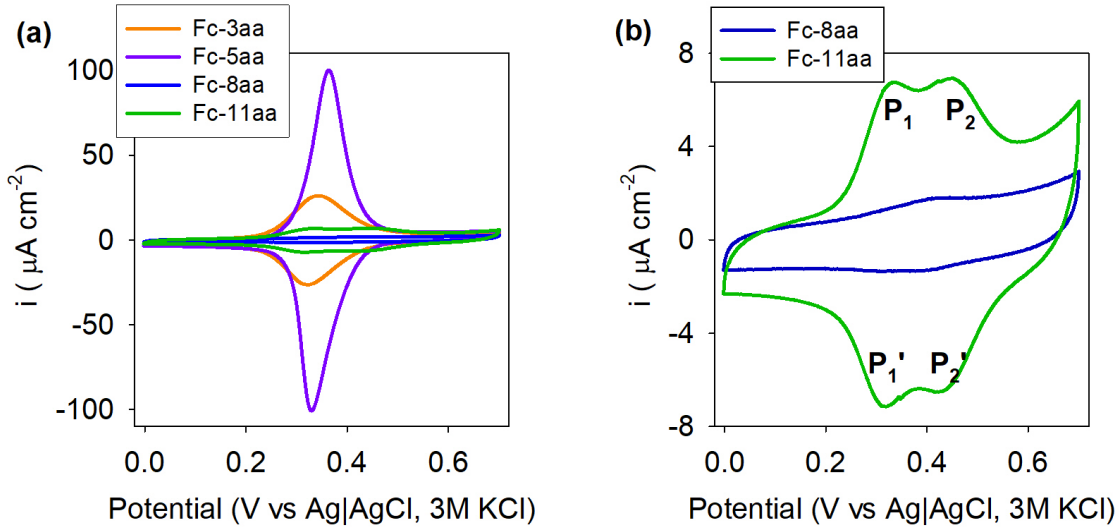

Figure 4.5: (a) CVs of Fc-3aa, Fc-5aa, Fc-8aa, and Fc-11aa redox-tagged peptides SAMs recorded at 0.4 V s^{-1}. (b) CVs of Fc-8aa and Fc-11aa SAMs, which exhibited the lowest oxidative and reductive i within the four SAMs analyzed in this study. The $i - V$ curves shown in both plots are representative (average) of each SAM analyzed over three separate gold electrode.

Source: Author (2024)

CV analysis, such as performed in the previous section, confirmed the successful formation of redox-tagged peptide SAMs by noting the linear relationship between i and s, derived from CVs at low s (Appendix M). Figure 4.5 *a* presents the CV recorded at 0.4 Vs^{-1}, which was selected for the classical electrochemical characterization of the ET process. This specific s was chosen for comparison purposes, as peptide SAMs with a higher number of amino acids did not show well-defined redox peaks at lower scan rates. The parameters related to electrochemical reversibility are summarized in Table 4.6, while Figure 4.5 displays representative CVs obtained from triplicate experiments for each SAM, which reveal a symmetric Gaussian profile for both anodic

and cathodic processes, centered around the V_{pa} and V_{pc} potentials, with ΔV ranging from 11 to 33 mV and i_a/i_c ratio close to the unity, suggesting a quasi-reversible ET dynamics for Fc-3aa and Fc-5aa SAMs (see Table. 4.6).

The current-potential curve for Fc-8aa SAM exhibits a significant capacitive contribution associated with oxidation and reduction peaks centered around the V_F with a lower reversibility noted by i_a/i_c = 0.6, which is attributed to a highly disordered SAM. The higher intensity of the oxidation peak compared to the reduction peak suggests an asymmetry in the kinetics between $Fc \rightarrow Fc^+ + e^-$ and $Fc^+ + e^- \rightarrow Fc$. The V_F of the SAM containing the peptide with eight amino acids, was higher compared to the SAM of peptide with fewer amino acids, suggesting that more energy is required to align the energy states of the electrode with those of the redox species in the SAM, whereas no significant differences were observed between the V_F values of Fc-3aa and Fc-5aa SAMs.

Table 4.6: Criteria parameters of reversibility obtained from CV profiles of ferrocene-tagged peptide SAMs with different number and nature of amino acids. ND represent the "not determined" parameters which could not be determined owing to experimental constraints.

Peptide	i_{pa}/i_{pc}	V_F	ΔV_p	FWHM
		mV		
Fc-3aa	0.98 ± 0.01	337 ± 4	11 ± 3	70 ± 6
Fc-5aa	0.98 ± 0.01	344 ± 9	33 ± 1	70 ± 1
Fc-8aa	0.6 ± 0.2	400 ± 12	24 ± 10	121 ± 13
Fc-11aa	ND	316 ± 9	15 ± 2	ND
	ND	442 ± 6	18 ± 5	ND

To analyze the parameters that describes the reversibility of the redox reaction of peptide SAMs with eleven amino acids, the process observed in the CVs were deconvoluted, as shown in Figure 4.6, and the observed response was attributed to the presence of two distinct SAM structures, as a result of the presence of an additional specie, as residue of the synthesis, as confirmed in the HPLC analysis obtained after the purification step (see Appendix L). Additionally, the presence of the amino acid Gln in the bridge appears to contribute to this heterogeneity, influencing the ET dynamics. The synthesis of cysteine-containing peptides presents challenges due to the inherent reactivity of sulfur in the side chain, which promotes disulfide bond formation during cleavage, extraction, and purification. This process complicates chromatographic separation between monomeric and dimeric species, ultimately reducing reaction yields. While disulfide bonds can be cleaved during self-assembly through interactions with gold atoms, as observed when L_a is used as a linker group,

the initial presence of dimeric species may still influence the final SAM organization. Furthermore, the presence of Gln generates structural effects in the SAM due to the amide group in its side chain that can participate in hydrogen bonding (PUNIHAOLE *et al.*, 2018), while its methanediyl (-CH_2-) group contributes to hydrophobic interactions (CHEN *et al.*, 2018), both of which can impact the arrangement of neighboring molecules in the SAM. In Fc-11aa, these structural effects appear to drive SAM reorganization, giving rise to two well-defined ET processes that are more pronounced than those observed in shorter peptide SAMs, such as Fc-8aa.

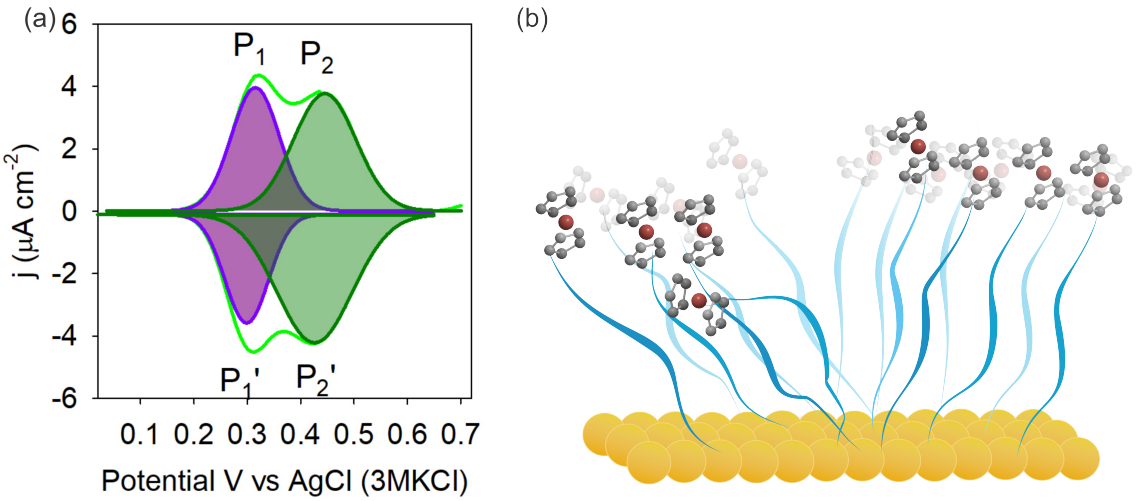

Figure 4.6: (a) CV of Fc-11aa showing two Gaussian-like peaks, referred to as P_1 and P_2, with P_1 exhibiting a lower V_F than P_2. The capacitive i contribution of each peak was subtracted from the total i to isolate the pure faradaic capacitive from the non-faradaic parasitic response. (b) Shows a schematic representation of the Fc-11aa SAM structure on a gold electrode depicting the structural heterogeneity that explains the presence of two redox processes observed in (a).

Source: Author (2024)

ECS analysis were performed at two potentials, V_F and V_{out}, from which a graphical capacitive Nyquist and equivalent circuit fitting analysis were performed for obtained R_q, G, C_q, and k, similarly to the analysis conducted in the previous section. For the Fc-11aa SAM, capacitive Nyquist plots were analyzed at two V_F values associated with P_1 and P_2 redox processes. The equivalent circuit analysis for each processes were evaluated and the relevant parameters are shown in the table. 4.7, in which k was determined using the QR method. The C_q varied across the four SAMs evaluated, as shown in Table. 4.7 *b* and Figure 4.7, with the highest C_q observed for Fc-5aa, while the lowest was obtained for Fc-8aa, with Fc-3aa and Fc-11aa showing intermediate values, but with the value of Fc-3aa higher than Fc-11aa. There was not a correlation between the number of amino acids in the bridge and C_q, as can be noted in the inset of Figure 4.7*b*. Furthermore, in the case of Fc-11aa, the values of C_q

for each P_1 and P_2 process were not significantly different, indicating that both SAMs contributes with an equivalent number of redox states.

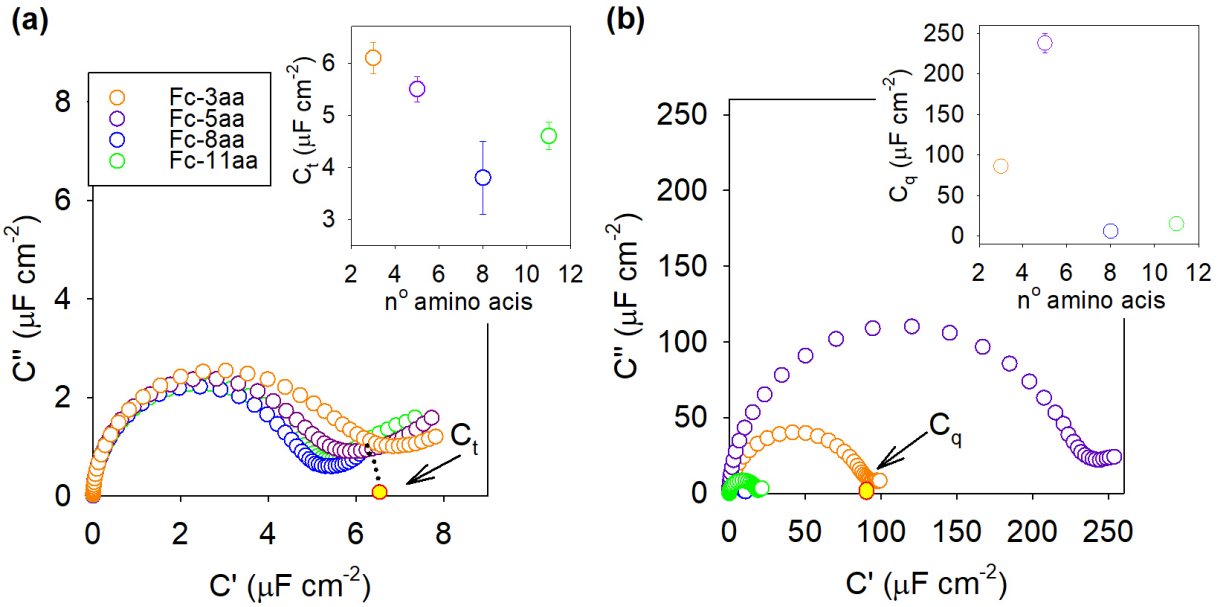

Figure 4.7: Capacitive Nyquist diagrams of SAMs formed by Fc-3aa, Fc-5aa, Fc-8aa, and Fc-11aa peptides, acquired at (a) V_{out} and (b) and V_F. C_t and C_q are determined from the semi-circle closures in (a) and (b). The insets display C_t (a) and C_q (b) as a function of the number of amino acids in each peptide forming the SAM. C^* diagrams correspond to a representative modified electrode of each SAM, but the analysis was conducted in a triplicate, using three independently modified electrodes.

Source: Author (2024)

As expected, note that the highest C_t response was observed for the SAM formed by the peptide containing only three amino acids (see Figure 4.7 *a*), which has the shortest length and, therefore, acted as the least effective insulator, leading to an increased charge storage capacity due to higher ionic permeability (GOES *et al.*, 2012). A general trend of decreasing average C_t with number of amino acids in the bridge (increasing peptide length) can be observed in the inset of Figure 4.7 *a*. However, within the experimental error (Table N.1, appendix N), the differences in C_t values for SAMs formed by peptides containing five, eight, and eleven amino acids are not significant. These results provide insights into the molecular ordering of the Fc-8aa and Fc-11aa SAMs, suggesting that their relatively high C_t values may be associated with structural defects, which enhance ionic permeability and disrupt the expected capacitance trend (GOES *et al.*, 2012).

A well-defined redox SAM should exhibit C_t significantly lower than C_q (BUENO; DAVIS, 2014), as was observed in this study for the Fc-3aa and Fc-5aa SAMs with C_t accounted for only 7% and 2% of C_q, respectively, ensuring that the capacitive response was primarily governed by faradaic processes rather than parasitic non-faradaic contributions (ALARCÓN; SANTOS; BUENO, 2021; SÁNCHEZ; SANTOS;

BUENO, 2022). However, the Fc-8aa and Fc-11aa SAMs exhibited C_t values of $\sim 70\%$ and 33% of C_q, respectively, suggesting that non-faradaic effects plays a significant role in these SAMs, likely due to structural defects and increased ionic permeability both of which contribute to higher C_t. The reduced C_q values observed for these peptides, despite the higher electronic coupling, is associated with a lower DOS. As a result, a quantum characterization of these SAMs is a challenging since the ET dynamics pattern associated with quantum RC states are significantly influenced by classical relaxation processes.

Table 4.7: Parameter related with the ET, within the QRT approach. k values were determined using Eq. 1.5. The resistance R_q was determined as the combined contribution of R_s and R_{qt}, according to $R_q = 2\pi(R_s + R_{qt})$. circuit elements, C_q, R_s, R_{qt}, were obtained by fitting the raw impedance data using the equivalent circuit (see Appendix N, Table. N.1).

Parameter	Fc-3aa	Fc-5aa	Fc-8aa	Fc-11aa
C_q (μF)	4.9 ± 0.2	9.9 ± 0.8	0.26 ± 0.01	0.7 ± 0.1 (P_1)
				0.6 ± 0.1 (P_2)
$R_q(\Omega)$	11,437 $\pm$ 83	12,600 $\pm$ 68	14,107 $\pm$ 736	41,600 $\pm$ 12,260 (P_1)
				40,879 $\pm$ 12,415 (P_2)
G (μS)	88 ± 1	77 ± 4	71 ± 4	24 ± 5 (P_1)
				25 ± 6 (P_1)
k (s^{-1})	36 ± 1	16 ± 1	537 ± 46	67 ± 10 (P_1)
				82 ± 18 (P_1)
N (x10^{12} states)	3.1 ± 0.1	6.4 ± 0.5	0.2 ± 0.0	0.5 ± 0.0
κ (x10^{-13})	3.6 ± 0.1	1.6 ± 0.1	5.4 ± 0.3	7.0 ± 1.0

The quantum nature of G, given by $G = G_0 N \kappa$, was modulated by the number of available ET pathways (N) and the efficiency with which these pathways were utilized, reflected in κ. The values of N varied across different bridge configurations, with the highest observed for Fc-5aa, followed by Fc-3aa, Fc-11aa, and the lowest for Fc-8aa (Table 4.7). Since κ is influenced by both β and L, their interplay was evident in the results, where the obtained values of κ followed the trend: Fc-11aa > Fc-8aa > Fc-3aa > Fc-5aa (Table 4.7). An exponential decay of κ with increasing peptide sequence length was expected, following $\kappa = \exp(-\beta L)$ (MARCUS, 1964) under the assumption that L increases with the number of amino acids[2] and that β remains constant. However, the observed trend deviates from this expectation, suggesting

[2]The L was estimated based on the peptide's extended length obtained from the PyMol program, with values of 1.2 nm, 1.8 nm, 2.8 nm, and 3.5 nm for Fc-3aa, Fc-5aa, Fc-8aa, and Fc-11aa, respectively. However, this estimation does not account for molecular interactions that influence peptide conformation in a real environment. For instance, MD simulation Fc-5aa yielded an L of 1.5 nm, compared

that additional factors, related to the energy barrier, influence the electronic transmission through N. One possible explanation is that the chemical composition of the peptide subtly alters the SAM environment, which, despite being a minor effect, can significantly impact κ due to its exponential dependence on β. specifically, the longer peptides, Fc-11aa and Fc-8aa, contain Gln, whose amide side chain is capable of forming hydrogen bonds, which may introduce a secondary structural framework that influences peptide folding and rigidity (MATSUSHITA; UJI; KIMURA, 2018; ZHU *et al.*, 2023; HUANG *et al.*, 2019; BELDING *et al.*, 2021), potentially altering β, and, consequently, κ. These findings highlight the complexity of ET processes in peptide-based SAMs, where sequence-dependent conformational effects and intermolecular interactions play a crucial role in modulating electrodynamics.

Finally, k was determined and analyzed following the QRT approach with the peptide comprising eight amino acids exhibiting the highest k value of 537 s^{-1}, followed by the Fc-11aa SAM, with 67 s^{-1} and 82 s^{-1} for the P_1 and P_2 processes, respectively. The lowest k of 16 s^{-1} was obtained for the Fc-5aa SAM, while the Fc-3aa SAM exhibited 36 s^{-1}. Interestingly, k was found to be inversely related to N, which accounts for the total DOS at the Fermi level, obtained from C_q. In other words, systems with a greater number of accessible electronic states exhibited lower ET rates (Table 4.7), underscoring the pivotal role of electronic structure in modulating kinetics of ET dynamics. Interestingly, while κ, the electronic coupling factor, plays a crucial role in ET, it does not exhibit a straightforward direct correlation with k, as was observed for the linker group study presented in the prior section. This finding suggests that the primary limiting factor is not the efficiency of electron tunneling through a given pathway but rather the fundamental availability of these pathways for ET. The observed correlation between k and C_q reinforces the significance of the QRT framework in capturing the intricate electronic structure contributions and different nuances the influence the ET. Hence, QRT provides a more comprehensive understanding of ET dynamics in molecular systems beyond traditional length-dependent (purely tunneling) interpretations.

4.4 Conclusion

This study provides a comprehensive investigation of the ET dynamics of redox-tagged peptide SAMs investigated through the application of the QRT, which offers a way of investigate how ET dynamics is influenced by the structure and assembly to the electrode by analyzing G, C_q and κ parameters, unraveling the intricate relationship between molecular structure, charge transport efficiency (through the electronic

to its PyMol estimate of 1.8 nm, a 0.3 nm discrepancy due to factors such as Lennard-Jones potentials and solvent effects

coupling) and DOS within non-adiabatic ET dynamics. Through a systematic variation of the linker groups and peptide bridge compositions, it was possible to identify some factors that influence ET electrodynamics.

The findings reveal that the total DOS, quantified by N at the Fermi level (obtained from C_q) is the dominant factor controlling ET rates. Both the linker group and the chemical composition of the peptide bridge significantly influence the total DOS, demonstrating that systems with a higher density of accessible states exhibit increased ET rates, whereas those with lower N shows a marked reduction in k. Although electronic coupling, analyzed through κ, was initially expected to play a crucial role in ET electrodynamics, its impact was system-dependent and not evident in all of the situations studied. In the case of linker group variation, bidentate linkers enhanced electronic coupling, leading to higher k. However, for variations in the peptide bridge structure, no direct correlation between k and κ was observed, indicating that the total DOS, rather than electronic coupling, governs the ET dynamics in these systems. These findings not only provide deeper mechanistic insights into ET at the molecular level but also establish a foundation for the rational design of electronic interfaces, in which the QRT model applies with advantages of permitting to test how above-mentioned parameters influences ET efficiency and dynamics in a heterogeneous settings, beyond those predicted by classical ET theories.

References

ALARCÓN, E. V. G.; SANTOS, A.; BUENO, P. R. Perspective on quantum electrochemistry. A simple method for measuring the electron transfer rate constant. **Electrochimica Acta**, Elsevier, v. 398, p. 139219, 2021.

ARIKUMA, Y. *et al.* Electron hopping over 100 Åalong an α helix. **Angewandte Chemie International Edition**, Wiley Online Library, v. 49, n. 10, p. 1800–1804, 2010.

ARIKUMA, Y. *et al.* Ultra-long-range electron transfer through a self-assembled monolayer on gold composed of 120-Å-long α-helices. **Langmuir**, ACS Publications, v. 27, n. 4, p. 1530–1535, 2011.

BAYLY, C. I. *et al.* A well-behaved electrostatic potential based method using charge restraints for deriving atomic charges: the RESP model. **The Journal of Physical Chemistry**, ACS Publications, v. 97, n. 40, p. 10269–10280, 1993.

BELDING, L. *et al.* Conformation, and charge tunneling through molecules in SAMs. **Journal of the American Chemical Society**, ACS Publications, v. 143, n. 9, p. 3481–3493, 2021.

BERENDSEN, H. J.; SPOEL, D. van der; DRUNEN, R. van. GROMACS: A message-passing parallel molecular dynamics implementation. **Computer Physics Communications**, Elsevier, v. 91, n. 1-3, p. 43–56, 1995.

BRANDÃO, S. T. *et al.* Designing Quantum Capacitive Peptide Interfaces for Electroanalytical Applications. **Analytical Chemistry**, ACS Publications, v. 95, n. 36, p. 13470–13477, 2023.

BROOKSBY, P. A. *et al.* Voltammetric and electrochemical impedance study of ferrocenyl containing β-peptide monolayers on gold. **The Journal of Physical Chemistry C**, ACS Publications, v. 115, n. 15, p. 7516–7526, 2011.

BUENO, P. R.; DAVIS, J. J. Elucidating redox-level dispersion and local dielectric effects within electroactive molecular films. **Analytical Chemistry**, ACS Publications, v. 86, n. 4, p. 1997–2004, 2014.

CHEN, Y. *et al.* Neglected hydrophobicity of dimethanediyl group in peptide self-assembly: a hint from amyloid-like peptide GNNQQNY and its derivatives. **The Journal of Physical Chemistry B**, ACS Publications, v. 122, n. 46, p. 10470–10477, 2018.

CORDES, M.; GIESE, B. Electron transfer in peptides and proteins. **Chemical Society Reviews**, Royal Society of Chemistry, v. 38, n. 4, p. 892–901, 2009.

ECKERMANN, A. L. *et al.* Electrochemistry of redox-active self-assembled monolayers. **Coordination Chemistry Reviews**, Elsevier, v. 254, n. 15-16, p. 1769–1802, 2010.

FELICIANO, G. T.; BUENO, P. R. Two-Dimensional Nature and the Meaning of the Density of States in Redox Monolayers. **The Journal of Physical Chemistry C**, ACS Publications, v. 124, n. 27, p. 14918–14927, 2020.

GARROTE, B. L.; LOPES, L. C., *et al.* Label-free ADAM10 capacitive assay for the early diagnosis of Alzheimer's disease. **Sensors and Actuators B: Chemical**, Elsevier, p. 137208, 2024.

GARROTE, B. L.; SANTOS, A.; BUENO, P. R. Label-free capacitive assaying of biomarkers for molecular diagnostics. **Nature Protocols**, Nature Publishing Group UK London, v. 15, n. 12, p. 3879–3893, 2020.

GARROTE, B. L.; SÁNCHEZ, Y. P., *et al.* Electron transmittance by means of quantum capacitive states as a signal amplification mechanism for biosensing applications. **Sensors and Actuators B: Chemical**, Elsevier, v. 399, p. 134786, 2024.

GOES, M. S. *et al.* A dielectric model of self-assembled monolayer interfaces by capacitive spectroscopy. **Langmuir**, ACS Publications, v. 28, n. 25, p. 9689–9699, 2012.

GRAY, H. B.; WINKLER, J. R. Electron flow through proteins. **Chemical physics letters**, Elsevier, v. 483, n. 1-3, p. 1–9, 2009.

HAN, B. *et al.* Systematic modulation of charge transport in molecular devices through facile control of molecule–electrode coupling using a double self-assembled monolayer nanowire junction. **Journal of the American Chemical Society**, ACS Publications, v. 142, n. 21, p. 9708–9717, 2020.

HORNAK, V. *et al.* Comparison of multiple Amber force fields and development of improved protein backbone parameters. **Proteins: Structure, Function, and Bioinformatics**, Wiley Online Library, v. 65, n. 3, p. 712–725, 2006.

HUANG, X. *et al.* Exploring the enhancement of electron tunneling induced by intermolecular interactions on surface of self-assembled monolayer. **Journal of Electroanalytical Chemistry**, Elsevier, v. 837, p. 143–150, 2019.

JORGENSEN, W. L.; TIRADO-RIVES, J. The OPLS [optimized potentials for liquid simulations] potential functions for proteins, energy minimizations for crystals of cyclic peptides and crambin. **Journal of the American Chemical Society**, ACS Publications, v. 110, n. 6, p. 1657–1666, 1988.

JUHANIEWICZ, J.; PAWLOWSKI, J.; SEK, S. Electron transport mediated by peptides immobilized on surfaces. **Israel Journal of Chemistry**, Wiley Online Library, v. 55, n. 6-7, p. 645–660, 2015.

KRAATZ, H.-B. *et al.* Electron transfer through H-bonded peptide assemblies. **The Journal of Physical Chemistry B**, ACS Publications, v. 108, n. 52, p. 20164–20172, 2004.

LAVIRON, E. Surface linear potential sweep voltammetry: Equation of the peaks for a reversible reaction when interactions between the adsorbed molecules are taken into account. **Journal of Electroanalytical Chemistry and Interfacial Electrochemistry**, Elsevier, v. 52, n. 3, p. 395–402, 1974.

MANDAL, H. S.; KRAATZ, H.-B. Electron transfer across α-helical peptides: Potential influence of molecular dynamics. **Chemical Physics**, Elsevier, v. 326, n. 1, p. 246–251, 2006.

MARCUS, R. A. Chemical and electrochemical electron-transfer theory. **Annual Review of Physical Chemistry**, v. 15, n. 1, p. 155–196, 1964.

MATSUSHITA, D.; UJI, H.; KIMURA, S. Effect of oscillation dynamics on long-range electron transfer in a helical peptide monolayer. **Physical Chemistry Chemical Physics**, Royal Society of Chemistry, v. 20, n. 22, p. 15216–15222, 2018.

MIURA, Y. *et al.* Formation of oriented helical peptide layers on a gold surface due to the self-assembling properties of peptides. **Langmuir**, ACS Publications, v. 14, n. 24, p. 6935–6940, 1998.

NOSÉ, S. A unified formulation of the constant temperature molecular dynamics methods. **The Journal of chemical physics**, AIP Publishing, v. 81, n. 1, p. 511–519, 1984.

PICCOLI, J. *et al.* Redox Capacitive Assaying of C-Reactive Protein at a Peptide Supported Aptamer Interface. **Analytical Chemistry**, v. 90, n. 5, p. 3005–3008, 2018. ISSN 0003-2700.

PUNIHAOLE, D. *et al.* Interaction enthalpy of side chain and backbone amides in polyglutamine solution monomers and fibrils. **The Journal of Physical Chemistry Letters**, ACS Publications, v. 9, n. 8, p. 1944–1950, 2018.

REDONDO-GÓMEZ, C. *et al.* Peptide-based self-assembled monolayers (SAMs): what peptides can do for SAMs and vice versa. **Chemical Society Reviews**, Royal Society of Chemistry, 2024.

SÁNCHEZ, Y. P.; SANTOS, A.; BUENO, P. R. Quantum Mechanical Meaning of the Charge Transfer Resistance. **Journal of Physical Chemistry C**, v. 126, p. 3151–3162, 6 2022.

SEPUNARU, L. *et al.* Electronic transport via homopeptides: The role of side chains and secondary structure. **Journal of the American Chemical Society**, ACS Publications, v. 137, n. 30, p. 9617–9626, 2015.

SHAH, A. *et al.* Electron transfer in peptides. **Chemical Society Reviews**, Royal Society of Chemistry, v. 44, n. 4, p. 1015–1027, 2015.

TAKEDA, K.; MORITA, T.; KIMURA, S. Effects of monolayer structures on long-range electron transfer in helical peptide monolayer. **The Journal of Physical Chemistry B**, ACS Publications, v. 112, n. 40, p. 12840–12850, 2008.

VERICAT, C. *et al.* Surface characterization of sulfur and alkanethiol self-assembled monolayers on Au (111). **Journal of Physics: Condensed Matter**, IOP Publishing, v. 18, n. 48, r867, 2006.

VON WROCHEM, F. *et al.* Efficient electronic coupling and improved stability with dithiocarbamate-based molecular junctions. **Nature Nanotechnology**, Nature Publishing Group UK London, v. 5, n. 8, p. 618–624, 2010.

WAIN, A. J. *et al.* Influence of molecular dipole moment on the redox-induced reorganization of α-helical peptide self-assembled monolayers: an electrochemical SPR

investigation. **The Journal of Physical Chemistry C**, ACS Publications, v. 112, n. 37, p. 14513–14519, 2008.

WATANABE, J.; MORITA, T.; KIMURA, S. Effects of dipole moment, linkers, and chromophores at side chains on long-range electron transfer through helical peptides. **The Journal of Physical Chemistry B**, ACS Publications, v. 109, n. 30, p. 14416–14425, 2005.

ZHU, X. *et al.* Charge migration of ferrocene-labeled peptide self-assembled monolayers at various interfaces: The roles of peptide composition. **Electrochimica Acta**, Elsevier, v. 454, p. 142419, 2023.

Chapter 5

Design and synthesis of *push-pull* heterocyclic molecules aiming for sensing applications

The ability to experimentally investigate the electronic behavior of nanoscopic systems in electrolyte environments represents a significant advantage of QRT over classical approaches, offering a framework for exploring electrodynamics in confined nanostructures such as graphene (LOPES; SANTOS; BUENO, 2021), quantum dots (PINZÓN *et al.*, 2024), and *push-pull* heterocyclic structures assembled over electrodes (NIETO *et al.*, 2024). These systems provide crucial insights into intrinsic electrodynamic properties, enabling a deeper understanding of charge transport processes at nanoscale interfaces. The application of the quantum RC model has proven particularly valuable in analyzing electronic communication within these interfaces, a fundamental step for the development of advanced sensing platforms, where changes in the electronic structure — such as those induced by biological recognition events — can be measured and used as transduction signals for sensing.

This chapter focuses on the design and synthesis of *push-pull* heterocyclic molecules with tailored structural features that enable their assembly on electrodes, such as gold and graphene, which is imperative for the study of their electrodynamic properties via QRT and their potential use in sensing applications. *Push-pull* heterocyclic molecules, defined as *D*-π-*A*, are π-conjugated systems, constituted by a π-bridge/spacer end-capped with an electron donor (*D*) and an electron acceptor (*A*) group, exhibit remarkable electronic properties due to their enhanced charge delocalization (BUREŠ, 2014). Despite synthesis challenges — such as the low solubility of the recognition/chemosensor cores and the instability of thiol protective groups — a viable route was developed to obtain molecules capable of forming assemblies on gold electrodes. Moreover, the synthesis of heterocyclic molecules designed for graphene- based assembly was successfully achieved by incorporating reactive head

groups, such as carboxylic acids, which are crucial for subsequent sensing modifications. The results of this chapter culminated in the filing of a patent entitled "*Attomolar Sensors and Applications of Photoelectric Devices with Quantum Resistive-Capacitive (RC) Transducer Signal from Single-Layer Graphene (SLG) Modified with Organic Semiconductor Quantum Dots*", which underscores the novelty and applicability of the molecular design strategy for graphene-based platforms and highlights the use of QRT to access the quantum properties and electronic structure.

Thus, this chapter has two primary objectives:

- ☑ To design and synthesize *push-pull* heterocyclic molecules with anchoring groups that facilitate their confinement on electrode surfaces, enabling access to their quantum electrodynamic properties through QRT and QRS.
- ☑ To incorporate functional head groups, such as carboxylic acids, into the chemical structure of *push-pull* heterocyclic molecules, enhancing their potential as (bio)sensing platforms.

5.1 Introduction

The DOS is a key concept in quantum mechanics, reflecting the number of available quantum-mechanical states within a given E range and is directly associated with electronic properties of a systems. The DOS, expressed as dn/dE, directly influences ν, and is closely related to C_q through the relationship DOS $= C_q/e^2 = dn/dE$ (see section 1.4, chapter 1). This connection highlights the fundamental interplay between the electronic structure of the system and its capacitance (BUENO, 2018). Using QRS, an experimental technique grounded in QRT, researchers can probe the DOS by applying a sinusoidal wave potential at a given ν (BUENO *et al.*, 2021; PINZÓN *et al.*, 2024; LOPES; PINZÓN, *et al.*, 2024; NIETO *et al.*, 2024). Time-dependent perturbations in the electronic states allow the determination of C_q, offering insights into the system's electronic structure. To accurately interpret the experimentally measured C_q at laboratory conditions, the statistical Fermi–Dirac distribution function $f(E) = [1 + \exp(-E/k_BT)]$ is used, as it describes the thermal distribution of electrons among the total available N. The C_q is then expressed as $C_q = e^2Nf(1-f)$, reflecting the temperature-dependent occupancy of quantum states. This method provides a direct means of studying the DOS under ambient conditions, making it a versatile tool for investigating electronic properties in electrolyte medium.

QRT is not limited to studying ET processes involving redox reactions and faradaic currents, such as those observed in redox-peptide SAMs, as discussed in previous chapters. It also offers a powerful framework for analyzing systems where ET does not occur and where ET_p is purely adiabatic. QRT has been successfully applied to

study the electrodynamics of various nanostructured materials, including graphene (LOPES; PINZÓN, *et al.*, 2024), quantum dots (PINZÓN *et al.*, 2024), and more recently, *push-pull* heterocyclic molecules that form films on electrodes (NIETO *et al.*, 2024), using QRS methodology. For instance, in graphene, QRS enabled the study of both electron and hole propagation through n, revealing the linear relationship between energy and momentum near the Dirac point (LOPES; PINZÓN, *et al.*, 2024). Similarly, in quantum dots, QRS was used to map discrete energy levels and examine how quantum confinement influences electron transitions, providing valuable information about the HOMO-LUMO gaps and their dependence on particle size (PINZÓN *et al.*, 2024). The unique advantage of QRS lies in its ability to prove these quantum properties under ambient conditions, unlike traditional methods that often require low temperatures or vacuum environments.

In a recent study, QRS was applied to analyze the electrodynamics of an interface composed of a π-conjugated heterocyclic molecule (NIETO *et al.*, 2024), based on pyrrole and thiophene, which simultaneously acts as π-bridge and auxiliary D groups, and a carboxylic group as the A moiety. In this experiment, the *push-pull* heterocyclic molecule was confined to a gold electrode using cysteamine as a linker (See Figure 1.4*a*). The amino group of cysteamine formed an amide bond with the carboxyl group of the *push-pull* heterocyclic molecule, a reaction facilitated by activating the carboxyl group beforehand. Once immobilized on the electrode surface, the system was subjected to a time-dependent potential perturbation of 10 mV (root mean square) around the OCP, a condition where there is no net current flowing in the interface. Unlike the V_F used in redox-active SAMs, such as in Fc-peptide systems discussed in previous chapters, the OCP represents an equilibrium state that even in the absence of a redox event, the applied perturbation induces fluctuations in charge distribution, leading to a measurable capacitance response associated with the perturbation of system, which reflected the electronic properties of the molecular junction as was demonstrated in this work (NIETO *et al.*, 2024). The capacitive behavior was analyzed and the resulting Nyquist plot displayed a semicircle that closed at a characteristic frequency as shown in Figure 1.4*b*, presented in Chapter 1. Once this frequency was identified, it was held constant, and C_q response was recorded as a function of the potential, exhibiting a Gaussian-like shape (see Figure 1.4*c*), characteristic of the DOS distribution that arises from the electronic communication between the electronic states of the π-conjugated heterocyclic molecule and those of the gold electrode. The peak of this curve, corresponds to the Fermi potential of the junction, marking the energy level at which the molecular and electrode states achieve maximum electronic communication, and therefore the maxima of C_q. The adiabatic nature of the process was further confirmed by the conductance value being close to the quantum limit, i.e. $G_0 = 77.5\ \mu$S.

Although the electrodynamic phenomenon is not yet fully understood, this study revealed the electronic states distribution of a particular and intrigued class of π-conjugated molecules. These findings have generated interest in exploring the electronic communication between these molecules and electrode surfaces in greater depth, particularly for potential applications in quantum RC sensing platforms. This aligns with the research group's expertise in nanostructured systems (GARROTE; SANTOS; BUENO, 2020; GARROTE; SÁNCHEZ, *et al.*, 2024; BRANDÃO *et al.*, 2023). An important factor in facilitating this electronic communication, as demonstrated in the study (NIETO *et al.*, 2024), was the confinement of the *push-pull* heterocyclic molecule on the electrode surface. This confinement was achieved using the anchor group, cysteamine, which required a carboxyl group in the *push-pull* heterocyclic molecule for effective bonding. However, for future applications, especially in sensing platforms, it is essential to have a free or accessible carboxyl group, which enable the attachment of biologically relevant molecules, such as DNA or antibodies, thereby advancing the development of biosensors (GARROTE; SANTOS; BUENO, 2020) in an ambient physiological electrolyte environment.

Hence, the work presented in this chapter emerged from the idea of the design and synthesis of *push-pull* heterocyclic molecules capable of forming molecular assemblies on electrodes, such as gold or graphene, with the main goal of accessing electrodynamics information through the QRT in pursuit of sensing platforms. These molecules were specifically designed to incorporate reactive head groups, such as carboxyl groups, which are crucial for constructing sensor platforms. Additionally, an alternative approach was developed by using recognition moieties as the reactive head group, which can coordinate ions. This is particularly interesting, given that one of the most significant applications of these types of π-conjugated heterocyclic organic molecules lies in ion sensing (WANG *et al.*, 2020; FERREIRA; RAPOSO; COSTA, 2018; OKDA *et al.*, 2019; NAITHANI *et al.*, 2023; PALANI; KARPAGAM, 2021; BATISTA; OLIVEIRA, *et al.*, 2007; GONÇALVES *et al.*, 2022), which play a critical role in various fields, including environmental monitoring, biomedical diagnostics, and industrial process control among others. Particularly, it was demonstrated that the successful application of these molecules to modify graphene, allowed a DNA sensing analysis.

5.2 Results and discussion

This section is divided into four main parts. The first two focus on the design and synthesis of molecules containing anchoring groups capable of assembling on electrodes. The third explores the quantum electrodynamics of a coupled molecule-graphene

system, which led to the development of a sensor platform described in the final (forth) part of this section.

5.2.1 Design and synthesis of thiol-modified *push-pull* heterocyclic molecules for assembly on gold electrodes

The design of *push-pull* heterocyclic molecules capable of forming molecular assemblies on a gold surface was inspired by seminal work conducted by Nieto *et al* (NIETO *et al.*, 2024). While this work successfully facilitated the molecule's assembly on the electrode using the carboxylic group and enabled electrodynamic studies through QRT, it also resulted in the unavailability of this group, essential for modifications needed in capacitive biosensors (GARROTE; SANTOS; BUENO, 2020). Consequently, there was a need to design *push-pull* heterocyclic molecules that incorporates a linker group, available for anchoring on gold electrodes, while retaining a free carboxylic acid (or other appropriate group) as the reactive head group of the assembly for further modification. Several important features were considered concerning the design of the desired molecules. Firstly, the functionalization of the molecule with a thiol group, which would allow the anchoring on gold electrodes (MALYTSKYI; SIMON, *et al.*, 2015; LI *et al.*, 2014) using the widely known self-assembly method (ULMAN, 1996). Another key characteristic considered in the design of the molecule was the incorporation of a functional head group, such as a receptor/binding moiety capable of chelating ions or a free carboxylic group, available for bonding with macromolecules with biological interest.

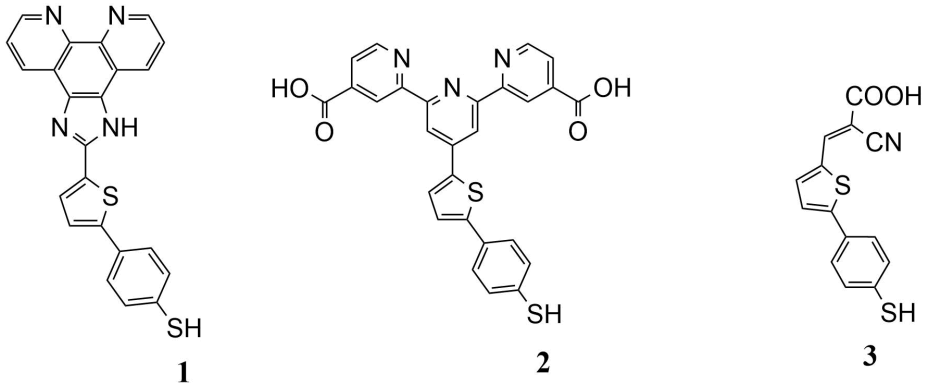

Figure 5.1: *Push-pull* heterocyclic molecules (**1-3**) containing a thiol group for anchoring on gold electrodes. (**1**): 4′-(5-(4-mercaptophenyl)thiophen-2-yl)-[2,2′:6′,2″-terpyridine]-4,4″-dicarboxylic acid; (**2**): 4-(5-(1*H*-imidazo[4,5-*f*][1,10]phenanthrolin-2-yl)thiophen-2-yl)benzenethiol; (**3**): 2-cyano-3-(5-(4-mercaptophenyl)thiophen-2-yl)acrylic acid.

Therefore, three π-conjugated heterocyclic molecules (**1-3**) were designed featuring a thiol group as their primary structural element to enable covalent bonding with

gold electrodes. Thiophenol, which is also an electron *D* group, was chosen as the anchoring group (Figure 5.1). For the π-spacer, linking the *D* to the *A* moiety, we selected the electron-rich thiophene heterocyclic ring, which served a dual role as both a π-spacer and an auxiliary *D* group. Concerning the *A* moieties, which contribute to the recognition/chemosensory properties of the molecular assemblies, we proposed two well-studied heterocyclic cores known for their ability to coordinate anions and cations: imidazophenanthrolines (NAITHANI *et al.*, 2023; BATISTA; COSTA, *et al.*, 2008) and terpyridines (FERNANDES *et al.*, 2018; KANG *et al.*, 2019) (Figure 5.1, compounds **1** and **2**). Additionally, a cyanoacetic acid moiety was chosen for compound **3** (Figure 5.1, compound **3**), due to its carboxyl functionality, which, as previously mentioned, served as a site for bonding with biologically relevant macromolecules. To synthesize the *push-pull* heterocyclic molecules containing the thiol group, two synthetic routes were explored: *Via a* (Scheme 5.1), starting from the larger molecular structures (imidazophenanthroline or terpyridine) and linking them to the smaller benzenethiol moiety, or *Via b*, proceeding from the smaller fragment (benzenethiol) to the larger molecular structures (imidazophenanthroline or terpyridine) (Scheme 5.2).

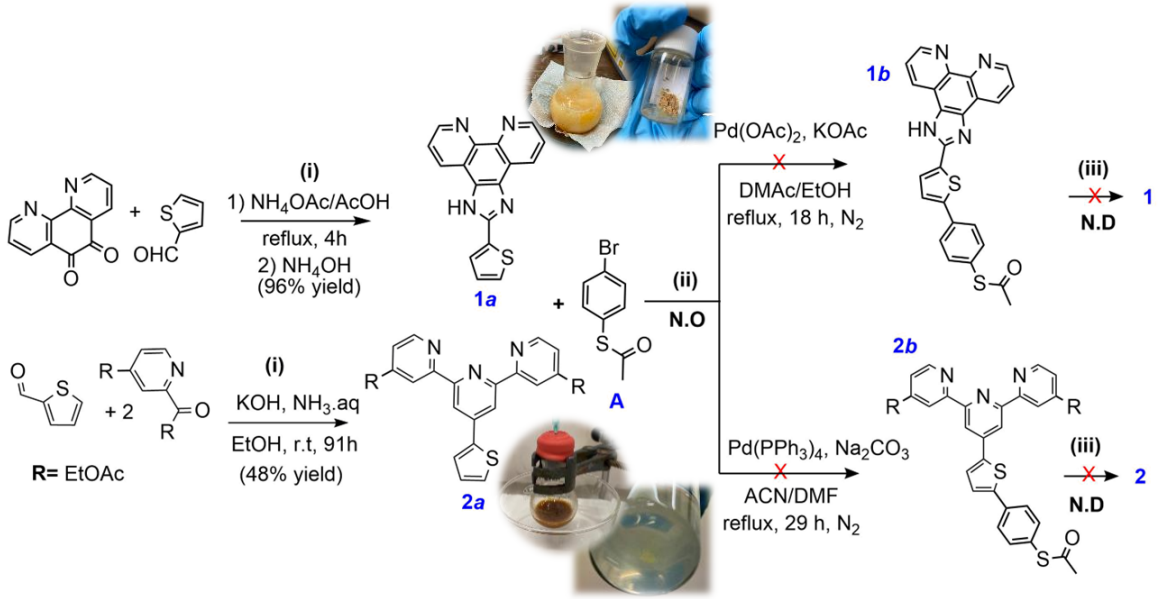

Scheme 5.1: Proposed synthetic route for molecules **1** and **2** planned in three stages. The intermediates **1*a*** and **2*a*** were successfully obtained. The green solid (**2*a***) was insoluble in several solvents, as illustrated in the image. The abbreviation "N.O." indicates that the respective compounds **1*b*** and **2*b*** were not obtained. While "N.D" refers to the step iii (HCl, MeOH, reflux) which was not done.

Via a

The proposed synthetic methodology to obtain compounds **1** and **2** (See Figure 5.1) was constituted by three steps, as shown in scheme. 5.1: i) synthesis of the receptor unity, either imidazophenanthroline (**1*a***) or terpyridine (**2*a***); ii) coupling of these cores to a benzenethiol moiety via direct arylation; and iii) cleavage of the ester groups in the terpyridine derivative, and removal of the S-protecting groups in both compounds. While the first stage was successful, the coupling in step ii) was unsuccessful, and as a result, step iii) was not carried out.

Synthesis of the ionic chemosensor receptors:

The synthesis of compound (**1*a***) was performed using the method proposed by the group of Raposo M.M.M (BATISTA; COSTA, *et al.*, 2008), based on the reaction of Radziszewski (A HERNANDEZ MUNOZ; J JUNIOR; MARTINS DA SILVA, 2014a), resulting in a 96% yield after 4 h of reaction. In the literature, two mechanisms have been proposed for these type of reaction (GELENS *et al.*, 2006). The first mechanism involves the condensation of the dicarbonyl compound with NH_4OAc in acetic acid (AcOH), giving a diamine. This diamine then undergoes further condensation with the aldehyde, which leads to the imidazophenanthroline core. The second proposed mechanism begins with the condensation between the ammonium source and the aldehyde in an acidic medium, forming a protonated aldimine. This protonated aldimine reacts with another equivalent of the ammonium source, generating an intermediate diamino. The diamino then reacts with the diketone, leading to the formation of the imidazole five-membered ring. Despite the mechanism isn't officially defined yet, it is the most common synthesis method to obtain imidazophenanthroline core in high yields (A HERNANDEZ MUNOZ; J JUNIOR; MARTINS DA SILVA, 2014b).

For the synthesis of compound **1*a***, the progression of the reaction was monitored through TLC, revealing a strong orange spot under 245 nm UV lamp after the first hour. The reaction was concluded after 4 h under reflux, being evident the disappearance of the starting reagent in the TLC assay. The pure compound precipitated after neutralization of the reaction medium with NH_4OH. The precipitate was washed with water three times, and after a final wash with ethyl ether, the pure compound was obtained as a yellow-bege solid (See Scheme. 5.1**1*a***), and characterized by ^{1}H NMR analysis in DMSO-d_6 (Figure O.1, Appendix O). The spectrum exhibited characteristic signals corresponding to the presence of 10 protons, with 9 concerning the aromatic rings (7-9 ppm) and 1 signal corresponding to the N*H* proton of the imidazole ring (13.86 ppm).

The 4'-(thiophen-2-yl)-[2,2':6',2''-terpyridine]-4,4''-dicarboxylic acid (compound

2*a*) with free carboxyl groups, was synthesized following a previously reported method (HUSSON; DEHAUDT; GUYARD, 2014). The enolate, derived from ethyl 2-acety- lisonicotinate (the source of acetyl pyridine), was generated by adding KOH under mild conditions. Subsequent aldol condensation with the aldehyde reagent results in the formation of an α,β-unsaturated carbonyl compound, followed by dehydration to yield a conjugated enone. A Michael addition between the enone and a second equivalent of enolate derived from the acetyl pyridine compound proceeds smoothly at room temperature, giving a soluble diketone intermediate. Finally, the central pyridine ring is formed in the presence of the nitrogen source (ammonium hydroxide). After 91 h of reaction, the pure dicarboxylic compound **2***a* was obtained, as a greenish precipitate, which was isolated by filtration and washing with a cool mixture of EtOH/water (yield: 48%). The solid was dissolved in DMSO-d_6, and after adding two drops of TFA to enhance solubility, it was characterized by ^{1}H NMR (Figure O.2, Appendix O). In the ^{1}H NMR spectrum, it was possible to identify the signals of 11 protons in the aromatic region. The characteristic signals include the broad singlet corresponding to 3'-H and 5'-H of the central pyridine ring (8.73 ppm), as well as the three signals concerning the thiophene protons at 7.25-7.28 ppm (m, 4'''-H), 7,78 (dd, 5'''-H), and 8.00 ppm (dd, 3'''-H). The analysis of the ^{1}H NMR spectrum proves that the terpyridine derivative **2***a* was obtained through the synthesis method described previously, in which the hydrolysis of the 2 ester groups occurred simultaneously, since it was not possible to observe the signals in the aliphatic zone (a triplet and a quartet concerning the protons of the OCH_2CH_3 group). The hydrolysis of the ester groups occurred probably due to the basic medium in which the reaction took place.

Direct arylation of chemosensor receptor/binding unity with S-(4-bromophenyl) ethanethioate:

The design of the *push-pull* molecules functionalyzed with a thiol group is a challenging task due to the reactivity of this group. Therefore, the initial decision was to identify a protecting group for the sulfur atom that could be easily cleaved in the final step of the synthesis. It was decided also to begin the synthesis of the receptor/chemosensory unit, and then connect this structure to 4-phenyl ethanethioate through direct arylation. Despite the successful completion of the first stage (See Scheme. 5.1(**1*a***)), attempts to couple the chemosensor/receptor core with the reagent containing the sulfur moiety proved to be unsuccessful.

The strategy for the initial direct arylation aimed at obtaining **1*b*** was based on previously reported synthesis conditions (CHEN *et al.*, 2011). Considering the electronic deficient nature of the heteroaromatic system, an imidazophenantroline bonded at position 2 of the thiophene, these conditions seemed to be appropriate. The resulting crude product was characterized by ^{1}H NMR in DMSO-d_6 (Figure P.1, Appendix P).

The spectrum exhibits the signals of the starting reagent (**1*a***), together with some additional low intensity signals. Several factors may have had an impact in the failure of this reaction. Notably, the reaction temperature exceeded the boiling point of the bromo-aryl reagent, which would have affected the stability of this precursor. In fact, the instability of the S-protecting group was observed under these reaction conditions in the TLC assay (See Figure 5.2 *a*), where a spot corresponding to 4-bromobenzenethiol was detected after the first hour of the reaction.

Considering these potential factors, a modification was made to the strategy for the second direct arylation coupling in order to obtain the molecule **2*b*** (See Figure 5.1). The attempt was conducted using conventional Suzuki-Miyaura reaction conditions in the solvent mixture ACN/DMF at 80 °C. However, after characterization by ^{1} H NMR (Figure P.2, Appendix P), it was concluded that the reaction did not proceed because the signals in the ^{1}H NMR spectrum correspond to the precursor **2*a***. One initial issue observed was the low solubility of the starting reagent **2*a*** in several solvents (See Figure 5.2*b*), even in the chosen solvent mixture. Although the reaction temperature was below the boiling point of the bromo-aryl reagent, a TLC assay after 2 h revealed a spot corresponding to the S-unprotected reagent **B**, together with a smaller amount of the protected reagent **A** (See Figure 5.2*b*). This cleavage could be attributed to the presence of H_2O in the standard Suzuki conditions, which involve an aqueous solution of Na_2CO_3 (2 M).

Via b

Due to the impossibility of synthesizing compound **1** through the precursor **1*b***, using *Via a* (Scheme. 5.1), an alternative approach was devised (Scheme. 5.2) in order to obtain the target molecule **1** (Figure 5.1). At this time, it was decided to initiate the Suzuki-Miyaura coupling in order to form the C-C bond between the bromo aryl reagent containing the protected-S (**A**) and the 5-formyl-2-thienylboronic acid. Subsequently, the imidazophenanthroline moiety would be synthesized from the aldehyde precursor (**1***b-1*). The proposed strategy had in mind surrounding the need for compound purification until the final stage, when typically the product precipitates under condensation conditions.

Although an attempt to couple the bromo-aryl compound with the thiophene moiety occurs under standard Suzuki-Miyaura conditions, the product was obtained only in a vestigial amount together with some impurities even after purification (see ^{1} H NMR spectrum Figure Q.1, AppendixQ). The ^{1}H NMR spectrum in $CDCl_3$ revealed the presence of the aldehyde proton signal, 8 protons in the aromatic region, and protons in the aliphatic region due to the methyl group together with impurities. Despite of the presence of some impurities, the distinct signals of thiophene

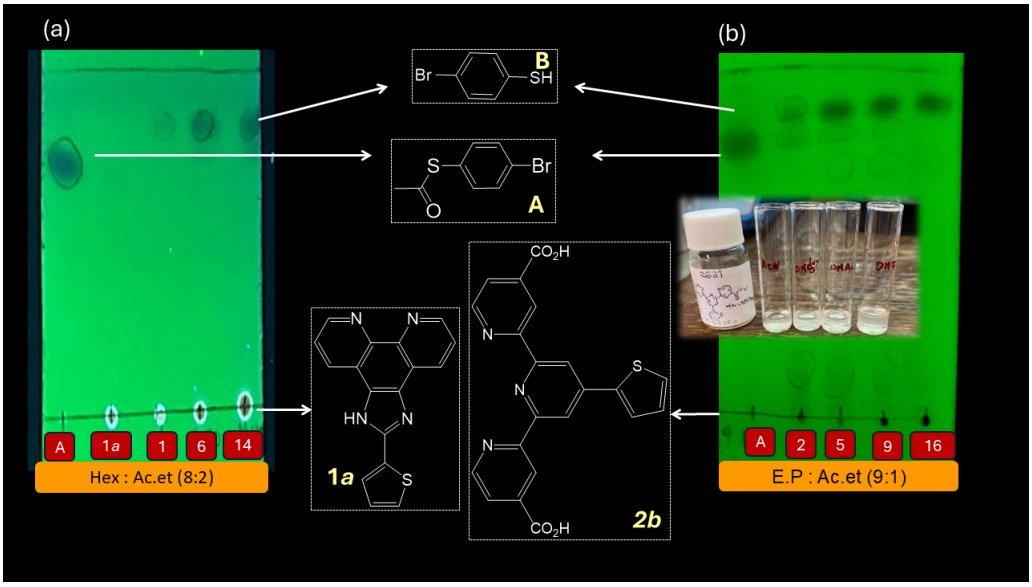

Figure 5.2: TLC performed for the second step of the synthesis (ii, Scheme- 5.1) to obtain compounds **1*b*** (a) and **2*b*** (b). The red squares, in the starting region of the plate, indicate the reaction time in hours and the starting reagents/precursors, **A** and **B**. Reagent **A** is the bromo-aryl molecule with an S-protecting acetyl group. In the case of the synthesis of **1*b***, the limiting reagent, **A**, fully decomposed to the S-deprotected bromo-aryl molecule (**B**) after 1 h of reaction. Concerning the synthesis of **2*b***, total decomposition of **A** occurred after 5 h under different reaction conditions. The eluents used for the TLCs were: (a) a mixture of Hex and A.C. et in a 8:2 ratio; (b) E.P and EtOAc 9:1. The photo inset in (b), shows the poor solubility of the started reagent **2*a***, in various organic solvents, including ACN, DME, DMAc, and DMF.

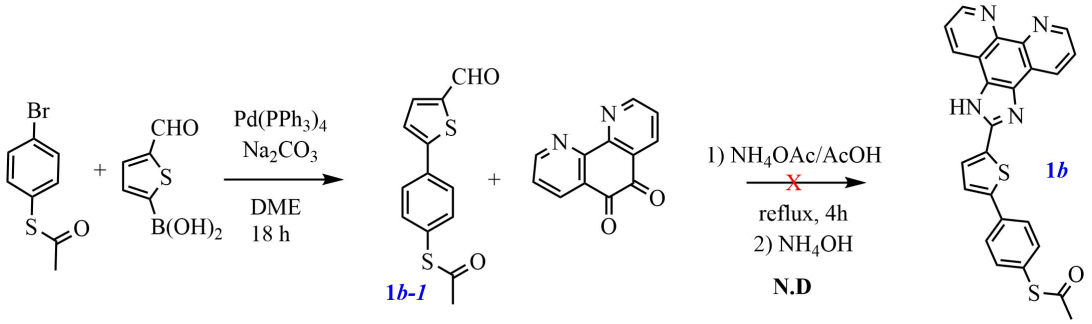

Scheme 5.2: New proposal for a synthetic route to prepare molecule **1** through precursor **1*b*** (Figure 5.1). The abbreviation "N.D." signifies that the corresponding step was "Not Done".

and benzene protons were identified, with coupling constants of J=4 Hz and J=8.8 Hz, respectively, along with the signal of the CH_3 group at lower ppm values. The TLC assay (Figure 5.3) revealed that the S-protecting group of S-(4-bromophenyl) ethanethioate (**A**) began to cleave after 4 h of reaction and was completely removed after 18 h. Therefore, only a vestigial amount of the product was obtained after purification, rendering this route impractical for synthesizing the compound.

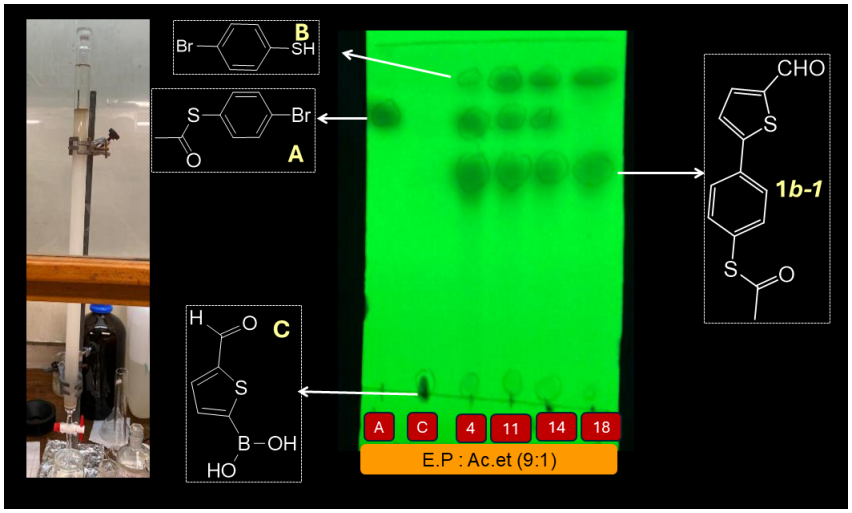

Figure 5.3: TLC conducted during the synthesis of compound **1***b-1*. The red squares, in the starting region of the plate, indicate the reaction time in hours (4, 11, 14, and 18 h) and the starting reagents/precursors, *S*-(4-bromophenyl) ethanethioate (**A**) and 5-formyl-2-thiopheneboronic acid (**C**). After 4 h of reaction, the decomposition of the S-protecting group in (**A**) into the deprotected thiol compound **B** was observed. The reaction mixture was purified with eluent: P.E and EtOAc in a 9:1 ratio.

The S-protecting group stable under Suzuki-Miyaura condition:

The concept of acquiring the aldehyde compound containing the moiety of the molecule with the thiol-anchored group, and subsequently modifying the aldehyde, either for the receptor/sensor core or to introduce the carboxylic group available for bonding with biologically relevant macromolecules, remained intriguing due to the difficulties to obtain **1***b-1* in a good yield in order to be used in the next step of the reaction. Along the way to reaching this point, two critical factors were identified: 1) the limited solubility of the receptor/sensor cores, which demanded a synthetic strategy which began with the preparation of the precursor aldehyde; 2) the undesired cleavage of the S-protecting group, which was observed, by TLC, in both experimental procedures through direct arylation and Suzuki-Miyaura couplings. To address this challenge, a literature search was carried out, which revealed the possibility of using a promising S-protecting group, which is stable under common Suzuki-coupling conditions (ITOH; MASE, 2006). Taking these factors into account, a new synthesis strategy was proposed (Scheme 5.3). In the first step, the bromo-aryl derivative **3*a***, containing the S-protecting group, was synthesized, subsequently, Suzuki coupling of precursor **3*a*** with the formyl thiophene boronic acid afforded compound **3*b***. In the third step, the aldehyde group of **3*b*** was converted to the cyanoacetic acid moiety. Finally, the last step would have involved the cleavage of the S-protecting group of compound **3*c*** in order to obtain the compound **3**.

Compound (**3*a***), was synthesized using an experimental procedure described earlier (ITOH; MASE, 2006). This method was successfully employed to obtain the bromo-aryl precursor, functionalized with the S-protecting group, in 62% yield. The ^{1}H NMR spectrum (See Figure R.1, Appendix R) of compound exhibited the signals corresponding to benzene in the aromatic region between 7.21-7.43 ppm and the characteristic signals of the S-protecting group in the aliphatic region of the spectrum, ranging from 0.8 to 4 ppm.

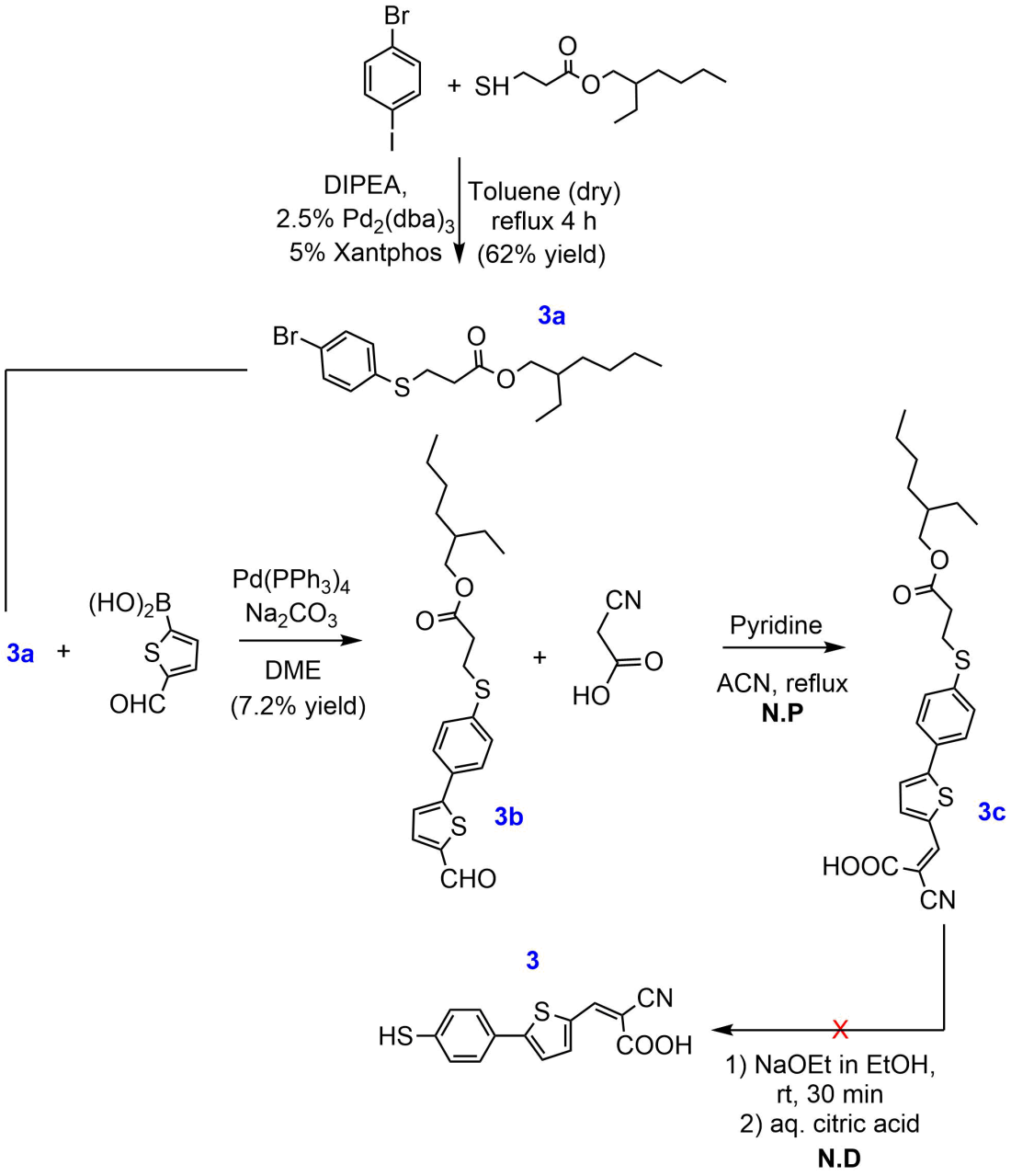

Scheme 5.3: Synthetic route for the preparation of molecule **3** (Figure 5.1). The abbreviation N.P. indicates that purification of the crude product was not performed. *Source: Author (2024)*

Synthesis of push-pull heterocyclic molecule containing a stable S-protecting group:

Following the successful synthesis of the bromo-aryl precursor incorporating the new S-protecting group **3*a***, the subsequent critical step involved a Suzuki-Miyaura coupling reaction between precursor **3*a*** and the thiophene boronic acid reagent functionalyzed with the formyl group. Despite the low yield (7.2%), it was possible to obtain the desired compound **3*b***, maintaining the integrity of the S-protecting group, as it was confirmed by the presence of the main signals of the protons from the S-protecting group (> 4 ppm) observed in the ^{1}H NMR spectrum (See Figure R.2, Appendix R). Additionally, the singlet of the CHO, concerning the aldehyde group (9.90 ppm) was also detected as well as the two doublets of the thiophene ring (7.38 and 7.74 ppm). During the purification stage by silica gel column chromatography, it was also possible to isolate and identify another product obtained in the reaction, the 2,2'-bithiophene-5,5'-dicarbaldehyde, in 8.2%, due to the homocoupling between the boronic acid reagent (See Figure R.3, Appendix R). The low yield for the desired molecule **3*b*** could be attributed to the homocoupling reaction of the formyl-2-thiopheneboronic acid, and also due to the difficulty in the isolation of the target product **3*b*** taking into account the similar polarities of both compounds.

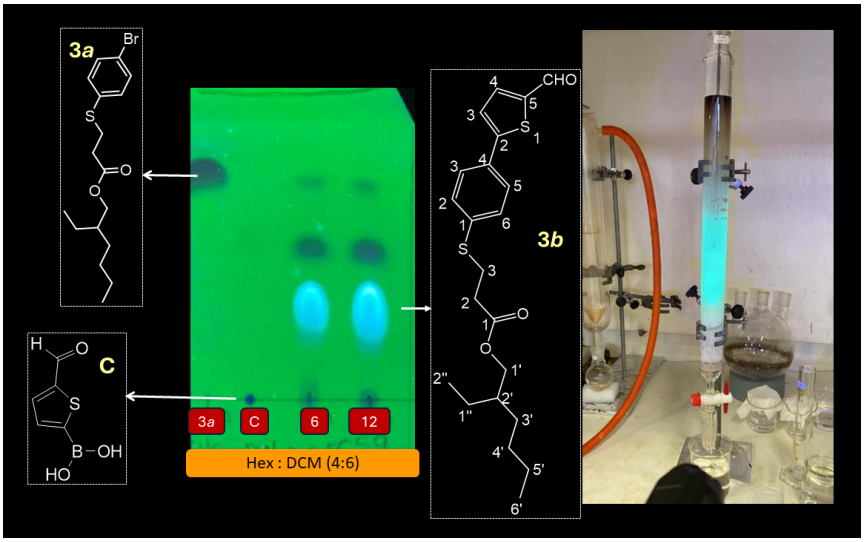

Figure 5.4: TLC conducted for the synthesis of compound **3*b***. The starting reagents/precursors were presented in the red squares as **3*a*** and 5-formyl-2-thiopheneboronic acid (**C**), together with the reaction mixture after 6 and 12 h. The blue fluorescent spot corresponds to **3*b*.**

Following the synthesis of the aldehyde compound containing the S-protecting group (**3*b***, Scheme.5.3), the subsequent step involved the condensation of the aldehyde to obtain the cyanoacetic acid *push-pull* molecule **3*c*** with the carboxylic group in order to bond with macromolecules of biological interest for sensing applications. As was evident in the ^{1}H NMR spectrum of the crude product, the disappearance of

the main signal associated with the aldehyde proton served as an indicator of the successful synthesis of the desired compound **3*c***, together with the presence of a singlet at a lower chemical shift than the aldehyde proton (see Figure S.1, Appendix S), due to the proton in the C*H*=C(CN)CO_2H group of the cyano acetic acid moiety. Additionally, the signals in the aliphatic region of the spectrum attested the stability of the S-protecting group under these basic conditions. This was further confirmed by MS (ESI) with the detection of ion [M-CO_2]$^-$ at 426.1511 (100%), corresponding to the loss of the CO_2 fragment (See Figure S.2, Appendix S). Additionally, a less intense fragment (49%) at 470.1402 was observed, corresponding to the deprotonated molecule [M-H]$^-$. Other low-intensity signals were also detected, which may correspond to additional fragmentation of the product. Up to this point, the next steps would typically include the purification of the compound **3*c*** and the subsequent cleavage of the protecting group. Unfortunately, due to time constraints, it was not possible to perform the synthesis and purification procedures in order to obtain the final product **3**. Nevertheless, we anticipate that this synthetic route pave the way to the synthesis of *push-pull* heterocyclic molecules functionalyzed at the same time with the cyanoacetic acceptor moiety and the thiol group, suitable for anchoring on gold electrodes.

5.2.2 Design of *push-pull* heterocyclic molecules with anchoring group for π-π stacking on graphene

Five *push-pull* heterocyclic molecules (Figure 5.5) were designed and synthesized having in mind the formation of molecular junctions on graphene electrode. The proposed *push-pull* heterocyclic molecules were functionalyzed with D/anchoring groups such as pyrene or naphthalene, connected through a π spacer with different electronic properties to A moieties such as carboxylic or cyanoacetic acid, to allow the future functionalization for sensing applications (GARROTE; SANTOS; BUENO, 2020). The tailored design of these molecules aims to study ET_p properties to identify a transduction signal in the context of sensing applications.

It is well-known that pyrene and its derivatives exhibit a highly conjugated planar aromatic system, capable of forming $\pi - \pi$-stacking interactions with graphene (LIU; TANG; GOODING, 2012). The overlapping of π-orbitals between pyrene and graphene depends on planarity, conformation, and the electron-withdrawing/donating nature of adjacent groups (ALIAKBAR TEHRANI; KIM, 2016). Consequently, modifying the structure of the molecules containing the pyrene group, affects the stability of this interaction and communication between its constituent parts. In this context, we

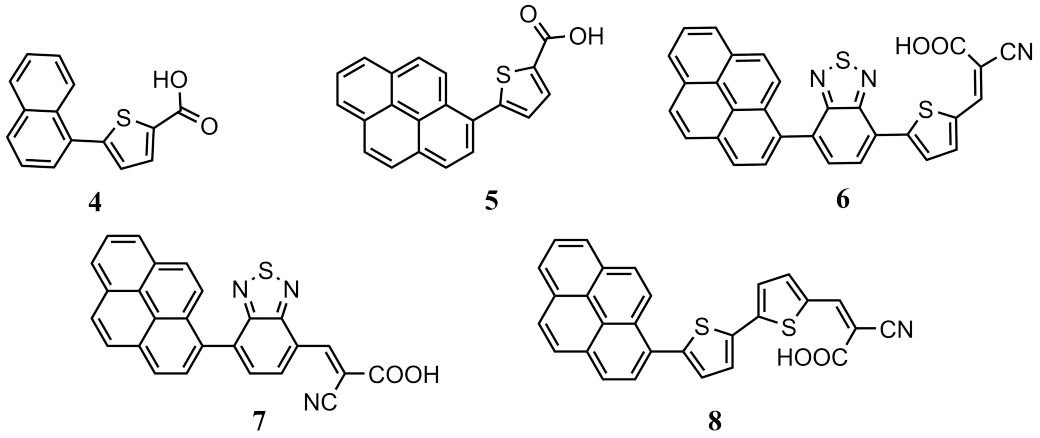

Figure 5.5: Pyrene (and naphthalene) heterocyclic molecules of the *push-pull* type: 5-(naphthalen-1-yl)thiophene-2-carboxylic acid (**4**); 5-(pyren-1-yl)thiophene-2-carboxylic acid (**5**); 2-cyano-3-(5-(7-(pyren-1-yl)benzo[*c*][1,2,5]thiadiazol-4-yl)thiophen-2- yl)acrylic acid (**6**); 2-cyano-3-(7-(pyren-1-yl)benzo[*c*][1,2,5]thiaiazol-4-yl)acrylic acid (**7**); and 2-cyano-3-(5′-(pyren-1-yl)-[2,2′-bithiophen]-5-yl)acrylic acid (**8**).

chose thiophene as an electron-rich spacer, which has been widely used for its excellent charge-transfer properties, high thermal stability, and photophysical properties (OKDA *et al.*, 2019; MALYTSKYI; GADENNE, *et al.*, 2017; OLIVA *et al.*, 2006). Additionally, an electron-deficient heterocyclic spacer, like benzothiadiazole, was also considered, which can be used as an auxiliary *A* group (FERNANDES *et al.*, 2018).

The synthesis methodology consisted of three distinct stages. In the first stage (a), the linker group, either pyrene or naphthalene, was attached to the π-spacer moiety. This moiety contains either a carboxylic acid *A* group, as in molecules **4** and **5** (see Scheme 5.4), or an aldehyde group (see Scheme 5.5). The second stage (b) involved the formation of the thienylbenzothiadiazole core, which served as the π -spacer for molecule **6**. Finally, the third stage (c) involved the transformation of the aldehyde group to the cyanoacetic acid group, which acted as the *A* moiety of the *push-pull* structure as well as a reactive head when the molecule is assembled on the graphene electrode (see Scheme 5.7). The final compounds **4-8** were characterized by ^{1}H NMR and Mass Spectrometry (MS). Nevertheless, it was not possible to perform ^{13}C NMR spectra of the compounds, due to insolubility reasons and/or due to the small amounts obtained.

a. Synthesis of compounds 4 and 5 via Suzuki-Miyaura cross-coupling reaction

The Suzuki-Miyaura coupling reaction was the basis for the formation of *push-pull* heterocyclic molecules **4** and **5** functionalyzed with the carboxylic acid group (Scheme 5.4) as well as the aldehyde precursors **6*a*-8*a*** (Scheme 5.5). Molecules **4** and **5**, bearing a naphthalene or pyrene *D*/anchoring group, a thiophene π-spacer, and a carboxylic acid *A* group, were synthesized in moderate to good yields (59% and 62%)

after reaction times of 5 and 6 h, respectively. The TLC performed during the reaction and the photo of the solids of compounds **4** and **5**, are displayed in Figure 5.6. The structure of compounds **4** and **5** was confirmed by ^{1}H NMR spectroscopy and HRMS for compounds **4** and MS for compound **5** (Appendix T and U, respectively). HRMS (ESI, negative mode) spectrum confirmed the identity of the compound **4** with m/z for $C_{15}H_9O_2S$, calcd 253.0314; found 253.032878 ([M-H]$^-$). The MS spectrum of the molecule **5** presented the ion at m/z 327.0422 ([M-H]$^-$, 100%), and another fragment of less intensity corresponding to the loss of a CO_2 at m/z 283.0500 ([M-44]$^-$, 35%). Compound **4** has been reported earlier in a patent (Patent Number WO2008101186) (VERDIN; SCOTT, 2008).

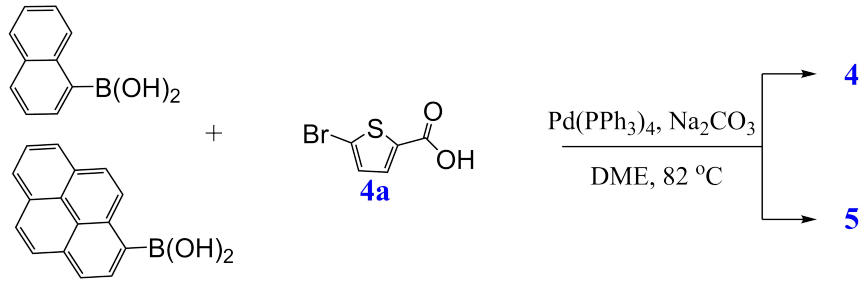

Scheme 5.4: Synthesis of naphthalene **4** and pyrene **5** derivatives via Suzuki-Miyaura coupling.

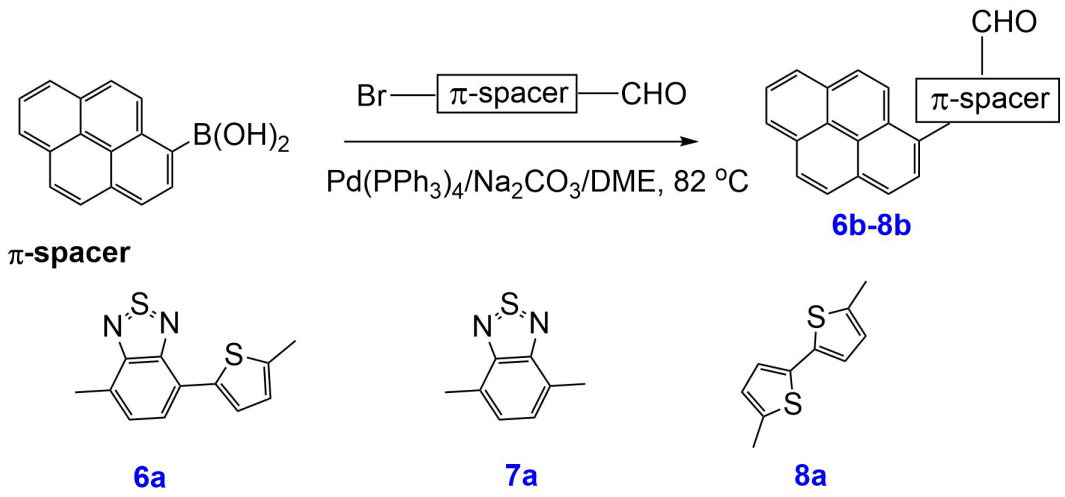

Scheme 5.5: Synthesis of pyrene aldehyde precursors **6b-8b** via Suzuki-Miyaura coupling.

b. Synthesis of the precursor 6a bearing the thienylbenzothiadiazole spacer

Precursors **4***a*, **5***a*, **7***a* and **8***a* (see Schemes 5.4 and 5.5) were commercially available reagents which were used in order to introduce different π-spacers in the final compounds **4**, **5**, **7-8***b*. However, the spacer **6***a* was also synthesized as depicted in the Scheme.5.6, through a Suzuki-Miyaura coupling of the bromide coupling component

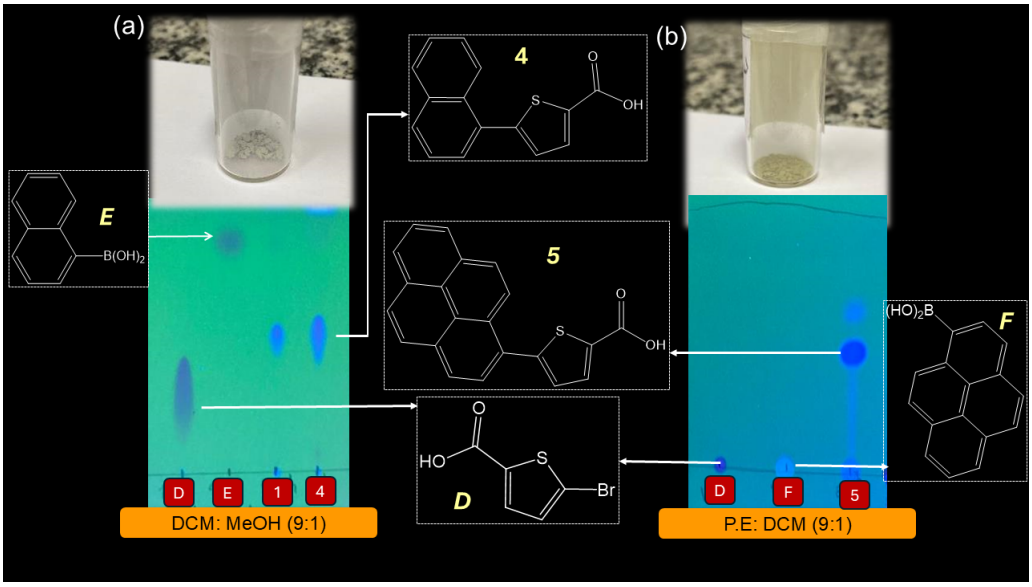

Figure 5.6: TLC was used to monitor the synthesis of molecules (a) **4** and (b) **5**. The red squares in the starting region of the TLC plates correspond to reaction mixtures (1 h and 4 h for reaction (a), and 5 h for reaction (b)), and to the starting/precursors materials: 5-bromo-2-thiophenecarboxilic acid (**D**), naphthalene-1-boronic acid (**E**), and pyrene-1-boronic acid (**F**). The progress of the reactions was followed by observing the disappearance of the limiting reagent **D**, in both reactions. A mixture of DCM and MeOH in a 9:1 ratio was selected as the eluent in order to observe the formation of compound **4** (a), while a mixture P.E. and DCM in a 9:1 ratio was used for the elution of the reaction mixture in the synthesis of compound **5** (b). Compounds **4** and **5** were obtain as gray and green solids respectively.

bearing the benzothiadiazole moiety with the thiophene-carbaldehyde boronic acid. The pure compound was obtained in 23% yield, which was used in the subsequent synthesis step, involving coupling with the boronic acid component.

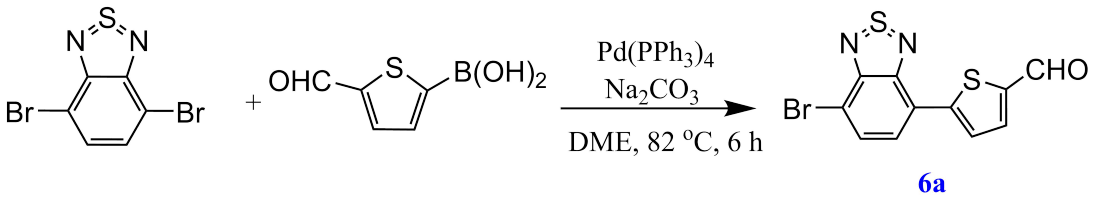

Scheme 5.6: Synthesis of precursor **6***a* via Suzuki-Miyaura reaction.

c. Synthesis of the *push-pull* compounds 6-8 through Knovenagel condensation

The synthesis of the final compounds **6-8** (Figure 5.5) involved the Knovenagel condensation of the aldehyde precursors **6***b*-**8***b* with cyanoacetic acid to transform this group to the stronger cyanoacetic *A* moiety (see Scheme.5.7). The structures of the molecules were confirmed by ^{1}H NMR, MS (for compounds **6** and **8**), and HRMS (for compound **7**, see Appendix X). It is important to note that the most abundant fragments observed in the MS correspond to the loss of CO_2 by the molecular ion

for compound **8** (Appendix Y), or the loss of the -CN group in the case of compound **6** (Appendix W). This last step was executed in good yields giving the target compounds **6**, **7**, **8**, in 82%, 74%, and 69% yields, respectively, making this synthetic route a promising approach for the preparation of *push-pull* heterocyclic molecules with unique characteristics. Compound **8** has been reported earlier by Baheti, *et al* (BAHETI *et al.*, 2011).

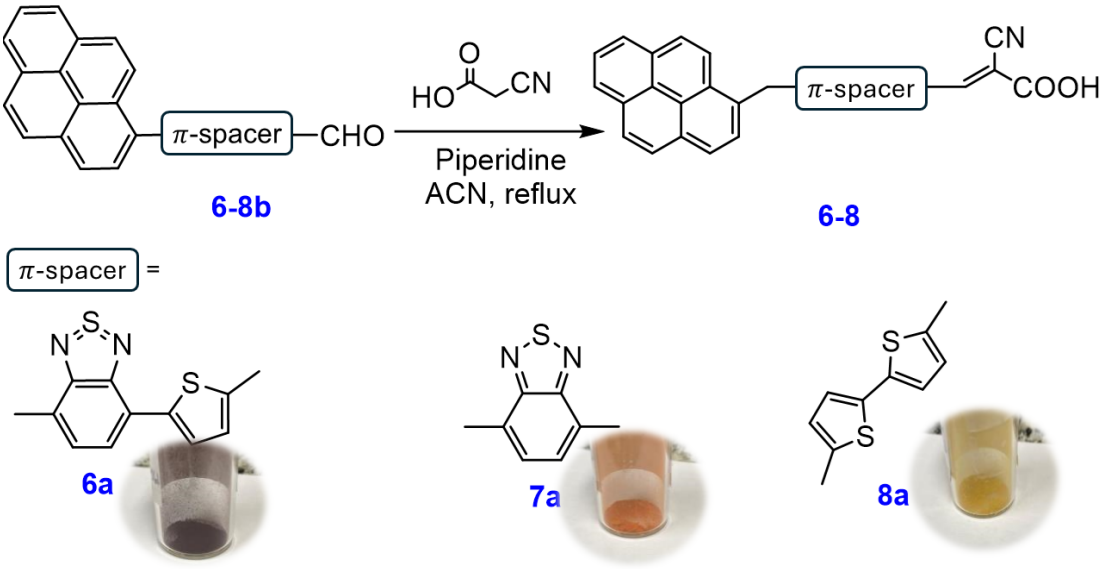

Scheme 5.7: General scheme for the synthesis of pyrene *push-pull* heterocyclic derivatives **6-8** functionalized with the cyanoacetic acid moiety.

5.2.3 Quantum dynamics of *push-pull* heterocyclic molecules anchored on graphene

The quantum electrodynamics nature of single-layer graphene (SLG) coupled with *push-pull* heterocyclic molecules was experimentally demonstrated through QRS, a methodology rooted in QRT. Prior studies employing this approach have provided key insights into the electronic structure of SLG systems, specifically, they revealed the symmetric V-shaped DOS characteristic of pristine graphene under ambient conditions in an electrolyte medium (LOPES; PINZÓN, *et al.*, 2024) and additionally the method permitted to investigate the Gaussian-shaped DOS of push-pull molecular assemblies on gold electrodes (PINZÓN *et al.*, 2024). Inspired by these findings, we designed, synthesized, and chemically characterized five distinct heterocyclic *push-pull* molecules, enabling the construction of a hybrid system in which these molecules were confined to SLG via π-π stacking interactions, Figure 5.7. The application of

QRS to this coupled system revealed the emergence of a modified electronic structure, confirming that molecular adsorption directly influences the quantum electrodynamics of graphene.

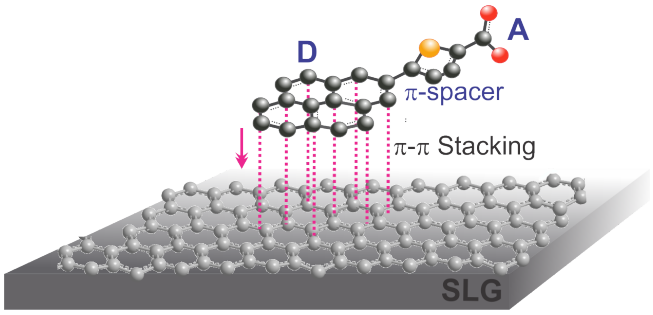

Figure 5.7: Molecule **5** anchored onto SLG via π-π stacking, facilitated by the molecule's planar structure and delocalized π-electron system in the anchor/D group. This is a representative illustration and applies similarly to the others studied systems involving *push-pull* heterocyclic molecules **4, 6-8** (Figure 5.5) with SLG.

Source: Author (2024)

A notable loss of symmetry in the characteristic capacitive V-shape of pristine graphene (LOPES; PINZÓN, *et al.*, 2024), along with a shift in the minimum C_q toward more negative potentials, were observed for all molecular junctions (see Figure Z.1*b-inset*). This shift indicated that the molecular layer perturbed the electronic structure of SLG, altering its intrinsic DOS. Additionally, a new electronic contribution emerged in the positive potential region of the DOS, appearing between 0.6 and 1.5 V vs Au, for all five evaluated molecular junctions as indicated by the blue-shaded region in Figure Z.1 *b*, with varying intensity depending on the molecular species. This suggests that the heterocyclic molecules introduced additional electronic states into the characteristic electronic DOS of graphene, enabling an energetic alignment or coupling at specific potentials from 0.6 to 1.5 V vs Au. Such, coupling facilitated efficient electronic communication between the molecular energy levels and the graphene states, reinforcing the quantum nature of ET_p within the hybrid system.

Further validation of the quantum behavior of the hybrid system was obtained through circuital fitting using the quantum RC model (Figure Z.4, Appendix Z), applied to a single *push-pull* heterocyclic molecule assembled on SLG. The extracted R_q (see Table Z.1) values at both the Dirac point (-0.35 V vs Au) and the molecular coupling point (1 V vs Au) (see Figure Z.3 *b*) were 13.4 $\pm$ 1.4 kΩ and 12.7 $\pm$ 0.6 kΩ, respectively, which exhibited deviations of only 8% and 2% from the theoretical quantum limit $R_q = 1/G_0 \approx 12.9$ kΩ, providing strong evidences that charge transport followed quantum electrodynamic principles. Moreover, these results confirmed the applicability of the QRT approach in analyzing the quantum electrodynamics of

systems with an adiabatic nature and Et_p where redox reactions are absent. This extended the applicability of QRT beyond the non-adiabatic regime and conventional redox-based ET processes discussed in previous chapters.

Building upon prior work that demonstrated the feasibility of SLG as a sensing platform by exploiting its quantum capacitance response (LUCAS GARROTE *et al.*, 2022), it was investigated how modifying SLG with *push-pull* heterocyclic molecules provides an alternative approach to quantum-based sensing sustained in monitoring the quantum RC dynamics upon the binding of the targets on receptors coupled the molecules assembled over SLG structures. The ability of graphene to act as a transduction element stems from its unique electronic structure, where molecular binding events induce variations in its C_q, thereby altering the system's quantum RC dynamics. By leveraging the confinement-induced quantum properties of these *push-pull* heterocyclic molecules on graphene, our findings opened new avenues for the development of sensing platforms, as was shown in the next subsection. The observed molecular-level electronic structure suggests that these hybrid systems served as highly sensitive transduction elements, where quantum electrodynamic interactions mediate signal transduction.

5.2.4 Quantum resistive-capacitive SLG sensing platforms modified with *push-pull* heterocyclic molecules

The successful modification of the *push-pull* heterocyclic molecules on SLG, laid the foundation for the development of a quantum RC sensing platform for DNA detection. By leveraging the minimum C_q at the Dirac point as a transducer signal, this approach provided an ultrasensitive method capable of detecting attomole-level concentrations of DNA. For biological sensing, 22-base single-stranded DNA (ssDNA) oligonucleotides associated with C228T mutation in glioblastoma (OLYMPIOS *et al.*, 2021)-commercially obtained and functionalized with and NH_2 group-were covalently conjugated to the molecule-SLG interface. This specific mutation, located 124 bp upstream of the ATG start site, is a cytosine-to-thymine substitution (c.-124C>T) that creates a novel ETS transcription factor binding motif, leading to increased TERT transcription and telomerase activity in cancer cells. It has been strongly associated with aggressive forms of thyroid (BAE *et al.*, 2016) and glioblastoma cancer (OLYMPIOS *et al.*, 2021). Each step of sensor construction was monitored by tracking changes in the C_q-V response (Figure Z.2, Appendix Z), particularly in the C_q at the Dirac point, which served as a highly sensitive indicator of hybridization events, even at the lowest target DNA concentrations, within the range of 1 aM to 10^{-5} aM tested in this study.

A systematic decrease in C_q at the Dirac-point with increasing DNA concentration enabled the construction of analytical calibration curves (Figure 5.8) for SLG monolayers incorporating each of the five synthesized push-pull molecules (**4-8**). The relative response (RR%) was calculated using the equation: $RR\% = [(1/C_q - 1/C_{q-blank})/(1/C_{q-blank})] \times 100$, where C_q corresponds to each target DNA concentration, and $C_{q-blank}$ to the blank measurement. The analytical curves of RR% as a function of target DNA concentration were fitted using the Langmuir isotherm model (see Fig 5.8*a*) which describes the molecular occupancy of target DNA on the receptor DNA immobilized at the interface (HALPERIN; BUHOT; ZHULINA, 2006). The sensitivity per decade of the DNA assay for each molecule-SLG system was determined by the slope (a) of the linear function obtained by mathematically fitting the data (see Fig 5.8*a*) as $RR\% = alog[C] + b$, where C was the target DNA concentration and b is the intercept. The limit of detection (LoD) and limit of quantification (LoQ) were estimated based on the standard deviation (σ), from three independent experimental measurements, using the equations $\text{LoD} = 10^{3\sigma/a-b}$ and $\text{LoD} = 10^{10\sigma/a-b}$, the calculated values are presented in Table. 5.1.

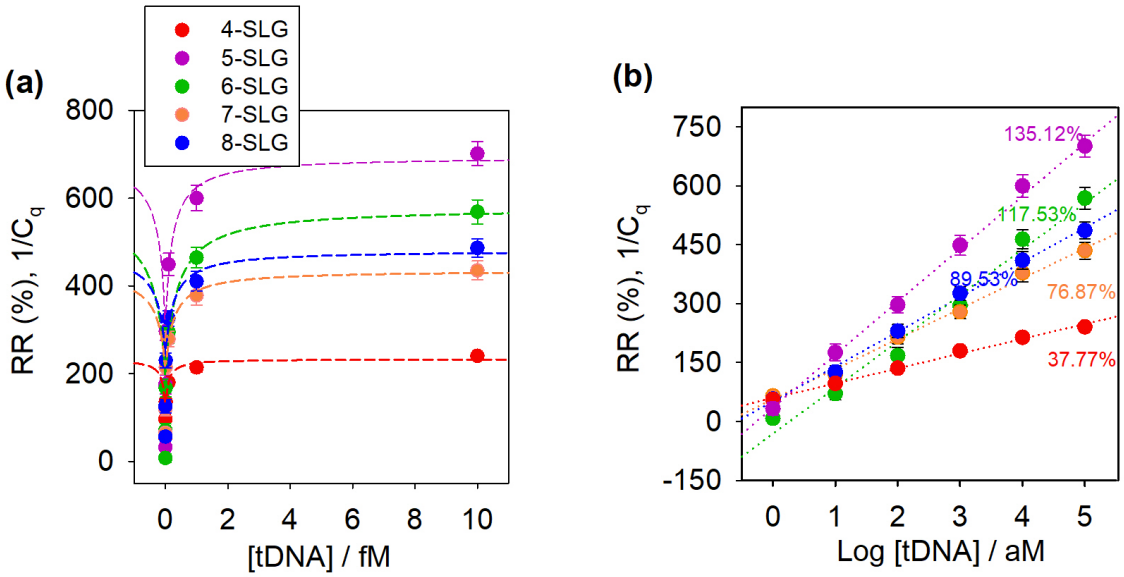

Figure 5.8: (a) Response RR% as a function of tDNA conentration, across the different SLG interfaces, each functionalized with the distinct heterocyclic *push-pull* molecules illustrated in Figure 5.5 and (b) the calibration curves derived from biological DNA sensing assays within their respective sensitivities. The standard deviation bars, based on three independent experiments, are shown for each data point in plots (a) and (b). The notation **4**-SLG refers to the monolayer constructed using molecule **4** anchored onto the SLG.

Source: Author (2024)

The DNA detection assays demonstrated exceptional sensitivity, with RR% values ranging from 76.87% to 135.12%. Notably, variations in sensitivity across the molecular series were directly linked to differences in the π-bridge and A groups which modulate the electronic properties and ET_p dynamics. Among all tested molecules,

Table 5.1: LoD and LoQ calculated for the different DNA sensing assays using five molecules **4-8** from Figure 5.5

Interface	LoD [aM]	LoD [aM]
4-SLG	0.33	2.12
5-SLG	0.11	1.37
6-SLG	0.21	1.73
7-SLG	0.34	2.15
8-SLG	0.24	1.80

compound **5** exhibited the highest sensitivity (132.12% per decade of DNA concentration) likely due to the synergistic effects of its pyrene donor, thiophene π-bridge, and carboxylic acid acceptor, which enhanced electronic communication, resulting in a improver molecular recognition. Additionally, molecule **5** achieved the lowest LoD of 0.11 aM, underscoring its high analytical precision (Table 5.1). These results reinforce the idea that by carefully tailoring the chemical structure of π-conjugated heterocyclic molecules, it is possible to fine-tune the sensing parameters.

Compared to conventional electrochemical DNA sensors, the newly developed quantum RC platform based on *push-pull* heterocyclic molecules represent a significant advancement in analytical sensitivity. While many established systems achieve detection limits in the femtomolar (fM) range, only a few state-of-the-art configurations have approached the attomolar (aM) regime, often relying on complex amplification strategies or sophisticated surface modifications (FERAPONTOVA, 2018). However, it is important to note that this system has thus far been evaluated only using commercially synthesized, amine-functionalized probe DNA in controlled hybridization assays. No tests have yet been conducted in complex biological matrices such as plasma. Nevertheless, these findings highlight the strong potential of quantum capacitance -based detection and the promising design of the molecular interface for future application in clinical diagnostics.

By constructing well-defined molecular assemblies, it was achieved the necessary confinement to access quantum properties such as C_q, unveiling the electronic structure of the system as captured in the DOS profiles. Notably, these quantum properties were accessed in an electrolyte medium at room temperature, without requiring vacuum conditions or specialized experimental setups typically associated with solid-state spectroscopy techniques. Within the framework of QRT, C_q was utilized as the key parameter, as established in previous chapters, to assess the occupancy of

electronic states, not in the context of redox events, but rather in relation to the delocalized π orbitals that become accessible at a system-specific ν. This approach, in the previous chapter applied to study the electrodynamics of ET processes in redox-tagged peptide SAM, where electronic coupling with the electrode follows a non-adiabatic regime, was extended to molecule-SLG systems, which exhibit adiabatic coupling. By doing so, we were able to evaluate electronic communication between states, thereby accessing the DOS and identifying the transduction signal necessary for sensor construction. While this study demonstrated the platform's effectiveness in DNA assays associated with brain cancer, it is crucial to emphasize that its applicability extends beyond nucleic acid detection. The molecular-SLG system features an available carboxyl functional group, allowing for facile modification with various biologically relevant targets, such as antibodies or DNA associated with other mutations. This versatility underscores the broader potential of the quantum RC sensing platform for the selective detection of a wide range of biomolecules, paving the way for future applications in molecular diagnostics.

5.3 Conclusion

In conclusion, the work presented in this chapter established a promising synthetic route for *push-pull* heterocyclic molecules designed for molecular assembly on gold electrodes, an essential step toward accessing their electrodynamic properties and electronic structure through the QRT framework. Despite challenges such as the low solubility of the molecules functionalyzed with the receptor/binding units, undesired reactivity of the thiol group, and instability of its protective group, significant progress was achieved. Notably, the stability of the S-protective group (propanoic acid, 2-ethylhexyl ester) under Suzuki-Miyaura and condensation reaction conditions allowed the synthesis of molecules with the required design.

Furthermore, the successful synthesis and chemical characterization of five molecules featuring a carboxylic acid head group and π-conjugated linker suitable for interaction with graphene electrodes marked a substantial advancement in the development of sensing platforms. By leveraging quantum properties such as C_q, the study demonstrated the ability to assess the electronic structure and identify the transduction signal necessary for sensing. The molecular-SLG system, with its demonstrated capability for detecting DNA associated with a brain cancer biomarker, exemplifies a versatile genosensing platform. Its structural adaptability allows for the integration of other biologically relevant targets, thus broadening the scope for applications in molecular diagnostics. The synthetic strategy outlined here, in tandem with QRT-based analysis, establishes a robust framework for advancing molecular sensor technologies and deepening our understanding of quantum electrodynamics processes

occurring in electrolyte environment. Ultimately, the analysis represented a step forward not only in the synthesis of innovative compounds but also in the development of sensing technologies in physiological environments, laying the groundwork for future breakthroughs in molecular diagnostics.

5.4 Materials and methods

The progress of the synthesis was monitored using TLC, under UV light. When necessary, crude products were purified by column chromatography on silica-gel. All intermediates and final compounds were characterized by ^{1}H NMR. NMR spectra were recorded on a Bruker Avance III 400 at an operating frequency of 400 MHz, using the solvent peak as an internal reference (δ relative to TMS). The structure of the final compounds was also confirmed by MS, recorded on a Bruker Maxis Impact system using ESI in negative mode.

5.4.1 Chemical reagents

Table.5.2 compiles the reagents used in the experimental work developed, concerning this chapter, the enterprise where they were purchased from, and their purpose are also presented in the table. All commercial reagents and solvents were used without purification.

Table 5.2: List of chemical reagents used in chapter 5.

Reagent	Company	Purpose
p-Bromoiodobenzene	Fluorochem	Synthesis of *p*-bromobenzene thioether
N,N-Diisopropylethylamine (*i*-Pr_2NEt)	Sigma-Aldrich	
4,5-*Bis*(diphenylphosphino)-9,9-dimethylxanthene (Xantphos)	Fluorochem	
Tris(Dibenzylideneacetone)dipalladium(0) ($Pd_2(dba)_3$)	Fluorochem	
2-Thiophenecarboxaldehyde	Fluorochem	Terpyridine synthesis
Ethyl 2-acetylisonicotinate	Fluorochem	
Pyrene-1-boronic acid	Fluorochem	
Naphthalene-1-boronic acid	Acros	
5-Formyl-2-thiopheneboronic acid	Acros	

Continued on next page

Table 5.2 – continued from previous page

Reagent	Company	Purpose
(1-(Triisopropylsilyl)-1*H*-pyrrol-3-yl)boronic acid	Fluorochem	Boronic acids for Suzuki-Miyaura Coupling
4,7-Dibromobenzo[*c*]-1,2,5-thiadiazole	Fluorochem	
5-Bromo-2-thiophenecarboxilic acid	Acros	
5′-Bromo-2,2′-bithiophene-5-carboxaldehyde	Sigma-Aldrich	Bromine-compounds for Suzuki-Miyaura Coupling
7-Bromo-2,1,3-benzothiadiazole-4-carboxaldehyde	Fluorochem	
S-(4-Bromophenyl) ethanethioate	Fluorochem	
Palladium(II) acetate ($Pd(OAc)_2$)	Fluorochem	Palladium catalysts for Suzuki-Miyaura coupling and direct arylation reactions
Tetrakis(triphenylphsphine)palladium(0) ($Pd(PPh_3)_4$)	Acros	
Potassium acetate (KOAc)	Fluorochem	Base of choice for palladium catalyzed reactions
Sodium carbonate (Na_2CO_3)	Acros	
Ammonium acetate (NH_4OAc)	Sigma-Aldrich	Reagents for Debus–Radziszewski imidazole synthesis
Glacial acetic acid	Sigma-Aldrich	
1,10-Phenanthroline-5,6-dione	Fluorochem	
2-Thiophenecarboxaldehyde	Fluorochem	
Tetrabutylammonium fluoride solution (1M in THF)	Sigma-Aldrich	N-protective group cleavage
Ammonium hydroxide (NH_4OH)	Sigma-Aldrich	Reagents for Debus–Radziszewski imidazole synthesis and Kröhnke pyridine synthesis
Cyanoacetic acid	Sigma-Aldrich	Active hydrogen compound for Knoevenagel condensation
Piperidine	Sigma-Aldrich	Base used for Knoevenagel condensation
Potassium hydroxide (KOH)	ITW Reagents	Base used for terpyridine synthesis

Continued on next page

Table 5.2 – continued from previous page

Reagent	Company	Purpose
Sodium chloride (NaCl)	Sigma-Aldrich	Reagents for the extraction and separation process
Sodium hydroxide (NaOH)	Sigma-Aldrich	
Magnesium sulphate anhydrous ($MgSO_4$)	ITW Reagents	
Dimethylacetamide (DMAc)	Fluorochem	Solvents for coupling, condensation and deprotection reactions
Dimethylformamide (DMF)	ITW Reagents	
Ethylene glycol dimethyl ether (DME)	Acros	
Acetonitrile (ACN)	Acros	
Ethanol (EtOH)	Sigma-Aldrich	
Tetrahydrofuran (THF)	Acros	
Hexane	Sigma-Aldrich	Organic solvents for silica-gel column chromatography
Dichloromethane (DCM)	Sigma-Aldrich	
Chloroform	Sigma-Aldrich	
Petroleum ether	Fisher Scientific	
Ethyl acetate	Fisher Scientific	

Table 5.3: Summary of the organic molecules with their full names and corresponding number used in the schemes. The number of compounds were assigned to each compound resulting from the synthesis attempts to obtain the final molecules shown in Figure 5.1, which are labeled by numbers. For example, in compound **1*a***, the number **1** corresponds to the intermediate leading to final molecule **1**, while the letter '*a*' indicates the specific intermediate in the synthesis pathway for that particular route.

Name of the compounds	Number of the compounds
2-(Thiophen-2-yl)-1*H*-Imidazo[4,5-*f*][1,10]phenanthroline	**1*a***
S-(4-(5-(1*H*-imidazo[4,5-*f*][1,10]phenanthrolin-2-yl)thiophen-2-yl)phenyl) ethanethioate	**1*b***
4′-(Thiophen-2-yl)-[2,2′:6′,2″-terpyridine]-4,4″-dicarboxylic acid	**2*a***
Dimethyl 4′-(5-(4-(acetylthio)phenyl)thiophen-2-yl)-[2,2′:6′,2″-terpyridine]-4,4″-dicarboxylate	**2*b***

Name of the compounds	Number of the compounds
S-(4-(5-Formylthiophen-2-yl)phenyl) ethanethioate	**1***b-1*
3-(4-Bromophenylsulfanyl)propionic acid 2-Ethylhexyl ester	**3*a***
2-Ethylhexyl 3-((4-(5-formylthiophen-2-yl)phenyl)thio)propanoate	**3*b***
2-Cyano-3-(5-(4-((3-((2-ethylhexyl)oxy)-3-oxopropyl)thio)phenyl)thiophen-2-yl)acrylic acid	**3*c***

5.4.2 Synthesis and characterization of *push-pull* heterocyclic molecules to be anchored on gold electrodes

In this subsection, we described the various compounds resulting from the synthetic attempts adopted to obtain the molecules represented in Figure 5.1. The ^{1}H NMR spectra for each compound provided in the annexes, and the rationalization behind the synthesis of all intermediates that were discussed in subsection. 5.2.1 of the results and discussion section. Due to the complexity and length of the molecular structures' names, each compound's full name was presented only once in the title of its synthesis part. For clarity and ease of reference, only the number of the compounds listed in Table 5.3 were used through the text.

Synthesis of 2-(thiophen-2-yl)-1*H*-imidazo[4,5-*f*][1,10]phenanthroline (1*a*)

The synthesis of **1*a*** (see Scheme. 5.1) was previously reported in the literature (BATISTA; COSTA, *et al.*, 2008). NH_4OAc (10.3 mmol) was added to 1,10-phenanthroli ne-5,6-dione (0.5 mmol) and 2-thiophenecarboxaldehyde (0.6 mmol) in glacial acetic acid (5 mL). The reaction mixture was stirred and heated at reflux for 5 h. The reaction progress was followed with TLC. After cooling at room temperature, NH_4OH, 5 M (15 mL) was slowly added. The yellow precipitated was filtered under vacuum and washed three times with water and finally with Et_2O to give the pure product (96%). Mp > 320 ° C. ^{1}H NMR (400 MHz, DMSO-d_6), δ (ppm): 13.86 (br s, 1H, N*H*), 9.02 (dd, 2H, J_1=4.2 Hz, J_2=1.6 Hz, 9-H and 6-H), 8.85 (d, 2H, J=8 Hz, 4-H and 11-H), 7.90 (dd, 1H, J_1=4 Hz, J_2=1.2 Hz, 5'-H), 7.83 (br s, 2H, 5-H and 10-H), 7.75 (dd, 1H, J_1=5.2 Hz, J_2=1.2 Hz, 3'-H), 7.28 (dd, 1H, J_1=5.2 Hz, J_2=4 Hz, 4'-H) (See Figure O.1, Appendix O).

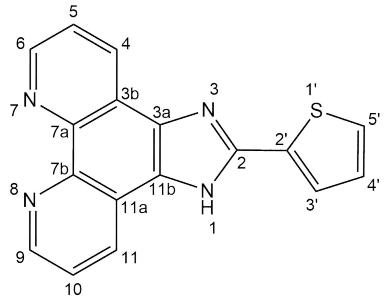

Attempt synthesis of *S*-(4-(5-(1*H*-imidazo[4,5-*f*][1,10]phenanthrolin-2-yl)thiophen-2-yl)phenyl)ethanethioate (1b)

The coupling reaction of the compound **1*a*** and *S*-(4-bromophenyl)ethanethioate (see Scheme. 5.1) was based on the direct arylation conditions reported by Lu Chen et al (CHEN *et al.*, 2011). **1*a*** (0.45 mmol), *S*-(4-bromophenyl)ethanethioate (0.28 mmol), $Pd(OAc)_2$ (0.5%), and KOAc (0.6 mmol) were dissolved in DMAc/EtOH (3:1) under N_2 atmosphere. The reaction mixture was stirring at 130 °C for 18 h. The reaction progress was monitored using TLC with DCM/MeOH (6:4) as the eluent to track the starting reagent **1*a***, and Hex/EtOAc (8:2) to observe the aryl bromide. The precipitated solid was filtered and washed with ethyl ether three times. The more intense signals in the ^{1}H NMR spectrum in DMSO-d_6 correspond to the precursor **1*a*** (See Figure P.1, Appendix P).

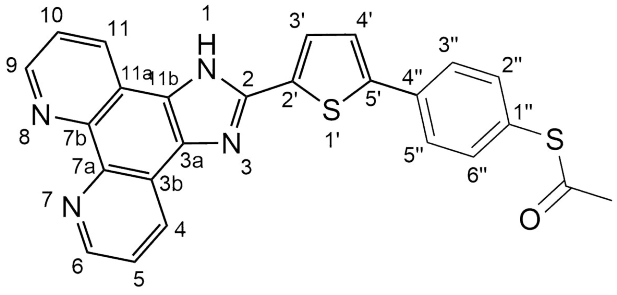

Synthesis of 4′-(thiophen-2-yl)-[2,2′:6′,2″-terpyridine]-4,4″-dicarboxylic acid (2a)

The compound **2*a*** (see Scheme. 5.1) was synthesized using the method previously reported for an analogous compound (HUSSON; DEHAUDT; GUYARD, 2014). 2-Thiophenecarboxaldehyde (0.24 mmol) and ethyl 2-acetylisonicotinate (0.48 mmol) were dissolved in 3 mL of EtOH. KOH in pellets (0.58 mmol) was added to the reaction mixture, and stirred during 30 min, at room temperature. Finally, 25% NH_4OH (2 mL) was added, and the reaction mixture was stirred at room temperature for 92 h. The progress of the reaction was monitored by TLC using a 1:1 Hex/DCM eluent. The precipitated was filtered under vacuum and washed three times with a cold mixture of EtOH/H_2O 1:1 and finally with cold EtOH. A green off-white solid was obtained (48%) and characterized by ^{1}H NMR in DMSO-d_6 (with some drops of THF

to permit the dissolution). δ (ppm): 9.02 (br s, 2H, 6-H and 6″-H), 8.96 (br d, 2H, J=4.8 Hz, 5-H and 5″-H), 8.73 (br s, 2H, 3′-H and 5′-H), 8.00 (dd, 1H, J_1=4 Hz, J_2=0.8 Hz, 3‴-H), 7.97 (dd, 2H, J_1=4.8 Hz, J_2= 1.6 Hz, 3′-H and 3″-H), 7.78 (dd, 1H, J_1=5 Hz, J2=1.2 Hz, 5‴-H), 7.26 (m, 1H, 4‴-H) (See Figure O.2, Appendix O).

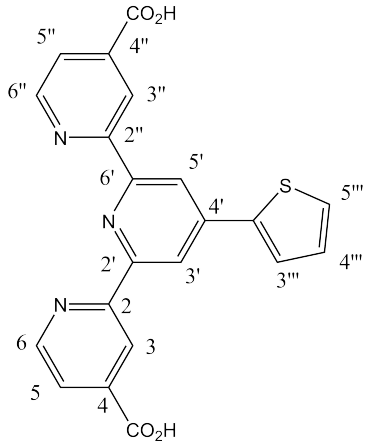

Attempt synthesis of 4′-(5-(4-(acetylthio)phenyl)thiophen-2-yl)-[2,2′:6′,2″-terpyridine]-4,4″-dicarboxylate (2b)

The conventional Suzuki-Miyaura conditions were used to the coupling of 4′-(thiophen-2-yl)-[2,2′:6′,2″-terpyridine]-4,4″-dicarboxylic acid, (**2*a***) and *S*-(4-bromophenyl) (see Scheme. 5.1). The reaction mixture of **2*a*** (0.156 mmol), aryl bromide (0.13 mmol), $Pd(PPh_3)_4$ (6%) and 2 M of Na_2CO_3 (130 μL) in ACN/DMF (2:1) was stirring at 82 °C, under N_2 atmosphere for 29 h. The reaction was monitored by TLC using as eluent P.E/EtOAc (9:1). The precipitated solid was filtered and washed three times with ACN and finally with Et_2O. The signals of the ^{1}H NMR spectrum of the solid in DMSO-d_6 with two drops of THF, correspond to the precursor **2*a*** (See Figure P.2, Appendix P).

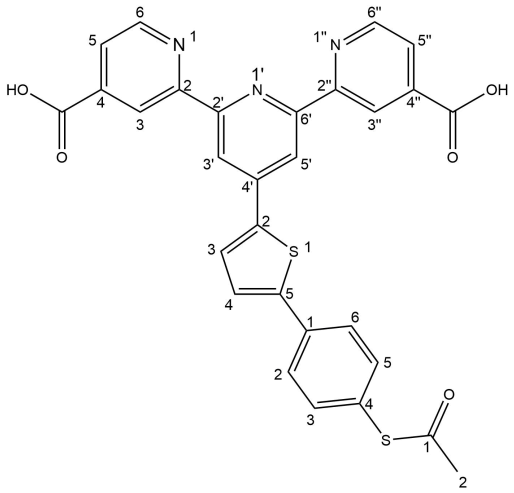

Synthesis of *S*-(4-(5-formylthiophen-2-yl)phenyl) ethanethioate (1*b*-*1*)

5-Formyl-2-thienylboronic acid (0.52 mmol) and *S*-(4-bromophenyl)ethanethioate (0.43 mmol) were coupled (Scheme. 5.2) in a mixture of $Pd(PPh_3)_4$ (6%) and 2 M of Na_2CO_3 (430 μL) in DME (5 mL). The reaction mixture was stirring at 82 °C for 18 h 30 min under N_2 atmosphere. The reaction was monitored by TLC using P.E/EtOAc 9:1 as eluent. The precipitated solid was filtered, and the reaction mixture was collected and extracted with chloroform (2x20 mL), the organic layer was separated from the aqueous layer after the addition of a saturated solution of NaCl (20 mL). Finally, the organic phase was washed with H_2O (2x20 mL), dried with $MgSO_4$, filtered, and the solvent was removed to give a crude product product, which was purified through a silica-gel chromatography using as eluent a mixture of P.E and EtOAc from 10:0 to 2:1. The purification afforded the desired product in trace amounts (1 mg), but it still contained impurities. ^{1}H NMR (400 MHz, $CDCl_3$), δ (ppm): 9.80 (s, 1H, CHO), 7.64 (d, 2H, J=4 Hz, 4'-H), 7.49 (d, 3H, J=8.4 Hz, 6-H, 2-H), 7.31 (d, 2H, J=8.8 Hz, 5-H, 3-H), 7.15 (d, 1H, J=4 Hz, 3'-H), 1.23 (s, 3H, CH_3) (See Figure Q.1, Appendix Q).

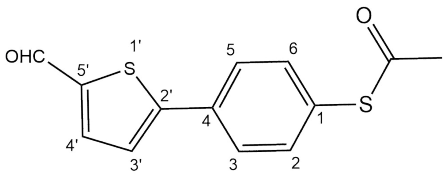

Synthesis of 3-(4-bromophenylsulfanyl)propionic acid 2-ethylhexyl ester (3a)

The *p*-bromobenzene thioether **3*a*** was synthesized followed the method reported by Itoh and Mase (ITOH; MASE, 2006). Briefly, *p*-bromoiodobenzene (1.6 mmol) and *i*-Pr_2NEt (3.2 mmol) were dissolved in dry toluene (6 mL) under stirring, and N_2 was filled and evacuated three times from the reactional bottom flask. Xantphos (0.08 mmol) and $Pd_2(dba)_3$ (0.04 mmol) were added to the reaction mixture. Finally, 2-ethylhexyl 3-mercaptopropanoate (1.6 mmol) was added and the reaction mixture was heated to reflux (4 h) keeping the nitrogen atmosphere. The precipitated solid was filtered, the organic layer collected, and the solvent evaporated. The pure product (62% yield) was obtained as a yellowish oil after purification through a silica gel column chromatography using a mixture of DCM and Hex (from 7:3 to 2:3) as eluent. ^{1}H NMR (400 MHz, $CDCl_3$), δ (ppm): 7.41 (dd, 2H, J_1=6.8 Hz, J_2=2 Hz, 3'''-H and 5'''-H), 7.23 (dd, 2H, J_1=6.8 Hz, J_2=2 Hz, 2'''-H, and 6'''-H), 4.05-3.98 (m, 2H, CH_2), 3.15 (t, J_1=8, 2H, CH_2), 2.61 (t, J_1=7.2, 2H, CH_2), 1.66-1.54 (m, 2H, CH_2), 1.39-1.26 (m, 4xCH_2), 0.91-0.87 (m, 6H, 2xCH_3) (See Figure R.1, Appendix R).

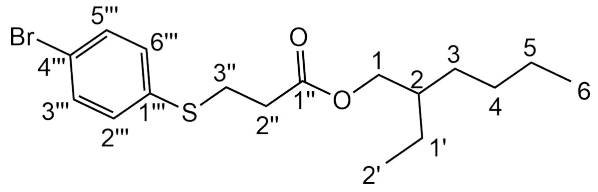

2-Ethylhexyl 3-((4-(5-formylthiophen-2-yl)phenyl)thio)propanoate (3b)

The coupling between the *p*-bromobenzene thioether **3*a*** (0.58 mmol) and 5-formyl-2-thiopheneboronic acid (0.70 mmol) was carried out using $Pd(PPh_3)_4$ (6%) as catalyst in a mixture of 2 M Na_2CO_3 (573 μL) in 4 mL DME/Toluene (4:1) under stirring at 80 °C for 15 h. The progress of reaction was followed by TLC using as eluent Hex:DCM 6:4. The reaction mixture was cooled at room temperature and the solid precipitate was filtered and the organic layer was extracted with chloroform (30 mL), and the organic and aqueous phases were separated after the addition of a saturated solution of NaCl (20 mL). The organic layer was finally washed with H_2O (2x20 mL), dried with $MgSO_4$, filtered and the solvent removed using a rotary evaporator to give the crude mixture, which was purified by column chromatography on silica gel (Hex:DCM from 1:1 to 0:10) to give the pure product (7.2%). ^{1}H NMR (400 MHz, $CDCl_3$), δ (ppm): 9.90 (s, 1H, CHO), 7.74 (d, 1H, 4''''-H), 7.61 (d, 2H, J=8.8 Hz, 2''''-H and 6'''-H), 7.40-7.37 (m, 3H, 3'''-H, 5'''-H and 3''''-H), 4.03 (dd, 2H, J_1=5.8 Hz, J_2=1.8 Hz, CH_2), 3.24 (t, J_1=7.4 Hz, 2H, CH_2), 2.68 (t, J_1=7.4 Hz, 2H, CH_2), 1.60 (d, 1H, J=8.8 Hz, CH), 1.38-1.29 (m, 8H, 4xCH_2), 0.92-0.87 (m, 6H, 2xCH_3) (See Figure R.2, Appendix R). It was also obtained as a by-product of the reaction the 2,2´-bithiophene-5,5´-dicarbaldehyde (See Figure R.3, Appendix R).

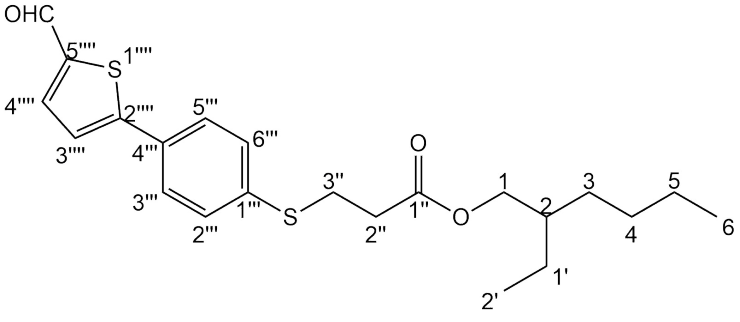

Synthesis of 2-cyano-3-(5-(4-((3-((2-ethylhexyl)oxy)-3-oxopropyl)thio)phenyl)thiophen-2-yl)acrylic acid (3c)

Compound **3*b*** (0.12 mmol) and cyanoacetic acid (0.23 mmol) were dissolved in ACN (6 mL). After stirring at room temperature for 10 min and under nitrogen atmosphere, piperidine (48 μL) was added and the reaction was stirred under reflux for 13 h. After cooling the reaction mixture at room temperature, the yellow precipitate

was filtered and washed with Et_2O. ^1H NMR (400 MHz, $CDCl_3$), δ (ppm): 9.57 (s br,CO_2H), 8.19 (s, 1H, CH=C(CN)(CO_2H), 7.60-7.57 (m, 3H, 3-H and 3'-H, 5'-H), 7.34 (d, 2H, J = 8.4 Hz, 2'-H and 6'-H), 7.31 (d, 1H, J = 4.0 Hz, 4-H), 4.02 (m, 2H, CH_2), 3.23-3.18 (m, 2H, CH_2), 2.66 (t, J_1= 7.4 Hz, 2H, CH_2), 1.90-1.55 (m, 1H, CH), 1.35-1.28 (m, 8H, 4xCH_2), 0.90-0.87 (m, 6H, 2xCH_3) (See Figure S.1, Appendix S). MS m/z (%)= 470.1402 ([M-H]$^-$, 48.6), 442.1455 ([M-H-CN]$^-$, 47), 426.1511 ([M-H-CO_2]$^-$, 100) (see Figure S.2, Appendix S).

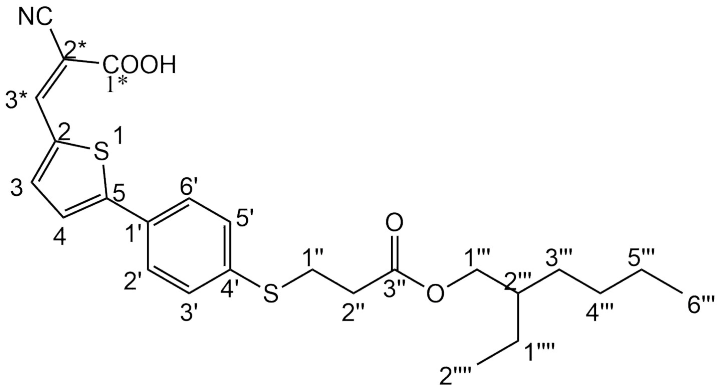

5.4.3 Synthesis and characterization of *push-pull* heterocyclic pyrene and naphtalene derivatives

A set of five heterocyclic molecules of the *push-pull* type, were designed and synthesized, functionalyzed with pyrene and naphthalene moieties (Figure 5.5). As in the previous subsection, the full name of the molecule is mentioned only once in the title of its synthesis section. Through all thesis only the number of the compounds will be used. Table 5.4 presents the name of the compounds and the corresponding number. The synthesis of the five molecules cited above was performed using similar procedures already described. Therefore, this subsection will be divided into four main procedures: (i) the synthesis of thiophene carboxylic acid derivatives, (ii) synthesis of the π-spacer, (iii) the synthesis of aldehydes, and (iv) the synthesis of the cyanoacetic acid derivatives.

(i) General procedure for synthesis of thiophene carboxylic acid derivatives 4 and 5

5-Bromo-2-thiophenecarboxylic acid (0.3 mmol) was coupled with boronic compounds of naphthalene or pyrene (0.36 mmol) under Suzuki-Miyaura conditions in 5 mL of DME. The $Pd(PPh_3)_4$ 5% served as the catalyst, and Na_2CO_3 (2 M, 300 μL) was used as the base. The reaction mixture was heated to 80 °C and stirred for 5 and 6 h, respectively, under a N_2 atmosphere. After cooling, the solid that precipitated was filtered and washed three times with H_2O and finally with MeOH. The structures

of the pure compounds as a grey (molecule **4**) or a green solid (molecule **5**), were confirmed by ^{1}H NMR in DMSO-d_6 and MS.

Table 5.4: Name of compounds presented in subsection 5.4.3, and their corresponding numbers.

Name of compound	Number of compound
5-(Naphthalen-1-yl)thiophene-2-carboxylic acid	**4**
5-(Pyren-1-yl)thiophene-2-carboxylic acid	**5**
5-(7-Bromobenzo[*c*][1,2,5]thiadiazol-4-yl)thiophene-2-carbaldehyde	**6a**
5-(7-(Pyren-1-yl)benzo[*c*][1,2,5]thiadiazol-4-yl)thiophene-2-carbaldehyde	**6b**
2-Cyano-3-(5-(7-(pyren-1-yl)benzo[*c*][1,2,5]thiadiazol-4-yl)thiophen-2-yl)acrylic acid	**6**
7-(Pyren-1-yl)benzo[*c*][1,2,5]thiadiazole-4-carbaldehyde	**7b**
2-Cyano-3-(7-(pyren-1-yl)benzo[*c*][1,2,5]thiaiazol-4-yl)acrylic acid	**7**
5′-(Pyren-1-yl)-[2,2′-bithiophene]-5-carbaldehyde	**8b**
2-Cyano-3-(5′-(pyren-1-yl)-[2,2′-bithiophen]-5-yl)acrylic acid	**8**

Synthesis of 5-(naphthalen-1-yl)thiophene-2-carboxylic acid (4)

The pure compound precipitated as a grey solid during the reaction (59% yield). ^{1}H NMR (400 MHz, DMSO-d_6), δ (ppm): 8.20-8.23 (m, 1H, 3-H), 7.99-7.97 (m, 1H, 4-H), 7.94-7.91 (m, 1H, 8-H′), 7.56-7.53 (m, 4H, 2′-H, 4′-H, 5′-H, 7′-H), 7.29-7.28 (m, 1H, 6′-H), 7.11-7.10 (m, 1H, 3′-H) (See Figure T.1, Appendix T). HRMS: (ESI, negative mode) m/z for $C_{15}H_9O_2S$, calcd 253.0315; found 253.032874, ([M-H]$^-$) (See Figure T.2, Appendix T).

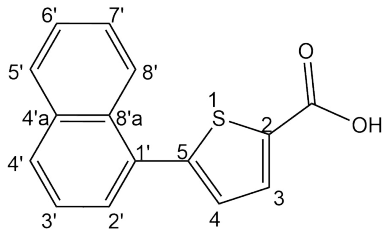

Synthesis of 5-(pyren-1-yl)thiophene-2-carboxylic acid (5)

The pure compound precipitated as a green solid during the reaction (72%). ^{1}H NMR (400 MHz, DMSO-d_6), δ (ppm): 8.52 (d, 1H, J=9.2 Hz, 2′-H), 8.33-8.21 (m, 6H, 3′-H, 4′-H, 5′-H, 6′-H, 7′-H, 8′-H), 8.11-8.09 (m, 2H, 3-H, 4-H), 7.38 (d, 1H, J=4 Hz, 9′-H), 7.27 (d, 1H, J=4 Hz, 10′-H) (See Figure U.1, Appendix U). MS m/z (%)= 327.04220 ([M-H]$^-$, 100); and 283.0500 ([M-H-CO_2]$^-$, 35) (See Figure U.2, Appendix U).

.

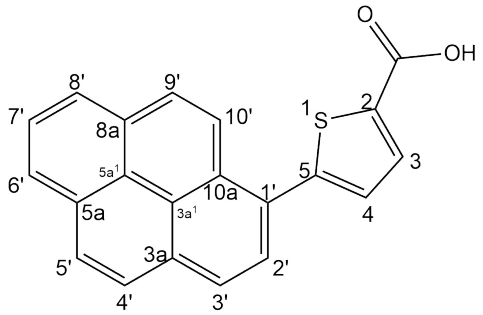

(ii) Synthesis of π-spacer: compound 5-(7-bromobenzo[c][1,2,5]thiadiazol-4-yl)thiophene-2-carbaldehyde (6a)

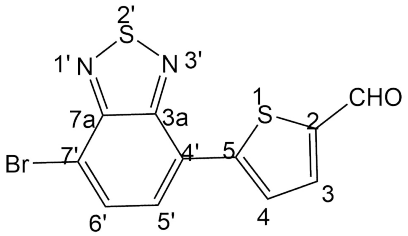

The precursor aldehyde **6*a*** was synthesized following the previously reported procedure (FERNANDES *et al.*, 2018). The coupling between 4,7- dibromobenzo [*c*] 1,2,5- thiadiazole (0.7 mmol) and 5-formyl-2-thiopheneboronic (0.5 mmol) was catalyzed with $Pd(PPh_3)_4$ (5% mmol) in the presence of 2 M of Na_2CO_3 in DME at 80 °C, by stirring during 6 h under nitrogen atmosphere. The reaction was monitored by TLC (eluent: P.E/EtOAc 2:1). After cooling, part of the product precipitated as an orange solid, which was filtered and washed with chloroform. The reaction mixture was transferred into a separatory funnel, and 20 mL of chloroform and 20 mL of a saturated solution of NaCl were added. The organic layer was separated from the aqueous layer. The organic layer was washed with distilled H_2O (20 mL x 2 times). Finally, the organic layer was dried with $MgSO_4$, filtered and the solvent evaporated. The crude solids obtained were purified by column chromatography on silica gel using as eluents Hex and DCM (from 10:0 to 2:8) giving the pure compound **6*a*** as an orange solid (23%). ^{1}H NMR (400 MHz, $CDCl_3$), δ (ppm): 9.99 (s, 1H, CHO), 8.20 (d, 1H, J= 4 Hz, 3-H), 7.93 (d, 1H, J=7.6 Hz, 6′-H), 7.86-7.85 (m, 2H, 4-H, 5′-H) (See

Figure V.1, Appendix V).

(iii) General procedure for the synthesis of aldehydes 6b, 7a and 8a through Suzuki-Miyaura coupling

The general synthesis of the pyrene precursors was carried out following Suzuki-Miyaura conditions previously reported by Raposo and coworkers (FERNANDES *et al.*, 2018). Briefly, pyrenyl boronic acid (0.29, 0.18, 0.36 mmol to obtain **6***b*, **7***b*, and **8***b*, respectively) was coupled with the bromo precursors **6***a* (0.24 mmol), **7***a* (0.15 mmol) and **8***a* (0.3 mmol) using $Pd(PPh_3)_4$ (5% mol), Na_2CO_3 (2M, 2 eq) in 6 mL DME. The reaction mixture was heated at 82 °C under an inert atmosphere and the progress of reaction was monitored by TLC, to determinate the reaction time (22 h for **6***b*, 18 h for **7***b*, 14 h for **8***b*). The first two compounds precipitated pure during the reaction and were filtered and washed with DME, H_2O and Et_2O. The crude compound **8***b*, precipitated from the reaction mixture, but part was still present in the organic phase. Therefore, chloroform (20 mL) and a saturated solution of NaCl (20 mL) were added and the organic and aqueous phases were separated. The organic layer was washed with H_2O (3x15 mL) and finally with an aqueous solution of NaOH (10%, 15 mL). The organic phase collected was dried with $MgSO_4$, filtered and the solvent evaporated. The pure product was obtained after column chromatography on silica gel, using a mixture of eluent with increasing polarity: Hex/DCM from 1:1 to 3:7.

Synthesis of 5-(7-(pyren-1-yl)benzo[*c*][1,2,5]thiadiazol-4-yl)thiophene-2-carbaldehyde (6b)

The pure compound was obtained as a red-purple solid (59%). ^{1}H NMR (400 MHz, $CDCl_3$), δ (ppm): 10.04 (s, 1H, CHO), 8.35-8.33 (m, 2H), 8.27-8.17 (m, 6H), 8.07-8.00 (m, 2H), 7.93-7.89 (m, 3H) (See Figure V.2, Appendix V).

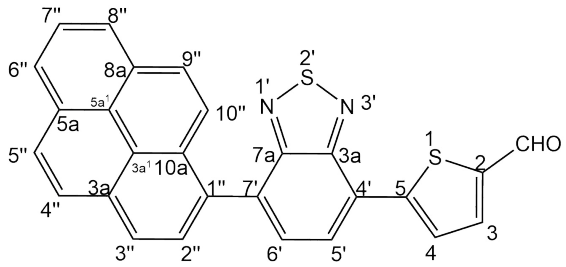

Synthesis of 7-(pyren-1-yl)benzo[*c*][1,2,5]thiadiazole-4-carbaldehyde (7b)

The pure compound precipitated as an orange solid during the reaction (61%). ^{1}H NMR (400 MHz, $CDCl_3$), δ (ppm): 10.91 (s, 1H, CHO), 8.46 (d, 1H, J=7.2 Hz, 5-H), 8.34 (d, 1H, J=8 Hz, Ar-H), 8.27 (dd, 1H, J_1=0.4 Hz, J_2=7.6 Hz, 7′-H), 8.22-8.15 (m, 4H, Ar-H), 8.06-8.02 (m, 3H, Ar-H, 6-H), 7.84 (d, 1H, J=9.2 Hz, 10′-H) (See Figure X.1, Appendix X).

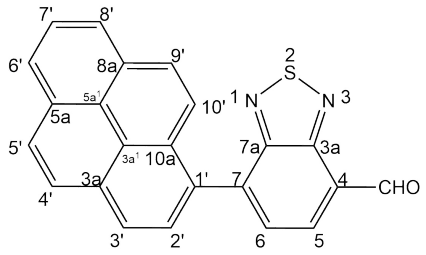

Synthesis of 5′-(pyren-1-yl)-[2,2′-bithiophene]-5-carbaldehyde (8b)

The pure compound was obtained as an yellow solid after silica gel column chromatography (81%). ^{1}H NMR (400 MHz, $CDCl_3$), δ (ppm): 9.91 (s, 1H, CHO), 8.54 (d, 1H, J=9.2 Hz, 2″-H), 8.25-8.21 (m, 3H, Ar-H), 8.16-8.06 (m, 5H, Ar-H), 7.73 (d, 1H, J=4 Hz, 4-H), 7.53 (d, 1H, J=4 Hz, 3-H), 7.37-7-35 (m, 2H, 3′-H, 4′-H) (See Figure Y.1, Appendix Y).

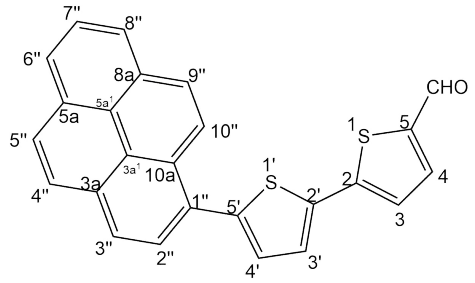

(iv) General procedure for the synthesis of cyanoacetic acid derivatives 6, 7 and 8

The aldehydes of pyrene **6***b* (0.15 mmol), **7***b* (0.12 mmol) and **8***b* (0.13 mmol) reacted with cyanoacetic acid (0.18 mmol, 0.15 mmol, 0.15 mmol, respectively) through a Knoevenagel condensation using piperidine as catalyst (63 μL **6***b*, 50.4 μ **7***b*, 5c; 53 μ **8***b*). The reaction mixtures of **6**, **7** and **8** were refluxed in acetonitrile (6 mL) for 30 h, 17 h and 13 h, respectively, under N_2. The precipitates formed in the reaction mixture of **7** and **8** were filtrated and washed with ACN and EtOAc (three times), giving the pure desired products. The compound **6** also precipitated during the reaction. However an amount persisted in the organic phase, which was extracted as usual and

evaporated. Therefore, the crude compound was purified through silica-gel column chromatography in order to obtain the pure product.

Synthesis of 2-cyano-3-(5-(7-(pyren-1-yl)benzo[*c*][1,2,5]thiadiazol-4-yl)thiophen-2-yl)acrylic acid (6)

The pure compound was obtained as a red-purple solid after purification by silica-gel column chromatography using Hex/DCM from 10:0 to 5:5; in a yield of 82%. ^{1}H NMR (400 MHz, DMSO-d_6, See Figure W.1, Appendix W), δ (ppm): 8.42-8.27 (m, 7H, 5′-H, 3-H, Ar-H), 8.23 (s, 1H, CH=C(CN)(CO_2H)), 8.18 (d, 1H, J=7.6 Hz, Ar-H), 8.10 (d, 1H, J=7.6 Hz, 8″-H), 8.06 (d, 1H, J=9.6 Hz, 9″-H), 7.97 (d, 1H, J=7.2 Hz, 6′-H), 7.90 (d, 1H, J=4.4 Hz, 4-H), 7.85 (d, 1H, J=9.2 Hz, 10″-H). MS m/z (%)= 512.0500 ([M-H]$^-$, 10.3), 485.2798 ([M-H-CN]$^-$, 100) (See Figure W.2, Appendix W).

.

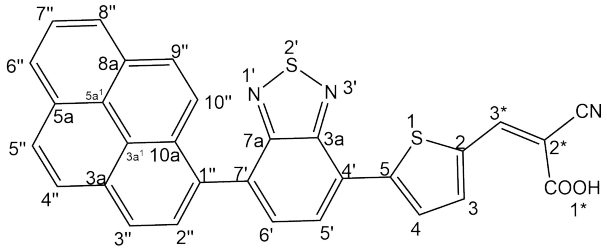

Synthesis of 2-cyano-3-(7-(pyren-1-yl)benzo[*c*][1,2,5]thiadiazol-4-yl)acrylic acid (7)

The pure compound precipitated from de reaction mixture as an orange solid after 17 h of reaction (yield: 74%). ^{1}H NMR (400 MHz, DMSO-d_6, See Figure X.2, Appendix X), δ (ppm): 8.87 (s, 1H, 3-H), 8.71 (dd, 1H, J_1=0.4 Hz, J_2=7.2 Hz, 5′-H), 8.42 (d, 1H, J=8 Hz, 2″-H), 8.35 (dd, 1H, J_1=0.8 Hz, J_2= 7.6 Hz, 7″-H), 8.30-8.27 (m, 3H, 4″-H, 5″-H, 6″-H), 8.19 (d, J=8 Hz, 3″-H), 8.12-8.07 (3H, 8″-H, 9″-H, 6′-H), 7.84 (d, 1H, 9.2 Hz, 10″-H). HRMS: (ESI, negative mode) m/z for $C_{25}H_{12}N_3S$, calcd 386.0735; found 386.0757, ([M-H-CO_2]$^-$, 100) (See Figure X.3, Appendix X).

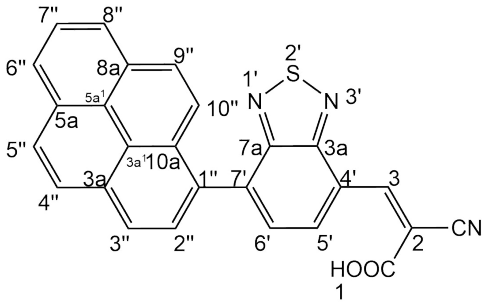

Synthesis of 2-cyano-3-(5′-(pyren-1-yl)-[2,2′-bithiophen]-5-yl)acrylic acid (8)

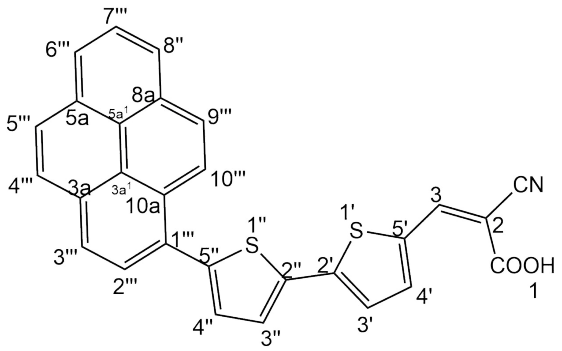

The pure molecule was obtained as a yellow solid which precipitate after 13 h of reaction (yield: 69%). ^{1}H NMR (400 MHz, DMSO-d_6, See Figure Y.2, Appendix Y), δ (ppm): 8.53 (d, 1H, J=9.2 Hz, 2‴-H), 8.37-8.18 (m, 7H, Ar-H), 8.13 (d, 1H, J=7.6 Hz, 10‴-H), 8.09 (s, 1H, 3-H), 7.72 (d, 1H, J=4 Hz, 4′-H), 7.67 (d, 1H, J=4 Hz, 3′-H), 7.55 (d, 1H, J=4 Hz, 3″-H), 7.52 (d, 1H, J=4 Hz, 4″-H). MS-ESI m/z (%)= 416.0532 ([M-H-CO_2]$^-$, 100); 460.0426 ([M-H]$^-$, 60).

5.4.4 Development of the sensing platform

The SLG surface was modified by incubating 20μL of a 1 mM solution of *push-pull* heterocyclic molecule, dissolved in DMF, for 4 h to form a molecule-SLG monolayer. This modification was performed using the five synthesized molecules, **4-8** (see Figure 5.5). To construct the sensing platform, the carboxyl groups on the molecule-SLG surface were first activated by incubating the surface with 20 μL of an aqueous solution containing 0.4 M EDC and 0.02 M NHS for 30 min. Following activation, 20 μL of 1 μM of DNA-probe in PB was incubated on the surface overnight to enable covalent bonding. To prevent non-specific interactions, unreacted carboxyl groups were blocked by incubating the surface with ethanolamine in PB for 30 min. Following this, the platform was incubated with 10 mM hybridization PB solution (the medium in which the DNA probe is dissolved) for 1 hour, repeated two or three times, this stage is considered as the blank measurement. Finally, the functionalized surface was exposed to 20 μL of target DNA at different concentrations,ranging from 1 aM to 100 fM in hybridization PB, and incubated for 1 hour to enable hybridization.

5.4.5 Electrochemical measurement

Electrochemical measurements were performed using graphene electrolyte-gated field-effect transistor devices, which were fabricated and supplied by the International Iberian Nanotechnology Laboratory (INL). The setup consisted of a two-electrode

configuration, where the counter electrode and reference electrode were short-circuited and connected to the transistor gate, while the working electrode corresponded to the SLG channels. All electrochemical measurements were performed in PB solution, serving as the supporting electrolyte.

EIS measurements were carried out at the OCP, across a frequency range of 100 kHz to 0.05 Hz, using a sinusoidal perturbation with a peak-to-peak amplitude of 10 mV. Initially, the equilibrium ν was identified from the Nyquist plot of C^* (acquired from EIS data as described in subsection. 2.2.5, in chapter 2), where the semicircle closes (see Figure Z.1, Appedix Z). This ν value was then applied for subsequent EIS measurements while systematically varying the applied potential from -2 V to 2 V, to construct the DOS profiles. The C_q at the Dirac point was determined and employed as the transduction signal in the DNA sensing assays. This methodology was applied throughout all stages of sensor platform fabrication, ensuring that modifications to the interface, were accounted for in the resulting variations in ν.

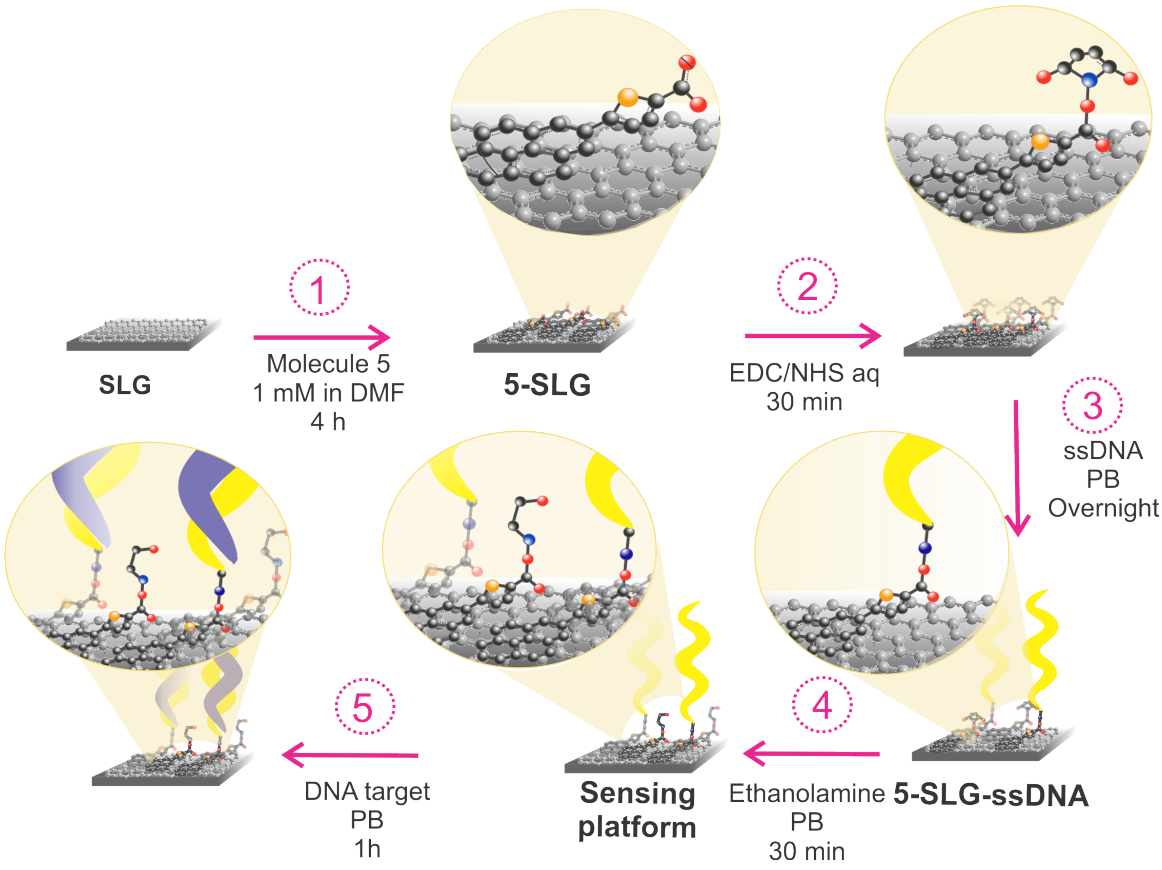

Figure 5.9: Sequential stages involved in constructing the sensing platform. (1) Surface modification: A pristine SLG electrode is functionalized with a *push-pull* heterocyclic molecule; (2) Interface activation of the carboxylic groups. (3) DNA probe immobilization. (4) Blocking of unreacted Residual activated carboxylic groups. (5) DNA hybridization assay: The functionalized surface is exposed to a complementary DNA target, which hybridizes with the immobilized DNA probe.

Source: Author (2024)

References

A HERNANDEZ MUNOZ, J.; J JUNIOR, J.; MARTINS DA SILVA, F. Radziszewski reaction: an elegant, easy, simple and efficient method to synthesise imidazoles. **Current Organic Synthesis**, Bentham Science Publishers, v. 11, n. 6, p. 824–834, 2014a.

A HERNANDEZ MUNOZ, J.; J JUNIOR, J.; MARTINS DA SILVA, F. Radziszewski reaction: an elegant, easy, simple and efficient method to synthesise imidazoles. **Current Organic Synthesis**, Bentham Science Publishers, v. 11, n. 6, p. 824–834, 2014b.

ALIAKBAR TEHRANI, Z.; KIM, K. S. Functional molecules and materials by π-interaction based quantum theoretical design. **International Journal of Quantum Chemistry**, Wiley Online Library, v. 116, n. 8, p. 622–633, 2016.

BAE, J. S. *et al.* Clinical utility of TERT promoter mutations and ALK rearrangement in thyroid cancer patients with a high prevalence of the BRAF V600E mutation. **Diagnostic pathology**, Springer, v. 11, p. 1–10, 2016.

BAHETI, A. *et al.* Pyrene-based organic dyes with thiophene containing π-linkers for dye-sensitized solar cells: optical, electrochemical and theoretical investigations. **Physical Chemistry Chemical Physics**, Royal Society of Chemistry, v. 13, n. 38, p. 17210–17221, 2011.

BATISTA, R. M.; COSTA, S. P., *et al.* Synthesis and characterization of novel (oligo) thienyl-imidazo-phenanthrolines as versatile π-conjugated systems for several optical applications. **Tetrahedron**, Elsevier, v. 64, n. 39, p. 9230–9238, 2008.

BATISTA, R. M.; OLIVEIRA, E., *et al.* Synthesis and ion sensing properties of new colorimetric and fluorimetric chemosensors based on bithienyl-imidazo-anthraquinone chromophores. **Organic Letters**, ACS Publications, v. 9, n. 17, p. 3201–3204, 2007.

BRANDÃO, S. T. *et al.* Designing Quantum Capacitive Peptide Interfaces for Electroanalytical Applications. **Analytical Chemistry**, ACS Publications, v. 95, n. 36, p. 13470–13477, 2023.

BUENO, P. R. **The Nanoscale Electrochemistry of Molecular Contacts**. Springer, 2018. (SpringerBriefs in Applied Sciences and Technology). ISBN 978-3-319-90486-3.

BUENO, P. R. *et al.* The density-of-States and equilibrium charge dynamics of redox-active switches. **Electrochimica Acta**, Elsevier, v. 387, p. 138410, 2021.

BUREŠ, F. Fundamental aspects of property tuning in push–pull molecules. **RSC Advances**, Royal society of chemistry, v. 4, n. 102, p. 58826–58851, 2014.

CHEN, L. *et al.* Phosphine-Free Palladium Catalytic System for the Selective Direct Arylation of Furans or Thiophenes bearing Alkenes and Inhibition of Heck-Type

Reaction. **Advanced Synthesis & Catalysis**, Wiley Online Library, v. 353, n. 14-15, p. 2749–2760, 2011.

FERAPONTOVA, E. E. DNA electrochemistry and electrochemical sensors for nucleic acids. **Annual review of analytical chemistry**, Annual Reviews, v. 11, n. 1, p. 197–218, 2018.

FERNANDES, S. S. *et al.* Benzothiadiazole derivatives functionalized with two different (hetero) aromatic donor groups: Synthesis and evaluation as TiO_2 sensitizers for DSSCs. **Dyes and Pigments**, Elsevier, v. 151, p. 89–94, 2018.

FERREIRA, R. C. M.; RAPOSO, M. M. M.; COSTA, S. P. Heterocyclic amino acids as fluorescent reporters for transition metals: Synthesis and evaluation of novel furylbenzoxazol-5-yl-l-alanines. **New Journal of Chemistry**, Royal Society of Chemistry, v. 42, n. 5, p. 3483–3492, 2018.

GARROTE, B. L.; SANTOS, A.; BUENO, P. R. Label-free capacitive assaying of biomarkers for molecular diagnostics. **Nature Protocols**, Nature Publishing Group UK London, v. 15, n. 12, p. 3879–3893, 2020.

GARROTE, B. L.; SÁNCHEZ, Y. P., *et al.* Electron transmittance by means of quantum capacitive states as a signal amplification mechanism for biosensing applications. **Sensors and Actuators B: Chemical**, Elsevier, v. 399, p. 134786, 2024.

GELENS, E. *et al.* Efficient library synthesis of imidazoles using a multicomponent reaction and microwave irradiation. **Molecular Diversity**, Springer, v. 10, p. 17–22, 2006.

GONÇALVES, R. C. *et al.* Bioimaging of lysosomes with a BODIPY pH-dependent fluorescent probe. **Molecules**, MDPI, v. 27, n. 22, p. 8065, 2022.

HALPERIN, A.; BUHOT, A.; ZHULINA, E. On the hybridization isotherms of DNA microarrays: the Langmuir model and its extensions. **Journal of Physics: Condensed Matter**, IOP Publishing, v. 18, n. 18, s463, 2006.

HUSSON, J.; DEHAUDT, J.; GUYARD, L. Preparation of carboxylate derivatives of terpyridine via the furan pathway. **Nature Protocols**, Nature Publishing Group UK London, v. 9, n. 1, p. 21–26, 2014.

ITOH, T.; MASE, T. Practical thiol surrogates and protective groups for arylthiols for Suzuki- Miyaura conditions. **The Journal of Organic Chemistry**, ACS Publications, v. 71, n. 5, p. 2203–2206, 2006.

KANG, S.-Y. *et al.* Chemosensing properties and logic gate behaviors of graphene quantum dot-appended terpyridine. **Materials Science and Engineering: C**, Elsevier, v. 99, p. 657–668, 2019.

LI, Y. *et al.* Self-assembly of intramolecular charge-transfer compounds into functional molecular systems. **Accounts of Chemical Research**, ACS Publications, v. 47, n. 4, p. 1186–1198, 2014.

LIU, J.; TANG, J.; GOODING, J. J. Strategies for chemical modification of graphene and applications of chemically modified graphene. **Journal of Materials Chemistry**, Royal Society of Chemistry, v. 22, n. 25, p. 12435–12452, 2012.

LOPES, L. C.; SANTOS, A.; BUENO, P. R. Measuring quantum conductance and capacitance of graphene using impedance-derived capacitance spectroscopy. **Carbon**, Elsevier, v. 184, p. 821–827, 2021.

LOPES, L. C.; PINZÓN, E. F., *et al.* Electrochemical measurement of the electronic structure of graphene via quantum mechanical rate spectroscopy. **Electrochimica Acta**, Elsevier, v. 480, p. 143837, 2024.

LUCAS GARROTE, B. *et al.* Reagentless quantum-rate-based electrochemical signal of graphene for detecting SARS-CoV-2 infection using nasal swab specimens. **ACS Sensors**, ACS Publications, v. 7, n. 9, p. 2645–2653, 2022.

MALYTSKYI, V.; GADENNE, V., *et al.* Synthesis and characterization of thiophene-based push-pull chromophores for tuning the electrical and optical properties of surfaces with controlled SAM formation. **Tetrahedron**, Elsevier, v. 73, n. 39, p. 5738–5744, 2017.

MALYTSKYI, V.; SIMON, J.-J., *et al.* Synthesis, self-assembly and characterization of a novel push–pull thiophene-based chromophore on a gold surface. **RSC Advances**, Royal Society of Chemistry, v. 5, n. 33, p. 26308–26315, 2015.

NAITHANI, S. *et al.* Imidazo [4, 5-f][1, 10] phenanthroline based luminescent probes for anion recognition: Recent achievements and challenges. **Coordination Chemistry Reviews**, Elsevier, v. 475, p. 214894, 2023.

NIETO, E. F. P. *et al.* Quantum rate electrodynamics and resonant junction electronics of heterocyclic molecules. **Electrochimica Acta**, Elsevier, v. 501, p. 144749, 2024.

OKDA, H. E. *et al. N*, *N*-Diphenylanilino-heterocyclic aldehyde-based chemosensors for UV-vis/NIR and fluorescence Cu (II) detection. **New Journal of Chemistry**, Royal Society of Chemistry, v. 43, n. 19, p. 7393–7402, 2019.

OLIVA, M. M. *et al.* Structure- Property Relationships in Push- Pull Amino/Cyanovinyl End-Capped Oligothiophenes: Quantum Chemical and Experimental Studies. **The Journal of Organic Chemistry**, ACS Publications, v. 71, n. 20, p. 7509–7520, 2006.

OLYMPIOS, N. *et al.* TERT promoter alterations in glioblastoma: a systematic review. **Cancers**, MDPI, v. 13, n. 5, p. 1147, 2021.

ORGANIZATION, W. I. P. E. Verdin; U. Scott. **Inhibitors for HDAC8**. Aug. 2008. WO2008101186A1. Patent.

PALANI, P.; KARPAGAM, S. Conjugated polymers–a versatile platform for various photophysical, electrochemical and biomedical applications: a comprehensive review. **New Journal of Chemistry**, Royal Society of Chemistry, v. 45, n. 41, p. 19182–19209, 2021.

PINZÓN, E. F. *et al.* Quantum rate as a spectroscopic methodology for measuring the electronic structure of quantum dots. **Journal of Materials Chemistry C**, Royal Society of Chemistry, v. 12, n. 13, p. 4606–4617, 2024.

ULMAN, A. Formation and structure of self-assembled monolayers. **Chemical Reviews**, ACS Publications, v. 96, n. 4, p. 1533–1554, 1996.

WANG, T. *et al.* Fluorescent chemosensors based on conjugated polymers with *N*-heterocyclic moieties: two decades of progress. **Polymer Chemistry**, Royal Society of Chemistry, v. 11, n. 18, p. 3095–3114, 2020.

Conclusions

The QRT approach establishes that ET reactions in redox-tagged peptide SAMs is inherently a quantum event, evidenced by the experimental determination of C_q, a measurable quantum property associated with electronic state occupancy during ET, which directly links with k and G, which are two parameters traditionally studied separately in chemistry and physics.

Accordingly, this thesis presented a quantum-based methodology based on QRT for determining k in redox-tagged peptide SAMs. By integrating time-dependent electrochemical techniques, particularly CV at low scan rates (where the condition $i \propto s$ hold), C_q was determined at V_F. As G reached its quantum limit G_0, k was calculated via the τ of a quantum RC circuit $\tau = R_q C_q = 1/k$, incorporating both spin g_s and electrostatic g_e degeneracies, as $k = g_e g_s e^2/hCq$. This QRT-based approach was further validated through EIS and yielded k values consistent with those obtained via Laviron's method, despite the fundamentally different theoretical interpretations of k.

The fundamental role of electroneutrality in QRT, defined by the relationship $C_q \sim C_e$, which represents the coupling between external (solvent) and internal (electronic structure) energy contributions, was demonstrated through the analysis of explicit solvent effects on the electrodynamics of ET reactions in redox-tagged peptide SAMs. Building on these findings, the equivalence between electrochemical energy in QRT and the reorganization energy λ was also established, further reinforcing the theoretical framework linking C_q to solvent-mediated ET dynamics.

The influence of the electrochemical environment, particularly the binary mixed solvent with a fixed supporting electrolyte, was evident in κ, the scattering parameter of G. Given that k is governed by both C_q and G, and C_q remained constant across varying water/ACN ratios, this explicit solvation effect on $k = g_e G/C_q$ occurs through κ, leading to variations in $E_\mu = hk$. When compared to a previous QRT-based study on solvent effects in ET, where the system followed the implicit solvation behavior that agrees with Marcus ET theory, these findings highlight the existence of distinct solvation mechanisms. This contrast underscores the limitations of classical ET models and demonstrates how QRT provides a more comprehensive framework for distinguishing and analyzing solvent effects in electrochemical systems.

The sensitivity of κ to structural modifications in redox-tagged SAMs backbone

was demonstrated by evaluating both the linker group and the molecular bridge. κ exhibited a strong dependence on molecular structure, with bidentate coordination in the linker leading to higher κ values compared to monodentate coordination. Additionally, variations in the peptide bridge also modulated κ. However, while κ influenced the kinetics of the process, the dominant factor governing k was the availability of electronic states, quantified by N. Both the linker and bridge studies revealed a clear inverse correlation, $N \propto 1/k$, underscoring that although κ is responsive to molecular structure, N is dominant for ET kinetics in this situation.

A promising synthetic route for *push-pull* heterocyclic molecules designed for molecular assembly on gold electrodes, with the aim of accessing their electrodynamics and electronic structure through the QRT framework, was here proposed. Heterocyclic molecules incorporating a carboxylic acid head group and π-conjugated systems were designed and synthesized to enhance $\pi - \pi$ stacking interactions with graphene electrodes, enabling the construction of molecular-SLG junctions. Through QRS analysis, it was possible to assess the electronic structure of molecular junctions and identify a transduction signal suitable for biosensing applications. The molecular-SLG system demonstrated its effectiveness for genosensor applications, highlighting its potential in the development of biological sensors and related-devices. The synthetic strategy presented here, combined with QRT-based analysis, establishes a solid foundation for advancing molecular biosensing technologies and deepening our understanding of quantum electrodynamics processes in electrolyte environments.

In conclusion, this study reinforces QRT as a powerful framework for integrating quantum mechanical principles into electrochemical methodologies, enabling the investigation of quantum phenomena in electrochemical environments under standard laboratory conditions. By designing and synthesizing molecules capable of be immobilized on electrode and featuring key electronic properties, such as redox-active centers or π-conjugated orbitals, critical factors were identified to influence quantum rate dynamics at the molecular level. This approach advances our understanding of ET in peptide-based redox systems and ET_p in *push-pull* heterocyclic molecules, expanding the potential for developing applications in molecular electronics and laying a solid foundation for next generation of biological sensors grounded on quantum mechanical principles.

Appendixes

Appendix A

Fc-EAACC characterization

The peptide Fc-Glu-Ala-Ala-Cys-Cys-NH_2 (Figure A.1*a*), was obtained with a purity higher than 93% as assessed by analytical HPLC. The retention time was 14.45 minutes using a linear gradient elution from 5% to 95% of solvent B over 30 min at a flow rate of 1 mL min^{-1}, with UV detection at 220 nm (see Figure A.1*b*). The peptide's identity was confirmed by ESI-MS, showing a predominant peak corresponding to the theoretical molar mass of 733.16 g mol^{-1} (see Fig. A.1*c*).

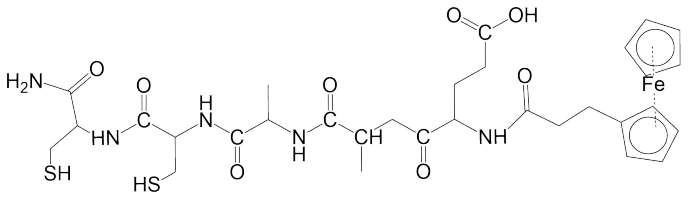

(a)

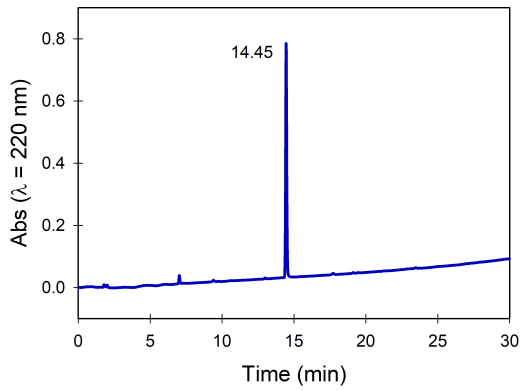

(b)

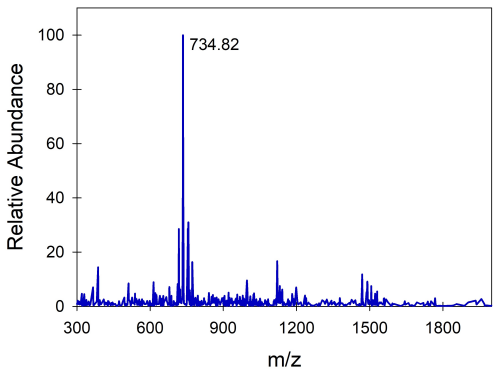

(c)

Figure A.1: (a) The skeletal structural formula of Fc-Glu-Ala-Ala-Cys-Cys-NH_2. (b) Chromatogram of the purified peptide with retention time of 14.45 min. (c) Mass spectrum of the peptide, obtained using a Brucker system in positive mode: 734.82 g mol^{-1}, corresponding to the peak of 14.45 min in (b).

Source: Author (2024).

Appendix B

Electrochemical characterization Fe-pep-SAM in mixed solvent

The successful immobilization of the Fc-pep-SAM on electrode was confirmed by the linear relationship between i_{pa} and i_{pc} with s (see Figure.B.1*a*). The CVs recorded at 0.2 V s^{-1} (see Figure B.1*b*) for the three different water/ACN mixtures, display a quasi-reversible electrochemical profile (HONEYCHURCH; RECHNITZ, 1998). This conclusion is based on the symmetric, Gaussian-shaped peaks observed, corresponding to Fc $\rightarrow$ $Fc^+ + e^-$ and $Fc^+ + e^-$ $\rightarrow$ Fc redox processes. Key indicators of reversibility include $\Delta V_p < 19$ mV, $i_{pa}/i_{pc} \approx 1$, and FWHM close to 90.6 mV are summarized in Table.B.1. As the % of ACN decreases, less energy is required to align the electronic states of the electrode and the redox species, which is reflected in the decrease in V_F (see Figure B.1 and Table B.1). The meaning of this shift is sensitive probe of the local microenvironment within the monolayer. Also, depending on the polarity of the solvent, it could lead conformational transformation of the redox moieties in the monolayer, resulting in changes of frontier orbitals distribution (i.e., HOMO-LUMO) and therefore changes of electronic overlap (NIKITINA *et al.*, 2018).

Table B.1: Reversibility parameters acquired from CV conducted at 0.2 Vs^{-2} in three different electrolytes: 20 mM $TBAClO_4$ in aqueous mixtures containing 20%, 50%, and 80% ACN. Measurements were conducted with three independently modified electrodes for each electrolyte system. The SD is presented for each value.

% ACN	i_{pa}/i_{pc}	V_F	ΔV_p mV	FWHM
20	0.98 ± 0.01	346 ± 2	19 ± 2	72 ± 0
50	0.97 ± 0.02	389 ± 1	16 ± 1	82 ± 0
80	0.97 ± 0.04	413 ± 3	13 ± 2	73 ± 4

Impedance-derived capacitance and equivalent circuit analysis: The characteristic equivalent circuit of the quantum RC model for the interface was determined by fitting the complex electrochemical capacitance using the equivalent circuit shown in

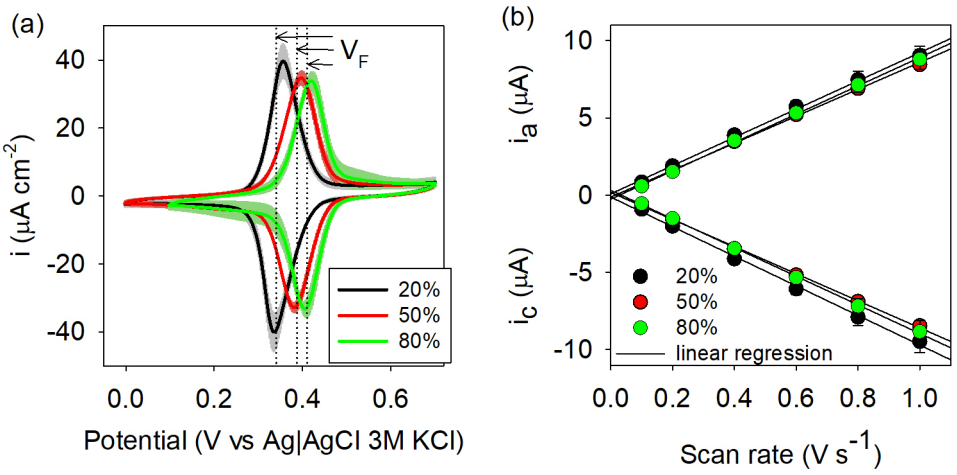

Figure B.1: (a) Comparison of representative CVs for redox-tagged peptide SAM in each electrolyte system, recorded at 0.2 Vs^{-1}. The displayed voltammogram is the average of electrochemical measurements conducted in triplicate. The standard deviation is represented by the shadow of the CV curves. (b) Linear regression *i versus s* from CVs recorded at *s* below 1 V s^{-1}. Each point represents the average of three measurements taken from three independently prepared modified electrodes for each electrolyte system, with standard deviation (SD) bars shown.

Source: Author (2024)

Figure2.2. No variation was observed in the monolayer capacitance, both without ion ingress (C_m) and with ion relaxation (C_t), across the three different electrolytes. Similarly, there were no significant changes in the resistance associated with ion relaxation (R_t) or in the quantum channel resistance (R_{qt}). In contrast, the series resistance (R_s), which includes both the solution and contact resistances, varied across the different electrolytes. The differences in electrolyte composition likely influenced the contact resistance by affecting the molecular orientation of the monolayer and the efficiency of electron coupling at the electrode-molecule interface. While the resistance of the solution would typically increase with a higher ACN content in the electrolyte, due to ACN's lower dielectric constant, the contact resistance appears to have a more significant effect on the total R_s.

Table B.2: Equivalent circuit elements obtained for the binary aqueous mixed solvent containing 20 mM $TBAClO_4$ an different proportions of ACN.

Parameter	ACN		
	20%	50%	80%
$R_t(k\Omega)$	0.44 ± 0.00	0.52 ± 0.07	0.54 ± 0.08
C_m (μF)	0.11 ± 0.00	0.11 ± 0.00	0.11 ± 0.00
C_t (μF)	0.25 ± 0.02	0.26 ± 0.02	0.25 ± 0.02
$R_s(k\Omega)$	1.96 ± 0.02	1.64 ± 0.04	1.22 ± 0.02
R_{qt} (Ω)	45 ± 2	45 ± 6	46 ± 2

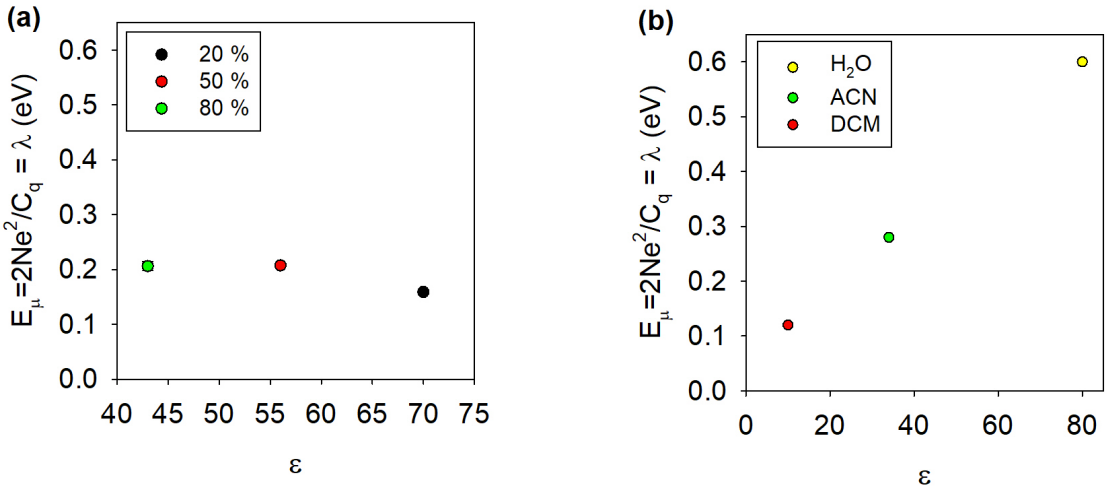

Figure B.2: Estimated λ value, obtained at the minimum point in E_μ distribution of Figure 3.4, in function of dielectric constantε of the electrochemical environments used to evaluate (a) Fc-pep-SAM and (b) Fc-C_{11}-SAM.

Appendix C

Bode plot- mixed solvents

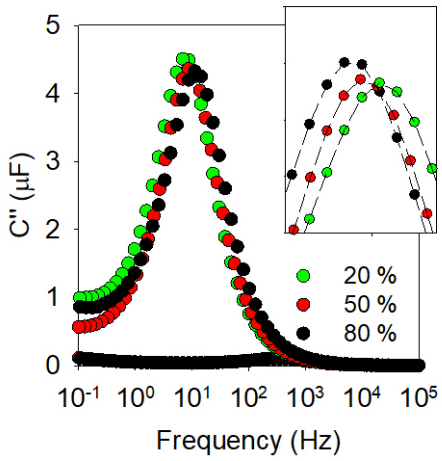

Figure C.1: Bode plot for the Fc-peptide SAM in mixed solvents containing 20 mM $TBAClO_4$ and varying proportions of H_2O-ACN (20%, 50%, and 80% ACN). The plot represent a representative experiment for each electrolyte composition. The inset shows a zoom of the maximum peak corresponding to the resonant frequency (f_r) at 6.8 $\pm$ 0.0 Hz (20 %), 9.3 $\pm$ 0.7 (50 %), 11.2 $\pm$ 0.0 (80 %), with values derived from three independent measurements and their corresponding standard deviations.

Source: Author (2024)

Appendix D

Fc-EAAC characterization

The peptide Fc-Glu-Ala-Ala-Cys-NH_2 was obtained with over 95% purity, in a retention time of 13.9 min under a linear gradient (5% to 95% solvent B) over 30 min at 1 mL min^{-1}, with UV detection at 220 nm. Its identity was verified by ESI-MS, which showed a peak corresponding to the theoretical molar mass of 631.1 g mol^{-1}.

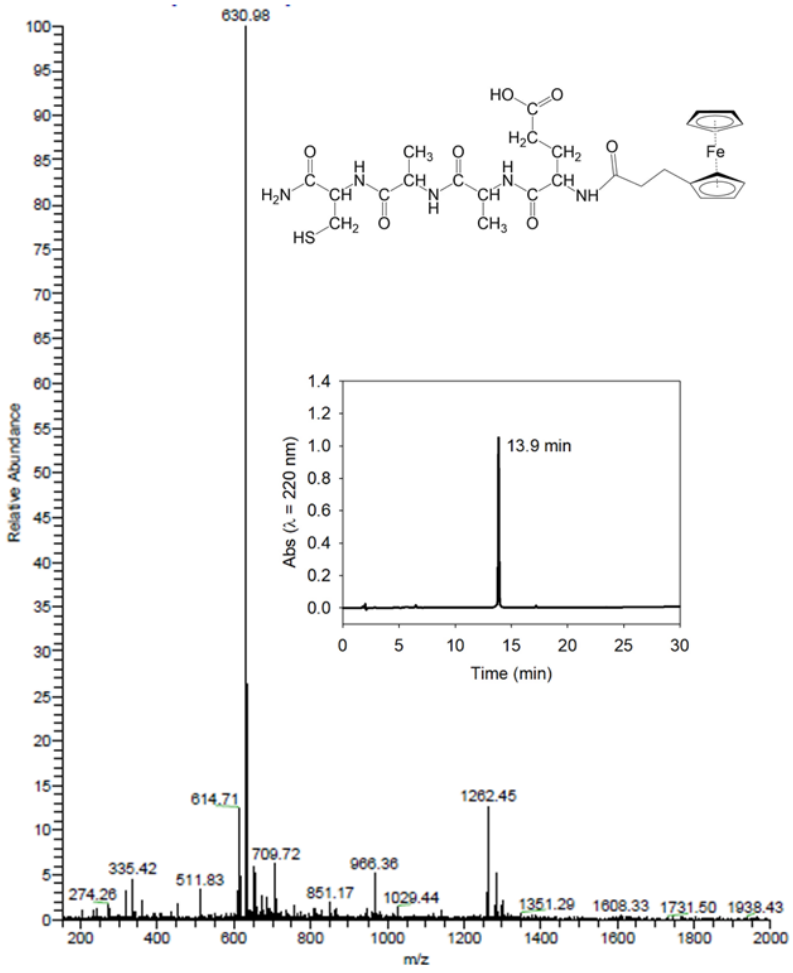

Figure D.1: Mass spectrum in positive mode: 630.98 g mol^{-1}. Inset, The skeletal structural formula, and the chromatogram of the purified peptide.

Source: Author (2024)

Appendix E

Fc-EAAK(L_a) characterization

The peptide Fc-Glu-Ala-Ala-Lys(L_a) was obtained with over 92% purity, in a retention time of 17.7 min under a linear gradient (5% to 95% solvent B) over 30 min at 1 mL min^{-1}, with UV detection at 220 nm. Its identity was verified by ESI-MS, which showed a peak corresponding to the theoretical molar mass of 844.5 g mol^{-1}.

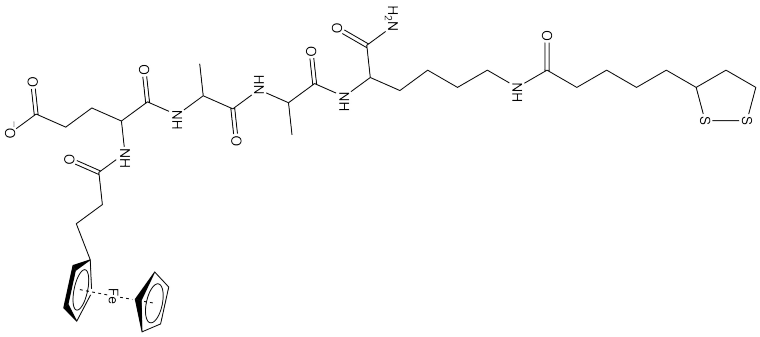

(a)

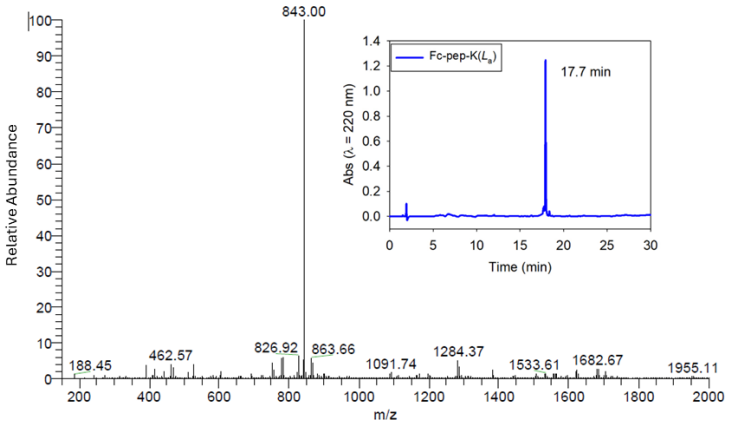

(b)

Figure E.1: (a) The skeletal structural formula of peptide, and (b) Mass spectrum and chromatogram profiles (inset) of the purified peptide Fc-pep-K(L_a).

Source: Author (2024).

Appendix F

SAM formation: linker group study

Linear regression plots of the highest i_{pa} and i_{pc} versus s, performed using CV, data obtained at scan rates ranging from 0.1 to 1 V s^{-1}, for (a) Fc-pep-C, (b) Fc-pep-CC, and (c) Fc-pep-K(L_a). The linear correlation between i and s demonstrated the formation of electrochemical diffusionless systems.

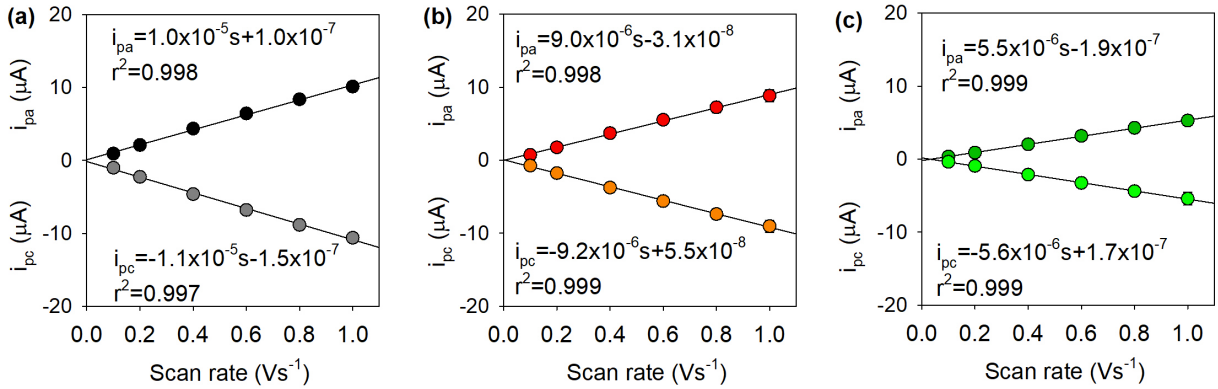

Figure F.1: i_{pa} and i_{pc} versus s Plots for (a) Fc-pep-C, (b) Fc-pep-CC, and (c) Fc-pep-K(L_a) SAM. The inset of each plot shows the linear equation and its corresponding r^2 value. The plots represent the average results with error bars, based on measurements from three different modified electrodes for each electro-active peptide SAM.

Source: Author (2024)

Appendix G

Electrochemical stripping

To examine the impact of different linker groups on the electrodynamics of redox-active peptide SAMs, three distinct peptide linkers were selected, each containing sulfur atoms for anchoring to the gold electrode surface. The Fc-pep-C peptide features a single thiol (-SH) from a Cys residue, Fc-pep-CC includes an additional thiol from a second Cys, and Fc-pep-K(L_a) incorporates a L_a moiety with a disulfide (-S-S) bond linked to Lys. The interaction between these sulfur-based linkers and the gold surface, which facilitates SAM formation, can be described by an oxidative addition mechanism (ULMAN, 1996). Before assessing the influence of the linkers on quantum rate kinetics within the framework of QRT, the nature of the gold-linker bond was investigated using electrochemical stripping analysis. While Fc-pep-C was expected to form a monodentate bond, Fc-pep-CC and Fc-pep-K(L_a) presented the potential for bidentate ligation due to the presence of two sulfur atoms. However, steric constraints could limit the formation of a second bond.

CV stripping experiments in 0.1 M NaOH, provided qualitative insights into the linker binding mode. The CV profile of Fc-pep-C SAM (see Figure G.1), exhibited two reduction peaks, corresponding to desorption from distinct crystallographic orientations of the polycrystalline gold electrode. In contrast, the Fc-pep-CC and Fc-pep-K(L_a) SAMs displayed an additional, more negative reduction peak, attributed to the desorption of a second sulfur-gold interaction, indicative of bidentate bonding. The assignment of desorption peaks to specific gold surface orientations was based on prior studies of thiolated SAMs conducted by Doneux and coworkers (DONEUX *et al.*, 2010), who compared the desorption CV profile of a decanethiol and other molecules SAM on polycrystalline gold electrode in basic media with that on single-crystal gold electrodes, such as Au(111), Au(100), Au(110), and Au(210). Therefore, the first reduction peak (V_1) was associated with desorption from Au(100), while the second (V_2) corresponded to Au(110). The presence of a third, more negative peak (V_3) exclusively in Fc-pep-CC and Fc-pep-K(L_a) suggested additional binding interactions, possibly involving Au(210) sites, which are characterized by step and kink defects (DONEUX *et al.*, 2010; NAITO; IIDA; TAKADA, 2019). This finding supports the conclusion that peptides with two sulfur atoms in their linker moieties can engage

in bidentate ligation, reinforcing the role of linker structure in dictating ET properties at the SAM-electrode interface.

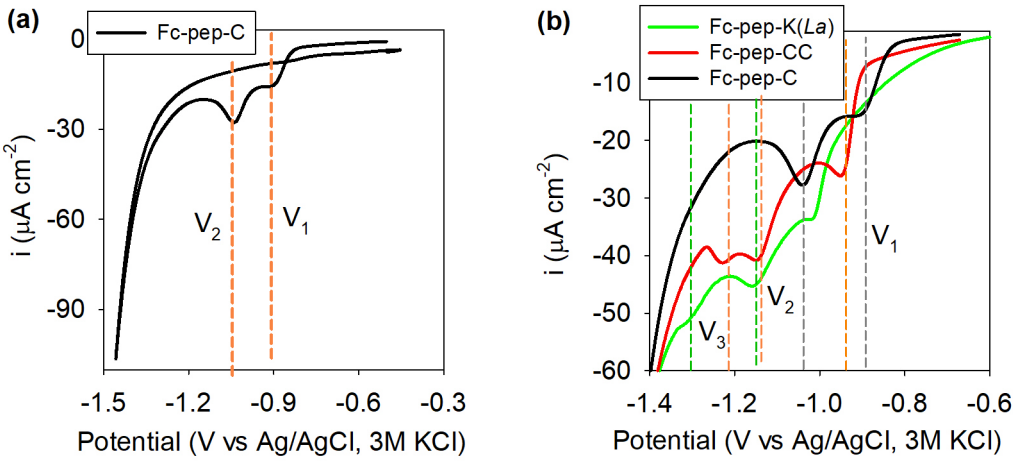

Figure G.1: (a) CV of the first cycle of Fc-pep-C SAM, recorded in 0.1 M NaOH at a scan rate of 0.01 V s^{-1}. (b) Superposition of the cathodic window from -0.8 to -1.4 V corresponding with the first cycle of CV of the three peptide SAM. The potential peaks, labeled from less negative to more negative, are denoted as V_1, V_2, and V_3. The plots illustrate measurements from a single modified working electrode. However, this study involved measurements from two different modified electrodes for each peptide SAM. The duplicate stripping measurements for each peptide SAM are presented in Figure G.2

Source: Author

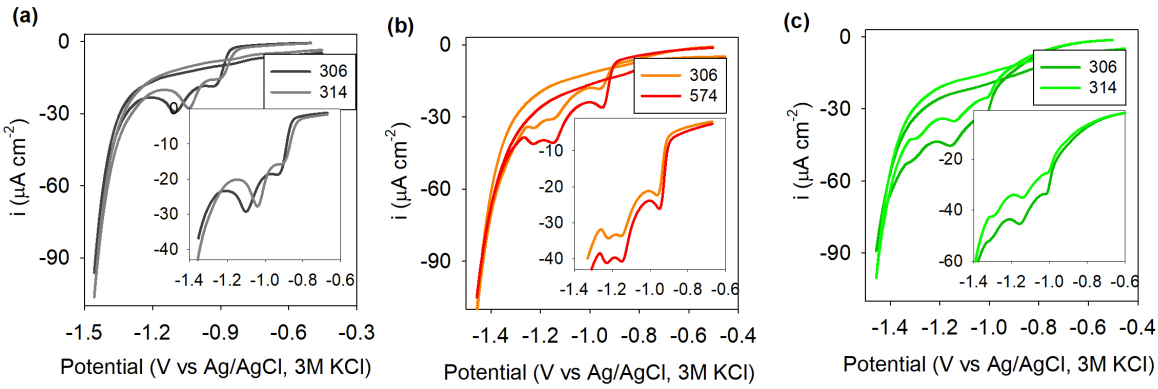

Figure G.2: Duplicate stripping measurements for each peptide SAM. The inset in each plot provides a zoomed-in view of the region highlighting the reductive peaks attributed to the SAM desorption.

Source: Author

Appendix H

Kinetic constant via Laviron's method

CV at different scan rates, where the condition $\Delta V_p \geq 200,\text{mV}$ was met, was performed to determine k using Laviron's method. V_{pa} and V_{pc}, were plotted against $\log(s)$. The slope of the linear regression was used to calculate the parameter α. The equilibrium charge dynamic states s_a and s_c were determined by extrapolating the linear branches to V_F. k was then calculated using Equations 2.1 and 2.2.

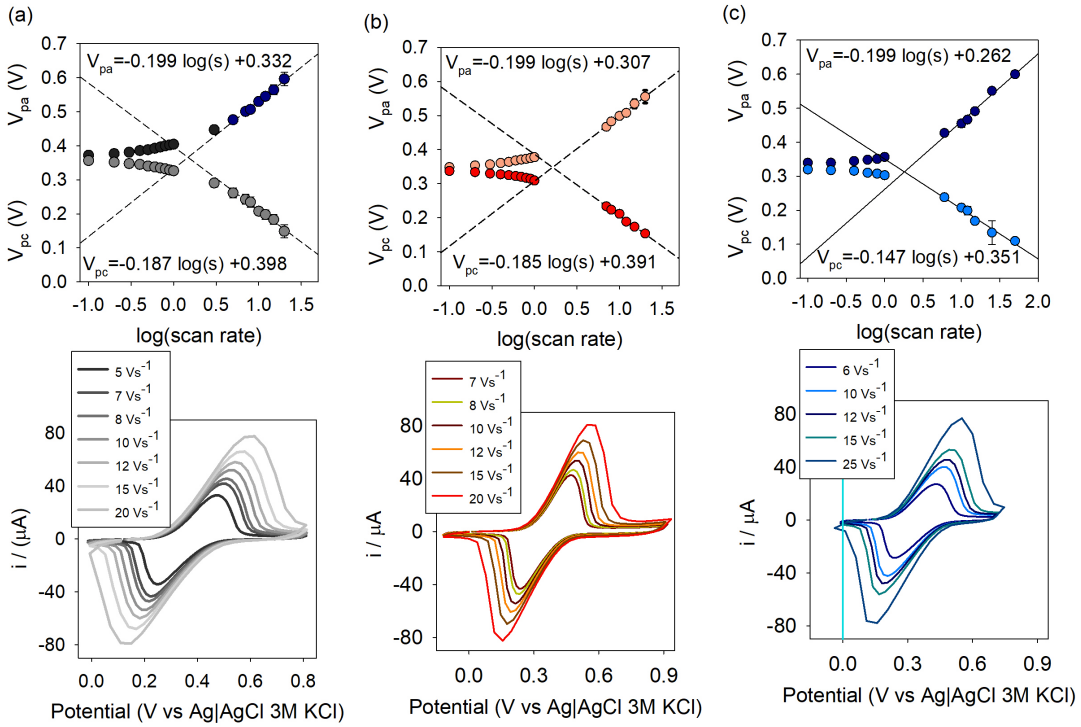

Figure H.1: At the top are plots of V_p versus the $\log(s)$ for electrodes modified with (a) Fc-pep-C, (b) Fc-pep-CC, and (c) Fc-pep-K(L_a) SAM. These were generated by extracting the V_{pa} and V_{pc} corresponding to the highest faradaic currents from the CV shown below, which were performed at different s. The CV was conducted in a solution of 20 mM $TBAClO_4$ in ACN/H_2O (1:4, v/v). The data points in the top plots represent the average of three independently modified electrodes, with error bars included. The bottom plots show representative current-potential curves for a single modified electrode from each SAM.

Source: Author

Appendix I

Capacitance-potential curves obtaining from CV and circuit elements from EIS data

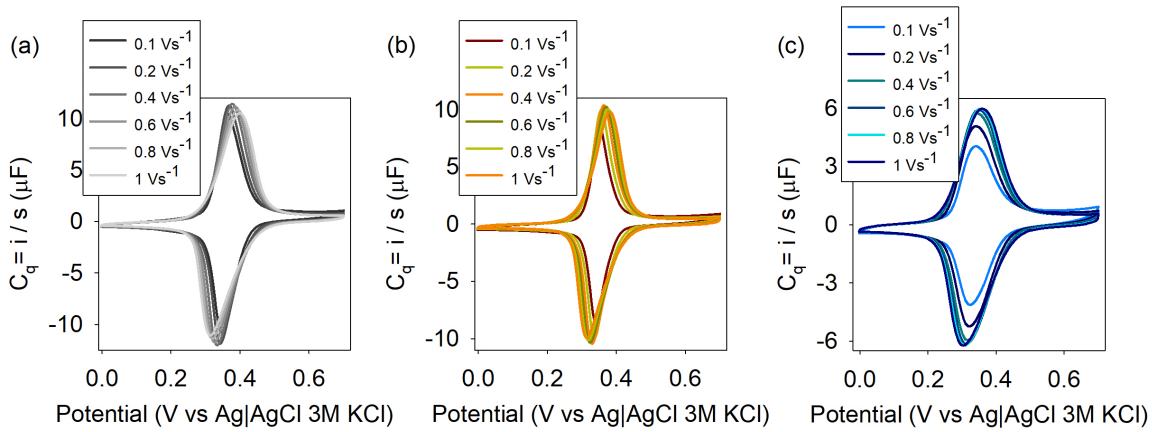

Figure I.1: Capacitance-potential curves for electrodes modified with SAMs of (a) Fc-pep-C, (b) Fc-pep-CC, and (c) Fc-pep-K(L_a). These curves were obtained by normalizing the current-potential data by the s, at scan rates lower than 1 V s^{-1}, according to the relation $C = i/s$. The normalized curves converge into a single master curve. The capacitance values, C_{qa} and C_{qc}, were determined at V_F.

Source: Author

Table I.1: Equivalent circuit elements obtained by fitting the raw impedance data using the equivalent circuit shown in Fig. 2.2 for the three SAMs with different linker groups

Parameter	Fc-pep-C	Fc-pep-CC	Fc-pep-K(L_a)
$R_t(k\Omega)$	0.77 ± 0.03	0.44 ± 0.01	0.90 ± 0.17
C_m (μF cm^{-2})	1.6 ± 0.1	2.4 ± 0.0	2.8 ± 0.1
C_t (μF cm^{-2})	3.9 ± 0.4	5.3 ± 0.0	5.2 ± 0.2
$R_s(\Omega)$	$1{,}992 \pm 29$	$1{,}935 \pm 68$	$1{,}968 \pm 20$
R_{qt} (Ω)	52 ± 10	50 ± 9	44 ± 2

Appendix J

Fc-ECC characterization

The peptide Fc-Glu-Cys-Cys-NH_2, was obtained with a retention time of 14.67 min and with a purity higher than 96.6% (HPLC, under linear gradient 5% to 95% of solvent B, 30 min at 1 mL min^{-1}, UV detection at 220 nm). Its identity was confirmed by ESI-MS, which showed a predominant peak corresponding to the theoretical molar mass of 591 g mol^{-1}.

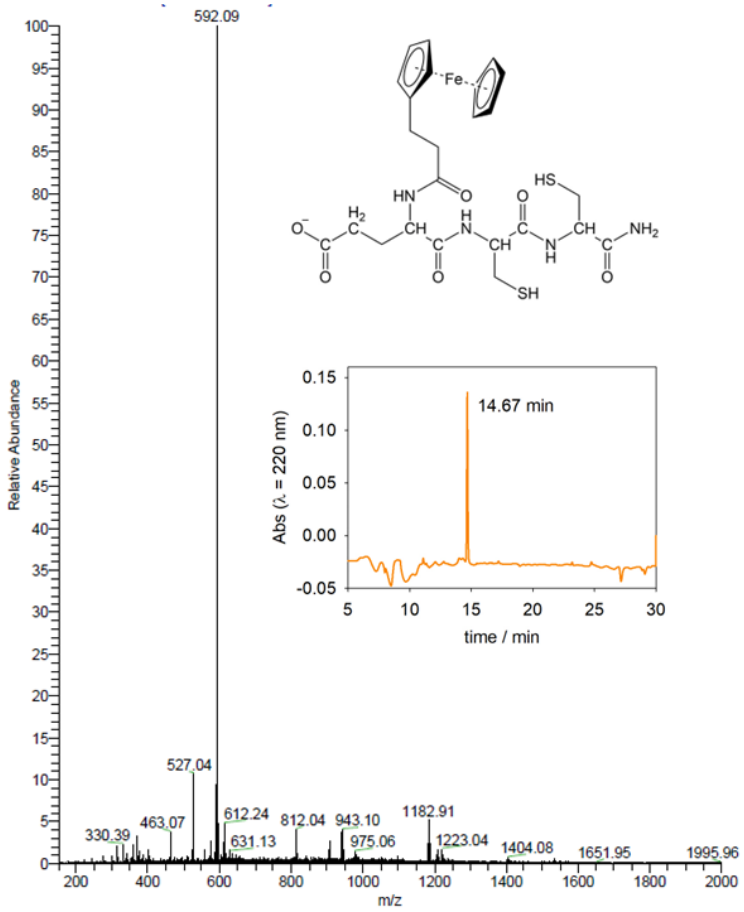

Figure J.1: Mass spectrum in positive mode: 592.09 m/z. Inset, The skeletal structural formula, and the chromatogram of the purified peptide.

Source: Author (2024)

Appendix K

Fc-EAAQAACC characterization

The peptide Fc-Glu-Ala-Ala-Gln-Ala-Ala-Cys-Cys-NH_2, was obtained with a retention time of 15.67 min and with a purity higher than 91% (HPLC, under linear gradient 5% to 95% of solvent B, 30 min at 1 mL min^{-1}, UV detection at 220 nm). Its identity was confirmed by ESI-MS, which showed a predominant peak corresponding to the theoretical molar mass of 1004.9 g mol^{-1}.

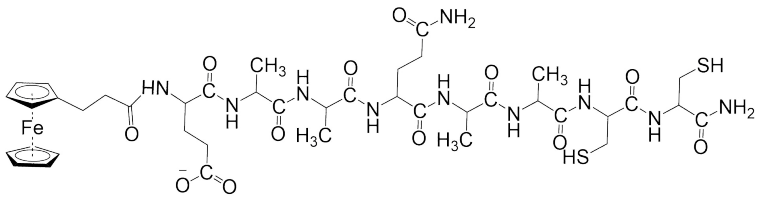

(a)

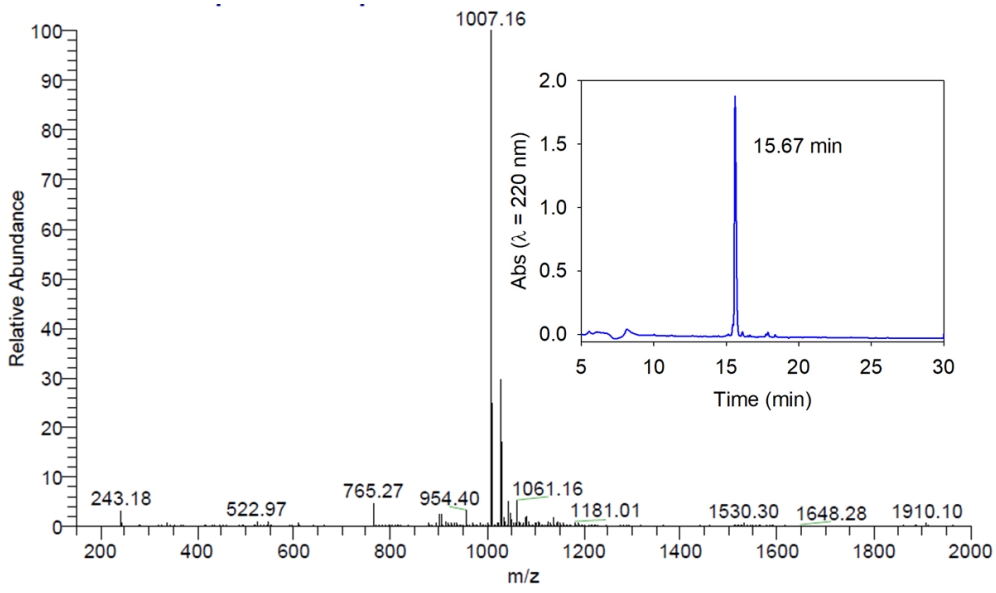

(b)

Figure K.1: (a) The skeletal structural formula of peptide, and (b) Mass spectrum and chromatogram profiles (inset) of the purified peptide.

Source: Author (2024).

Appendix L

Fc-EAAQAAQAACC characterization

The peptide Fc-Glu-Ala-Ala-Gln-Ala-Ala-Gln-Ala-Ala-Cys-Cys-NH_2, was obtained with a retention time of 15.3 min and with a purity higher than 78% (HPLC, under linear gradient 5% to 95% of solvent B, 30 min at 1 mL min^{-1}, UV detection at 220 nm). Its identity was confirmed by ESI-MS (negative mode), which showed a predominant peak corresponding to the theoretical molar mass of 1274 g mol^{-1}.

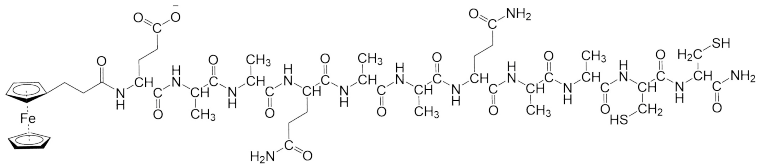

(a)

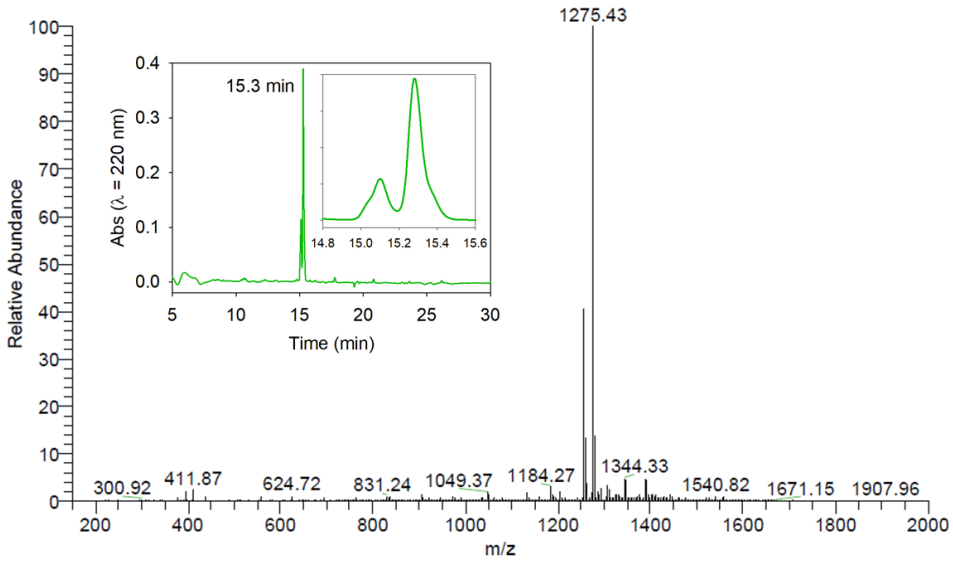

(b)

Figure L.1: (a) The skeletal structural formula of peptide, and (b) Mass spectrum and chromatogram profiles (inset) of the purified peptide.

Source: Author (2024).

Appendix M

Characterization of diffusionless ET: peptide-bridge study

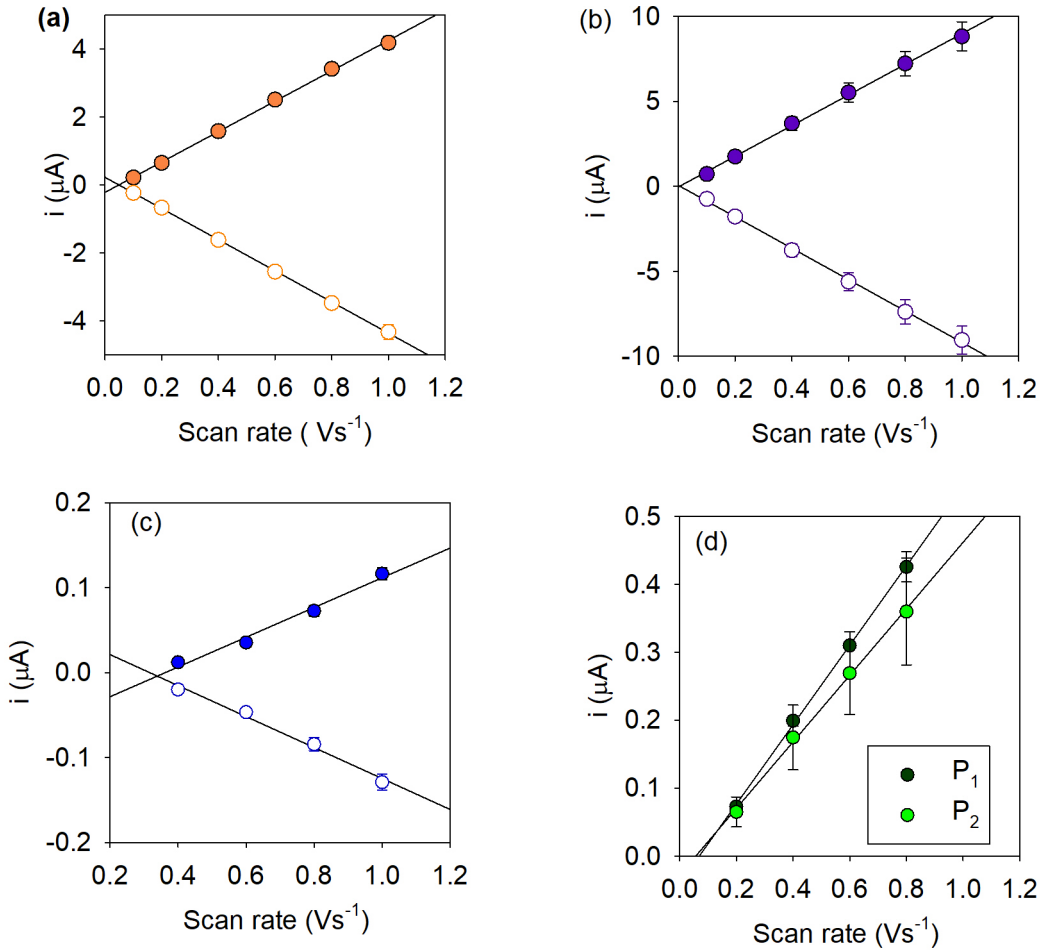

Figure M.1: Plots of i_{pa} and i_{pc} versus s are shown for (a) Fc-3aa, (b) Fc-5aa, and (c) Fc-8aa SAMs. For (d) Fc-11aa SAM, only the i_{pa} versus s plot is presented, where i_{pa} was obtained after deconvolution of two process, P1 and P2. The plots represent average values with error bars, based on measurements from three different modified electrodes for each electroactive peptide SAM.

Source: Author (2024)

Appendix N

Circuit elements- Bode plot

Table N.1: Equivalent circuit elements obtained by fitting the raw impedance data using the equivalent circuit shown in Fig. 2.2 (Chapter 2) for the four redox-tagged peptide SAMs. The R_q was determined as the combined contribution of R_s and R_{qt}, according to $R_q = 2\pi(R_s + R_{qt})$

Parameter	Fc-3aa	Fc-5aa	Fc-8aa	Fc-11aa
$R_t(k\Omega)$	0.8 ± 0.1	0.44 ± 0.01	0.8 ± 0.4	2.4 ± 0.9
C_m (μF)	0.15 ± 0.01	0.11 ± 0.00	0.14 ± 0.03	0.13 ± 0.01
C_t (μF)	0.35 ± 0.03	0.23 ± 0.02	0.16 ± 0.05	0.20 ± 0.02
$R_s(\Omega)$	$1{,}751 \pm 15$	$1{,}935 \pm 68$	$2{,}004 \pm 163$	$6{,}168 \pm 1{,}298$
				$6{,}163 \pm 1{,}303$
R_{qt} (Ω)	59 ± 6	50 ± 9	241 ± 46	551 ± 91
				507 ± 178

Appendix O

^{1}H NMR of compounds 1a and 2a

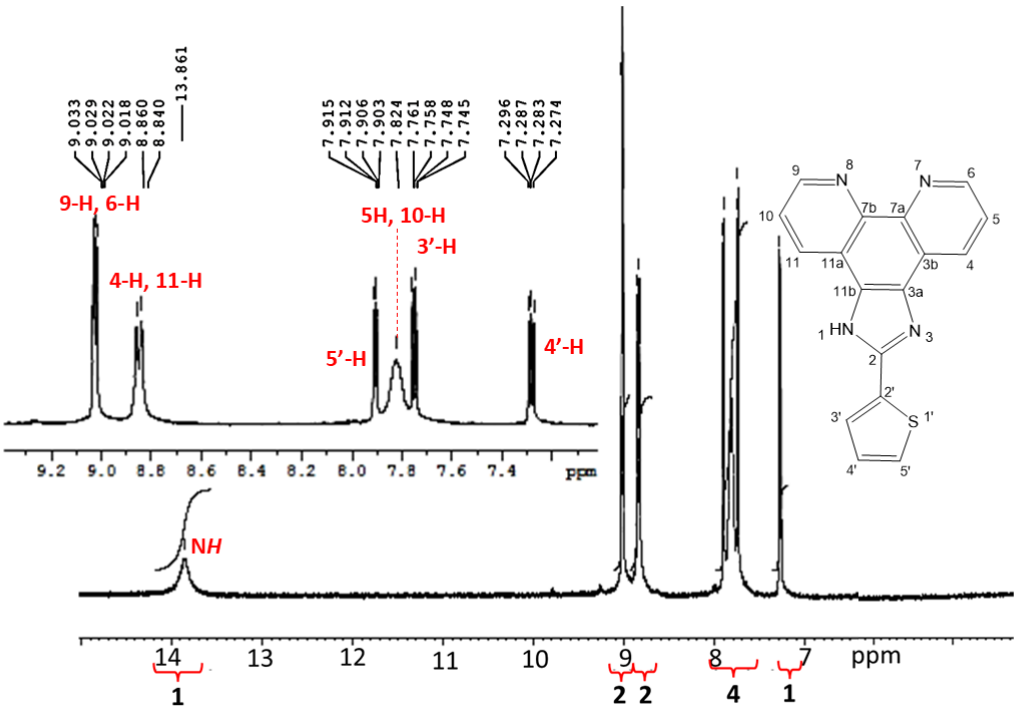

Figure O.1: ^{1}H NMR spectrum of **1***a*: 2-(thiophen-2-yl)-1*H*-imidazo[4,5-*f*][1,10]phenanthroline (DMSO-d_6, 400 MHz).

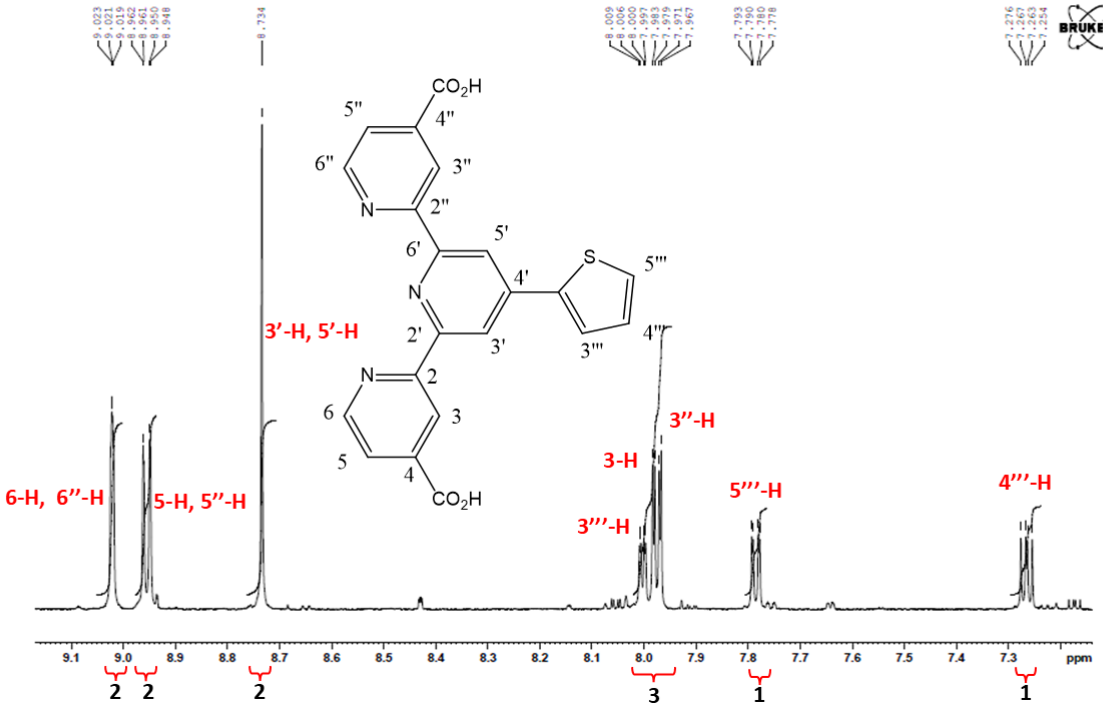

Figure O.2: ^{1}H NMR spectrum of **2***a*: 4′-(thiophen-2-yl)-[2,2′:6′,2″-terpyridine]-4,4″-dicarboxylic acid dissolved in DMSO-d_6 and 2 drops of TFA at 400 MHz.

Appendix P

^{1}H NMR of the reaction mixtures of the attempted synthesis of compounds 1b and 2b

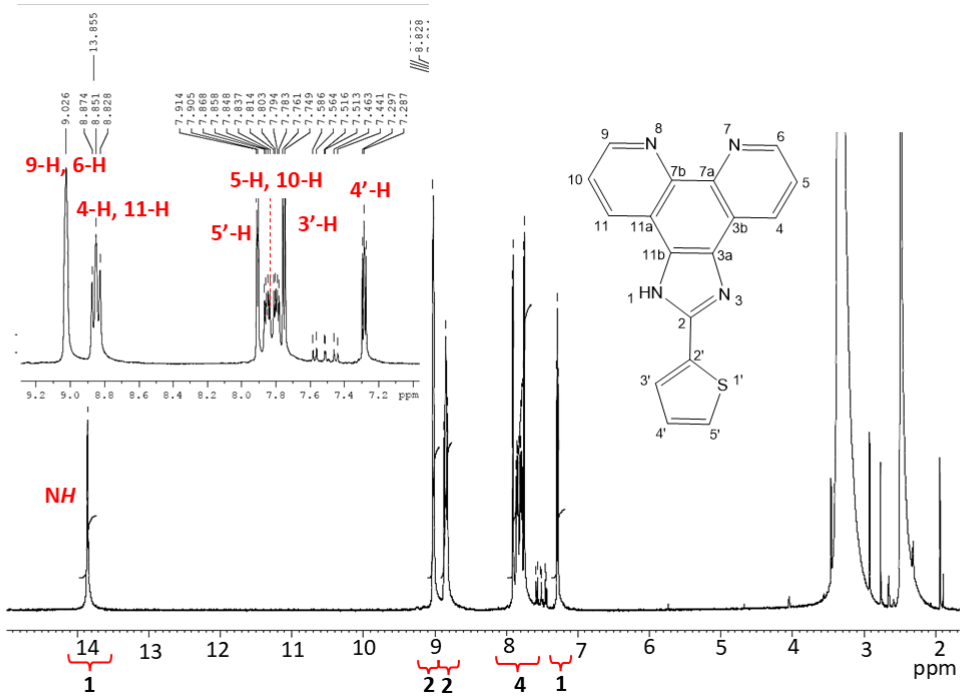

Figure P.1: ^{1}H NMR spectrum of the reaction mixture of the attempt of synthesis of **1***b* from which only precursor **1***a* was identified (DMSO-d_6, 400 MHz).

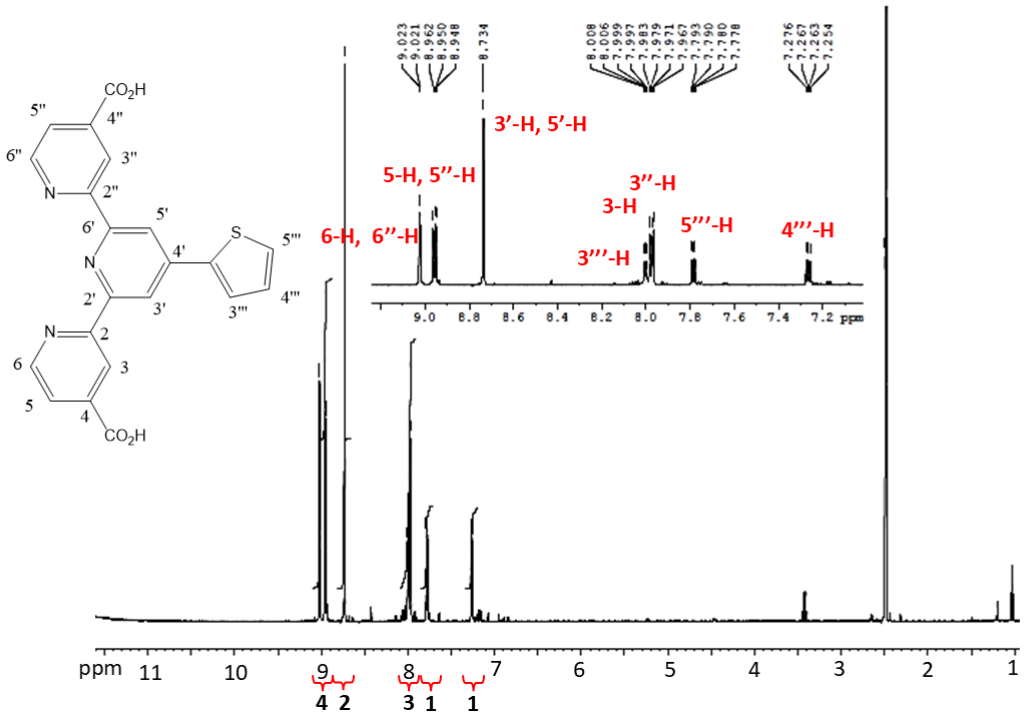

Figure P.2: ^{1}H NMR spectrum of the reaction mixture of the attempt of synthesis of **2***b* from which only precursor **2***a* was identified (DMSO-d_6 and 2 drops of TFA at 400 MHz).

Appendix Q

^{1}H NMR of compound 1b-*1*

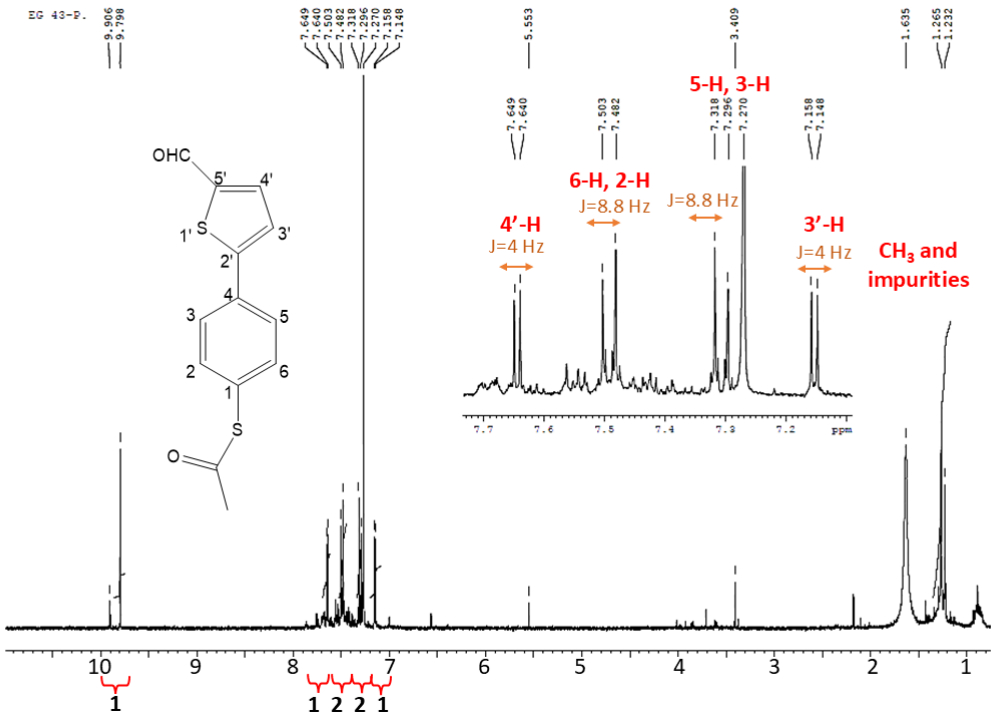

Figure Q.1: ^{1}H NMR spectrum in $CDCl_3$ with expanded aromatic region of compound **1***b-1* (400 MHz).

Appendix R

^{1}H NMR of compounds 3a, 3b, and byproduct [2,2′-bithiophene]-5,5′-dicarbaldehyde

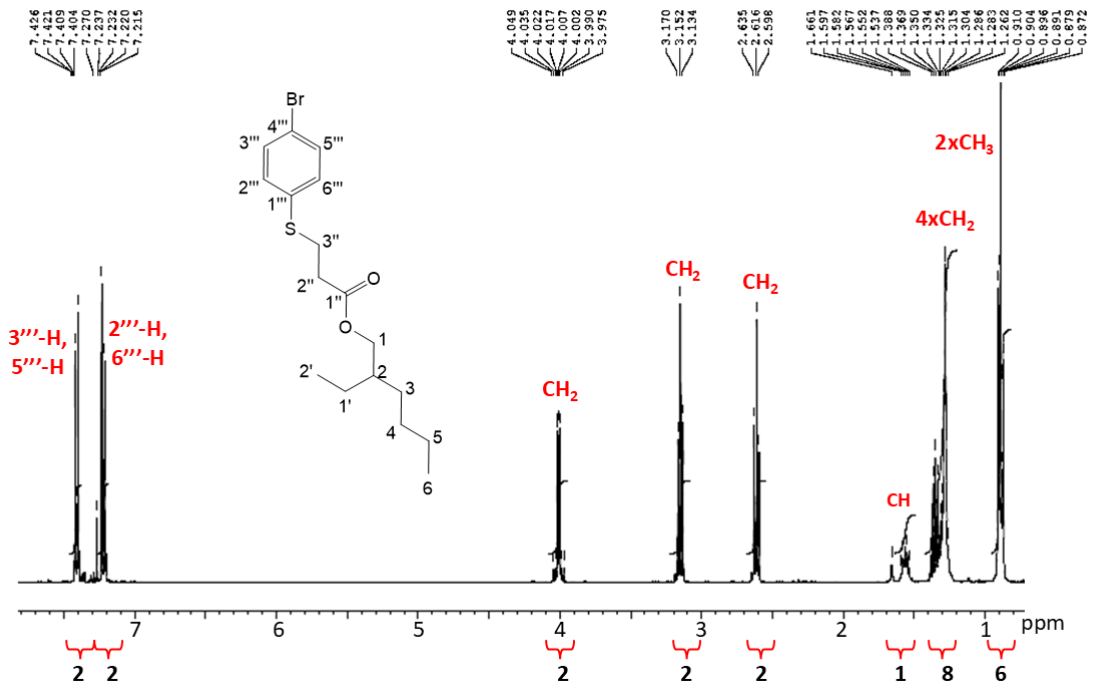

Figure R.1: ^{1}H NMR spectrum in $CDCl_3$ of **3***a* (400 MHz).

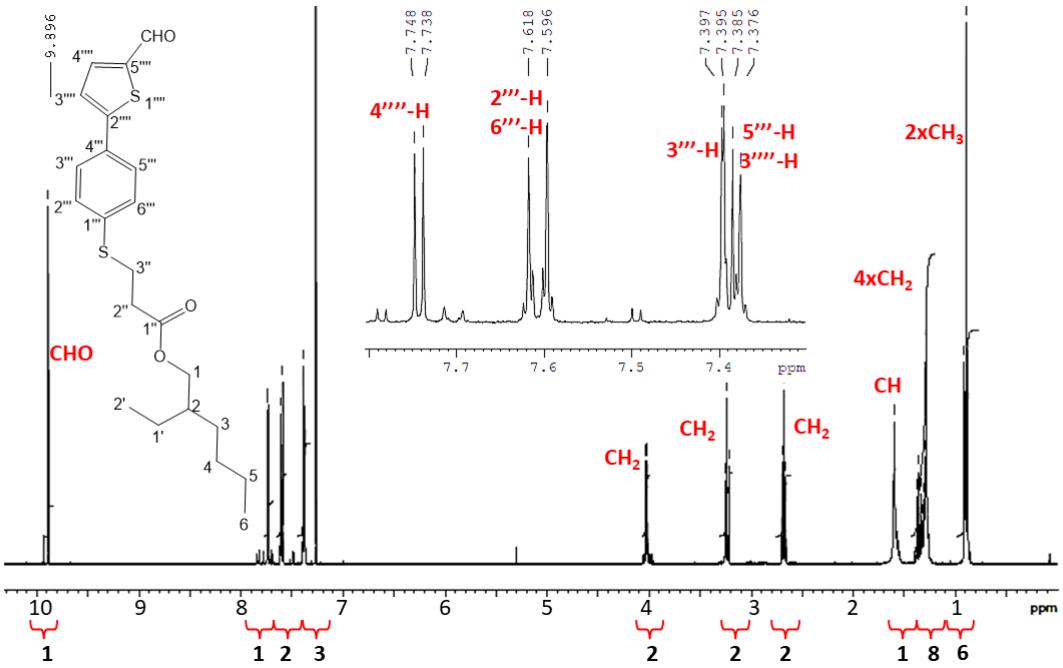

Figure R.2: ^{1}H NMR spectrum in $CDCl_3$ with expanded aromatic region of **3***b* (400 MHz).

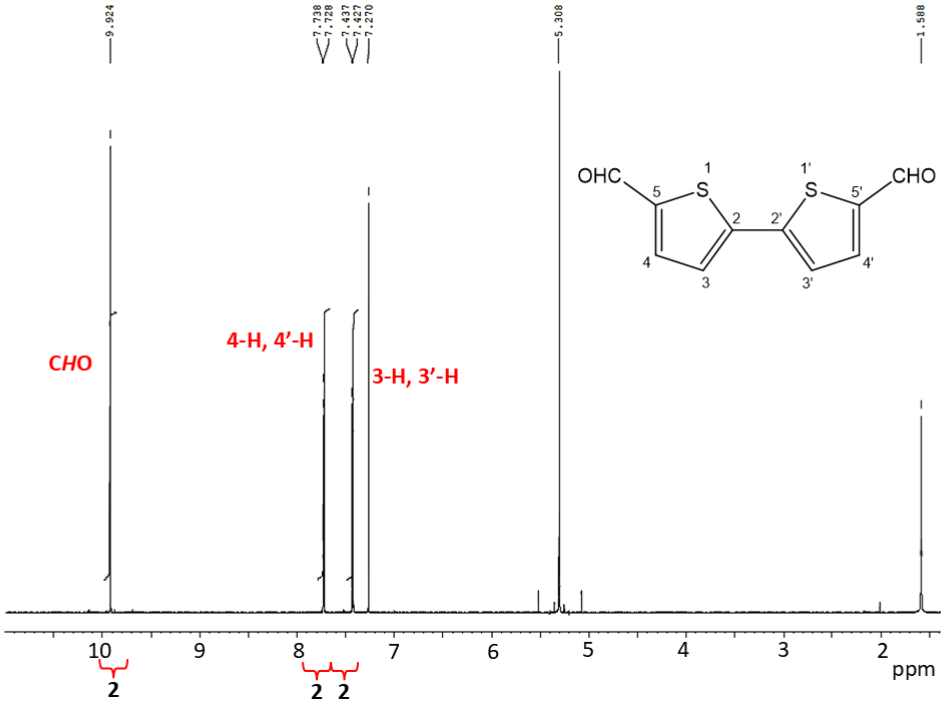

Figure R.3: ^{1}H NMR spectrum in $CDCl_3$ of the byproduct [2,2′-bithiophene]-5,5′-dicarbaldehyde obtained during the synthesis of **3***b*, (400 MHz).

Appendix S

^{1}H NMR and MS of compound 3c

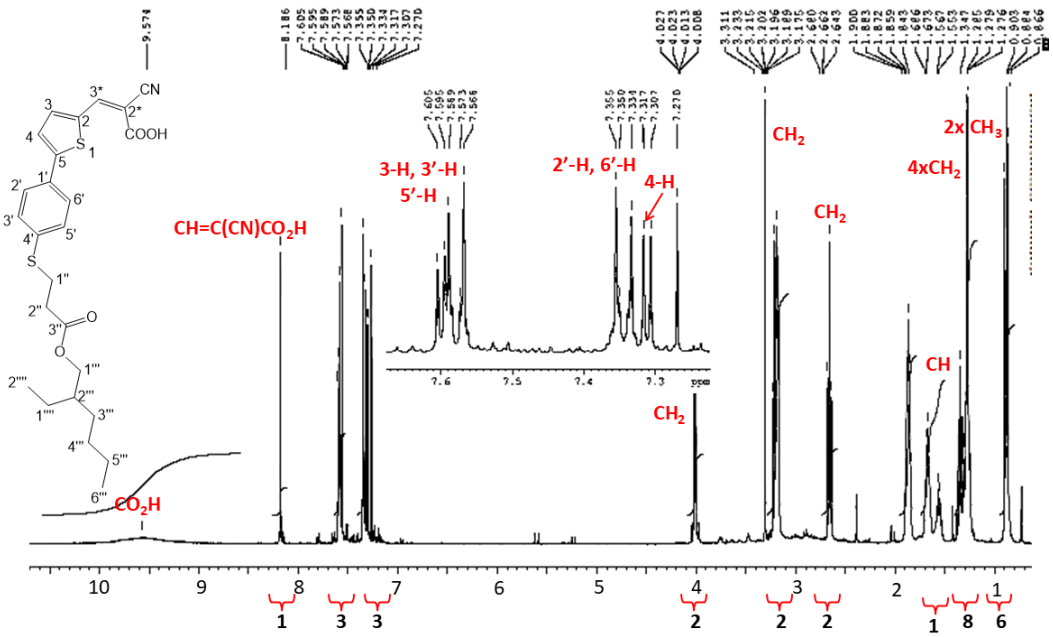

Figure S.1: ^{1}H NMR spectrum in $CDCl_3$ with expanded aromatic region of **3***c* (400 MHz).

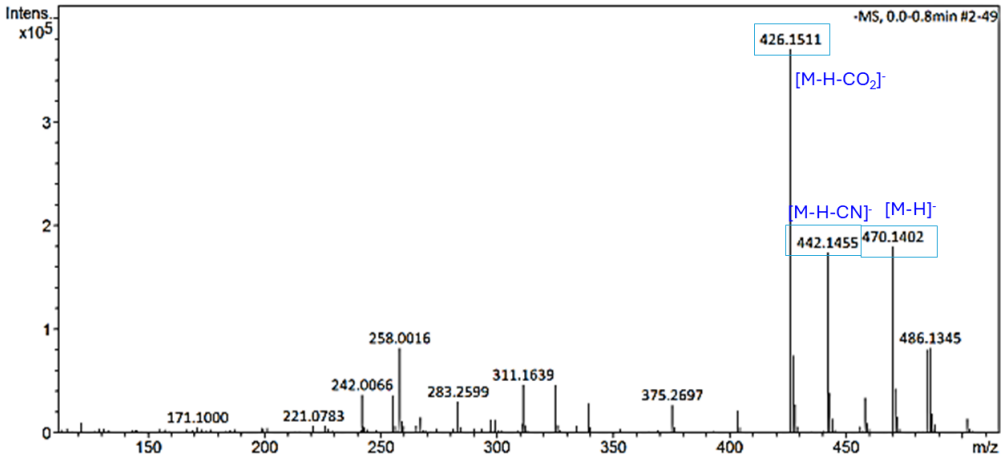

Figure S.2: Negative ion mass spectra at m/z 470 of compound **3***c*.

Appendix T

^{1}H NMR and HRMS of compound 4

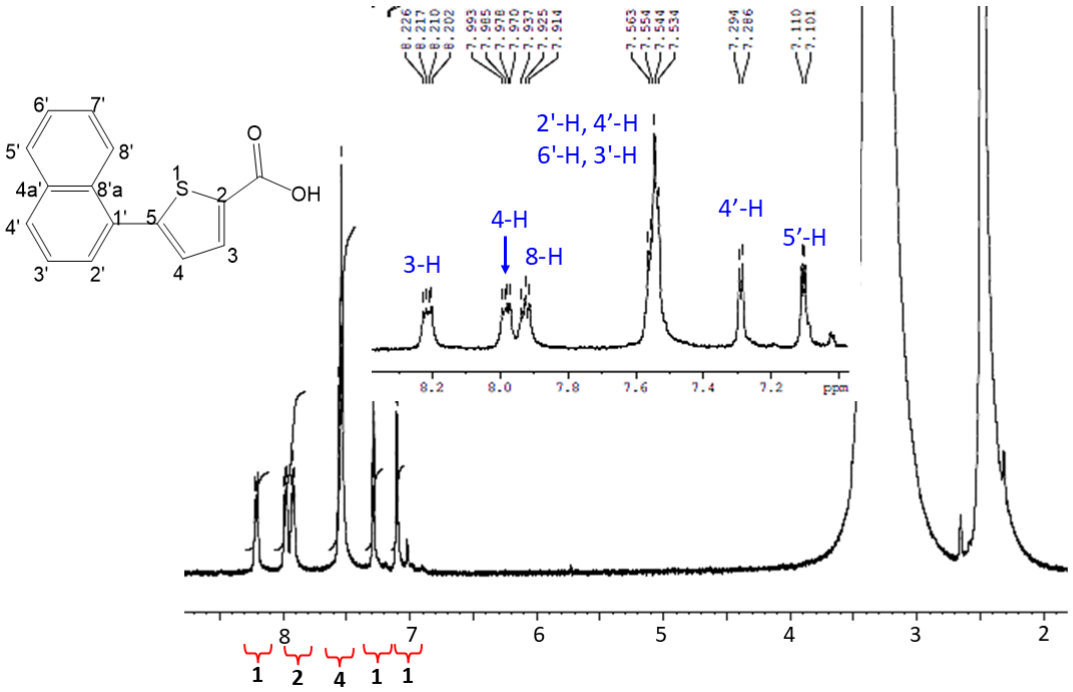

Figure T.1: ^{1}H NMR spectrum in DMSO-d_6 with expanded aromatic region of compound **4** (400 MHz).

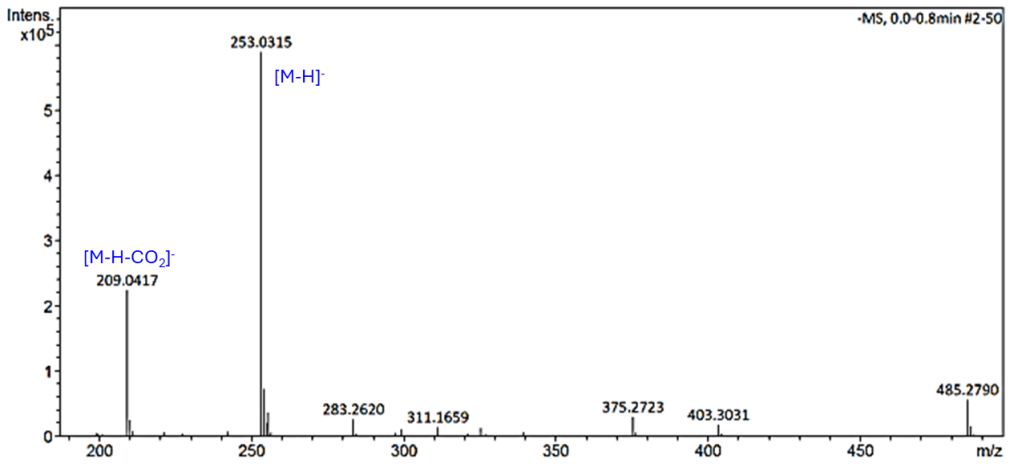

Figure T.2: Negative ion mass spectra at m/z 253 of compound **4**.

Appendix U

^{1}H NMR and MS of compound 5

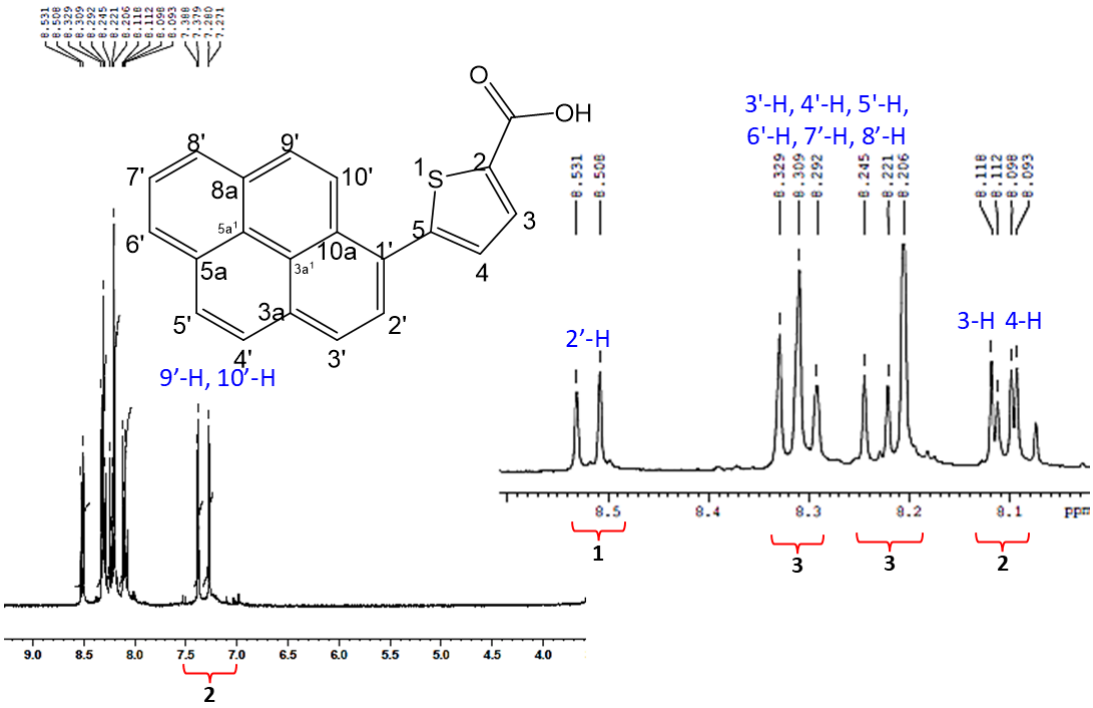

Figure U.1: ^{1}H NMR spectrum in DMSO-d_6 with expanded aromatic region of compound **5** (400 MHz).

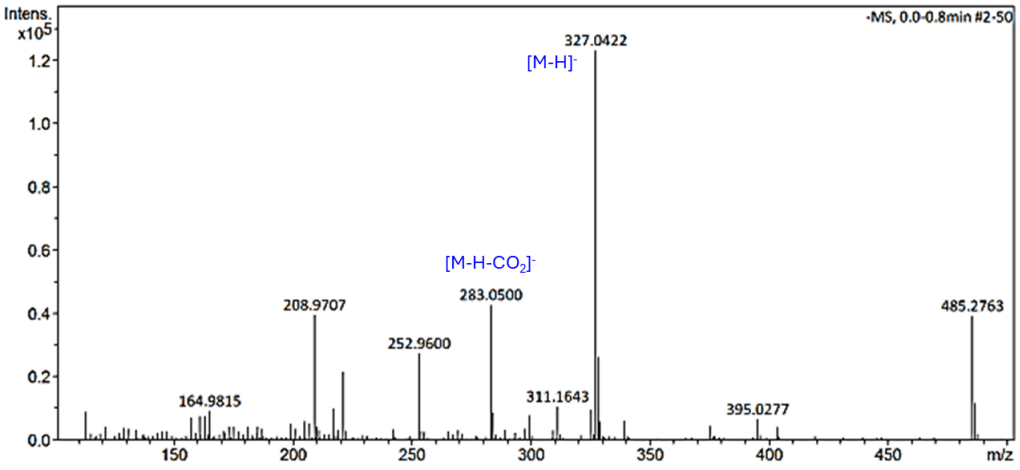

Figure U.2: Negative ion mass spectra at m/z 327 of compound **5**.

Appendix V

^{1}H NMR of compounds 6a and 6b

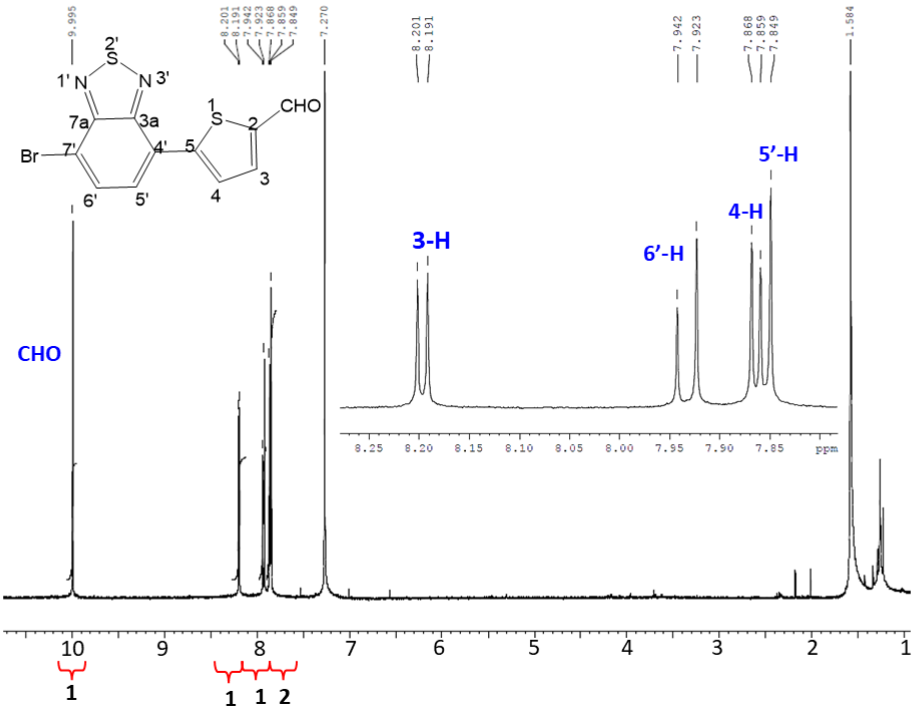

Figure V.1: ^{1}H NMR spectrum in $CDCl_3$ with expanded aromatic region of compound **6*a*** (400 MHz).

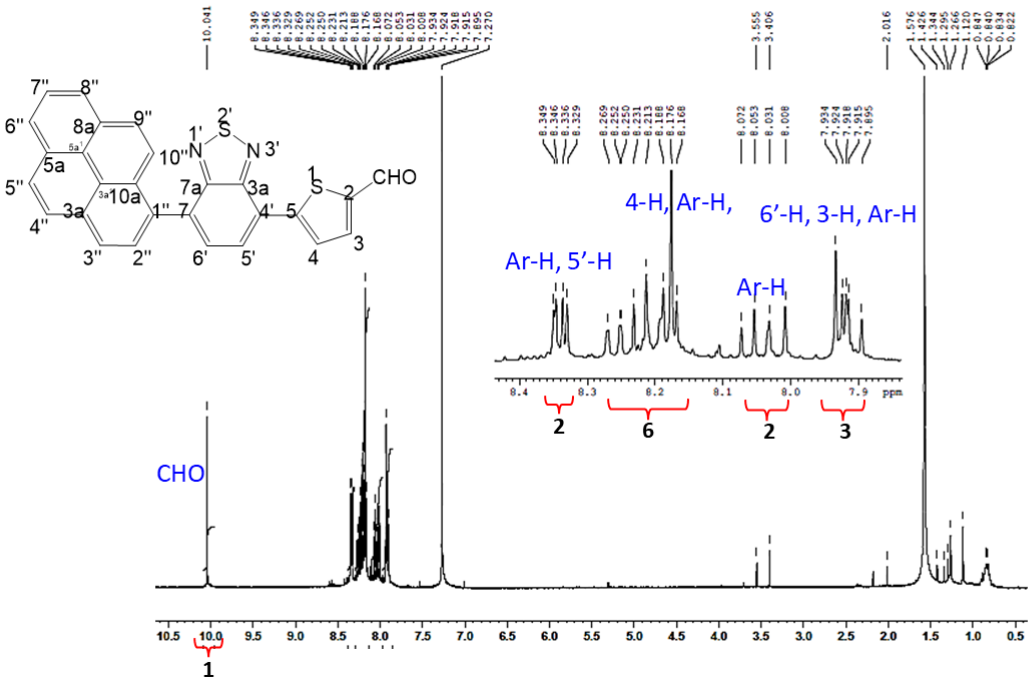

Figure V.2: ^{1}H NMR spectrum in $CDCl_3$ with expanded aromatic region of compound **6***b* (400 MHz).

Appendix W

^{1}H NMR and MS of compound 6

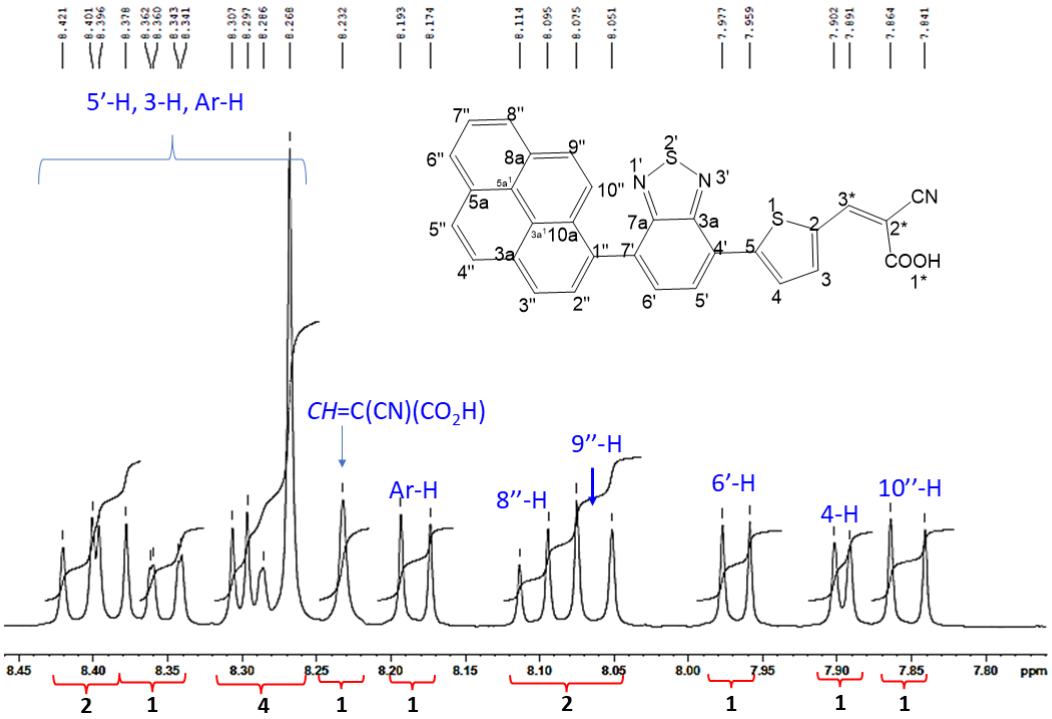

Figure W.1: Part of the expanded aromatic region of the ^{1}H NMR spectrum in DMSO-d_6 of compound **6** (400 MHz).

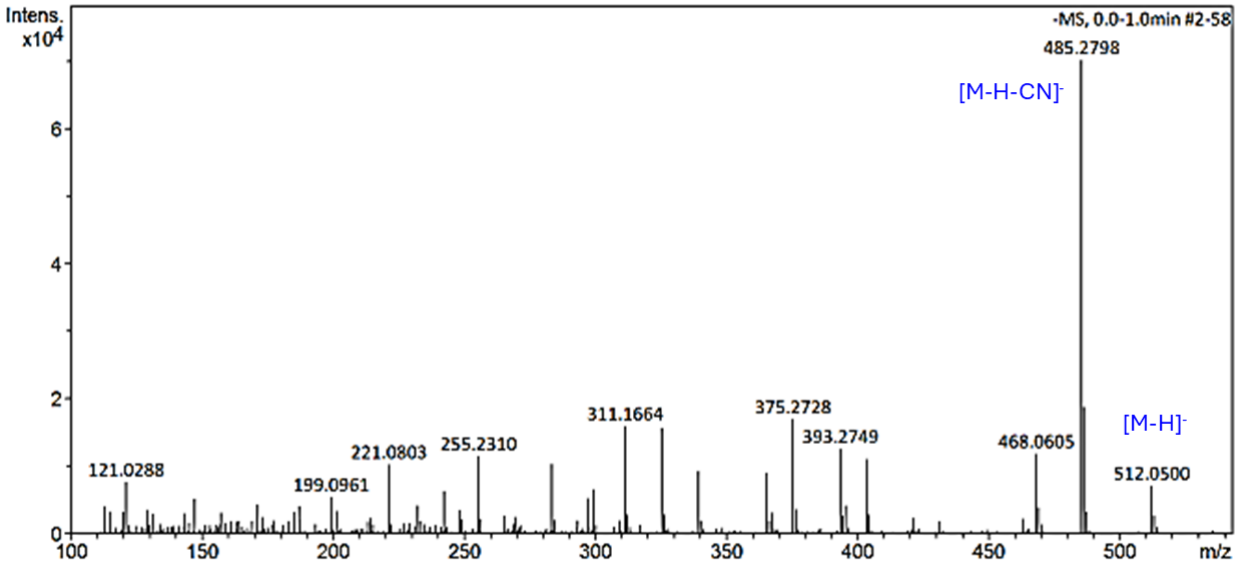

Figure W.2: Negative ion mass spectra at m/z 512 of compound **6**.

Appendix X

^{1}H NMR of compounds 7b and 7, and HRMS of compound 7

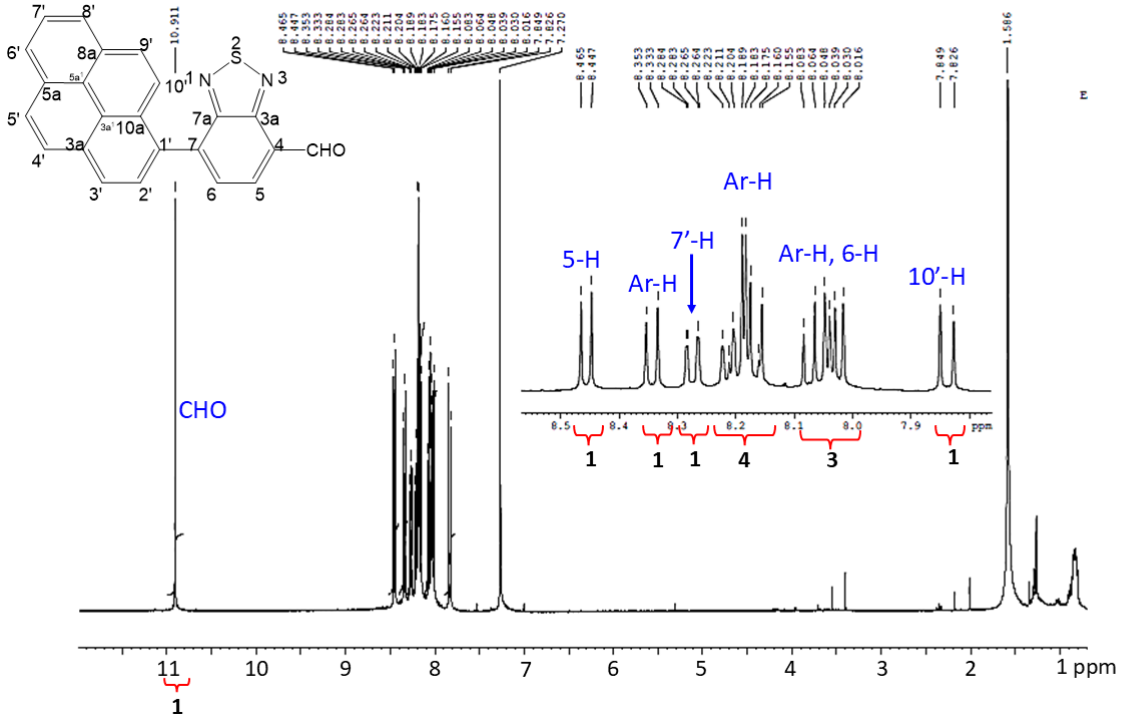

Figure X.1: ^{1}H NMR spectrum in $CDCl_3$ with expanded aromatic region of compound **7***b* (400 MHz).

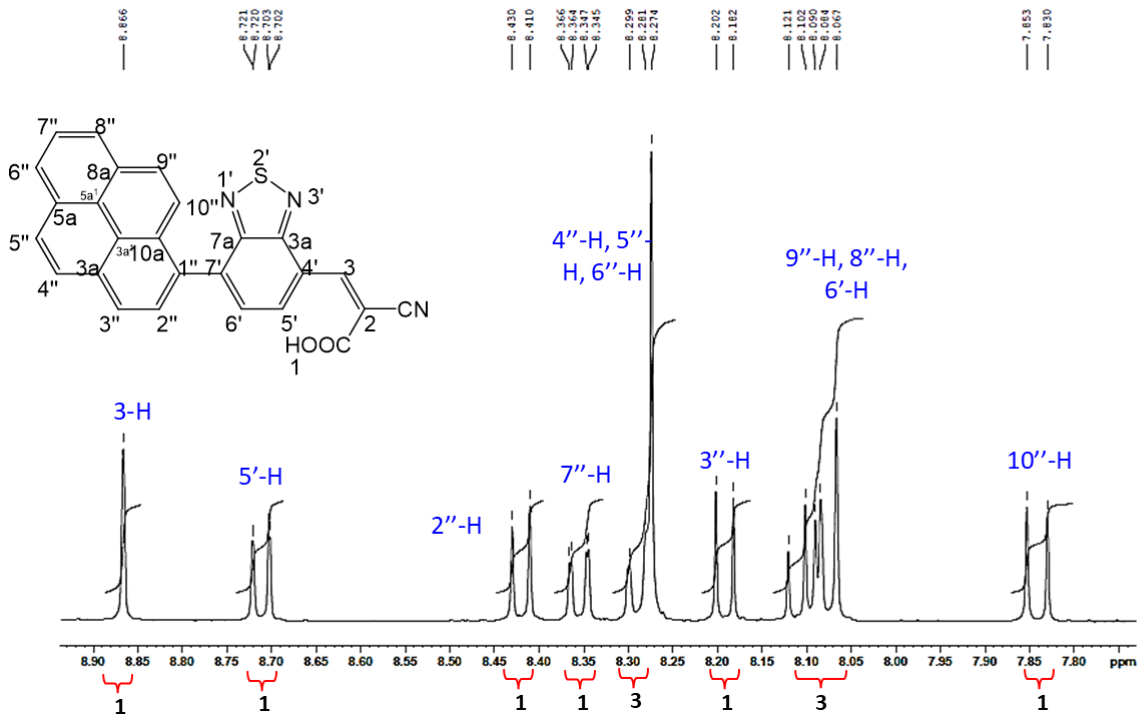

Figure X.2: Part of the aromatic expanded region of the ^{1}H NMR spectrum in DMSO-d_6 of compound **7** (400 MHz).

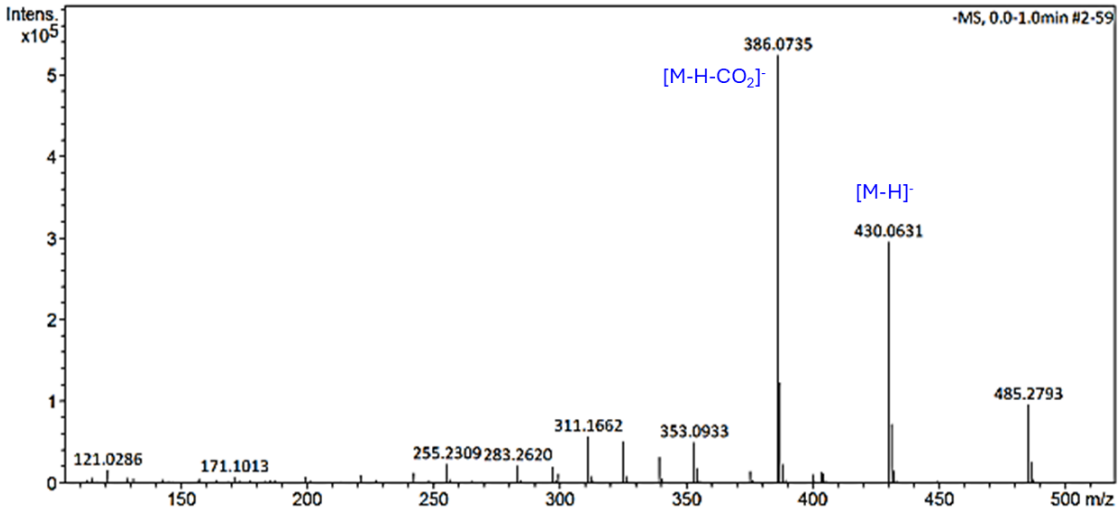

Figure X.3: Negative ion mass spectra at m/z 430 of compound **7**.

Appendix Y

^{1}H NMR of compounds 8b and 8, and MS of compound 8

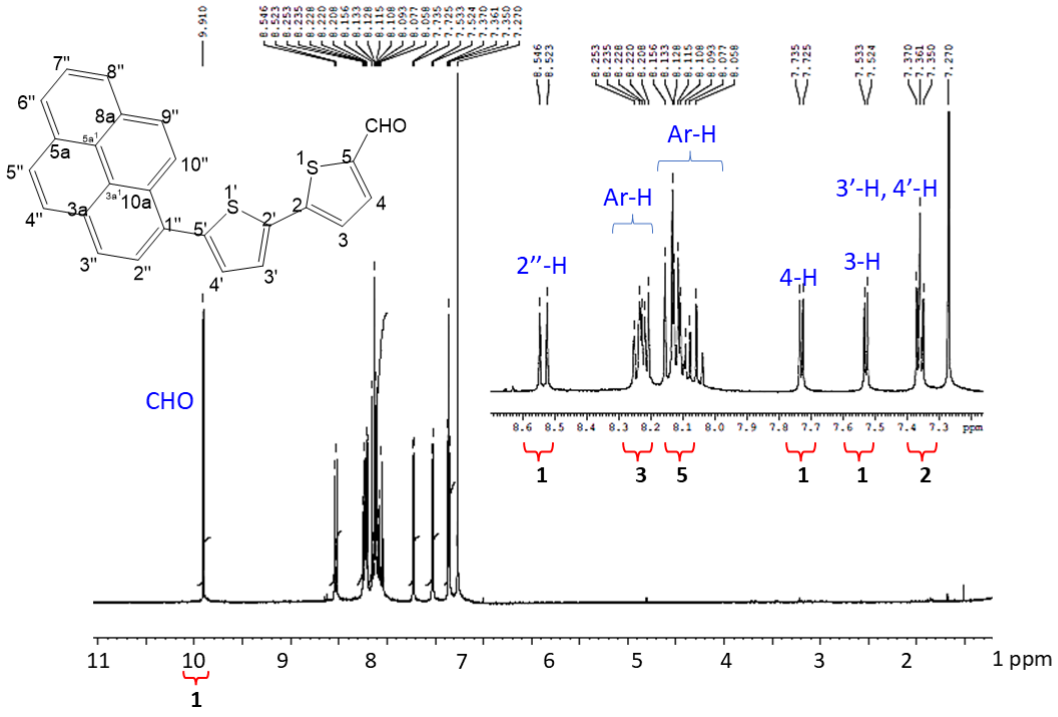

Figure Y.1: Part of the expanded ^{1}H NMR spectrum in $CDCl_3$ with expanded aromatic region of compound **8***b* (400 MHz).

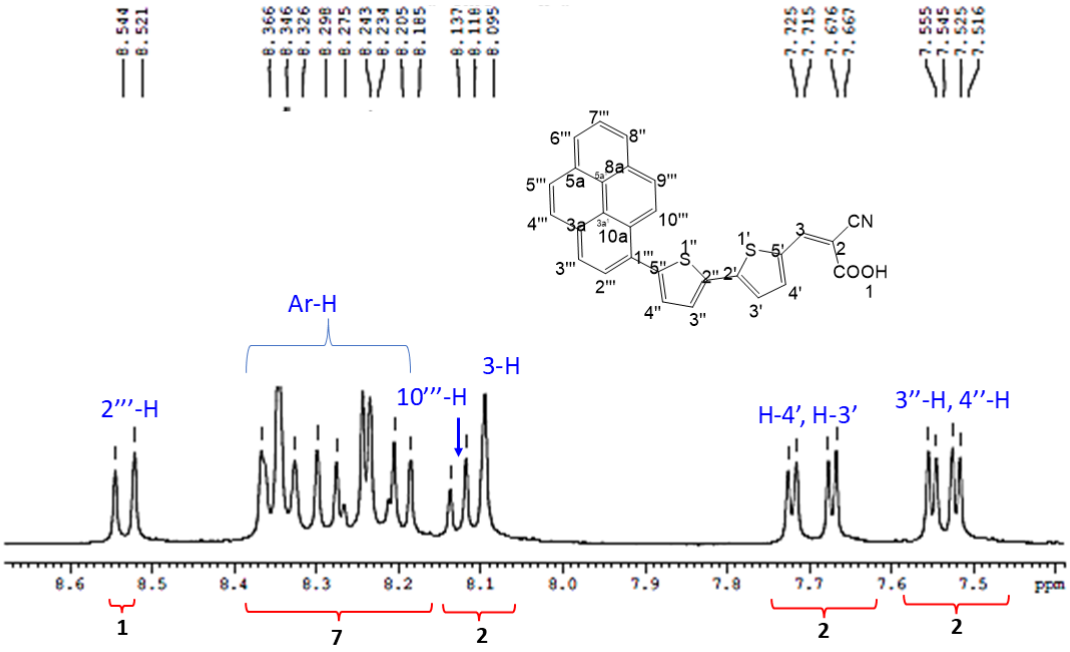

Figure Y.2: Part of the expanded aromatic region of the ^{1}H NMR spectrum in DMSO-d_6 of compound **8** (400 MHz).

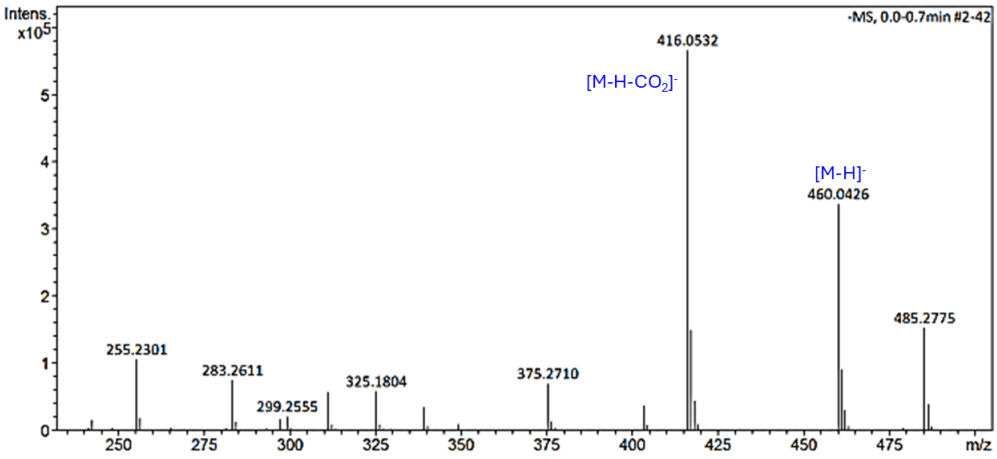

Figure Y.3: Negative ion mass spectra at m/z 460 of compound **8**.

Appendix Z

DOS profiles: molecule-SLG interfaces

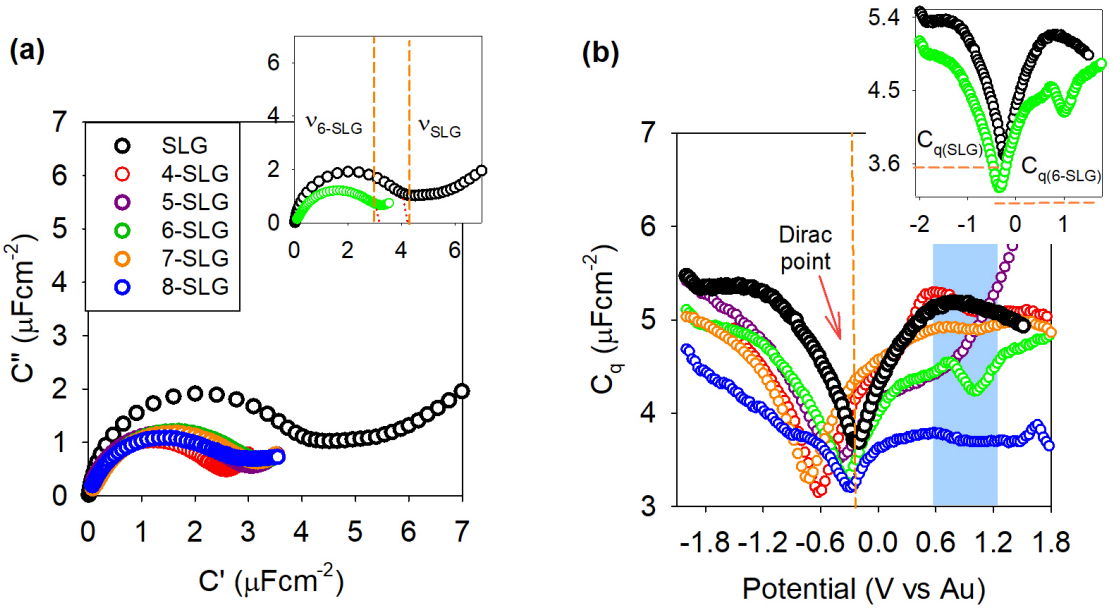

Figure Z.1: (a) Capacitive Nyquist plot acquired at OCP, recorded for both the pristine SLG and the *push-pull* heterocyclic molecules assembled on SLG, immersed in phosphate buffer (PB) solution. *Inset:* Nyquist plot comparing pristine SLG with the **6**-SLG interface, included to better highlight the differences in ν. (b) The $DOS = C_q/e^2$, revealed by applying ν and measuring the C_q as a function of electrode potential for the pristine SLG and the molecular assemblies shown in (a), where the potential region of the new contribution of the molecular coupling is indicated by a blue-shaded box. *Inset:* DOS of pristine SLG contrasted with the **6**-SLG interface, where an additional V-shaped feature with a minimum C_q attributed to molecular coupling, is noticed. Additionally, a decrease in C_q at the Dirac point was identified. The notation for the interfaces corresponds to the molecular numbering in Figure 5.5, followed by "-SLG". Thus, the monolayer formed by molecule **6** on SLG is denoted as **6**-SLG.

Source: Author (2024)

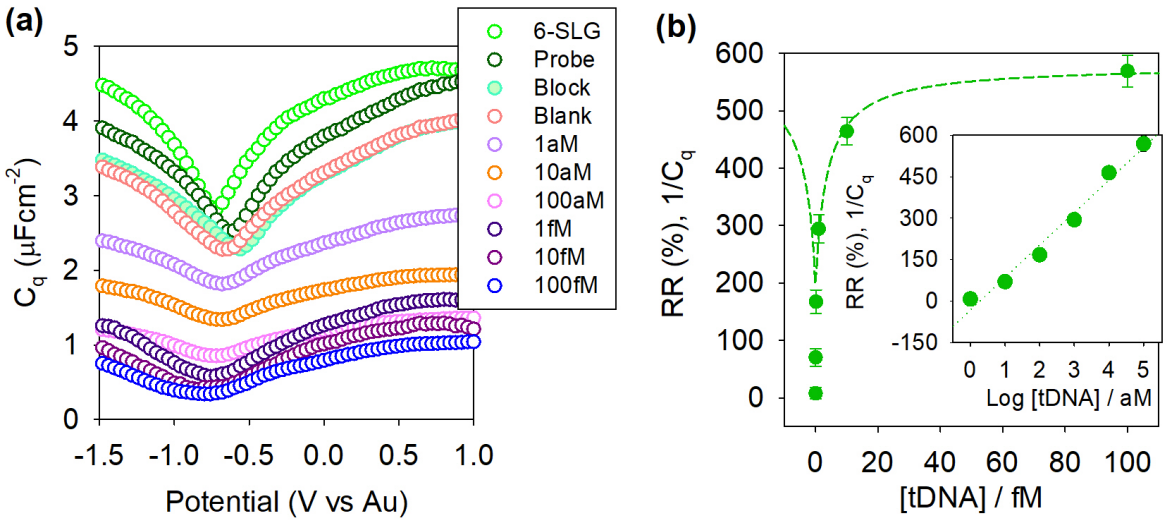

Figure Z.2: (a) C_q measured at *nu* as function of potential of electrode, conducted for the different stage of the interface construction: SLG modified with molecule **6**, DNA probe coupling, blank response, and incubation with six different concentrations of target DNA. (b) RR% response of 6-SLG as a function of target DNA concentration. *Inset:* Logarithmic scale of target DNA concentration.

Source: Author (2024)

Table Z.1: Equivalent circuit elements obtained by fitting the raw impedance data using the equivalent circuit shown in Fig. Z.4, for the four responses obtained at the Dirac point and molecular coupling point.

Parameter	Dirac point	Molecular coupling point
R_qt (kΩ)	1.45 ± 0.15	1.36 ± 0.03
C_∞ (μFcm^{-2})	0.04 ± 0.00	0.04 ± 0.00
C_q (μFcm^{-2})	0.61 ± 0.01	1.23 ± 0.08
R_s (Ω)	0.78 ± 0.08	0.66 ± 0.07

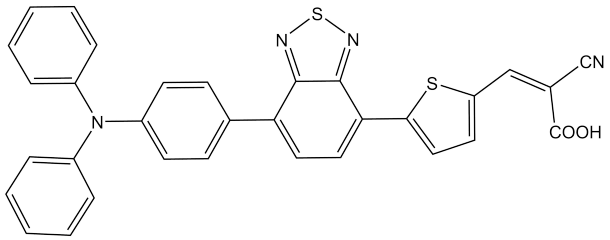

(a)

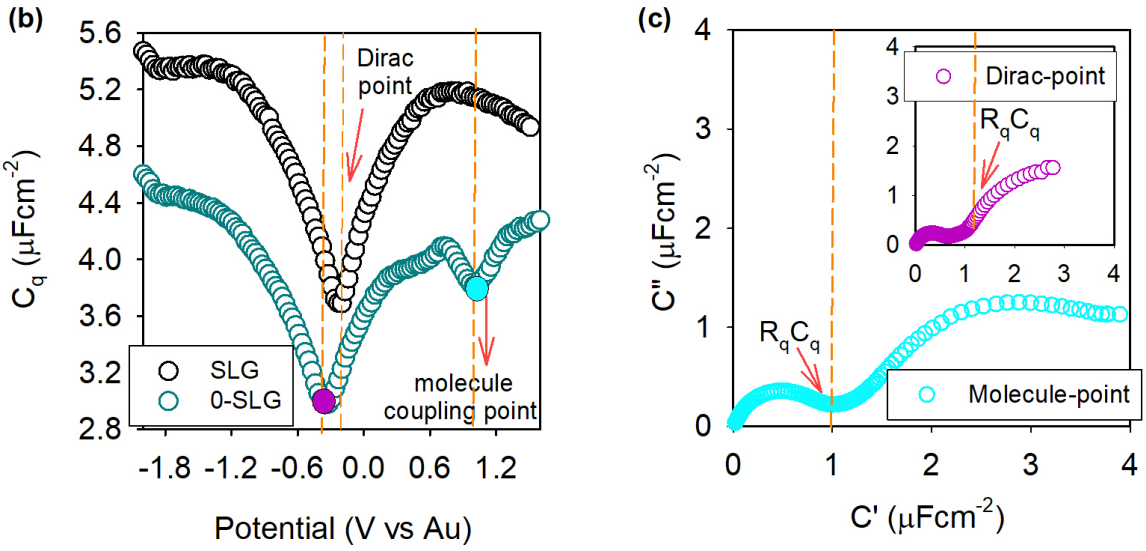

(b)

Figure Z.3: (a) *push-pull* heterocyclic molecule 0, provided by the research group of Prof. Maria Manuela Marques Raposo (FERNANDES *et al.*, 2018). (b) C_q measured at equilibrium (ν) as a function of the electrode potential, revealing the DOS of the interface for SLG and molecule **0**-SLG. The Dirac point is observed at -0.5 V, while the contribution from the coupling of the molecule becomes evident around 1.0 V. (c) The capacitive Nyquist diagram recorded for the **0**-SLG interface, obtained by applying the potentials of 0.1 V and, as shown in the inset, -0.5 V, as identified previously in (b). The quantum RC electrodynamics is identified at the first semicircle closes ($\tau = R_qC_q$). The measurements were carried out in electrolyte medium comprises of a PB solution.

Source: Author (2024).

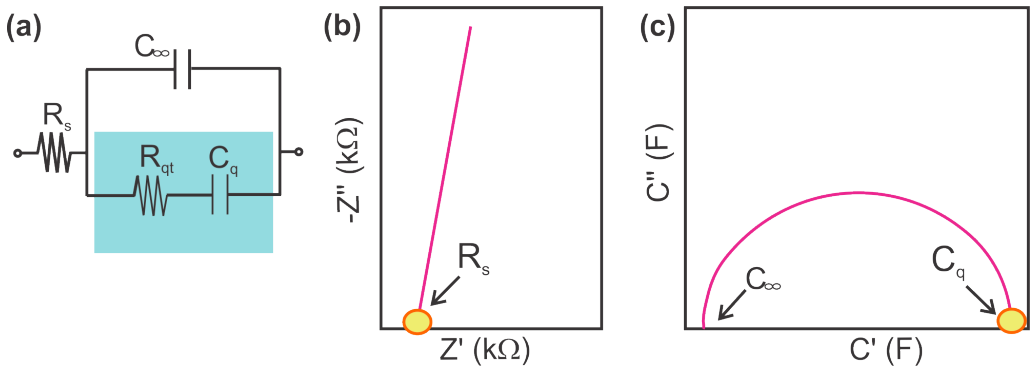

Figure Z.4: (a) Equivalent circuit that describes the electrodynamics of SLG-molecule system, which is governed by a quantum characteristic $\tau = R_q C_q$, where the total quantum resistive component Rq is determined by $Rq = 2\pi(R_{qt} + R_s)$. (b) Representation of an impedimetric Nyquist plot for the SLG surface, where R_s is identified at high frequencies. (c) Illustrative of complex capacitive diagram of (b) indicating the C_q at low frequencies and C_∞ at hight frequencies.

Source: Author (2024)